Modifications of SiO_x, TiO_2 and PDMS surfaces & their Interactions with DNA and Cell

By

Indrani Mishra

PHYS07200904005

Institute of Physics, Bhubaneswar

A thesis submitted to the
Board of Studies in Physical Sciences

In partial fulfillment of requirements
For the Degree of

DOCTOR OF PHILOSOPHY
of
HOMI BHABHA NATIONAL INSTITUTE

April, 2017

STATEMENT BY AUTHOR

This dissertation has been submitted in partial fulfillment of requirements for an advanced degree at Homi Bhabha National Institute (HBNI) and is deposited in the Library to be made available to borrowers under rules of the HBNI.

Brief quotations from this dissertation are allowable without special permission, provided that accurate acknowledgment of source is made. Requests for permission for extended quotation from or reproduction of this manuscript in whole or in part may be granted by the Competent Authority of HBNI when in his or her judgment the proposed use of the material is in the interests of scholarship. In all other instances, however, permission must be obtained from the author.

Indrani Mishra

DECLARATION

I, hereby declare that the investigation presented in the thesis has been carried out by me. The work is original and has not been submitted earlier as a whole or in part for a degree/diploma at this or any other Institution/University.

(Indrani Mishra)

List of publications arising from the thesis

Journal

1. Low Energy Ion Irradiation of TiO_2 (110) - Understanding Evolution of Surface Morphology and Scaling studies,
   Indrani Mishra, Shalik Ram Joshi, Subrata Majumder, Ashis Kumar Manna and Shikha Varma, Radiation Effects and Defects in Solids,**2016**, 171, 594-605.

2. Surface Modification of poly(dimethylsiloxane) through Oxygen and Nitrogen Plasma Treatment to Improve its Characteristics towards Biomedical Applications,
   N Gomathi, **Indrani Mishra**, Shikha Varma S Neogi, Surf. Topogr.: Metrol. Prop., **2015**, 3, 035005.

3. Effect of Self Affine Morphology of Natively oxidised Silicon(100) on Wetting, Scaling Properties and DNA Fractal Dimension,
   Indrani Mishra, Shalik Ram Joshi, Subrata Majumder, U. Subudhi and Shikha Varma, (Under Review).

4. Unzipping of DNA via interactions with Nano- patterned SiO_x Surfaces
   Indrani Mishra, Subrata Majumder, Shalik Ram Joshi, U. Subudhi and Shikha Varma (Under Review).

5. Higher Order transition of DNA molecule on UV irradiation modified TiO_2 single crystal,
   Indrani Mishra, Subrata Majumder, Shalik Ram Joshi, U. Subudhi and Shikha Varma (to be submitted).

Conferences

1. Swift heavy Ions in Materials Engineering and Characterisation (SHIMEC), October 2014, IUAC, New Delhi, India

Oral presentation– Conformational modifications and Interaction of DNA on Ion Sputtered Surfaces.

2. Phd School on application of SPM in Life Sciences, Soft matter, Nanofabrication, August 2013, Aalborg University, Denmark
   Oral presentation– Electrostatic Softening Of Plasmid on interaction with ion sputtered Si(100).

3. 3rd International Conference on Physics at Surfaces and Interfaces(PSI2014), 2014, Puri, India
   Poster– Depth Dependant Compositional Variation of Si(100)surfaces after Low Energy Ion Beam Irradiation.

4. Phd School on application of SPM in Life Sciences, Soft matter, Nanofabrication(Aalborg University -Denmark) aug 2013
   Poster – Interaction of Plasmid with surfaces, Modification in flexibility Of DNA & Biocompatibility with surfaces.

5. International Conference and Workshop on Nanostructured Ceramics and other Nanomaterials(ICWNCN)" 2012 (New Delhi, Delhi University)
   Poster– Photoactivity of TiO_2 single crystal and its interaction with biomolecules.

6. Swift heavy Ions in Materials Engineering and Characterisation(SHIMEC 2012), IUAC, New Delhi
   Poster– Nano-structures of biomolecules on modified TiO_2 single crystal.

Date: **Indrani Mishra**

To the angel of our life Agrata

Acknowledgments

To all who have given me advise, friendship, humor, company and kept me sane these past six years, thank you. Past six years of research work that led to this thesis were the most defining years of my life. I am grateful to a lot of people who have been instrumental in making them so. It humbles me to acknowledge them all.

A person who has been the reason behind me writing this thesis and acknowledgment, has to be my advisor Prof Shikha Varma. She has been one the biggest influences in my life. I consider myself to be extremely fortunate to have known, worked together with and been supervised by Mam. She has manged to keep me motivated in my research as well as encouraged me in all my efforts and endevours. Mam has been extremely patient with me. Apart from all these she has provided me with every possible opportunity to develop myself as a researcher. I will ever be indebted to Prof Shikha Varma.

I have been fortunate enough to have some of the most talented, wonderful and helpful lab-mates. I want to thank Gomathi didi, Anupama didi, Subrata Bhaiya, Vanaraj Bhaiya, Shalik and Asish. Over the years we have been more of friends and less of colleagues.

I take this opportunity to thank Santosh sir for his help in XPS measurements. The time spend with him and his family will always be cherished.

I am thankful to Dr. Umakant Subudhi for providing DNA samples and useful discussions, which were the core of my research projects.

Through this acknowledgment, i would like to thank Ajit sir for all the tea time interesting discussions and sky watching sessions those are the most valued moments and indeed i am going to miss them the most. What i am taking back from my stay at IOP are two people Ajit Sir and Shikha Mam, who have been and i know will always be a big support.

To Saumia didi, Pramita and Shalik thank you so much for being there for

me always and giving me your friendship. I would like to thank khan sir for his support and help, and for being available even with just one phone call. I am grateful to my sister in law Swarnima for her unconditional support, at a time when it was needed the most.

Blessed are people who have supportive and loving family, and thanking them for their love, care and encouragement seems to be a formality . Even though i take this opportunity to thank my entire family for understanding and believing in my dreams. My very first physics teacher was my father, who has been my inspiration. My mother always taught me to be tension free and do what i love to. Vinay chacha and Manisha aunty thankyou for your guidance and support. Indeed i am a blessed child. Equally supportive have been my father in law and mother in law.

A person whose presence makes me feel confident, who has been a partner in every true sense, my pillar of strength is my husband Anshumaan. He has been a silent subject of all my frustrations and anger. A person who never let me give up on my research even though there were times when i wanted to do so.

Finally to the lovely kids of my family Abhishek, Sushmita, Vishnu, Ved, Aryash, Presha , Riddhima, Riyansh and my sweet little daughter Agrata thank you, for letting me be a child with you all. A special thankyou to my little girl Agrata, who has been a very supportive and understanding child.

Contents

Synopsis

Nanostructures show variety of novel properties owing to their confined nano-sizes and large surface to volume ratio. Many efforts have been made to synthesize nanostructures and nano-patterned surfaces in order to tailor useful functional properties and to understand their characteristic behaviors. Nanostructured surfaces can be prepared by variety of top down or bottom up routes and display surface morphology and chemical nature very different from the bulk material [1]. Understanding the interactions of DNA and cells with such surfaces is immensely important for fundamental understanding as well as in many applications. They form the significant framework in several crucial fields like bio-medicine, tissue engineering, bio sensors, surgical implants, etc. [2–9]. Growth of fields like biotechnology and biosensing display many attractive scenarios on interaction of biological molecules with surfaces [5, 6, 10]. They also present many theoretically challenging problems related to the adsorption of soft and complex molecules on hard surfaces, electrostatic forces between them, conformations of molecules and their transitions to other stable configurations [11]. In the field of life sciences also, bio molecule microarrays and bio-sensors form important research tools whose many characteristic properties are controlled by the surfaces on which they are fabricated [12, 13]. Hence, the development of surfaces that exhibit biocompatible nature, with reduced toxicity and site specific immobilization, display attractive potential in numerous areas [10, 13]. Homogeneity of the surface structures, surface architecture, surface tension, wetting properties, etc. are important parameters that can influence the outcome in many applications [10, 12].

Various approaches can be taken for regulating the behavior, properties

and functionality of the surfaces by locally altering the surface chemistry. Among these some primary techniques are based on modification of surfaces via physical processes (e.g. physical adsorption, Langmuir blodgett films), chemical process (oxidation by strong acids, ozone treatment, chemisorption, and flame treatment) and radiation methods (using glow discharge, corona discharge, photo (UV) activation methods, laser, ion beams, plasma immersion, ion implantation, electron beam lithography, and γ-irradiation).

Mica has been utilized for long time as a substrate for studying DNA origami. It has however limited practical application in-comparison to many semiconductor and polymer materials which exhibit many advanced properties with applications in multiple research areas. Silicon oxide is an exceptional material with wide range of applications in microelectronics. In recent years, it has exhibited many interesting characteristics which play important role in understanding physio-chemical processes involving biological macromolecules [14,15]. Natively oxidized silicon surfaces display non-covalent type interactions with biological molecules and bio-species. They play crucial role in many disciplines of biological cell integration as well as in the development of biomimetic materials for tissue engineering [16, 17]. TiO_2 is a light weight material that displays good mechanical strength, fascinating bio-compatible nature and corrosion resistance properties [18]. With these characteristics, TiO_2 is considered an exceptional material for many hard tissue replacements, such as dental implants, bone plates and artificial hip joints [18–20]. Polydimethylsiloxane (PDMS) is a low cost material and shows many interesting properties like gas permeability, optical transparency, low auto fluorescence, and easy moldability [21–23]. Modified PDMS has received immense attention as a substrate of choice in several mechano-biological [24–26] and micro-fluid applications [27, 28].

Plasmid pBR322 DNA is widely used for the analysis of prokaryotic transcription and translation as well as for understanding topological changes in DNA conformations [29]. Branched DNA also plays an important role in many applications in nanotechnology and the motifs based on branched DNA molecules can be linked together by sticky ends to tailor many impressive objects, periodic arrays and nanomechanical devices [30]. Fibroblast 3T3 cells are immortalized cells which can be grown indefinitely in the culture and can be cloned to give rise to a clonal population. Produced through in-vivo growth techniques [31], these cells present a cost effective method for monitoring the toxicity in compounds and drugs.

Functionalization, with proper chemical groups, is a necessary step in achieving site- specific immobilization of biological molecules on the surfaces. Oxidized silicon surfaces can be functionalized via thiol groups [32], carboxylic and amines groups [33], whereas TiO_2 can be functionalized by carboxy acid groups [34]. Adsorption of DNA oligonucleotides on both anatase TiO_2 nanoparticles and rutile TiO_2 has been observed [35]. Lithography and irradiation methods are also remarkable routes of surface functionalization. Immobilization and alignment of DNA origami on patterned surfaces fabricated by variety of techniques like e- beam lithography, DIP-Pen lithography, Nanografting, Nanoshaving, Nanocontact Printing, etc. exhibits the importance of such surfaces in advancing site specific DNA- attachment [36]. Patterned surfaces sometimes show development of chemical and charged species which can be effectively utilized as functional units. Functionalization of such surfaces, attained without any additional chemical treatment, display frontier techniques for immobilizing species [37]. Ion beam induced patterning is usually a single step, cost effective technique that leads to formation of

self assembled, self organized nanostructures avoiding the need of expensive lithographic techniques [15]. Photo-irradiation with ultra violet (UV) radiation promotes many chemical modifications on the TiO_2 surface [17] and is frequently used for the sterilization and and photo-immobilization [38] of this surface. This also promotes site selective binding of many molecules to these surfaces [39]. Irradiation with high-energy ion plasma [40, 41], UV [42] and corona discharge [43] introduce hydroxyl groups on the surface of PDMS. Chemical vapor deposition [44], silanization [45], phospholipid bilayer formation [9, 46] and poly-electrolyte multilayers [47] produce functional groups on this surface which support immobilization. For PDMS, the most direct method to increase its bio-compatibility is via its exposure to high energy gaseous plasma [48–50]. Energetic photons, electrons or ions present in plasma break bonds, within the polymer backbone, resulting in many surface modifications. Carbon containing fragments leave the surface, in the form of volatile organic species, and the silicon and oxygen radicals recombine through the bridging Si-O-Si bonds creating an oxygen enriched silica-like layer on the surface [51]. This layer enhances the ability of the polymer to maintain electro-osmotic flows, cellular adhesion as well as favorable wettability conditions [47].

Present thesis discusses the modification of SiO_x, TiO_2 and PDMS surfaces by irradiation methods. Natively oxidised silicon and TiO_2 surfaces have been modified with the technique of low energy ion irradiation. TiO_2 surfaces have also been investigated after UV irradiation. All these SiO_x and TiO_2 surfaces were also interacted with DNA. PDMS surfaces were modified with oxygen plasma and nitrogen plasma and exhibit many physico-chemical changes. PDMS surfaces show enhanced attachment of cells after plasma treatment.

The first part of the thesis discusses the modification of natively oxidized silicon surfaces (Si/SiO_x) via low energy ion irradiation and their interaction with plasmid DNA. The wetting and scaling properties of the surfaces have been investigated to understand the behavior of DNA conjugation on the surfaces. The surfaces were ion irradiated under UHV conditions using 3keV Ar^+ at various fluences of 6×10^{15}, 1.2×10^{16} and 1.8×10^{16} ions/cm^2. This leads to spontaneous development of self organized nanostructures on the surfaces. The resultant morphology of the surfaces is produced via competition between the roughening processes due to sputtering, and the diffusion enhanced smoothening processes. Scanning Probe Microscopy (SPM) technique was utilized to study the changes in the morphology of the ion irradiated surfaces. Scaling studies of these surfaces have been performed via height height correlation function (HHCF). The results indicate that these surfaces are self affine in nature. Wetting properties of the surfaces have been investigated via contact angle (CA) measurements. The wetting behaviors of these surfaces depend on the fractal dimension of the surface, reflecting a crucial role of surface jaggedness. A decrease in the thickness of native oxide layer, after ion irradiation, is observed by X-Ray photoelectron spectroscopy (XPS) technique. These natively oxidised surfaces were interacted with plasmid pBR322 DNA. A strong influence of the fractal dimension of the surfaces on the DNA moiety has been observed here. This also leads to changes in the structural as well as fractal dimension of DNA. Surprisingly, after DNA interaction, the irradiated SiO_x surfaces exhibit smooth morphology and do not show self-affine properties [52].

The structural as well as chemical modifications in a plasmid DNA, after its immobilization on the nanostructured Si/SiO_x surfaces, have been

discussed here. The nanopatterned surfaces have been generated via the technique of ion irradiation. A 2D-network, of approximately a single DNA layer, is observed on the nanostructured surfaces. The power spectral density (PSD) technique has been utilized to evaluate the structural parameters like inter-molecular separation (ξ) and persistence length (P) of DNA. A significant decrease in ξ and P of DNA is observed on the nanostructured SiO_x surfaces, indicating a strong chemical interaction of DNA with the surfaces. Appearance of Si_3N_4 complex as well as denaturing of DNA- base pairs further demonstrate this. Absence of H_2PO_4 feature in XPS also suggests charge transfer from the DNA backbone to the surface [53]. The strong chemical interaction stimulates charge induced electrostatic softening of DNA resulting in the formation of a highly flexible DNA molecule.

In the second part of the thesis, modification of $TiO_2(110)$ surfaces, via ion-irradiation and UV-irradiation techniques, as well as their interactions with the branched DNA have been discussed. Low energy 3 keV Ar^+ ion irradiation has been utilized for the fabrication of nanostructures on the TiO_2 surfaces. Fluences of 6.0 $\times 10^{15}$, 1.8×10^{16} and 1.5 $\times 10^{19}$ ions/cm^2 were utilized for these studies. Ion irradiation leads to the formation of Ti^{3+} vacancy states, on the surface, due to preferential sputtering of oxygen atoms. The Ti rich sites present on surface act as the nucleation sites for promoting the creation of nanostructures. SPM and XPS techniques have been used to investigate the evolution of these ion irradiated surfaces. Scaling studies of the surfaces indicate a shape transition of the nanostructures from being more elliptical at lower fluences to less elliptical at higher fluences. An increase in the roughness exponent (H) and slope of the PSD function (γ) with increasing fluence reveal that the surfaces becomes less jagged at small length scales due to the increased diffusion. Moreover, an increase in the correlation length is

attributed to the enlargement of nanostructures at high fluences [54]. These ion irradiated TiO_2 surfaces have been interacted with branched DNA. Long entangled structures of DNA have been observed on the surfaces.

UV irradiation produces reactive oxygen components on the TiO_2 surfaces. These species contribute to the formation of surface hydroxyl states as well as induce physical adsorption of water molecules. Evolution of such surfaces as well as immobilization of branched DNA on them has been investigated here. Presence of reactive species stimulate globule like conformal transitions in DNA. Transformation of DNA into condensed rods and toroid structures is observed here indicating structural transitions of DNA into higher order structures [55].

The last part of the thesis discusses the surface modification of PDMS (poly-dimethyl silcoxane) by oxygen and nitrogen plasma irradiation. The changes in the physico-chemical properties of PDMS have been studied by Fourier transform infrared spectroscopy (FTIR), XPS, scanning electron microscopy (SEM) and SPM techniques. Wetting and ageing properties of these surfaces have been studied using CA measurements. Plasma treated surfaces show an enhancement in the polarity as well as surface energy. Biocompatibility of these surfaces have also been studied by investigating their adhesive properties to the fibroblast cells through MTT tests. A substantial enhancement in the bio- compatibility is demonstrated by 5 minutes nitrogen plasma treated surface. These nitrogen plasma treated PDMS surfaces also show highest polarity (0.4) and surface energy (33.3 N/mm^2). The highest enhancement in cell adhesion and viability, expressed in term of cell surface area, could be attributed to the high polarity and surface energy of these surfaces [56].

Thus, this thesis present results on the modification of SiO_x, TiO_2 and PDMS surfaces by irradiation methods. Low energy ion irradiation methods have been utilized for patterning of SiO_x as well as TiO_2 surfaces. Presence of 2- dimensional DNA networks on silicon oxide surfaces and elongated DNA networks on TiO_2 surfaces have been observed. UV- irradiated TiO_2 surfaces show transition of DNA structures into condensed forms. Nitrogen plasma treatment of PDMS produces highly bio-compatible surfaces with enhanced polarity and surface energy. These surfaces display good adhesion and viability for the fibroblast cells.

Bibliography

[1] George M. Whitesides and Bartosz Grzybowski, Science, **295**, 2418 (2002).

[2] P. Gong, C. Y. Lee, L. J. Gamble, D. G. Castner, D. W. Grainger, Anal. Chem, **78**, 332 (2006).

[3] D. Y. Petrovykh, H. Suda Kimura, L. J. Whitman, M. J. Tarlov, J. Am. Chem. Soc, **125**, 5219 (2003).

[4] Patrick M. McLendon, Daniel J. Buckwalter, Erica M. Davis, and Theresa M. Reineke, Mol. Pharmaceutics, **7(5)**, 1757 (2010).

[5] Fabiane C. de Abreu, Francine S. de Paula, Danielle C. M. Ferreira, Valberes B. Nascimento, Alexandre M. C. Santos, Marcelo M. Santoro, Carlos E. Salas, Julio C. D. Lopes, and Marlia O. F. Goulart, Sensors, **8**, 1519 (2008).

[6] N. M. Fahrenkopf, P. Z. Rice, M. Bergkvist, N. A. Deskins, N. C. Cady, ACS Appl Mater Interfaces, **4**, 10 (2012).

[7] Jiri Gallo, Martin Holinka, and Calin S. Moucha, Int J Mol Sci, **15**, 8, 13849 (2014).

[8] Stuart B. Goodman, Zhenyu Yao, Michael Keeney, and Fan Yang, Biomaterials, **34**, 13, 3174 (2013).

[9] Mark J. Jackson, Waqar Ahmed, Surface Engineered Surgical Tools and Medical Devices (Springer Science Business Media, (2007)).

[10] Mukesh Digambar Sonawane and Satish Balasaheb Nimse, Journal of Chemistry, **2016**, 1 (2016).

[11] David Pastr, Olivier Pitrement, Stphane Fusil, Fabrice Landousy, Josette Jeusset, Marie-Odile David, Loc Hamon, Eric Le Cam, and Alain Zozime Biophys J., **85**, 2507 (2003).

[12] Scott Taylor, Stephanie Smith, Brad Windle, and Anthony Guiseppi-Elie, Nucleic Acids Res, **31**, 16, 87 (2003).

[13] Bong Jin Hong, Vijaya Sunkara, and Joon Won Park, Nucleic Acids Res, **33**, 16, 106 (2005).

[14] L. H. Lie, S. N. Patole, A. R. Pike , L. C. Ryder, B. A. Connolly , A. D. Ward, E. M. Tuite, A. Houlton, B. R. Horrocks, Faraday Discuss, **125**, 235 (2004).

[15] Bezuayehu Teshome, Stefan Facsko and Adrian Keller, Nanoscale, **6**, 1790 (2014).

[16] D. Cole, Surface chemistry and adhesive properties of Oxidised Si Surfaces, (Thesis Queens College, University of Cambridge, 2007).

[17] B. A. Weisenberg and D. L. Mooradian, J. Biomed. Mater. Res, **60**, 283 (2002).

[18] M. Niinomi, Mater. Trans, **49**, 2170 (2008).

[19] C. N. Elias, J. H. C. Lima, R. Valiev, M. A. Meyers, J. Miner. Met. Mater. Soc, **60**, 46 (2008).

[20] Y. Okazaki, Materials, **5**, 1439 (2012).

[21] D. C. Duffy, J. C. McDonald, O. J. A. Schueller and G. M. Whitesides, Anal. Chem., **70**, 4974 (1998).

[22] J. C. McDonald and G. M. Whitesides, Acc. Chem. Res., **35**, 491 (2002).

[23] A. Mata, A. J. Fleischman and S. Roy, Biomed Microdevices, **7**, 281 (2005).

[24] X. Q. Brown, K. Ookawa and J. Y. Wong, Biomaterials, **26**, 3123 (2005).

[25] J. Y. Park, S. J. Yoo, E. J. Lee, D. H. Lee and J. Young, BioChip J, **4**, 230 (2010).

[26] R. N. Palchesko, L. Zhang, Y. Sun and A. W. Fenberg, PLoS One, **7**, 13, (2012).

[27] S. Chung, Lab Chip, **9**, 269 (2009).

[28] D. Huh, G. A. Hamilton and D. E. Ingber, Trends Cell Biol, **21**, 745 (2011).

[29] B. S. Aytar, M. R. Prausnitz, D. M. Lynn, ACS Appl Mater Interfaces, 4, **5**, 2726 (2012).

[30] Nadrian C. Seeman, Furong Liu, Chengde Mao, Xiaoping Yang, Lisa A. Wenzler, Ruojie Sha, Weiqiong Sun, Zhiyong Shen, Xiaojun Li, Jing Qi, Yuwen Zhang, Tsu-Ju Fu,Junghuei Chen and Erik Winfree, Journal of Biomolecular Structure Dynamics, **11**, 253 (2000).

[31] Amelia Ahmad Khalili and Mohd Ridzuan Ahmad, Int. J. Mol. Sci, **16**, 18149 (2015).

[32] Jorge Escorihuela, Mara-Jos Bauls, Rosa Puchades and ngel Maquieira , J. Mater. Chem. B, **2**, 8510 (2014).

[33] N. Salehi-Nik, G. Amoabediny, M. A. Shokrgozar, K. Mottaghy, J. Klein-Nulend, B. Zandieh-Doulabi, Biomed Mater, 10, **1**, 015024 (2015).

[34] Tatjana Paunesku, Tijana Rajh, Gary Wiederrecht, Jrg Maser, Stefan Vogt, Natas Stojic, Miroslava Protic, Barry Lai, Jeremy Oryhon, Marion Thurnauer and Gayle Woloschak, Article Nature Materials, **2**, 343 (2003).

[35] Andrew G. Thomas and Karen L. Syres, Chem. Soc. Rev., **41**, 4207 (2012).

[36] Paula M Mendes, Chun L Yeung and Jon A Preece, Nanoscale Research Letters, **2**, 37 (2007).

[37] J. Vicente Prez-Girn, M. Hirtz, C. McAtamney, A.P. Bell, J. Antonio Mas, M. Jaafar, O. de Luis, H. Fuchs, J. Jensen, R. Sanz, Nuclear Instruments and Methods in Physics Research B, **339**, (2014), 67 (2014).

[38] H. Gudnason, M. Dufva, D. D. Bang, A. Wolff, BioTechniques, **45**, 261 (2008).

[39] H. Aita, W. Att, T. Ueno, M. Yamada, N. Hori, F. Iwasa, N. Tsukimura, T. Ogawa, Acta Biomater, **5**, 3247 (2009).

[40] J. A. Vickers, M. M. Caulum and C. S. Henry, Anal. Chem., **78**, 7446 (2006).

[41] Z. Zhang, X. Feng, F. Xu, X. Liu and B. F. Liu, Electrophoresis, **31**, 3129 (2010).

[42] K. Efimenko, W. E. Wallace and J. Genzer, J. Colloid Interface Sci., **254**, 306 (2002).

[43] V. Di Virgilio, S. Bermejo and L. Castaer, Langmuir, **27**, 9614 (2011).

[44] J. Xu and K. K. Gleason, Chem. Mater., **22**, 1732 (2010).

[45] C. Sguin, J. M. McLachlan, P. R. Norton and F. Lagugn-Labarthet, Appl. Surf. Sci., **256**, 2524 (2010).

[46] T. Yang, S.-Y. Jung, H. Mao and P. S. Cremer, Anal. Chem., **73**, 165 (2000).

[47] H. Makamba, J. Kim, K. Lim, N. Park, and J. Hahn, Electrophoresis, **24**, 21, 3607 (2003).

[48] J. Lai, Y. Lin, Y. Denq, S. Shyu, and J. Chen, Journal of Adhesion Science and Technology, **10**, 3, 20, 231 (1996).

[49] C. P. Pennisi, V. Zachar, L. Gurevich, A. Patriciu, J. J. Struijk . 32nd Annual International Conference of the IEEE EMBS Buenos Aires, Argentina.

[50] Ville Jokinen, Pia Suvanto, and Sami Franssil, Biomicrofluidics, **6**, 1 (2012).

[51] F. Katzenberg, Surface and Coatings Technology, **200**, 20, 1097 (2005).

[52] Indrani Mishra, Shalik Ram Joshi, Subrata Majumder, U. Subudhi and Shikha Varma, Physics Letters A (Under Review)

[53] Indrani Mishra, Subrata Majumder, Shalik Ram Joshi, U. Subudhi and Shikha Varma , (Under Review)

[54] Indrani Mishra, Shalik Ram Joshi, Subrata Majumder, Ashis Kumar Manna and Shikha Varma, Radiation Effects and Defects in Solids, in press (2016) doi 10.1080/10420150.2016.1225067.

[55] Indrani Mishra, Subrata Majumder, Shalik Ram Joshi, U. Subudhi and Shikha Varma (to be submitted).

[56] N Gomathi, I.Mishra, Shikha Varma and S Neogi, Surf. Topogr.: Metrol. Prop. **3**, 035005 (2015).

List of Figures

List of Tables

Chapter 1

Introduction

1.1 Introduction :

Nano-dimensional structures, with many fascinating and intriguing applications, have led to frontier research in numerous fields. Their characteristics like large surface to volume ratio and manifestation of many superior properties have contributed to their immense stimulation to many disciplines and technological applications related to nano-optics, nano-electronics, nano-devices, nano-photonics, spintronics, photo-catalysis, solar cells, opto-electronics, gas sensing, bioimplants, medicine, sensors etc. [1, 2]. Advanced properties of nanostructures are, however, crucially dependent on their careful and systematic fabrication methods [1, 3]. Designing nanostructures with tuned sizes and controlled properties are the hallmark of attractive technological applications as well as numerous challenges in the field of nanosciences.

The *top down approach* and the *bottom up approach* are the two fundamental techniques for fabricating nanostructures. Successive disintegration of a material into nanosizes is achieved via top down method, whereas building-up of a nanostructure through assembling atom by atom or molecule by molecule constitutes the bottom up approach. The top-down approach for nanoscale patterning includes electron-beam lithography, soft lithogra-

phy, nanoshaving, nanografting, dip-pen nanolithography, colloid lithography, block copolymer micelle lithography, and extreme ultraviolet (EUV)-interference lithography [4]. The bottom-up technique involves self-assembly of atoms and molecules onto surfaces by molecular recognition and specific interactions [5–7].

Adsorption of bio-molecules like DNA and cells on a biocompatible surface can have immense potential and multiple implications in the development of biosensors, micro-arrays, surgical implants, tissue engineering, biomedicines etc. [8–10]. The mechanism of such interactions are usually complex. Many phenomenon such as adsorption, precipitation, reconstruction of surface, transmission of ions, flow of small molecules, redox reactions, surface kinetics etc. play a concerted role [11]. An understanding of involved mechanisms in such processes present a formidable challenge and invoke overwhelming interest in widely varying areas like astrobiology, ecology, biology, biotechnology, engineering, and medicine [11–14]. Considerable attention with compelling focus has emerged for designing biocompatible materials for implants, drug delivery and nanodevices for diagnosis and therapy [15, 16]. Tailoring surfaces with desired properties and suitable interactions is the goal in such studies [11, 15, 17, 18]. Deliberate modification of surface properties like wetting behavior, surface charge, morphology, curvature, reactive sites, dissolution/reprecipitation equilibrium, reduced toxicity, enhanced bio-compatibility etc. can tremendously influence its interactions with biomolecules and cells [19]. Such intentional control and regulation of surfaces can be achieved in variety of ways including physical processes (e.g physical adsorption, Langmuir Blodgett film deposition, etc.), chemical processes by using chemical agents and functional group incorporation (during surface oxidation, hydrolysis, chemical grafting, surface coating, etc.), corona discharge treatment, plasma etching, ultraviolet (UV) radiation exposure, laser

ablation treatment, gamma irradiation, ion beam irradiation (IBI), X-ray irradiation, etc. [20].

Conjugation of biomolecules on surfaces also demands special attributes such that specific functional groups or designated sites can participate in interactions to achieve biomolecular recognition. Many such studies involve expensive lithographic techniques and elaborate chemical functionalization of the substrate for selectively immobilizing the biomolecules [21]. Ion beam irradiation (IBI) is an advanced but simple technique for inducing variety of surface modifications. These can be achieved in a technologically single step through spontaneous self assembled processes [22]. Generation of nanostructures, like corrugations, ripples, dots, etc., are accompanied by defects which together play significant role in many fascinating properties exhibited by these surfaces [3]. UV irradiation of surfaces can also produce many crucial modifications in their chemical and physical properties [23] leading to the development of important reactive sites, which can be useful in designing surface behavior [24, 25]. Plasma etching is another attractive technique used in polymers (e.g. thermoplastic films, fibers, non-wovens, membranes, biomedical devices, etc.), with distinct advantage that it mostly remains confined to the surface layer without affecting bulk behavior [26–28]. Such modified surfaces present very important route for biomolecular interaction with immense significance in biosensor applications, medicine, drug delivery, etc. [29].

In the present thesis, formation of nanostructures as well as development of chemical states on the surfaces have been investigated. Variety of methods like ion beam irradiation, UV irradiation and plasma etching have been utilized to modify surfaces of Natively Oxidized Silicon (SiO_x), Titania (TiO_2) and Poly dimethyl Siloxane (PDMS). This chapter is organized as following: Section 1.2 discusses the basis of ion solid interaction. Process of sputtering,

its theoretical aspects, and discussion on pattern formation during IBI is also presented. Process of UV irradiation is discussed in the section 1.3. Section 1.4 explains the mechanism of plasma etching. Interaction mechanism of DNA on surfaces has been discussed in section 1.5.

1.2 Ion-Solid Interaction

Interaction of ions with the surface, solids and nanostructures play an important role in the fundamental and applied research. Once an energetic particle beam hits a solid material, it transfers energy to the latter. These energetic ions gradually lose their energy in the solid material through electronic and nuclear interactions. They can be finally deposited at a range defined by the energy and species of the ion. The ion-atom interactions have been elaborated in the following figure:

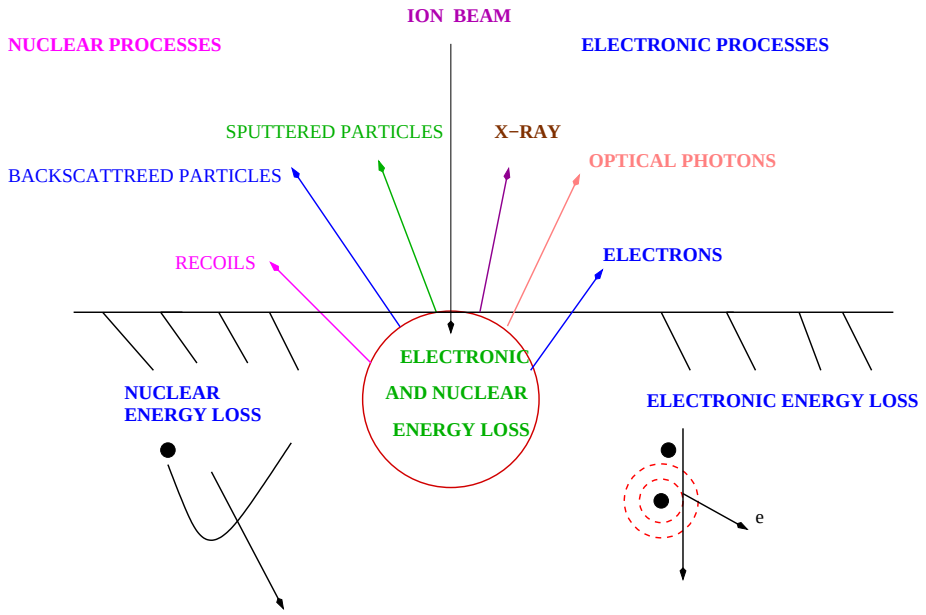

Figure 1.1: Basic Ion-Solid Interactions

1. Electronic interaction:- Ions interact with electrons and cause excitation as well as ionization of inner shell electrons.

2. Elastic nuclear interaction is the collision of ions with atoms or nuclei in which atomic displacement takes place as an elementary process.

Both these energy loss mechanisms i.e. the nuclear and electronic stopping cause modifications to the structure of the material. Stopping power of a particle is defined as a measure of the average energy loss per unit path length of the particle due to its interaction with atoms in the medium

$$S = \frac{dE}{dx} \tag{1.1}$$

E is the kinetic energy of the particle and x is the distance along the particle trajectory in the medium. The stopping power for an ion in a medium depends upon its energy E, atomic number Z_1 as well as on the density ρ and the atomic number Z_2 of the target element. The total stopping power for ion is S_{tot}=$S_{electronic}$ + $S_{nuclear}$. With ions of energies of few keV, a dominance of nuclear energy loss is observed, whereas inelastic electronic energy loss is predominant for ions with energies of few MeV. Fig. 1.2 shows the Nuclear and electronic stopping powers in Si for Ar^+ ions as obtained from SRIM. Note that the x-axis is logarithmic. Related to stopping power is the total range of ions, i.e. the path length of the ions in the target where they come to rest.

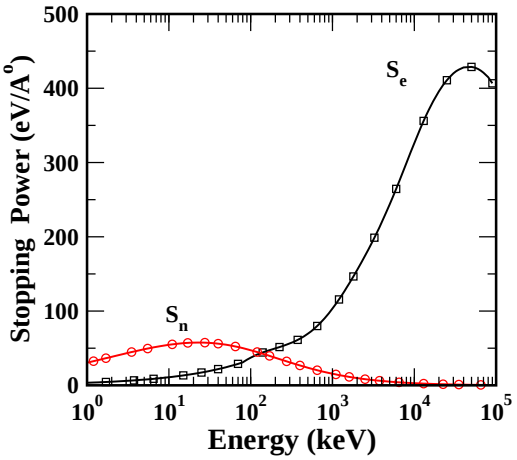

Figure 1.2: Variation of Nuclear (Sn), and Electronic (Se) energy losses, respectively, as a function of ions kinetic energy via. SRIM simulation code [30], for argon ions in Silicon target.

A more useful quantity is the projected range perpendicular to the surface, or how deep into the target the ions have penetrated. With an assumption that the energy loss is continuous, total range can be calculated from the plot of stopping power as a function of energy. Knowledge of stopping powers and ranges is important in both ion beam analysis and materials modification.

1.2.1 Sputtering

Sputtering is a process of removal of material from the surface of solids because of the impact of energetic particles. This phenomena is characterized by sputtering yield (Y), which is described as

Y= mean number of emitted atoms / incident particles

The sputtering yield depends upon the structure and composition of target material, and also on the parameters of incident ion beam and the experimental geometry.

In the sputtering process, atoms are ejected from the outer surface layers. The bombarded ion transfers energy during collisions to the target atoms.

These atoms recoil with sufficient energy which in turn create more recoils. Few of the backward recoils approach the surface with enough energy to escape the solid. Various complex series of collisions are involved in the sputtering process. These collisions involve a series of angular deflections and energy transfer processes between many atoms in the solid. The most important parameter in this process is the energy deposited at the surface. The sputtering yield is proportional to the number of recoiled or displaced atoms. If the linear cascade regime is considered, then the energy deposited per unit depth during nuclear energy loss process is proportional to the number of recoils.

$$Y = \Delta F_D(E_0) \tag{1.2}$$

where F_D (E_0) is the energy deposited per unit length in the nuclear process at the surface, and Δ is the material factor.

F_D (E_0) depends upon the type, energy and direction of the incident ion as well as the composition of the target. F_D (E_0)=α N $S_n(E_0)$, where N is the atomic density of the target atom, α is the correction factor which depends upon the angle of incidence of the beam to the surface and $S_n(E_0)$ is the nuclear stopping cross section at the energy E_0

1.2.2 Theory of pattern formation

Ion beam sputtering is determined by the atomic processes that take place within a finite penetration depth of a bombarded material. Pattern formation due to ion beam sputtering can be understood through the Sigmund model demonstrating the instability of a planar surface to uniform ion beam erosion.

Sigmund Theory Of Sputtering

The erosion rate due to ion bombardment on a surfaces is dependent upon the sputtering Yield Y. For the calculation of the yield and prediction of the

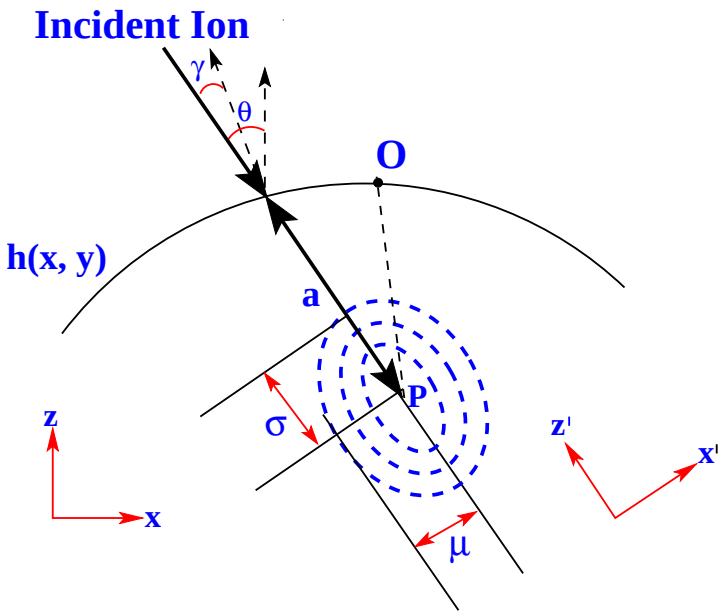

Figure 1.3: Schematic illustration of the energy distributed by an incident ion.

surface morphology due to ion bombardment, understanding of sputtering mechanism is important. Consider an ion that penetrates a distance "a" inside the bulk of the target material, before losing or spreading out its kinetic energy. It releases its energy at point P in the solid which contributes some energy at point O on the surface. At the surface point"O" the atoms will break their bonds and either leave the surface or diffuse along. The average energy E ($\acute{r}$) deposited at the point O due to the ion that reached point P is given as:

$$E(\acute{r}) = \frac{\epsilon}{(2\pi)^{3/2}\sigma\mu^2} \exp \frac{-\acute{z}^2}{2\sigma^2} - \frac{\acute{x}^2 + \acute{y}^2}{2\mu^2} \tag{1.3}$$

where $\acute{z}$ is the distance measured along the ion trajectory and $\acute{x}$, $\acute{y}$ are measured in the plane perpendicular to it. ϵ is the kinetic energy of the ion, and σ, μ are the widths of distributions in the directions parallel and perpendicular to the incoming beam respectively.

The energy distribution presented in eq. 1.3 reflects the scenario where the

mass of projectile (M_1) is larger than the target mass (M_2). Sigmund [31,32] and Winterbom [33] showed that the electronic stopping does not affect the shape of the deposited energy distribution. Monte Carlo simulations of the sputtering processes have demonstrated that the deposited-energy distribution and damage distribution can be well approximated by a Gaussian as presented by eq. 1.3. Many ions penetrate the solid at different points. The velocity of erosion, v, at O is dependent upon the total energy E contributed by all ions deposited within the range R as per the following equation.

$$v = p\int_R dr\Phi(r)E(r) \tag{1.4}$$

here, $\phi(r)$ is the local correction to the uniform flux J of the bombarding ions and p is the material constant that depends upon the surface binding energy and scattering cross-section [31,32]. In order to calculate v following assumptions are made

1. (x,y,z) surface in laboratory fame can be described by a single value height function h(x,y,z,t) at time t measured from an initial flat configuration which lies in the (x,y) plane

2. The angle between the ion beam direction and the local normal to the surface is a function of the angle of incidence θ and the value of the slopes $d_x h$ and $d_y h$. Under these assumptions the above equation can be expanded as

$$\frac{dh}{dt} = -v_0 + \gamma\frac{dh}{dx} + v_x\frac{d^2h}{dx^2} + v_y\frac{d^2h}{dy^2} + \frac{\gamma_x}{2}\left(\frac{dh}{dx}\right)^2 + \frac{\gamma_y}{2}\left(\frac{dh}{dy}\right)^2 - D\acute{x}\frac{d^4h}{dx^4} - D\acute{y}\frac{d^4h}{dx^y} \tag{1.5}$$

v_0 is the erosion rate, second term represents the uniform motion of the surface feature along the x direction. v_x and v_y represent the ion induced

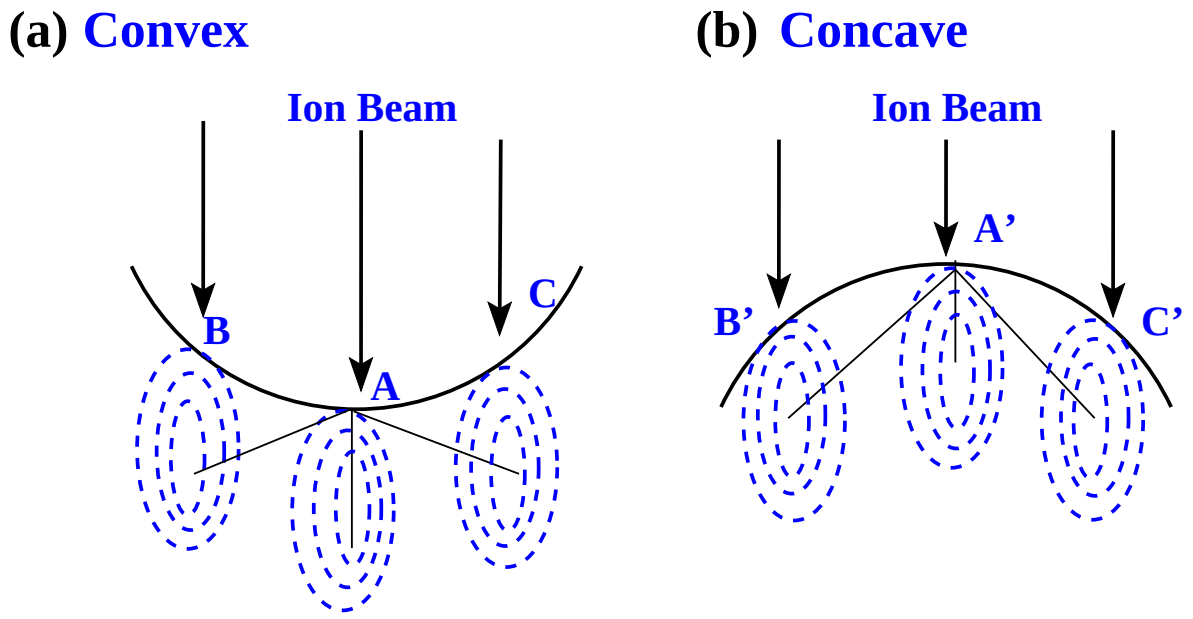

Figure 1.4: Schematic illustration of the physical origin of the instability during ion erosion of nonplanar surfaces. A surface element with convex geometry (a) is eroded faster than that with a concave geometry (b) due to the smaller distances (solid lines) the energy has to travel from the impact point to the surface (A or A′ points).

surface tension. γ_x and γ_y characterize the slope dependence of the erosion rate, while D$\acute{x}$ and D$\acute{y}$ are the ion-induced effective surface diffusion coefficients. The coefficients v_x and v_y were first calculated by Bradley and Harper (BH) [34]. The evolution of a surface morphology is an effect of sputtering yield, which is strongly dependent on the nature of the surface topography. The origin of nanostructures and ripple formation during ion sputtering is an ion-induced instability which is caused by the competition between the erosive and diffusive processes undergoing on the surface. Fig. 1.4 shows two surfaces of ion bombardment (a) valley and (b) crest. The erosion velocity normal to the surface at a point (x, y) at the surface is proportional to the total energy deposited there from ion impacts at nearby points. As shown by Sigmund ([31]) the energy density deposited at point A due to the ions

striking at B is larger than the energy deposited at A′ due to the ions striking B′. This is due to the fact that A′B′ > AB and leads to the valleys getting eroded faster than the crests. The difference in height of valley and crest leads to a negative surface tension and is expressed by negative v_x and v_y coefficients in the equation 1.5. At short wavelength this instability is balanced by surface diffusion.

In the present thesis natively oxidized SiO_x and TiO_2 surfaces have been investigated after their irradiation with low energy ion beam.

1.3 UV Illumination of Surfaces

When a semiconductor is illuminated with light, its electrical conductivity is increased due to the generation of additional free electrons and holes in the semiconductor. However, semiconductors are sensitive to a certain spectral band due to their intrinsic band gap (Eg) energy. Ultra Violet (UV) irradiation of a semiconductor causes band gap excitations and leads to a charge separation followed by scavenging of the electrons and holes by absorbed species on the surfaces. High-energy UV photons have the ability to break up molecular organic bonds on the surface, thus leading to the creation of open bonding sites. These sites strive to return to a chemically stable condition. The atmospheric oxygen molecules which are adsorbed on the surface react with these bonding sites. These open bonds are saturated and new compounds are created on the surface. As a result of the UV treatment under normal ambient atmosphere, formation of hydroxyl, carbonyl and carboxyl groups have been reported [35]. Surfaces can be cleaned and modified by short wavelength, UV light, for enhancement of adhesion, deposition and sticking properties.

Advantages of UV illumination method

1. Improved wettability due to higher surface energies

2. Environmentally friendly because of no use of chemicals.

3. Gentle on the materials.

4. Simple method.

Photo-excitation of semiconductor oxides by UV illumination produces electron/ hole (e_{cb} /h^+_{vb}) pairs. The electron in the conduction band e_{cb} can reduce molecular oxygen to produce superoxide anion radical ($O_2 \cdot -$). Holes in the valence band h^+_{vb} have the potential to oxidize surface adsorbed H_2O or hydroxyl groups to generate HO· radicals [36].

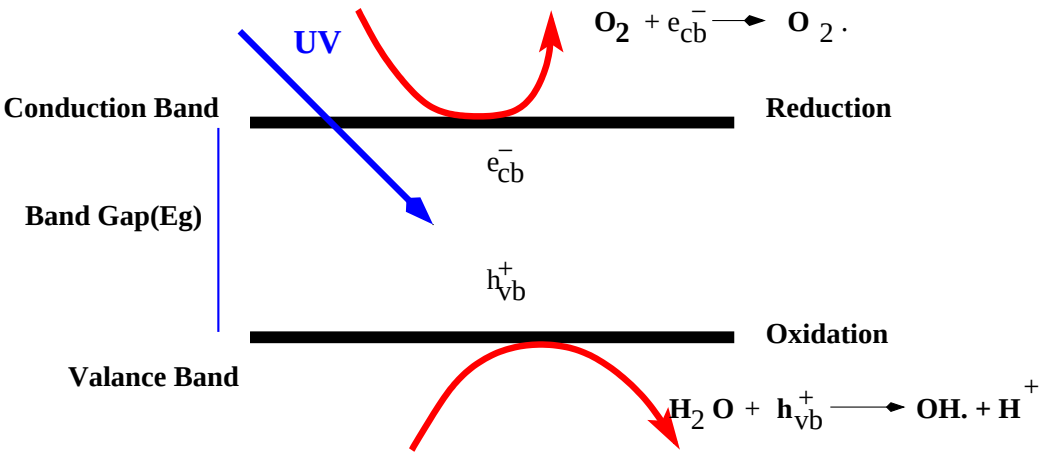

Figure 1.5: A schematic diagram showing the effect of UV irradiation on a semiconductor

These reactive states determine the ability of biomolecules to bind with the surface.

In the present thesis $TiO_2(110)$ surfaces have been modified with UV irradiation technique. UV illumination of TiO_2 also leads to the generation of oxygen vacancy sites. These sites have high affinity towards the chemisorbed water from the atmosphere and result in the formation of hydrophilic domains. The hydrophilic domains have their origin in the polar surface chem-

ical functionalities created due to UV irradiation. The induced hydrophilic states are unstable and revert to the initial hydrophobic state with time [37]. These hydrophilic states created after the hydroxyl adsorption, make the surface energetically unstable. As oxygen adsorption is thermodynamically favored, oxygen is more strongly bonded on the defect sites than on the hydroxyl groups. Consequently, the hydroxyl groups adsorbed on the defective sites can be replaced gradually by oxygen atoms when the UV-irradiated surfaces are placed in the dark [38]. Heat treatment can also accelerate the elimination of surface hydroxyl groups.

1.4 Plasma Etching

Plasma is an energetic medium, composed of electrons, positively and negatively charged ions, radicals, atoms and molecules, which can be generated by an energetic source [39]. Modifications of a solid substrate by utilizing plasma exposure is used for etching, cross linking, surface orientation and pre-deposition processes [40, 41]. The plasma exposure induces physico-chemical changes on a polymeric surface. Polymers have low density, high flexibility and can be easily manufactured. They are important in coating, bio-application etc. However these surfaces need modifications in order to have appropriate wettability, bio-compatibility, transmission of gases within their micro-channels, as well as good adhesive and frictional properties. The interaction of plasma with the polymer surface causes separation of hydrogen from polymeric chains and creation of free radicals. In addition to the surface chemistry, plasma treatment also affects the surface topography, [42, 43] which modifies the wettability properties of the surface. Plasma etching of polymers creates active sites, which are subjected to atmospheric reactions. This leads to aging of the polymer, an effect which is controlled by external

parameters like adsorption and oxidation as well as internal influences of restructuring and diffusive properties of the polymer [44]. Plasma treatments thus can be used to modify the surface properties of polymers to improve their performance in various applications. Hydrophilization of polymers by oxygen or nitrogen plasma has been used in various applications. Plasma hydrophilization can improve the bio-compatibility of the polymers [45], affect the density of attached cells [46, 47] as well as enhance adsorption of proteins [48]. Furthermore, plasma hydrophilization can be used for improved adhesion and bonding of polymers.

In the present thesis, plasma etching technique has been utilized for modifying the PDMS surfaces. PDMS is an extremely hydrophobic and chemically inert polymer due to the closely packed methyl groups on its surfaces. The extreme hydrophobicity limits its use in many biological devices. However PDMS is also flexible and nontoxic material which is extensively used in many medical applications.

Exposure of the PDMS to high energy gaseous plasma [50, 51] is an effective and most direct method to enhance its biocompatibility. Energetic photons, electrons or ions found in a plasma break bonds within the polymer backbone. Carbon-containing fragments leave the surface in the form of volatile organic species, while low-molecular weight polymer chains and stable radicals remain on the polymers surface. Silicon and oxygen radicals recombine through bridging Si-O-Si bonds creating an oxygen enriched silica-like layer on the surface [52–54]. The formation of a silica-like layer results in a decrease in its hydrophobicity thus increasing its ability to maintain electro-osmotic flow and cellular adhesion. However this hydrophilic surface is transient, as the polymer can undergo hydrophobic recovery [55–57]. Two main reasons

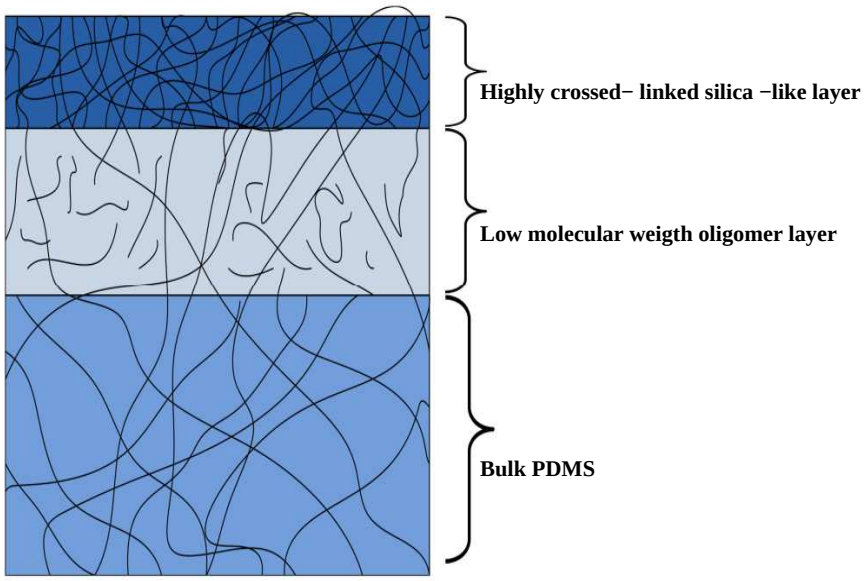

Figure 1.6: Layered structure of plasma treated PDMS [49].

for the hydrophobic recovery of the polymer surface are the movement of polar groups from the surface towards the bulk which reduces the surface energy, and diffusion of polar chemical groups in the polymeric matrix [58].

1.5 DNA Interaction With Surfaces

Deoxyribonucleic acid (DNA) is a long double helix linear polymer found in the nucleus of a cell. It is composed of nucleotides and is associated with the transmission of genetic information. DNA is composed of negatively charged backbone PO_4^-, four nitrogen base (A, T, G, C) attached with the sugar molecule. Its interaction with surface is the foundation of modern microarray and bio-sensing technologies. These are widely used in applied genomics for genotyping, drug discovery, gene expression profiling etc. [9,10,12,13,59]. There are mainly two important mechanisms for immobilization of DNA on the surfaces

(a) Physical adsorption

(b) Covalent immobilization

Physical adsorption is the simplest of all immobilization methods as it is based on the ionic interactions that occur between the negatively charged groups present on the DNA and the surface charges. As each molecule can form many contacts in different orientations to minimize repulsion, the immobilized DNA is likely to be randomly oriented.

Chemisorption and covalent interactions are the two common *covalent attachment methods* for immobilization of DNA on the surfaces. It requires chemical modification of the surfaces and involves various functional groups for the attachment.

Theory of Interaction

A negatively charged DNA interacts with a positive charged surface by means of physical adsorption, however for the adsorption of the negatively charged DNA on negatively charged surface, a charge-inversion is essential. A brief discussion on this charge inversion for adhesion of DNA on negatively charged surfaces like SiO_x, is given here. The charge inversion is promoted by the presence of cations, e.g divalent Mg cations, in the buffer solution. The self assembly of the DNA on the surfaces is then produced by the weak electrostatic interaction between the DNA and the surface via formation of an electrical double layer. The concept of electrical double layer (EDL) plays an important role in the interaction of DNA with any surface. On a surface charged- centers can be present at various locations, like on oxygen in oxides. On the other hand, in the solution there are two types of ions, which are usually defined with respect to the sign of charges on the surface. Ions having

same sign, as the surface charges, are called co-ions whereas those of opposite sign are counter-ions. To satisfy the charge neutrality condition for the full system (surface and solution) more counter-ions than the co-ions will be attracted to the surface. Simultaneously, however, due to the thermal movement of the ions in solution, the co-ions and counter ions also extend over in the solution and form a diffused-extended layer [60]. This extended layer along with the surface charge centers form the electrical double layer (EDL). This is also common in biological and artificial membranes [61] in liquid crystals [62], clays [63] and solid electrolyte [64]. Negatively charged DNA in the buffer containing divalent Mg^{2+} counter-ions form a diffused extended- layer in the solution. This layer on a negatively charged surface will constitute an electrical- double- layer. A simple 2D model with a negatively charged DNA as well as negatively surface is shown in fig. 1.7.

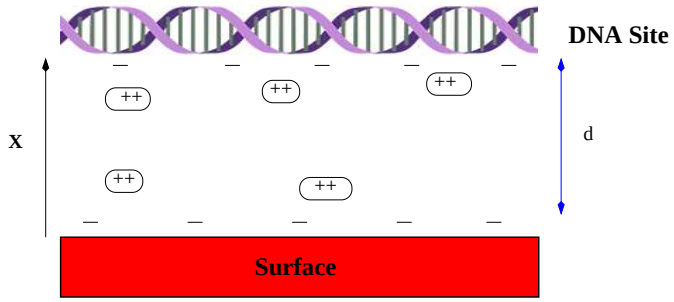

Figure 1.7: Interaction of DNA with negatively charged surfaces.

The divalent Mg^{2+} ions act as counter-ions and are relatively more strongly attached to the surface. The electrical -double layer thus formed, promotes the DNA binding on the surface. Formation of the electrical double layer with mobile divalent ions placed between two charged surfaces, e.g. DNA and negatively charged surface creates a double- layer force. This force is primarily composed of two factors namely an electrostatic repulsion between the counter- ion clouds and a thermal pressure. This is a many body prob-

lem and the force can be derived by solving the Poisson- Boltzmann (PB) equation. The PB equation, however, becomes one-dimensional due to translation invariance. Considering the surface (with charge density σ_s) and DNA (with charge density σ_d) as two charged planes located at $x = 0$ and d, respectively, $n(x)$ as the external charge density and $\phi(x)$ as the electrostatic potential due to the two charged surfaces, PB equation for a single plane can be written as:

$$\frac{\partial^2\phi(x)}{\partial x^2} + \kappa^2 \exp^{-\phi(x)} = \frac{l_b}{z} n(x) \tag{1.6}$$

The normalized dimension-less electrostatic potential $\phi(x) = e\psi(x)/k_BT$. ψ is the electric potential, z is the valency of the ions, k_B is the Boltzmann constant, T is the temperature, e is the electron charge, Bjerrum length $l_b = \frac{e^2}{\epsilon k_B T}$, ϵ is the dielectric constant, and κ is a constant that depends on the boundary conditions. With boundary conditions $\frac{\partial\phi(x)}{\partial x} = \frac{\sigma_s l_b}{ze}$ at the surface and $\frac{\partial\phi(x)}{\partial x} = \frac{\sigma_d l_b}{ze}$ at the DNA, the pressure P(d) between these two planes separated by distance d is given as:

$$P(d) = \frac{k_BT}{dl_b} \int \partial x \left[\frac{1}{2} (\frac{\partial\phi}{\partial x})^2 - \frac{\partial}{\partial x} (\frac{\partial\phi}{\partial x}) \right] \tag{1.7}$$

The first term of the integral is the repulsive term due to the thermal pressure of the counter-ions. One notes that it produces repulsive thermal pressure even for two oppositely charged-layers at small d. Hence, the repulsive force is present even when surface charge is partially reversed due to the presence of divalent cations. The second term is due to the electrostatic stress of the counter- ion clouds and is attractive in nature. It is important to note that $P(d)$ does not depend on bulk ion concentration, though it depends significantly on the valence (z) of the counter- ions. The pressure $P(d)$ will be positive when force is repulsive and it will be negative for the attractive force. Moreover at lower d, repulsion is more significant whereas at larger separa-

tions attraction becomes important. Some correlations among counter- ions can also generate stronger short- ranged electrostatic force which produce attractive interactions between DNA and surface. A stable configuration is produced when the electrostatic attraction overcomes the thermal repulsion. The adsorption of DNA on a surface is assisted by a weakening of the repulsive thermal pressure conjugated with an increasing attractive interaction. This is primarily controlled by the ratio of the surface charges. In the experiments it is tuned by modifying DNA concentration in the buffer solution. Attractive short- ranged electrostatic force, between DNA and surface, can also be produced by correlations among the counter- ions. The ionic strength of the ions is a significant parameter in this process since the screening of counter- ion charges can effect this interaction. The screening length of the electrostatic potential in water is described by the Debye length $\lambda_D \sim \frac{0.33\ nm}{\sqrt{I}}$, where I ($\sim \frac{0.5}{n\ z^2}$) is the ionic strength of a solution and n is bulk concentration of the ions. Thermal vibrations at ambient temperatures can also effect this attraction force. λ_D is greater than the average separation between the charges on the DNA or surface ($\sim 1\ nm$) when ionic concentrations are small ($I < 0.1\ M$). Under this situation it has been shown that the divalent ions will be effected by each other as well as by the negative charges on the DNA and the surface. Correlations between the counter-ions will be strong in this case exhibiting some staggered geometries for the divalent ions. These correlations lead to short ranged attractive interactions between DNA and the surface. The interactions can lead to 2-dimensional DNA network on the surfaces. Depending on the concentration of DNA and cations in the buffer, isolated DNA structures or 2-dimensional DNA networks can be obtained.

1.5.1 Interaction with Mica surface

Mica is an atomically smooth and chemically inert surface. It has been extensively utilized for DNA immobilization studies [65–67]. With immense literature present for DNA adsorption on Mica surfaces, it presents a good reference substrate for DNA adsorption studies. Cleaved surface layers of Mica are negatively charged due to the deficiency of K^+ ions [66]. For interacting negatively charged DNA with these surfaces, presence of cations, as discussed earlier is necessary. The interactions occur through charge inversion and formation of electrical double layer. Divalent cations like Mg^{2+} have also been used in charge inversion for adhesion of DNA on mica surfaces [66]. Following image (fig. 1.8) shows scanning probe microscopy (SPM) images of Plasmid DNA and the Branched DNA on mica surfaces. The figure shows isolated (fig. 1.8(a)) as well as 2-dimensional (fig. 1.8(b)) of Plasmid DNA on the mica surface. Weather one obtains isolated DNA or a network of DNA depends on the concentration of DNA and Mg^{2+} cations in the buffer. Fig. 1.8(c) displays a Branched DNA structure. Both these DNA, Plasmid and Branched DNA, have been studied in the present thesis on SiO_x and TiO_2 surfaces, respectively.

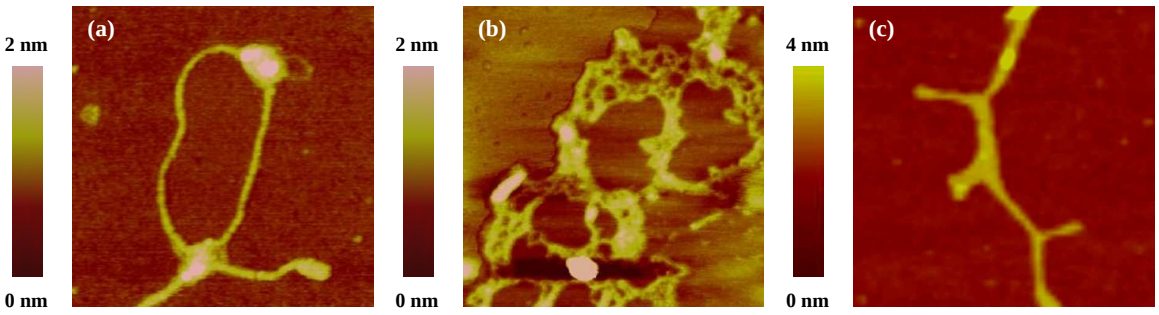

Figure 1.8: (a) Isolated Plasmid pBR322, (b) 2-dimensional network of Plasmid pBR322 (c) Branched DNA on mica surface

1.5.2 Interaction with natively oxidised Silicon surface

Silicon is one of the most common material used to fabricate micro and nanoscale bio-medical devices [68, 69], however it is passivated with a thin native oxide (SiO_x) layer under atmospheric conditions. The biocompatibility of this layer provides a suitable environment for the immobilization of DNA [70]. The SiO_x layer present on the natively oxidized silicon surface is negatively charged [71]. This surface also requires presence of positively charged cations to interact with DNA. The adsorption of DNA on the silicon substrate is thus enabled by monovalent or divalent cations like Na^+ or Mg^{2+} in the buffer which induce a charge inversion of the Si/SiO_x surface. The adsorption of DNA on this substrate is thus driven by electrostatic interactions.

1.5.3 Interaction with TiO_2 surface

The biocompatible property of TiO_2 material makes it applicable in medicinal science for immunoassay, orthopedic implants, cancer treatment and drug delivery [72, 73]. The surface modifications of TiO_2 play an important role in the immobilization of DNA on this surface. Ion irradiation and UV illumination of the surface can be utilized for modification of this surface. Ion irradiation creates oxygen vacancy states (Ti^{3+}) due to the preferential sputtering of oxygen [74]. UV illumination of this surface leads to changes in its chemical and physical properties which play an important role in the photo-immobilization and binding of biomolecules [75]. Consequently the wetting behavior of these surfaces changes from being hydrophobic to hydrophilic [76] which promotes the attachment of biomolecules. UV irradiation of TiO_2 surface also causes photo-reduction of Ti^{4+} states to Ti^{3+} states, thus creating

oxygen vacancies on the surfaces. The damaged TiO_2 has defect states as well as available dangling sites, which act as centers for photo- immobilization of DNA [76]. Here oxygen vacancy sites also play an important role [77]. In the interaction of TiO_2 surfaces with DNA, the amine base from the latter conjugate with the surface defect as well as functional groups [77, 78]. Surface functional groups, such as $\equiv TiOH_2^-, \equiv TiO^-, \equiv TiOH$, or surface-adsorbed water can undergo inner and outer sphere interaction with the potential binding energy sites of exocyclic amino groups of adenine and cytosine. Cleaves et.al [79] showed that the DNA is adsorbed on hydrated TiO_2 surfaces through a condensation process, forming Ti-O-PO_3H_2 groups.

The thesis is organized in the following form. Chapter 2 discusses the experimental techniques that have been utilized in this thesis. Chapter 3 presents the results on SiO_x surfaces after their nanopatterning with low energy ion beams. Formation of nanostructures and ripples along with their interaction with plasmid DNA have been investigated here. Structural modifications to the morphological parameters of DNA are also presented. Roughening behavior, wetting properties and the scaling properties of the ion irradiated nanopatterned SiO_x surfaces have been investigated in chapter 4. Modifications in the scaling and fractal properties after DNA adsorption are also presented here. In chapter 5, nanopatterning of TiO_2 surfaces during ion irradiation with low energy beams has been investigated. The nanostructures show a shape transition at high fluences. TiO_2 surfaces have also been modified using UV irradiation and results are presented in chapter 6. The ion beam modified as well as the UV irradiated surfaces were interacted with branched DNA. For the UV modified surfaces, DNA condensation into toroidal structures is observed, whereas no such formation is seen on the ion sputtered surfaces. PDMS surfaces undergo many physico - chemical changes

upon plasma etching. Interaction of fibroblast cells with these surfaces has been investigated in chapter 7 and the results show enhanced adhesive behavior. The conclusion is presented in chapter 8.

Bibliography

[1] George M. Whitesides and Bartosz Grzybowski, Science, **295**, 2418 (2002).

[2] A. D. Maynard, R. J. Aitken, T. Butz, V. Colvin, K. Donaldson, G. Oberdorster, M. A. Philbert, J. Ryan, A. Seaton, V. Stone, S. S. Tinkle, L. Tran, N. J. Walker, and D. Warheit, Nature, **444**, 267 (2006).

[3] Shawn. J. tan, J. Mol. Eng. Mater., **02**, 1440011 (2014)

[4] Paula. M. Mendes, Chun. L. Yeung, and Jon. A. Preece, Nanoscale Res Lett., **2(8)**, 373 (2007).

[5] Michael Breitenstein, Ralph Hlzel and Frank F Bier, Journal of Nanobiotechnology, **8**, 10 (2010).

[6] Nurxat Nuraje, Ipsita. A. Banerjee, Robert. I. MacCuspie, Lingtao Yu, and Hiroshi Matsui, J. Am. Chem. Soc., **126 (26)**, 8088 (2004).

[7] W. Lu, C. M. Lieber, Nat. Mater., **6**, 841 (2007).

[8] P. Gong, C. Y. Lee, L. J. Gamble, D. G. Castner, D. W. Grainger, Anal. Chem, **78**, 332 (2006).

[9] D. Y. Petrovykh, H. Suda Kimura, L. J. Whitman, M. J. Tarlov, J. Am. Chem. Soc, **125**, 5219 (2003).

[10] Patrick M. McLendon, Daniel J. Buckwalter, Erica M. Davis, and Theresa M. Reineke, Mol. Pharmaceutics, **7(5)**, 1757 (2010).

[11] A. E. Nel, L. Madler, D. Velegol, T. Xia, E. M. V. Hoek, P. Somasundaran, F. Klaessig, V.Castranova, M. Thompson, Nature Materials, **8**, 543 (2009).

[12] O. Cohavi, S. Corni, F. De Rienzo, R. Di Felice, K.E. Gottschalk, M. Hoefling, D. Kokh, E. Molinari, G. Schreiber, A. Vaskevich, R. C. Wade, Journal of Molecular Recognition, **23**, 259 (2010).

[13] H. Chen, L. Yuan, W. Song, Z. K. Wu, D. Li, Progress in Polymer Science, **33**, 1059 (2008).

[14] M. Corno, A. Rimola, V. Bolis, P. Ugliengo, Physical Chemistry Chemical Physics, **12**, 6309 (2010).

[15] P. Thevenot, W.J. Hu, L. P. Tang, Current Topics in Medicinal Chemistry, **8**, 270 (2008).

[16] Stuart. C. McBain, Humphrey. H. P. Yiu, and Jon Dobson, Int J Nanomedicine., **3(2)**, 169 (2008).

[17] A. Nel, T. Xia, L. Madler, N. Li, Science, **311**, 622 (2006).

[18] D. B. Warheit, Toxicological Sciences, **101**, 183 (2008).

[19] Ivana Fenoglio, Bice Fubini, Elena M. Ghibaudi, Francesco Turci, Ivana Fenoglio, Bice Fubini, Elena M. Ghibaudi, Francesco Turci Advanced Drug Delivery Reviews, **63**, 1186 (2011).

[20] S. L. McArthur, K. M. McLean, Surface Modification. In: Wnek, GE, Bowlin, GL (eds.) Encyclopedia of Biomaterials and Biomedical Engineering, Informa Healthcare, New York, (2008).

[21] Maozi Liu , Nabil A. Amro , Christine S. Chow , and Gang-yu Liu, Nano Letters,**2 (8)**, 863 (2002).

[22] Bezuayehu Teshome, Stefan Facsko and Adrian Keller, Nanoscale, **6**, 1790 (2014).

[23] J. Vicente Prez-Girn , M. Hirtz , C. McAtamney , A. P. Bell, J. Antonio Mas, M. Jaafar, O. de Luis, H. Fuchs, J. Jensen, R. Sanz. Nuclear Instruments and Methods in Physics Research B, **339**, 67 (2014).

[24] R. Wang, K. Hashimoto, A. Fujishima, M. Chikuni, E. Kojima, A. Kitamura, M. Shimohigoshi T. Watanabe. Nature, **388**, 431 (1997).

[25] H. Gudnason, M. Dufva, D. D. Bang, A. Wolff. BioTechniques, **45**, 261 (2008).

[26] Harinarayanan Puliyalil and Uro Cvelbar, Nanomaterials, **6**, 108 (2016).

[27] A. I. Aria, B. J. Lyon, M. Gharib, Carbon, **81**, 376 (2015).

[28] J. W. Coburn, H. F. Winters, J. Appl. Phys., **50**, 3189 (1979).

[29] Yunling Bai, "Surface modifications for enhanced immobalization of Biomolecules: Applications in biovatalysis and Immuno-Biosensor" Thesis, The Ohio State University, (2006).

[30] J. F. Ziegler, Handbook of Stopping Cross sections for Energetic Ions in all Elements, Peragmon Press, (1980).

[31] P. Sigmund, Phys. Rev., **184**, 383 (1969).

[32] P. Sigmund, J. Mat. Sci., **8** , 1545 (1973).

[33] K. B. Winterbon, Radiat. Eff., **13**, 215 (1972).

[34] R. M. Bradley, J. M. E. Harper, J. Vac. Sci. Technol. A, **6**, 2390 (1988).

[35] G. Katara, N. Hemvani, S. Chitnis , V. Chitnis , D. S. Chitnis, Indian J Med Microbiol, **26**, 241 (2008).

[36] Bin Yan, Junguang Tao, Christina Pang, Zhe Zheng, Zexiang Shen, Cheng Hon Alfred Huan, and Ting Yu, Langmuir, **24**, 10569 (2008).

[37] Rong Wang, Kazuhito Hashimoto, Akira Fujishima,Makoto Chikuni, Eiichi Kojima, Atsushi Kitamura, Mitsuhide Shimohigoshi, and Toshiya Watanabe, Adv. Mater., **10**, 2 (1998).

[38] M. Miyauchi, N. Kieda, S. Hishita, T. Mitsuhashi, A. Nakajima, T. Watanabe and K. Hashimoto, Surf. Sci., **511**, 401 (2002).

[39] F. Djurabekova, J. Samela, H. Timko, K. Nordlund, S. Calatroni, M. Taborelli, W. Wuensch, Nuclear Instruments and Methods in Physics Research Section B: Beam Interactions with Materials and Atoms, **272**, 374 (2012).

[40] E. M. Liston, L. Martinu, M. R. Wertheimer J. Adhesion Sci. Technol., **7**, 1091 (1993).

[41] A. C. Fozza, J. E. Klemberg-Sapieha, M. R. Wertheimer, Plasmas Polym., **4**, 183 (1999).

[42] K. Tsougeni,N. Vourdas, A. Tserepi, E. Gogolides, C. Cardinaud, Langmuir, **25(19)**, 11748 (2009).

[43] J. Chai, F. Lu, B. Li, D. Y. Kwok , Langmuir, **20(25)**,10919 (2004).

[44] Dirk Hegemann, Herwig Brunner, Christian Oehr, Nuclear Instruments and Methods in Physics Research B, **208**, 281 (2003).

[45] R. L. Williams, D. J. Wilson, N. P .Rhodes, Biomaterials, **25(19)**, 4659 (2004).

[46] C. Ozcan, P. Zorlutuna, V. Hasirci, and N. Hasirci, Macromol. Symp., **269**, 128 (2008).

[47] M. T. Khorasani, H. Mirzadeh, and S. Irani, Radiat. Phys. Chem., **77**, 280 (2008).

[48] K. Tsougeni, P. S. Petrou, A. Tserepi, S. E. Kakabakos, and E. Gogolides, Microelectron. Eng., **86**, 1424 (2009).

[49] Jessica M. Dechene, thesis Surface Modifications of Poly(dimethylsiloxane)for Biological Application of Microfluidic Devices The University of Western Ontario (2010).

[50] C. Seguin, J. McLachlan, P. Norton, and F. Lagugne-Labarthet, Appl. Surf. Sci., **256**, 2524 (2010).

[51] J. Lai, Y. Lin, Y. Denq, S. Shyu, and J. Chen, Journal of Adhesion Science and Technology, **10(3)**, 231 (1996).

[52] J. Kim, M. Chaudhury, and O. M. J., Journal of Colloid and Interface Science, **226(2)**, 231 (2000).

[53] F. Katzenberg, Surface and Coatings Technology, **200**, 1097 (2005).

[54] H. Hillborg, J. Ankner, U. Gedde, G. Smith, H. Yasuda, and K. Wikstrom, Polymer, **41**, 6851 (2000).

[55] H. Hillborg, N. Tomczak, A. Olah, H. Schonherr, and G. Vancso, Langmuir, **20(3)**, 785 (2004).

[56] A. Olah, H. Hillborg, and G. Vancso, Applied Surface Science, **239**, 410 (2005).

[57] G. Bausch, J. Stasser, J. Tonge, and M. Owen, Plasmas and Polymers, **3**, 23 (1998).

[58] David J. Guckenberger, Erwin Berthier, Edmond W. K. Young, and David J. Beebe, Lab Chip., **12(13)**, 2317(2012).

[59] Juewen Liu ,Phys. Chem. Chem. Phys., **14**, 10485 (2012).

[60] J. N. Israelachvili, Intermolecular and Surface Forces. (Academic Press Inc., San Diego, (1992)).

[61] D. Andelman, in: R. Lipowsky, E. Sackmann (Eds.),Handbook of Biological Physics, vol. 1B, Elsevier, Amsterdam, (1995).

[62] R. J. F. L. Decarvalho, E. Trizac, J. P. Hansen, Phys. Rev.E, **61**, 1634 (2000) .

[63] G. Barbero, L. R. Evangelista, N. V. Madhusudana, Eur.Phys. J. B, **1**, 327 (1998).

[64] B.R. Horrocks, R. D. Armstrong, J. Phys. Chem. B, **103**, 11332 (1999).

[65] Yajing Kan, Qiyan Tan, Gensheng Wu, Wei Si Yunfei Chen, Scientific Reports, **5**, 8442 (2015).

[66] David Pastr, Olivier Pitrement, Stphane Fusil, Fabrice Landousy, Josette Jeusset, Marie-Odile David, Loc Hamon, Eric Le Cam, and Alain Zozime, Biophys J., **85(4)**, 2507 (2003).

[67] Helen G Hansma, Annu. Rev. Phys. Chem., **52**, 71 (2001).

[68] D. M. Hartmann, M. Heller, S. C. Esener, D. Schwartz, G. Tu, J. Mater. Res., **17**, 2 (2002).

[69] Vladimir V. Mitin, Viatcheslav A. Kochelap, Michael A. Stroscio, Introduction to Nanoelectronics: Science, Nanotechnology, Engineering, and Applications Cambridge University Press, (2008).

[70] Hamsa Jaganathan and Biana Godin,Adv Drug Deliv Rev., **64(15)**, 1800 (2012).

[71] R. J. Kershner, L. D. Bozano, C. M. Micheel, A. M. Hung, A. R. Fornof, J. N. Cha, C. T. Rettner, M. Bersani, J. Frommer, P. W. K. Rothemund and G. M. Wallraff, Nat.Nanotechnol, **4**, 557 (2009).

[72] T. Wang, H. Jiang, L. Wan, Q. Zhao, T. Jiang, B. Wang, S. Wang, Acta Biomater., **13**, 354 (2015).

[73] Jin Huang, Ping Dong, Weichang Hao, Tianmin Wang, Yayi Xia, Guozu Da, Yubo Fan, Applied Surface Science, **313**, 172 (2014).

[74] Tapobrata Som, Dinakar Kanjilal, Nanofabrication by Ion-Beam Sputtering: Fundamentals and Applications CRC Press, (2012).

[75] J. Vicente Perez-Giron, M. Hirtz, C. McAtamney, A. P. Bell, J. Antonio Mas, M. Jaafar, O. de Luis, H. Fuchs, Jens Jensen and R. Sanz Nuclear Instruments and Methods in Physics Research B,**339**, 67 (2014).

[76] R. Wang, K. Hashimoto, A. Fujishima, M. Chikuni, E. Kojima, A. Kitamura, M. Shimohigoshi, T. Watanabe, Nature, **388**, 431 (1997).

[77] Andre E. Nel, Lutz Mdler, Darrell Velegol, Tian Xia, Eric M. V. Hoek, Ponisseril Somasundaran, Fred Klaessig, Vince Castranov and Mike Thompson Nature Materials, **8**, 543 (2009).

[78] Na Li, Linglan Ma, Jue Wang, Lei Zheng, Jie Liu, Yanmei Duan, Huiting Liu, Xiaoyang Zhao, Sisi Wang, Han Wang, Fashui Hong, and Yaning Xie, Nanoscale Res Lett., **5(1)**, 108 (2010).

[79] H. James Cleaves II, Caroline M. Jonsson, Christopher L. Jonsson, Dimitri A. Sverjensky, and Robert M. Hazen Astrobiology, **10**, 3 (2010).

Chapter 2

Experimental Techniques, Methods and Materials

2.1 Introduction

The present thesis explores modification of Natively Oxidised Silicon (SiO_x), Titania (TiO_2) and Poly dimethyl Siloxane (PDMS) surfaces by ion irradiation, UV illumination and plasma etching. These modified surfaces are interacted with Deoxyribonucleic acid (DNA) and Fibroblast Cell. The morphological and chemical changes in these surfaces prior to and post interaction have been studied by utilizing the techniques of X-ray Photoelectron spectroscopy, Atomic Force Microscopy, Contact angle measurements, Fourier-Transform infrared Spectroscopy and Scanning Electron Microscopy. Technique of ion irradiation through Electron Cyclotron Resonance (ECR) source as well as low energy Ion source has been utilized to create nanostructures on SiO_x and TiO_2 surfaces. Surface of TiO_2 was also modified with an exposure of UV light. Modification in the surface of PDMS is executed by oxygen and nitrogen plasma etching. The interaction of the plasmid DNA, branched DNA and fibroblast cells with the surfaces post and prior to modification has been investigated here.

In section 2.2, we discuss the experimental techniques of ion irradiation, UV

illumination and plasma etching. Section 2.3 discusses various characterization techniques utilized in the thesis. Structures of Si, SiO_x, PDMS, TiO_2, DNA and fibroblast cell are also discussed in section 2.4

2.2 Ion irradiation techniques

2.2.1 Ion irradiation with ECR

Electron Cyclotron Resonance (ECR) ion source was utilized to ion irradiate TiO_2 at low energy but at high fluence. This source is also called a hot plasma ion source. Electron cyclotron resonance is a phenomenon observed in plasma physics, condensed matter physics, and accelerator physics. In ECR plasma source, plasma is produced by matching the cyclotron frequency of an electron (ω_{cye}) in a external static magnetic field, with the microwave frequency (ω_{rf}), i.e. the ECR condition ($\omega_{cye} \simeq \omega_{rf}$ [1]). An electron in a static and uniform magnetic field will move in a circle due to the Lorentz force. The circular motion may be superimposed with a uniform axial motion, resulting in a helix, or with a uniform motion perpendicular to the field, e.g., in the presence of an electrical or gravitational field, resulting in a cycloid. The angular frequency ($\omega = 2\pi$f) of this cyclotron motion for a given magnetic field strength B is given as

$$\omega_{rf} = \omega_{cye} = \frac{e}{m}B \tag{2.1}$$

e and m are the charge and mass of the electron, respectively. The plasma electrons are confined in a superposition of an axial magnetic field component which is produced by solenoids or permanent magnets and the radial magnetic field of a multipole magnet. A minimum B [3, 4] structure is created as the magnetic field has a minimum in the middle and further increases in all directions. Thus a closed surface is created where electron cyclotron resonance condition is fulfilled and the electrons passing through that surface

can be accelerated resonantly. However, the high ratio of maximum magnetic field strength to minimum magnetic filed strength i.e the mirror ratio of the magnetic field, results in a long confinement time for the plasma electrons. These electrons can pass the resonance region and gain high energies which ionize the plasma atoms and ions into high charge states through successive single ion ionization. Because of their large mass, the ions in the plasma do not get accelerated and remain in thermal condition.

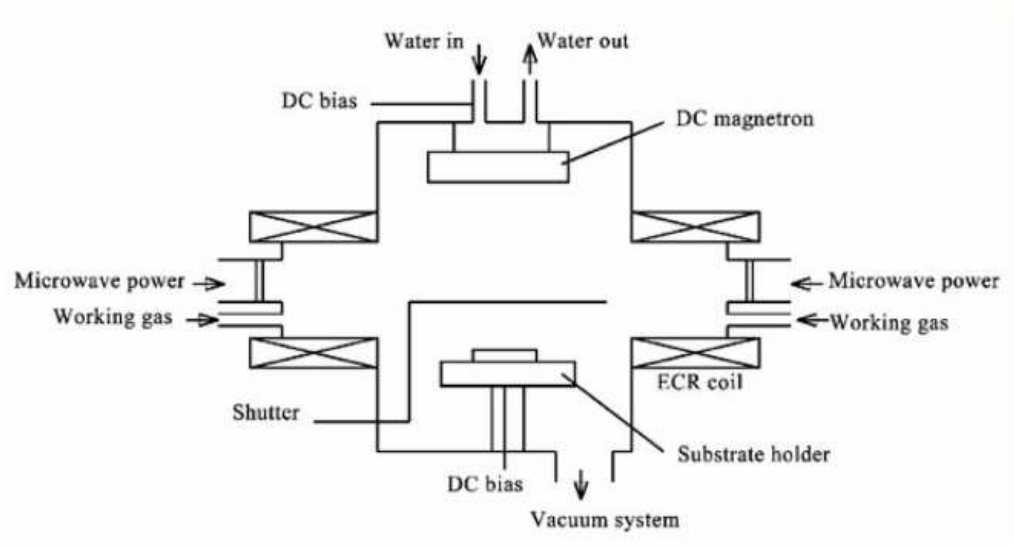

Figure 2.1: Operation and Schematic illustration of the ECR ion source set up [1]

The plasma ions are not confined by the magnetic field but by the space charge potential of the electrons . The confinement is not perfect and electrons leave the plasma. As the plasma tends to stay neutral, ions are effectively followed by electrons. By use of a suitable extraction geometry and application of high voltage, ions can be extracted from the ion source. The accelerated beam quality was determined by parameters like extraction voltage and geometry, intensity, and magnetic field in the extraction region.

After extraction at +10KV, the beam widens up because of space charging. Fig. 2.1 shows the schematic of the ECR ion source set up.

2.2.2 UHV Ion Gun

Thermo Scientific Ar ion source (EX03) was utilized for ion irradiation of TiO_2 and SiO_x. EXO3 is an ion gun which is based on electron impact source and is designed to be used in the presence of inert gases. The source is installed in a UHV system with vacuum of 10^{-11} Torr. The vacuum is achieved with the help of ion, turbo and rotary pump. EX03 ion gun is mounted on a 70 mm diameter flange with a 34 mm outside diameter flange for the gas input. The ion gun consists of two parts (a) the gas line cover and (b) lens column.

EXO3 ionizes gas atoms in the source region of the ion gun and further accelerates them. These ions are transfered to the sample via the lens column. These ions are produced at a high positive potential and are thus accelerated through the gun to produce a beam of ions whose energy lies between 500eV and 3 keV. The gas is directly fed into the source region. A filament in the source region is heated to emit electrons, these electrons are accelerated in the source cage. The electrons traverse the source region and collide with the gas atoms, removing electron and forming positive ions. The ions produced in the source region are accelerated through an aperture in the extractor lens element by a positive potential. This beam is then shaped and focused onto the sample with the help of an electrostatic lens to control the diameter of the ion beam. The current of the ion beam is essentially controlled by the gas pressure and emission current. The gas pressure determines the number of atoms within the ionization region and emission current is the electron

current flowing from the filament to the source cage. Emission current indicates the number of electrons flowing through the ionization chamber.

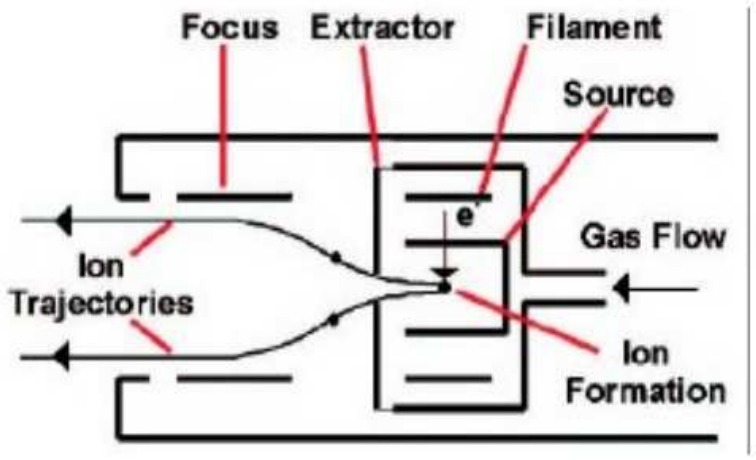

Figure 2.2: Schematic diagram of EX03 ion gun [2].

Schematic diagram of EX03 ion gun is shown in figure. 2.2. Specification of EXO3 ion gun

1. Energy Range :- 0.3 to 3 keV
2. Target Current:- $>$ 20 μA (3keV), $>$ 10 μA(500eV)
3. Working distance :- 50 to 200 mm
4. Gas species:- inert gas
5. mounting flange :- 70 mm UHV

EX03 UHV ion gun utilizing Ar ion source at a flux of 1×10^{13} ions/cm^2 sec with the beam size of 30 mm diameter was utilized to sputter TiO_2 (110), and SiO_x single crystals at an angle of 15^0.

2.2.3 UV illumination Lamp

Chemical modifications have also been achieved by utilizing UV light to create new functional groups on the surfaces. High-energy UV photons break up molecular organic bonds on the surfaces. The opened bonding sites strive to return to a chemically stable condition as quickly as possible. These open bonds are saturated by the atoms and radicals formed from ambient oxygen due to UV radiation and new compounds are created on the surface. Hydroxyl, carbonyl and/or carboxyl groups created as a consequence of UV irradiation have higher polar character, effecting the wetting and surface energy properties of the surface.

In the present thesis a EiKO F15T8/BLB 18 inch, 15 watt tube, with a T-8 bulb and G13 base is utilized to modify TiO_2 surfaces. This lamp is a blue black UV (365 nm) lamp with a mercury content of 5 mg.

A typical UV lamp is shown in fig. 2.3.

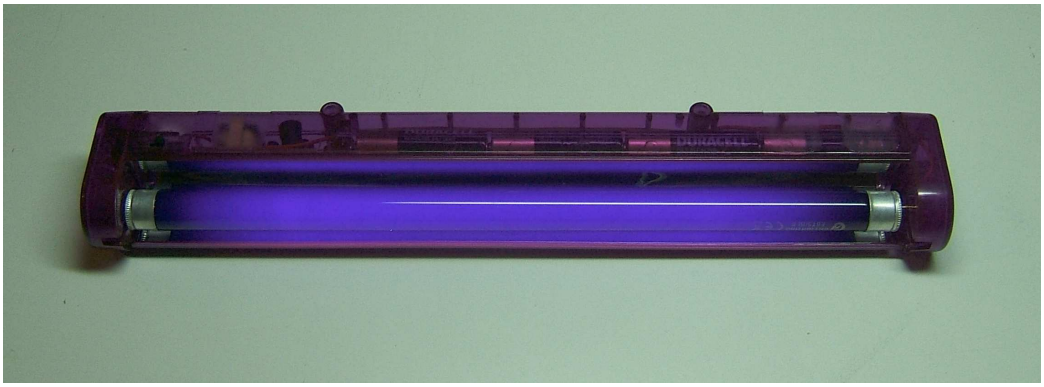

Figure 2.3: UV lamp

2.2.4 Plasma Reactor

Plasma medium and its properties are mainly described by its temperature and electronic density. Electrical discharges are commonly used to produce a plasma from a gas. These plasma can be divided in two categories: equilibrium and non-equilibrium plasma. The glow discharge plasma is a non-equilibrium plasma in which the electrons are hotter than the ions. They can be produced by an electric field (DC or alternating) which delivers energy to the gas to ignite the plasma and maintain it. One of the most used configurations is the radio-frequency (RF) discharge between two plane electrodes. In this configuration, the plasma is capacitively coupled and the power supply interacts with the plasma almost exclusively by displacement current [5]. The advantage is that one can use the plasma even with electrodes covered by an insulating material. The frequency range is from a few kHz to 200 MHz but the usual frequency used for RF discharge plasma is 13.56 MHz [6]. The RF plasma being a non-equilibrium plasma has hot electrons (T_e few eV), ions and neutral species at the gas temperature. At megahertz frequencies, only electrons follow the electric field oscillations [6]. A non-reactive gas is introduced into the discharge, in the inter-electrode space. Atoms or molecules are dissociated and (or) ionized by the electronic collisions to form ions or radicals. These ions and radicals can stay in the plasma and react with other species, or they can diffuse to the reactor walls and to substrate. The radicals and the ions react with the substrate (and walls) surface and modify it. Volatile components can be created that will leave the surface. This results in an etching of the surfaces exposed to the plasma. The principle of operation of rf capacitively coupled plasma reactor is represented in fig. 2.4.

The plasma treatment of PDMS was carried out in a plasma reactor (M-PECVD-1A [S]). The samples were placed on the substrate holder inside the

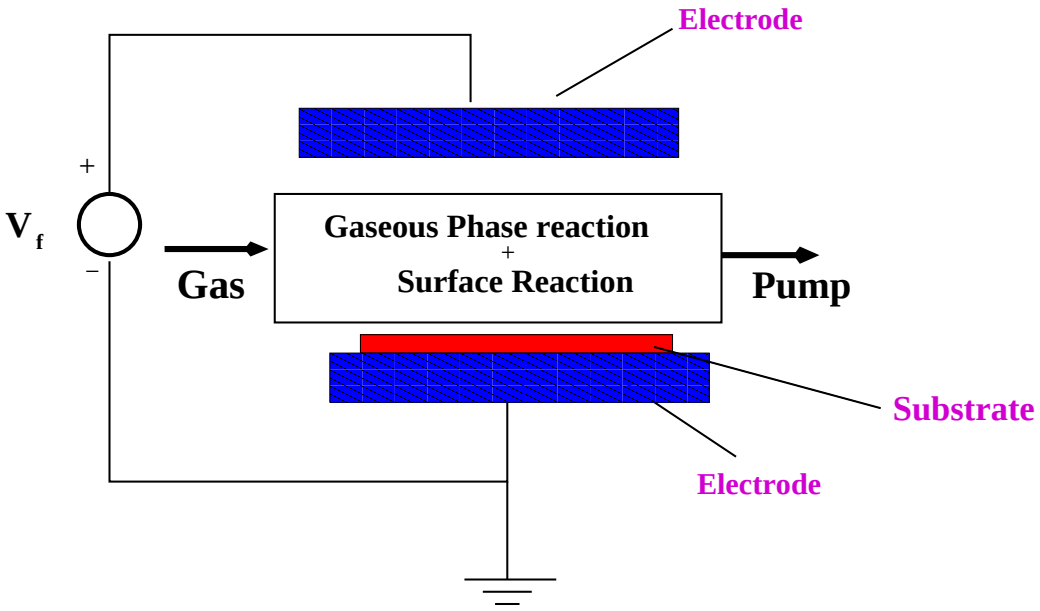

Figure 2.4: Radio-frequency, capacitively coupled plasma reactor, principle

reactor chamber. The reactor was evacuated to 0.1 Pa during the roughing stage and the desired process pressure was obtained through closed loop pressure control during which the pressure was maintained by butterfly valve. Capacitively coupled RF discharge at the frequency of 13.56 MHz was created by supplying 50 W power between the powered electrode and grounded electrode by ionizing the process gas that was supplied to the reactor at the flow rate of 10 sccm. The polymer samples were exposed to the plasma for the desired time (1 min/5min) at the pressure of 20 Pa.

2.3 Characterization Technique

2.3.1 X-Ray Photoelectron Spectroscopy -(XPS)

XPS is a surface sensitive spectroscopic technique which measures the elemental composition, chemical state, empirical formula and electronic states of the elements that exist within a material. XPS is also called ESCA (Electron Spectroscopy For chemical analysis). In 1981 Siegbahn won the Nobel Prize for his contribution to the field of XPS [7]. It is a very helpful technique in obtaining information about oxidation states and atomic composition of the analyzed compounds. XPS involves a single electron process which is based on photo-electron effect described by Albert Einstein. This technique is used to measure:

1. Elemental composition of the surface (top 0 to 10 nm usually)
2. Empirical formula of pure materials
3. Elements that contaminate a surface
4. Chemical or Electronic state of each element in the surface
5. Uniformity of elemental composition across the top surface (line profiling or mapping)
6. Uniformity of elemental composition as a function of ion beam etching (depth profiling)

The spectra are obtained by irradiating a solid surface with a beam of X-rays and then measuring the kinetic energy of the electrons that are emitted from the top 1-10 nm of the material. A photo-electron spectrum is recorded by counting ejected electrons over a range of electron kinetic energies. Peaks appear in the spectrum from atoms emitting electrons of a particular characteristic energy. The energies and intensities of the photo-electron peaks

enable identification and quantification of all surface elements (except hydrogen and helium) [8]. Photoelectric effect is the fundamental basis of the XPS technique.

As shown in the figure. 2.5, incident photons (of energy $h\nu$) are absorbed

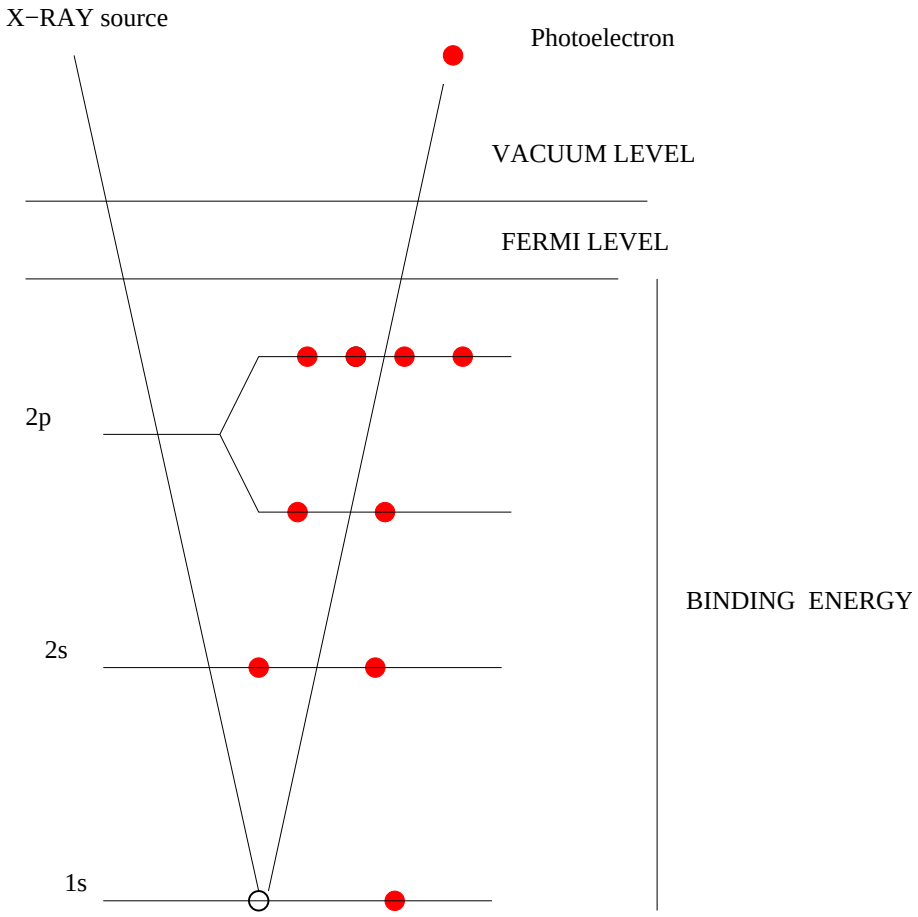

Figure 2.5: Schematic of core level X-ray photo-electron emission process

by various atoms or molecules leading to the ionization and the emission of a photo-electron.

$$M + h\nu \rightarrow M^{+} + e^{-} \tag{2.2}$$

Based on the principles of conservation of energy, the above equation can be interpreted as follows:

$$h\nu - E(e^-) = E(M^+) - E(M) \tag{2.3}$$

where E(M) and E(M^+) are the energies of the atom or molecule M and the ion M^+ formed by ionization, and E(e^-) is the kinetic energy of the photo-electron. Since hν is known and E(e^-) can be measured, the difference between the energies of the ion and the original molecule can be calculated. The difference in energy between the ionized and neutral atoms is generally referred to as the binding energy (BE) which leads to the following equation.

$$KE = h\nu - BE \tag{2.4}$$

The BEs in solids are measured with respect to the Fermi-level of the solid, rather then the vacuum level. From the energy diagram shown in figure. 2.6, it is observed that an additional energy is required to raise an electron from the solid to the energy level corresponding to an electron at rest in vacuum. This energy difference is referred to as the work function ϕ . Thus the above equation can be expressed as

$$KE = h\nu - BE - \phi \tag{2.5}$$

Where ϕ is the work function of the spectrometer as illustrated from the calculations of the Figure 2.6.

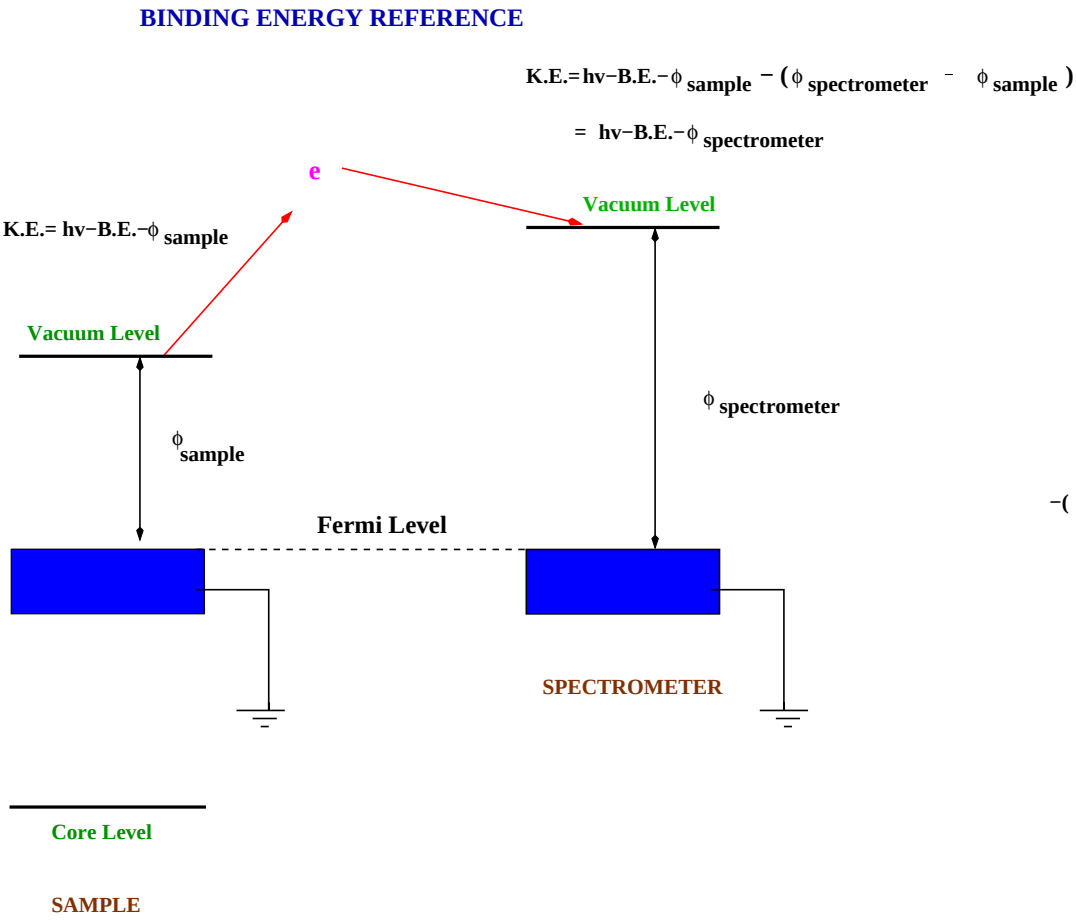

Figure 2.6: Typical schematic to evaluate the Binding energy, BE of the electron inside the atom

XPS instrumentation(as shown in fig. 2.7) consists of an X-ray source, a sample, an electrostatic lens system, an electron energy analyzer, an electron detector and a computer system for data collection and processing [9, 10]. Analysis is done in an Ultra-High Vacuum so as to remove adsorbed gases and eliminate adsorption of contaminants on the sample. The X-rays are generated by bombarding a metallic anode with high energy electrons (10-15 keV) and are then focused onto the sample though use of a monochromator. The energy of the generated x-rays is determined by the anode material which is usually Al or Mg. An electrostatic lens system collects a portion

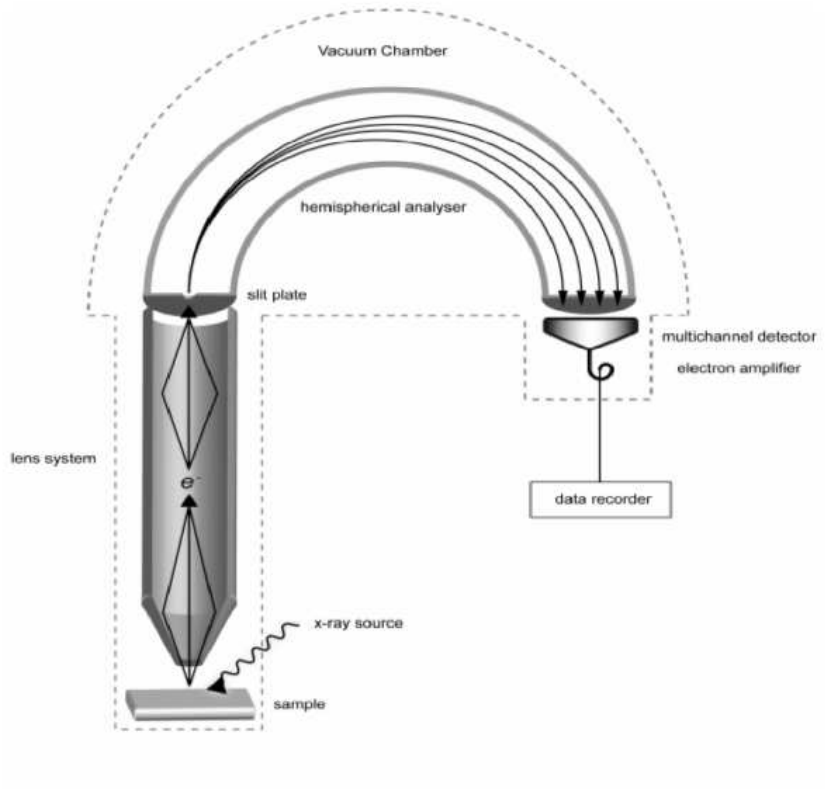

Figure 2.7: Schematic diagram of X-ray Photo-electron system. The key components include X-ray source, channeltron, hemispherical analyzer, and computer system [9].

of these emitted electrons and focuses them into an electron energy analyzer called a concentric hemispherical analyzer (CHA). This analyzer consists of two hemispheres. Different voltages are applied to each hemisphere creating an electric field between them. Electrons entering the analyzer with a higher energy will contact the outer hemisphere while those with lower energy will be attracted to the inner one. In this capacity, only electrons in a narrow energy region, referred to as the pass energy, are able to travel the distance of the analyzer and reach the detector. A variable retarding voltage is applied

to a deceleration element in the transfer lens of the CHA. Therefore, only electrons that leave the target with a specific energy enter and pass through the analyzer to the detector. The commonly used electron detector is referred to as a channeltron. This consists of a bent tube coated with an insulating material which when struck by an electron emits a number of secondary electrons that are accelerated through the channeltron. This process is repeated throughout the length of the tube producing a large number of secondary electrons and therefore an amplified signal. The spectrum is obtained by recording the numbers of electrons as a function of the retarding voltage. This allows the energy resolution to be constant over the entire spectrum.

XPS Spectra Analysis

The intensity of a peak depends on how the x-ray interacts with specific electrons to cause the photoemission process to occur. The efficiency of the photon interaction with the electron is determined by the photo-electron cross section, σ. Each spectral line has a specific width or resolution which is usually defined as the full-width at half maximum. There are three main contributors that affect the photo-electron line width in an XPS spectrum.

1. Heisenberg Uncertainty principle, which states that if the lifetime (Δt) of an atom or molecule in an electronically excited state is quite short, the variability in its energy (ΔE) is consequently greater. Thus the broadening of the spectral line is observed (h is the planck's constant).

$$\Delta E \Delta t \leqslant \frac{h}{4\pi} \tag{2.6}$$

2. The natural line-width of the anode material used as the X-ray source usually limits the overall energy resolution. Thus use of a monochromator does reduce line width and therefore improves the resolution.

3. Resolution is also affected by the pass energy and slit width of the analyzer.

XPS peaks are fitted using a convolution of a Gaussian function to account for the principal X-ray line and instrumental response, and a Lorentzian function to model the lifetime broadening due to the uncertainty principle.
The background shape is also as important as the line shape of the spectra. Since X-rays penetrate far into the material compared to the depth from which electrons of a given kinetic energy can escape, without energy loss from the surface, thus there are changes in the background resulting from energy loss occurring as the photoelectrons are ejected from the material. Therefore, XPS spectra characteristically show an increase in the intensity of the background level on the high energy side of all peaks in an XPS spectrum. This phenomenon is a result of inelastic scattering. For instance, only electrons close to the surface can escape without energy loss. Electrons deeper in the surface lose energy from inelastic scattering and emerge from the sample with reduced KE, and therefore increased BE. Electrons very deep in the surface lose all energy and cannot escape at all. Inelastic scattering is caused from photoelectrons traveling though the solid and interacting with other electrons in the material. The energy loss can result from the primary photo-electron losing energy from a single scattering event as it leaves the sample or multiple scattering events causing secondary low energy electrons to be ejected from the material [11, 12].
As the electrons have spin, electrons ejected from core levels with primary quantum numbers p, d, f show two observable peaks. The separation between the two peaks is referred to as spin-orbit coupling [13, 14]. These doublet states are characterized by total angular momentum, j.

$$j = l \pm 1 \tag{2.7}$$

The relative intensities of these doublet pairs can be calculated from 2j + 1. Thus for p electrons where the angular momentum equals one, the relative intensities are 1:2, while for d electrons the doublet pairs are in the proportion 2:3 and for f electrons the ratio is 3:4.

In the present thesis XPS experiments were done using a VG system (Figure. 2.8). The base pressure was maintained at 1×10^{-10} Torr. The load lock chamber of the system has an UHV Ar ion gun. The system has twin Mg-Al anodes X-Ray source, this source generates non monochromatic X-rays with emission energies of 1253.6 eV and 1486.6 eV for Mg- K_α and Al- K_α lines respectively. The hemispherical analyser attached to the system is operated at 200 eV pass energy, for larger survey scans and at 20 eV pass energy for high resolution scans. The instrumental resolution of the system is 0.9 eV. All the spectra obtained from XPS, reported in the thesis are fitted using VGX-900 software.

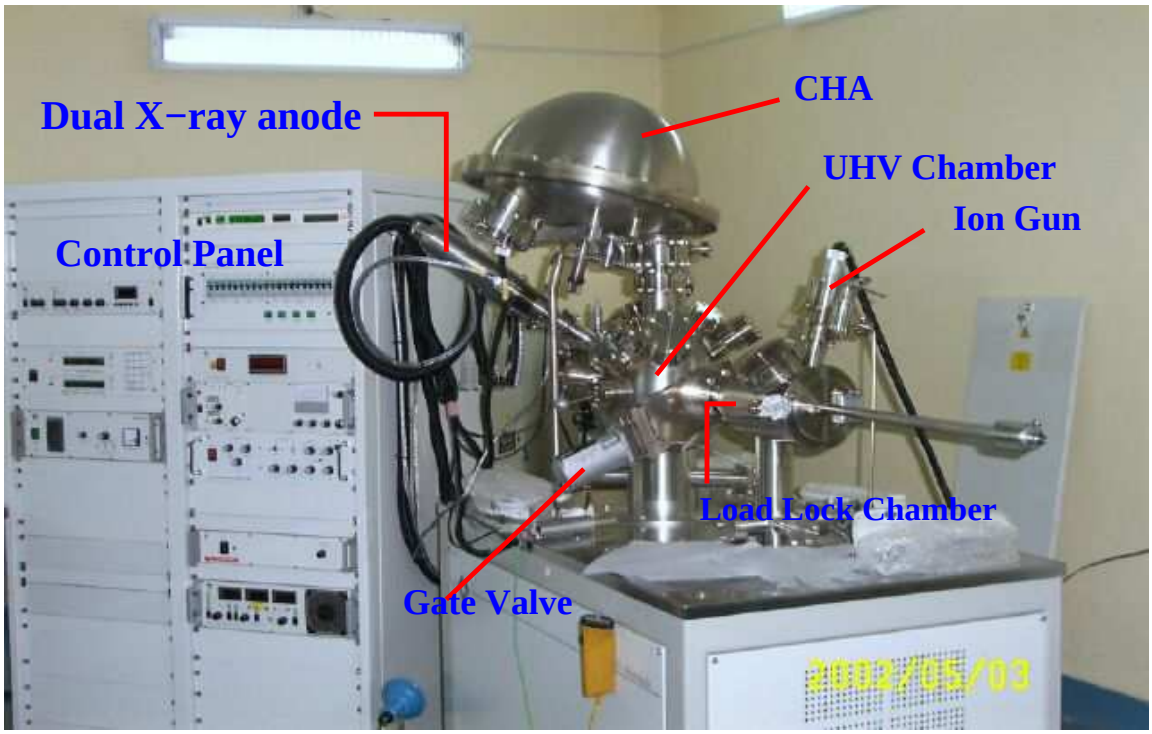

Figure 2.8: XPS system at IOP

2.3.2 Scanning Probe Microscopy- (SPM)

Scanning probe microscopes (SPMs) are a family of tools that are used to make images of nanoscale morphologies of the surfaces and structures, including investigations at atomic scales. A physical probe is used which can scan back and forth over the surface of a sample. During this scanning process, computer gathers data that is used to generate an image of the surface. In addition to visualizing nanoscale structures, some techniques of SPMs can be used to manipulate individual atoms and move them to make specific patterns. SPMs are much different than the optical microscopes where surfaces can be visualised directly. Instead, the SPM probe feels the surface and creates an image to represent it. SPM has a probe tip mounted on the end of a cantilever. The tip rasters the surface of the sample. When the tip is near

the sample surface, the cantilever is deflected by a force [15]. SPMs measure deflections caused by several forces like

1. mechanical contact
2. electrostatic forces
3. magnetic forces
4. chemical bonding
5. van der Waals forces
6. capillary forces

The deflection of the tip is measured by a laser that is reflected off the top of the cantilever and into an array of photo-diodes (similar to the devices used in digital cameras). There are several types of SPMs. Atomic force microscopes (AFMs) measure the electrostatic forces between the cantilever tip and the sample. Scanning tunneling microscopes (STMs) measure the electrical current flowing between the cantilever tip and the sample. In 1981 invention of STM by Binning and Rohrer [16, 17] at IBM zurich reserach lab established the field of nanotechnology.

ATOMIC FORCE MICROSCOPY

The first AFM was invented by Binnig, Quate and Gerber in 1986 and measures the interactions between probe and sample on the atomic level. It works on the principle of measurement of the interactive forces between the tip and the sample surface (separated by distance r) with the help of special probes made up of elastic cantilevers with a sharp tip at the end. Force applied to the tip by the surface, results in the bending or deflection of the cantilever. Schematic of a typical AFM operation is shown in fig. 2.9.

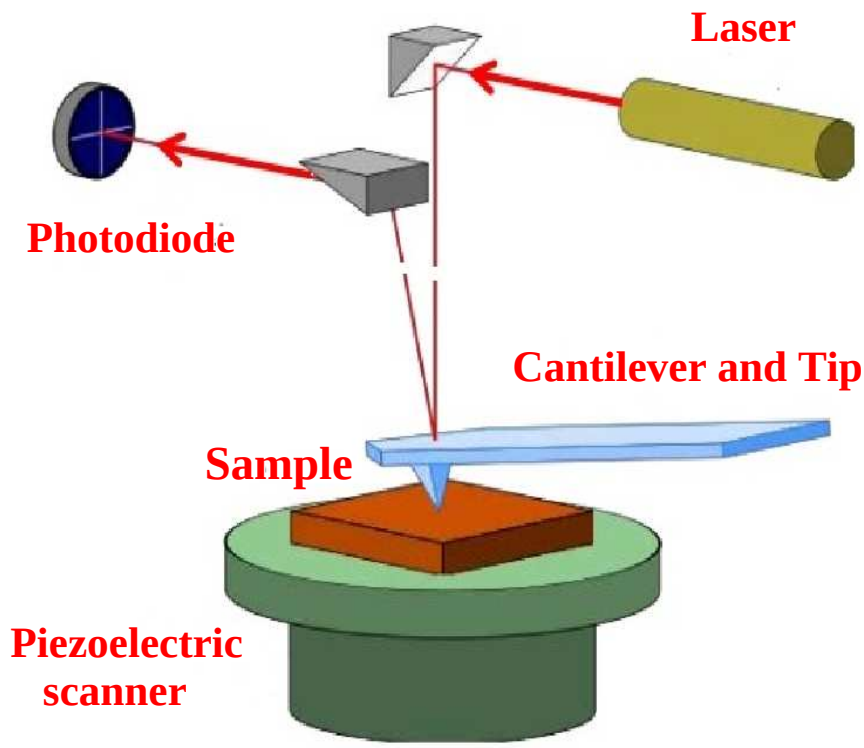

Figure 2.9: The schematic representation of the AFM operation

The interactive forces measured by AFM can be qualitatively explained by attractive van-der-Waals forces and Pauli repulsion forces due to the overlapping electron orbitals. These forces can be described by the Lennard-Jones-potential:

$$U(r) = U_0\left\{ -2\left[\frac{r_0}{r}\right]^6 + \left[\frac{r_0}{r}\right]^{12}\right\} \tag{2.8}$$

The first term describes the long-distance attractions caused, by dipole-dipole interactions and the second term takes into account the short range repulsion due to the Pauli exclusion principle. The energy of interaction is given as

$$W_{PS} = \iint U(r - \acute{r})\eta_p(\acute{r})\eta_s(r)dVd\acute{V} \tag{2.9}$$

where $\eta_p(\acute{r})$ and $\eta_s(r)$ are the densities of atoms in the sample and in the tip whereas d$\acute{V}$ and dV are their respective volumes. The force affecting the tip from a surface can be calculated as:

$$\overrightarrow{F} = - \bigtriangledown (W_{PS}) \tag{2.10}$$

MODES OF OPERATION

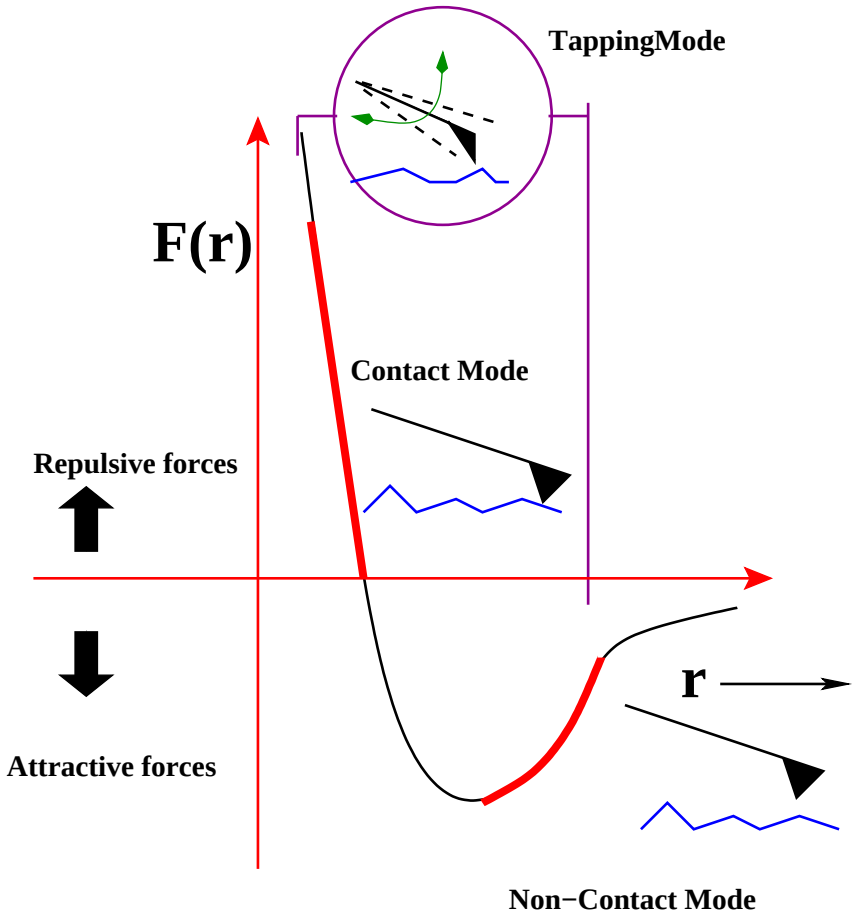

Figure 2.10: Force (F) versus Distance (r)

Fig. 2.10 shows a force versus distance graph. Also different modes of AFM operation are depicted in the figure.

1. Contact mode:- In contact mode, AFM tip and sample are always in contact. The vertical deflection Δx of the cantilever (spring constant k) is directly proportional to forces (F) acting on the tip. According to Hooke s law,

$$F = -k\Delta x \tag{2.11}$$

   The AFM tip is brought in contact with the sample surface and is set to scan the sample in the x-y raster pattern. A feedback loop maintains a 'pre-set' constant deflection (force) of the cantilever with respect to the sample surface by moving the z scanner for each x-y coordinate. The change in z axis corresponds with the topographical height at the sample at each given point. By adjusting the pre-set force, the image contrast can be varied and the damage to the sample can be minimized.

2. Non Contact Mode:-In this mode the tip hovers 50 - 150 Angstrom above the sample surface. Attractive van der Waals forces acting between the tip and the sample are detected, and topographic images are constructed by scanning the tip above the surface. Unfortunately the attractive forces from the sample are substantially weaker than the forces used by contact mode. Therefore the tip is given a small oscillation so that AC detection methods can be used to detect the small forces between the tip and the sample by measuring the changes in amplitude, phase, or frequency of the oscillating cantilever in response to force gradients from the sample.

3. Tapping Mode:-This mode overcomes problems associated with friction, adhesion, electrostatic forces, and other difficulties that plague conventional AFM scanning methods. The tip is placed in contact with the

surface to provide high resolution, and then the tip is lifted off the surface to avoid dragging it across the surface. Tapping mode imaging is implemented in ambient air by oscillating the cantilever assembly at or near the cantilever's resonant frequency using a piezoelectric crystal. During tapping mode operation, the cantilever oscillation amplitude is maintained constant by a feedback loop. When the tip passes over a bump in the surface, the cantilever has less room to oscillate and the amplitude of oscillation decreases. Conversely, when the tip passes over a depression, the cantilever has more room to oscillate and the amplitude increases. When the tip contacts the surface, the high frequency (50k - 500k Hz) makes the surfaces stiff (viscoelastic), and the tip-sample adhesion forces are greatly reduced. Tapping Mode inherently prevents the tip from sticking to the surface and causing damage during scanning.

AFM analysis via Height-Height Correlation and Power Spectral Density Analysis of Surface:

Statistical functions like Height-Height Correlation (fig. 2.11(a)) and Power Spectral Density functions (fig. 2.11(b)) have been utilized in this thesis for deriving the surface properties and its scaling nature. This knowledge is useful in understanding the growth behavior of the surface.

1. Height - Height correlation function (HHCF): Let h(r) be the height of a surface at position r. Mean square of height difference between two surface positions separated by a lateral distance r provides the HHCF ($G(\mathbf{r})$) and is given as:

$$G(\mathbf{r}) = \langle [h(r) - h(0)]^2 \rangle \tag{2.12}$$

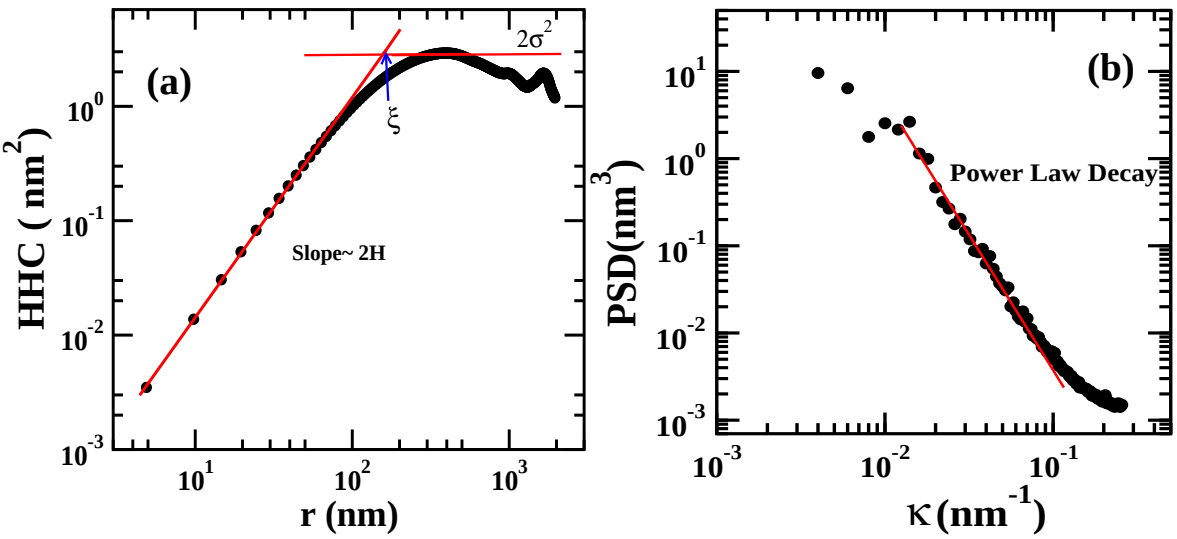

Figure 2.11: (a) HHCF plot (b) PSD plot

For a scale invariant and isotropic surface, $G(\mathbf{r}) \sim r^{2H}$ for r$\ll \xi$ and $G(\mathbf{r}) \sim 2\sigma^2$ for r$\gg \xi$, here ξ is the lateral correlation length and σ is the rms roughness of the surface.

The parameter H is called the roughness exponent or Hurst exponent (0$<$ H $<$1), and is directly related to the local surface fractal dimension D_f. H = d +1 - D_f, where d + 1 is the dimension of the embedded space [18, 19]. The quantity ξ is the lateral correlation length, within which the surface heights of any two points are correlated. Three parameters, σ, ξ, and H, are independent from each other and completely characterize any surface. They represent the growth nature of the surface. A phenomenological scaling function of form $G(\mathbf{r}) \sim \frac{\sigma^2}{2}\left(1 - \exp(-(r/\xi)^{2H}\right)$ can be utilized to obtain values of σ, ξ, H [20].

2. Power spectral density (PSD) :-HHCF discusses the topographical properties of a surface in real space. Another way to understand the topog-

raphy of a surface is in Fourier space (or reciprocal space). To consider the frequency properties of a surface, an expression in reciprocal space is much more informative. The most important statistical function in reciprocal space is the power spectrum. PSD function of a surface profile $h(r)$ at the position r, is defined as:

$$PSD(\kappa) = \frac{1}{L}\left| \int_{-L/2}^{L/2} h(r) \exp^{-i\kappa r}\, dr \right|^2. \tag{2.13}$$

Here, L is the scan length and κ is the spatial frequency. The power law decay behavior in the high κ regime indicates the nature of the evolving surface [21].

This thesis utilizes multimode AFM (Figure. 2.12) from Bruker with a Nanoscope V controller. AFM images reported in this thesis have been acquired under ambient conditions in tapping mode by utilizing RTESPA (phosphorus doped Si) tips. They have a force constant of 20-80 N/m, and resonant frequency of 280-316 kHz. All the images were analyzed using Nanoscope software.

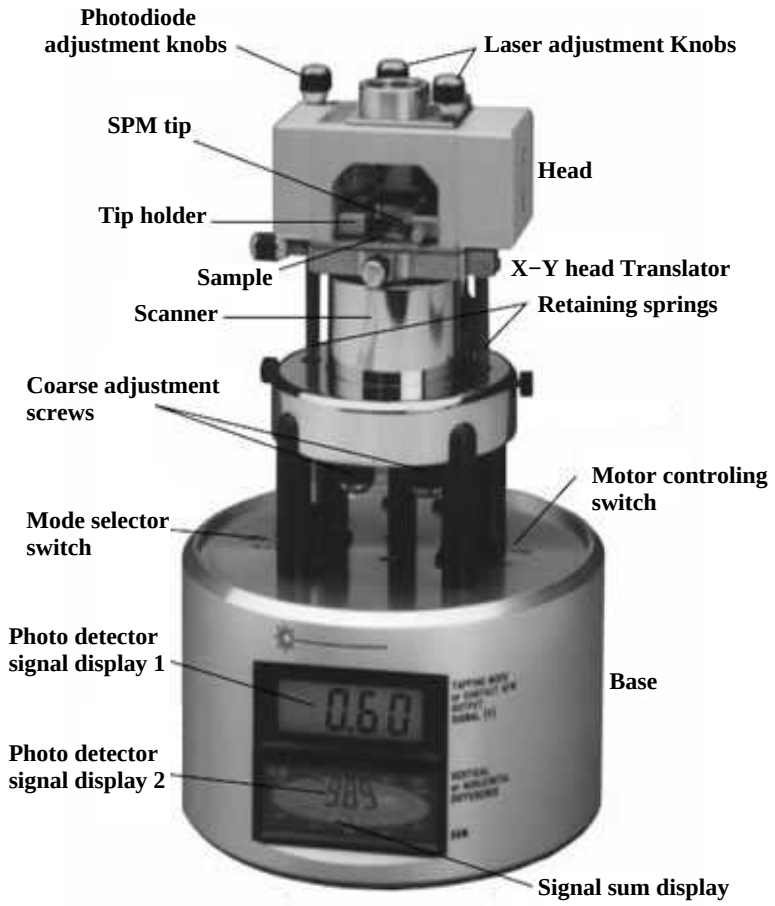

Figure 2.12: AFM system at IOP

2.3.3 Contact angle measurements

Microscopic characteristics of surface like its roughness, surface energy and surface coating play an important role in its wetting behavior for a given liquid. Wettability studies involve measurement of contact angles. Small contact angles ($\theta < 90^0$) correspond to high wettability, whereas large contact angles ($\theta > 90^0$) show low wettability. The contact angle is defined as the angle formed by the intersection of liquid- solid interface and the liquid - vapor interface, which is geometrically acquired by applying a tangent line from the contact point along the liquid -vapor interface in the droplet profile.

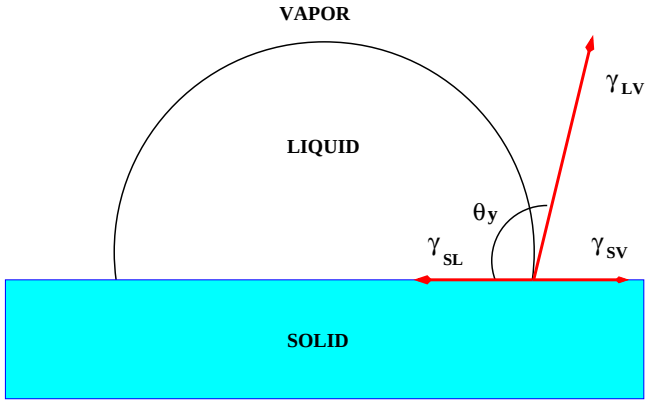

Figure 2.13: Young's Model of Sessile Drop showing relationship between Interfacial Tensions

The interface where solid, liquid and vapor co-exist is referred to as the three-phase contact angle. When a liquid spreads on the surface, a small contact angle is observed, while a large contact angle is measured if liquid beads on the surface. The shape of the liquid droplet is determined by the surface tension of the liquid. For pure liquid each molecule in the bulk is pulled equally in every direction by the neighboring liquid molecules, resulting in a net zero force. Molecules exposed on the surface do not have neighboring molecules in all direction, thus the net force experienced by the surface molecule is not balanced and results in creation of internal pressure. This internal pressure leads to the contraction of the liquid (decrease in the surface area), so as to maintain the lower surface free energy. The intermolecular force that contract the surface is called surface tension and is responsible for the shape of the liquid droplets. In practice certain external forces such as gravity can also deform the droplet. Thus, contact angle is determined by a

combination of surface tension and external forces. Thomas Young in 1805 described the contact angle (θ_y) of a liquid drop on an ideal solid surface. It is defined by the mechanical equilibrium of the drop (Figure. 2.13) under the action of three interfacial tensions [22].

$$\gamma_{LV} cos\theta_y = \gamma_{SV} - \gamma_{SL} \tag{2.14}$$

Here γ_{LV} is the surface tension for liquid vapor interface, whereas γ_{SV} and γ_{SL} are the surface tensions for solid vapor and solid liquid interface.

The most widely used technique of contact angle measurement is a direct measurement of the tangent angle at the three-phase contact point on a sessile drop profile. The equipment consists of a horizontal stage to mount a solid sample, a micrometer pipette to form a liquid drop, an illumination source, and a telescope equipped with a protractor eyepiece. The measurements are achieved by simply aligning the tangent of the sessile drop profile at the contact point with the surface and reading the protractor through the eyepiece (Figure. 2.14).

The contact angle measurements have been performed on SiO_x surfaces as well as on PDMS surfaces at ambient humidity and temperature. For SiO_x surfaces wetting properties have been investigated with water droplets on Dataphysics 0CA15EC system. Contact angle goniometer in static mode was used for sessile drop method. For wetting studies of PDMS surfaces, three liquids namely deionized water, formamide and diiodomethane were utilized. Sessile drop wetting studies were performed on Rame-Hart 500-F1 advanced goniometer (Rame-Hart Instrument Co., Netcong, NJ, USA).

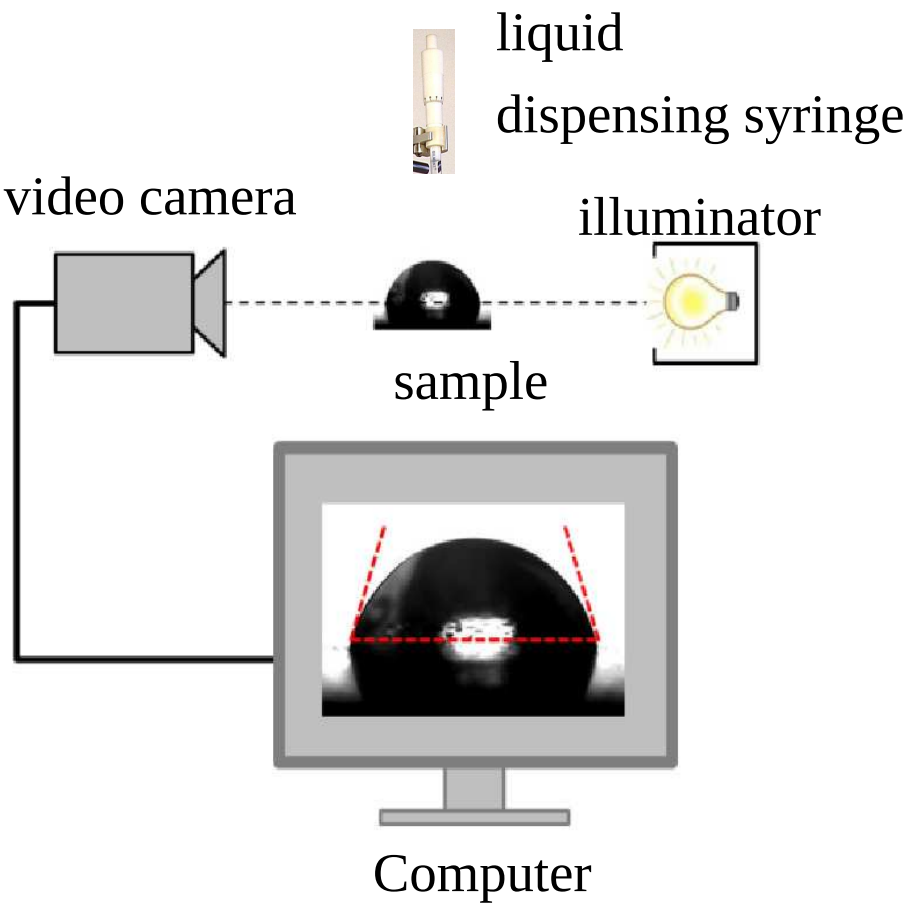

Figure 2.14: Experimental setup schematic of Contact Angle measurement Instrument

2.3.4 Fourier Transform Infrared (FT-IR) Spectroscopy

Infrared radiation is electromagnetic wave whose wavelength is longer than red end of the visible light and shorter than microwave. Infrared spectrum is divided into three regions (a) far infrared (wavenumber 400-100 cm^{-1}) (b) mid infrared (400- 4000 cm^{-1}) and (c) near infrared (14285-4000 cm^{-1}) [23]. Light interacts with the molecules in various manners, for instance by absorption, scattering, reflection etc.. The absorption of the radiation by matter leads to the vibrations of the chemical bonds. A molecule absorbs energy and this causes the intermolecular distance between the atoms to change.

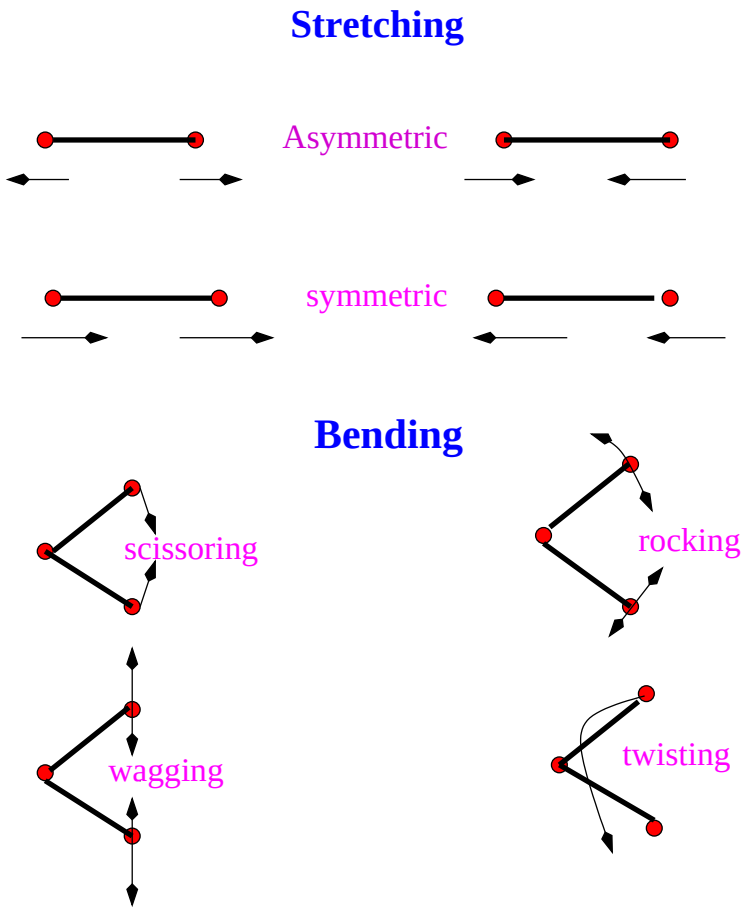

Figure 2.15: Types of Vibrations [24]

This energy is called the vibrational energy. The oscillations of atoms which correspond to the normal modes of vibration can be categorized in two forms.

1. Stretching:- It is a symmetric or antisymmetric movement of atoms along the bond axis

2. Bending:- This vibration occurs when the bond angle between two atoms or group of atoms changes relative to the remaining molecule. These motions are known as scissoring, wagging, rocking, and twisting.

Figure. 2.15 shows the stretching and bending modes [24].

Fourier Transform Infrared Spectroscopy (FT-IR) utilizes IR radiation to obtain information on the vibrational modes of the molecule through fourier tranforming the signal from sample. The apparatus is comprised of a source, beam splitter, two mirrors, a laser and a detector (fig. 2.16). The source emits infrared light which is aimed at the beam splitter. As its name implies, the beam splitter separates the infrared beam into two separate beams. One of which passes on to a stationary mirror and the other to a moving mirror. The moving mirror travels at a constant velocity, which is timed according to the laser wavelength in the system. Both beams from the two mirrors are reflected back to the beam splitter where they are recombined. The beam from the moving mirror travels a different distance in comaparision to beam from the stationary mirror. This creates an interference pattern called an interferogram as some of the wavelengths combine constructively, while others combine destructively. At this point the combined beams are aimed at the specimen. As the beam interacts with the specimen, some of the energy is absorbed and the remaining energy is transmitted through the specimen. The transmitted energy is then measured by the detector which analyses every wavelength simultaneously. To obtain the infrared spectrum, the detector signal is sent to the computer, and an algorithm called Fourier transform is performed on the interferogram to convert it into a single beam spectrum [24]. This is a transmittance spectrum and by taking the log10 of this spectrum an absorbance spectrum can be obtained. The resulting spectrum display the molecular absorption and transmission features, creating a molecular fingerprint of the sample [25]. This allows identification and quantification of the materials in the substance. FTIR involves the twisting, rotating, bending, and vibration of the chemical bonds. If incident infrared radiation has intensity Io, and I is the intensity of the beam after it interacts with the sample then the plot of I/Io as a function of frequency of light gives

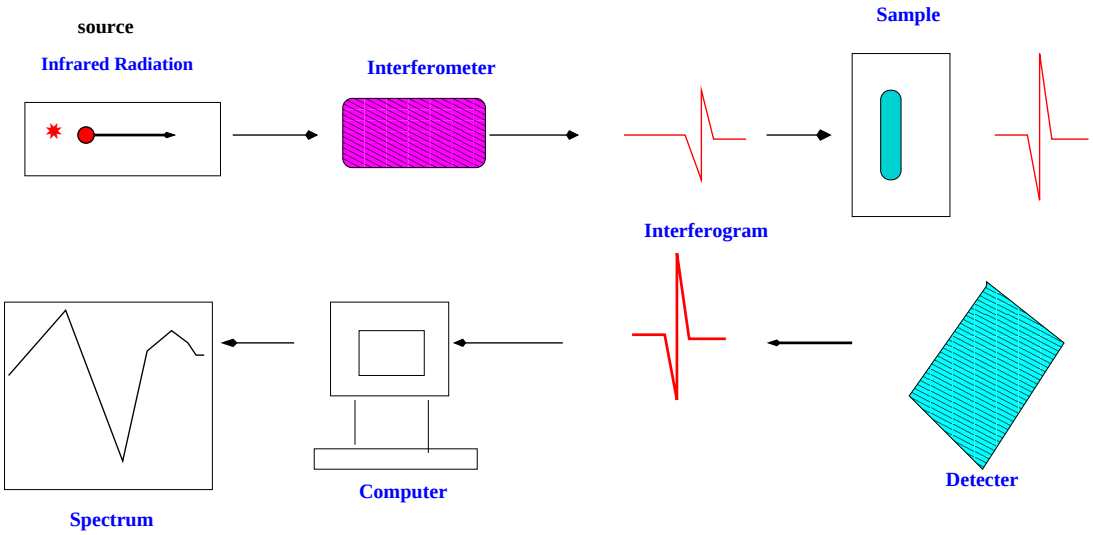

Figure 2.16: Experimental setup schematic of FT-IR

a spectrum, which can be in three formats: transmittance, reflectance, and absorbance. The multiplicity of vibrations occurring simultaneously produce a highly complex absorption spectrum. This is a unique characteristic of the functional groups of the molecules present. A detector is used to measure the intensity of light after it interacts with the sample.

The effects of various plasma treatments on the surface chemistry of PDMS have been investigated using Fourier transform infrared (FTIR). Spectra of untreated and modified polymers were obtained in attenuated total reflectance (ATR) mode using a Thermo Nicolet Nexus 870 FTIR system (Thermo Nicolet Corporation, North America, Madison, WI) equipped with ZnSe crystal. They were recorded in the range of 4000-600 cm^{-1} with a resolution of 4 cm^{-1}.

2.3.5 Scanning Electron Microscope -(SEM)

The fundamental principle of Scanning Electron Microscopy (SEM) is the interaction of high energy beam of electrons with the sample producing a multitude of signals that contain information about the sample's surface topography and other properties such as electrical conductivity etc..

When electrons interact with a surface, they interact with the atoms of the specimen via elastic and inelastic scattering processes. The incident electron which undergoes elastic scattering, continues in its path after the interaction without losing kinetic energy. During inelastic scattering, the incident electron loses a part of its kinetic energy and can activate other electrons or excite atoms of the specimen.

On a basic level, the SEM is composed of a column, specimen stage and number of detectors. Column consists of electron gun, scanning coils, aperture and magnetic lens (fig. 2.17). The electron beam is created by the electron gun situated at the top of the column. The electron guns can be categorized into thermionic guns and field emission guns (FEG). The generated electrons are accelerated down. These electrons pass through a combination of lens and apertures to produce a focused beam of electrons which becomes incident on the surface of the sample.

The magnetic lenses in SEM play the same role of the optical lenses in a traditional microscope. They can control/manipulate the electron beam. The diameter of the electron beam on the sample surface defines the resolution of the microscope. The smaller the diameter, the better is the resolution. Specimen stage is the place where the sample is mounted. The specimen in SEM is usually fixed to a stub consisting of a metal disc, which is mounted on the stage. This stage allows the linear x,y,z movements and rotations around a vertical and a horizontal axes of the specimen. The position of the electron beam on the sample is controlled by the scan coils situated above the objec-

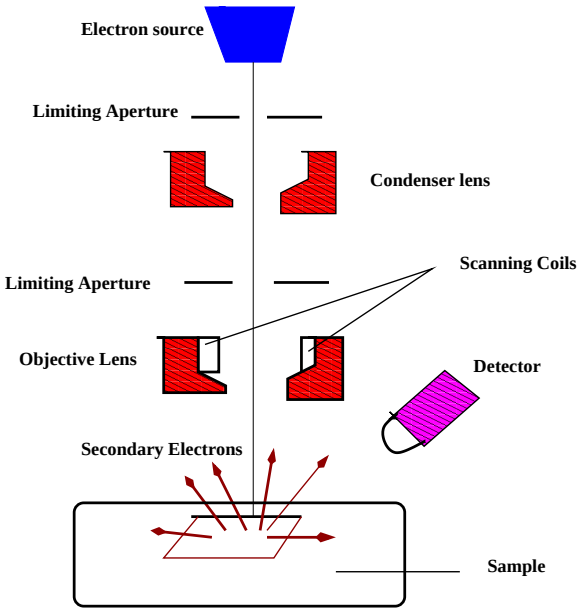

Figure 2.17: Experimental setup schematic of SEM

tive lens. These coils allow the beam to be scanned over the surface of the sample. The scanning or rastering of the beam enables the information from the sample surface to be collected [26]. The whole column, electron gun and the specimen chamber are placed in vacuum. Interaction of electrons with the surface produces a variety of signals like secondary electrons (SEs), back-scattered electrons (BSEs), characteristic and bremsstrahlung X-rays, Auger electrons, light (cathodoluminescence), specimen current, electron beam induced current (EBIC) (in semiconductors) and transmitted electrons (thin samples).

The surface morphology of the untreated and plasma treated PDMS were examined with Jeol JSM-5800 (JEOL, Tokyo, Japan) scanning electron microscope (SEM). Samples were coated with a thin conductive layer of gold in vacuum conditions prior to analysis.

2.4 DNA Structure and Crystal Structure

2.4.1 Structure of Deoxyribonucleic acid (DNA)

DNA subunits

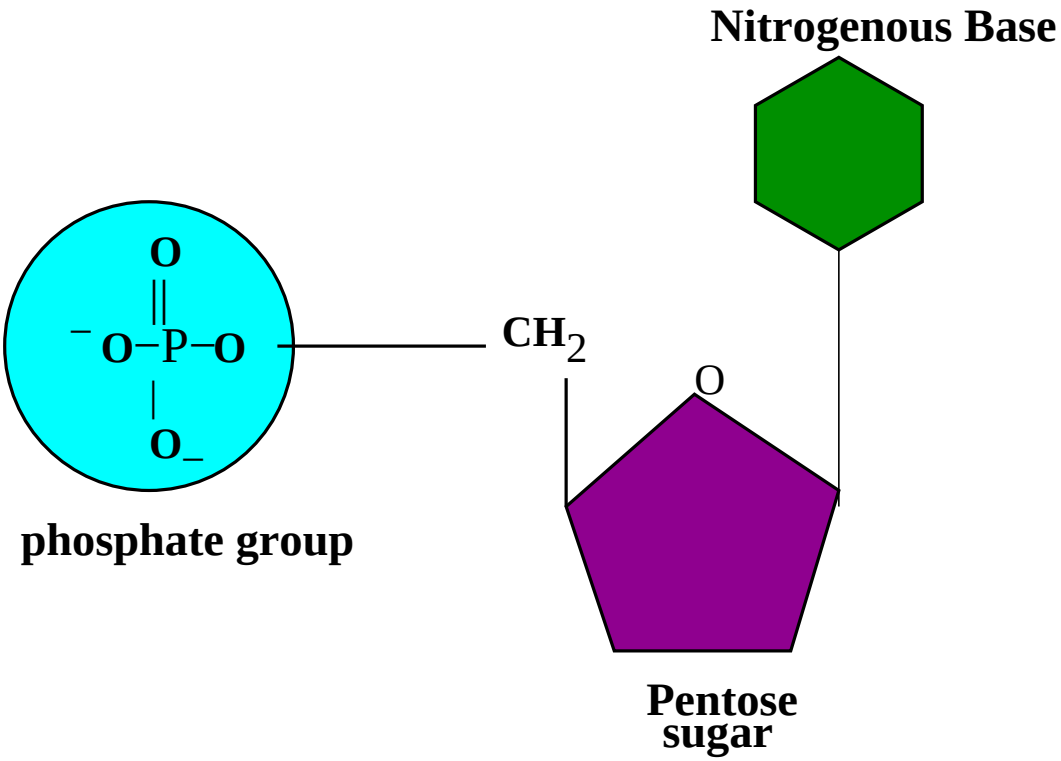

Figure 2.18: Nucleotide Structure

DNA is composed of monomeric units of nucleotide. Each nucleotide consists of a sugar, a nucleobase and a phosphate group (Figure 2.18). The sugar in DNA is the cyclic -D-furanose form of ribose and is referred to as -D-2′-deoxyribose as the hydroxyl group on the 2′ carbon of the ribose ring is replaced with hydrogen. Four major nucleobases found in DNA are derived from the two parent compounds of purine and pyrimidine. The two major purine bases are adenine (A) and guanine (G) whereas the two major pyrimidine bases are cytosine (C) and thymine (T). Each nucleobase is attached

to the sugar through a -glycosyl C1′N linkage (N1 of pyrimidines and the N9 of purines) whereas the phosphate is attached to the sugar through an ester bond at the 5 ′ carbon. In the absence of the phosphate group, the molecule is referred to as a nucleoside.

A strand of DNA is formed by nucleotides covalently linking to each other through a phosphodiester bond in which the 5 ′-phosphate group of one nucleotide is attached to the 3′-hydroxyl group of the next nucleotide creating a polynucleotide chain.

The antiparallel nature of two polynucleotide chains is the main reason behind the double helix of the DNA. One chain of the helix runs in 5′to 3′ orientation whereas the other chain runs from 3′ to 5′ [27]. Figure. 2.19 shows the chemical structure of DNA.

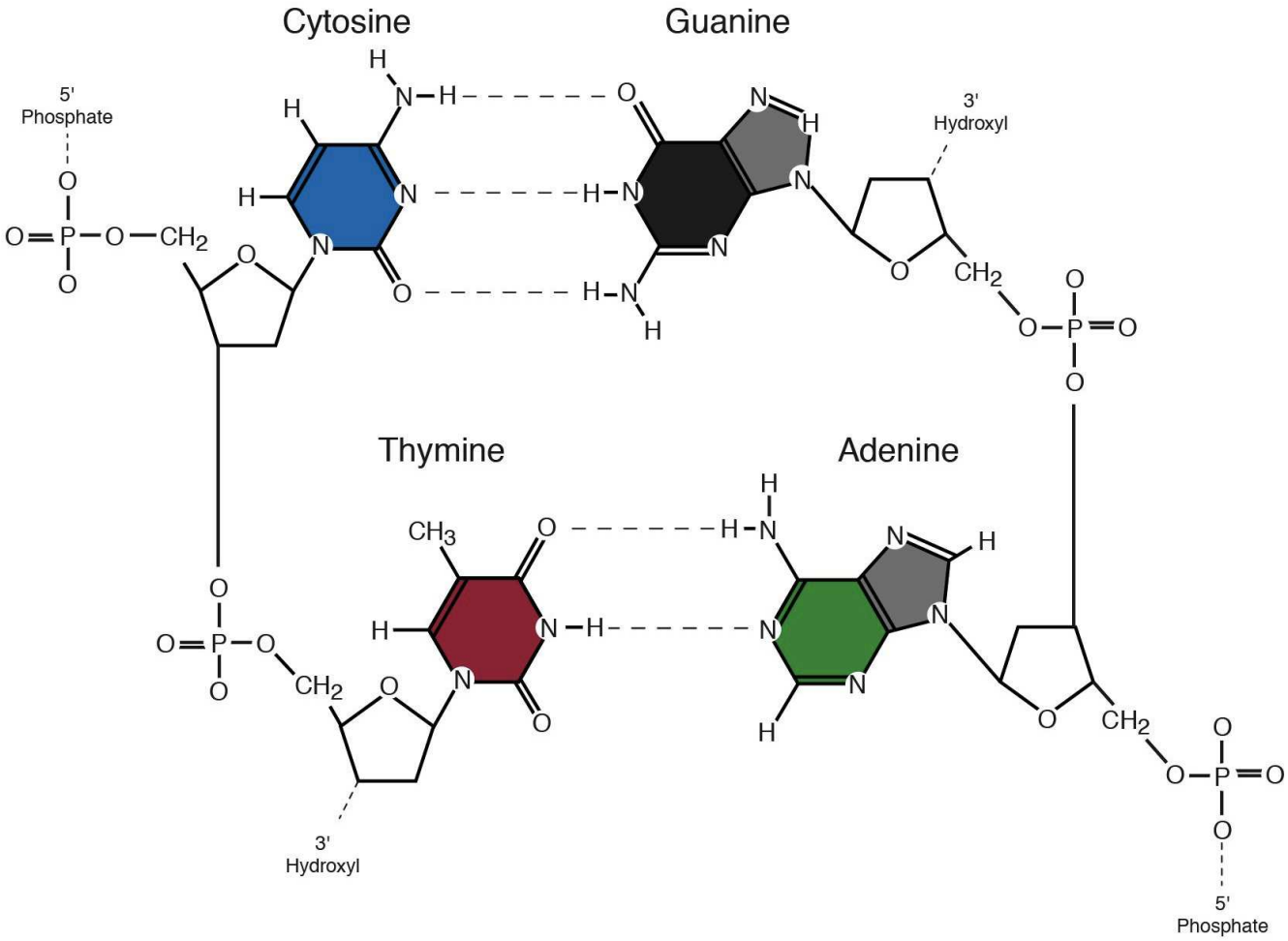

Figure 2.19: DNA chemical Structure [27]

In the year of 1953, James Watson and Francis Crick attempted to build molecular models of DNA [28]. With the combination of Francklin's diffraction patterns, and Chargaff's rules [29], Watson and Crick (WC) proposed the famous double helix model. This model as shown in Figure 2.20, has following major features

1. Two long polynucleotide chains coiled around a central axis, forming a right-handed double helix. This means that the turns are clockwise when looking down the helical axis.

2. The two chains are antiparallel; that is, each chain has a specific orientation, and these run in opposite directions.

3. The bases of both chains are flat structures, lying perpendicular to the axis. They are stacked on one another, 0.34 nm apart, and are located on the inside of the helix.

4. The nitrogenous bases of opposite strands are paired to one another by hydrogen bonds.

5. Each complete turn of the helix is 3.4 nm long. This means that just over ten bases from each strand (10.5 bp) form one complete turn of the helix.

6. Along the molecule, alternating larger major grooves and smaller minor grooves are apparent.

7. The double helix measures approximately 2 nm in diameter.

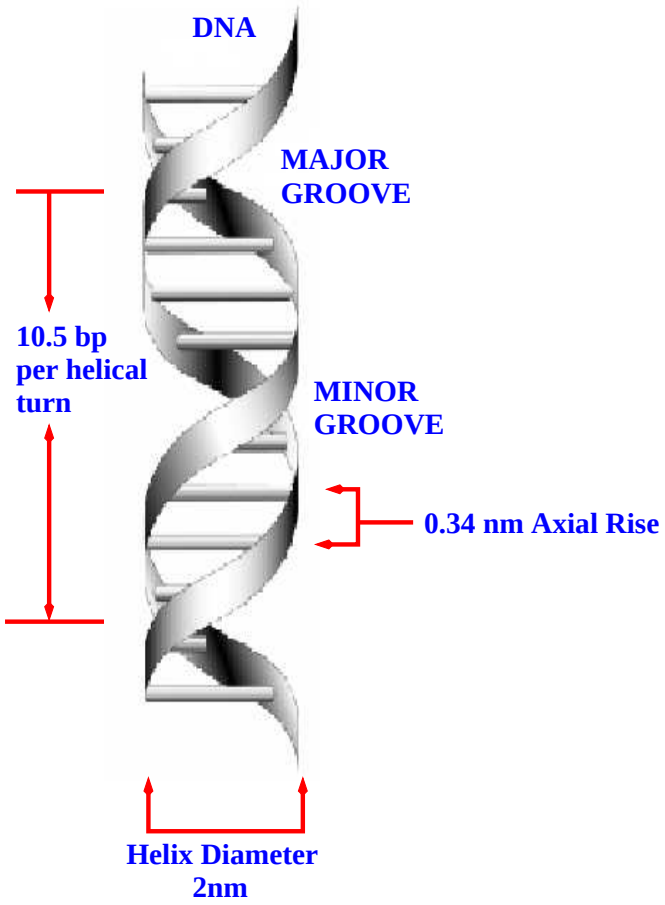

Figure 2.20: The major structural feature of WC base paired DNA [28]

DNA BASE PAIRING

Adenine (A) binds to thymine (T) whilst, guanine (G) binds to cytosine (C). This base pairing is referred to as complementary base pairing, hence the base pairs are called complementary base pairs. The base pairs are bound together by hydrogen bonds. G-C base pairs are bound by three hydrogen bonds whilst, A-T base pairs are bound by two hydrogen bonds as illustrated in the figure. 2.21.

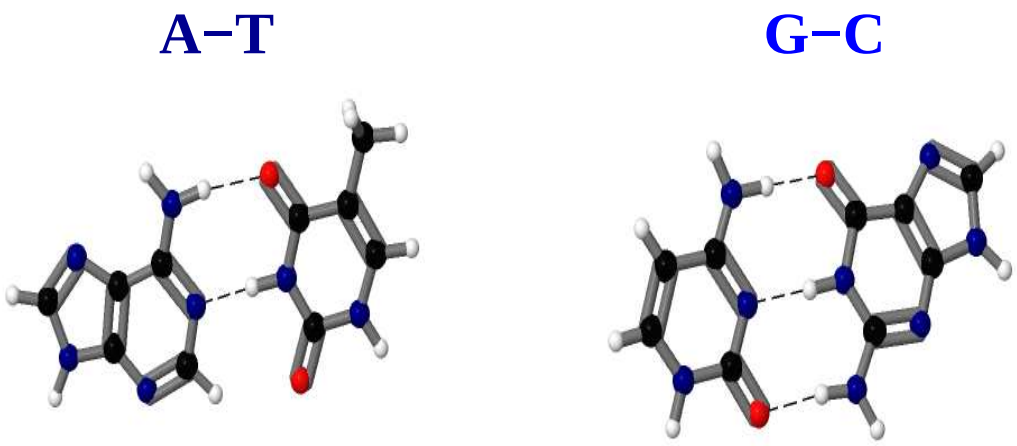

Figure 2.21: DNA Base Pairing.

2.4.2 pBR322

pBR322 (fig. 2.22) is a plasmid DNA and was one of the first widely used E. coli cloning vectors. Created in 1977 in the laboratory of Herbert Boyer at the University of California, San Francisco, it was named after the postdoctoral researchers who constructed it. The p stands for "plasmid," and BR for "Bolivar" and "Rodriguez." pBR322 is 4361 base pairs in length and harbors the origin of replication of plasmid pMB1, a close relative of the plasmid ColE1 [30].

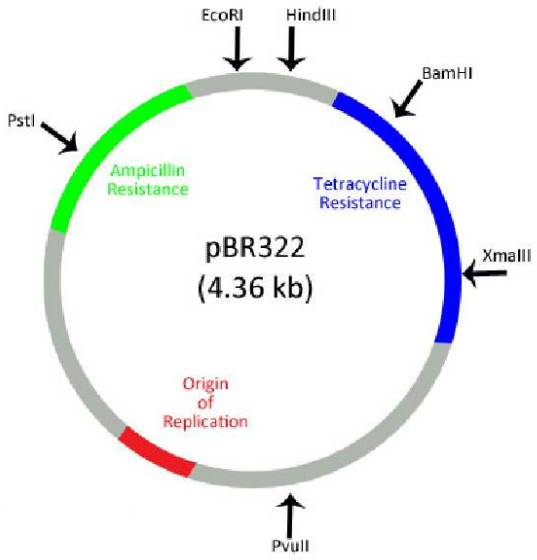

Figure 2.22: Plasmid pBR322 [30]

2.4.3 Branched DNA

The DNA molecule has appealing features for use in nanotechnology: its minuscule size, with a diameter of about 2 nanometers, its short structural repeat (helical pitch) of about 3.4-3.6 nm, and its stiffness', with a persistence length (a measure of stiffness) of around 50 nm. As a chemically based assembly system, DNA plays a key role in bottom-up nanotechnology. The origin of this approach started during 1970s, when an in vitro genetic manipulation was first performed by tacking together molecules with sticky ends [31]. A sticky end is a short single-stranded overhang protruding from the end of a double-stranded helical DNA molecule. Two molecules with complementary sticky ends (having complementary arrangements of the nucleotide bases) will cohere to form a molecular complex. Sticky-ended cohesion is arguably the best example of programmable molecular recognition: there is significant diversity to possible sticky ends, and the product formed at the site of this cohesion is the classic DNA double helix. The axes of DNA double helices

are unbranched lines. Joining DNA molecules by sticky ends can yield longer lines, perhaps with specific components in a particular linear or cyclic order in one dimension [32]. In the figure. 2.23 a simple mechanism for forma-

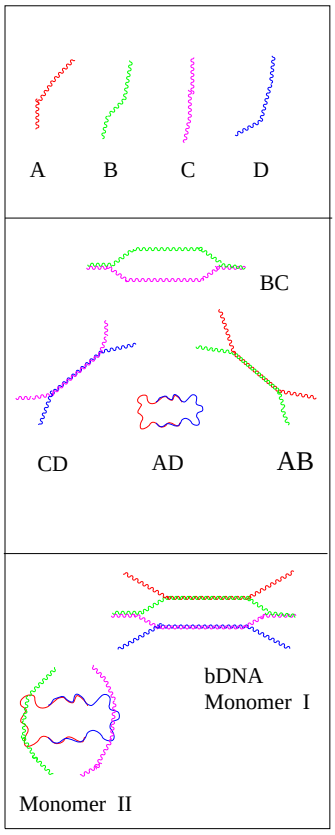

Figure 2.23: Branched DNA

tion of branched DNA is presented, where single stranded DNA (A, B, C, D) have been utilized to form multiple structures (AB, AD, CD, BD). All these structures have sticky edges and can be used to make branched DNA monomers.

2.4.4 Fibroblast Cell

The fibroblast cells manufacture and maintain connective tissues which are the structural framework that support the organs of all animals. Fibrous

proteins and ground substance secreted by fibroblast cells, forms the extracellular matrix which is the basis of connective tissue. Ground substance is composed of varying amounts of water and specialized molecules that help determine how firm or soft the extracellular matrix will be. Thus, fibroblasts give connective tissue its strength, form, and the ability to adhere to other tissue types [33]. Figure. 2.24 shows a typical Fibroblast cell.

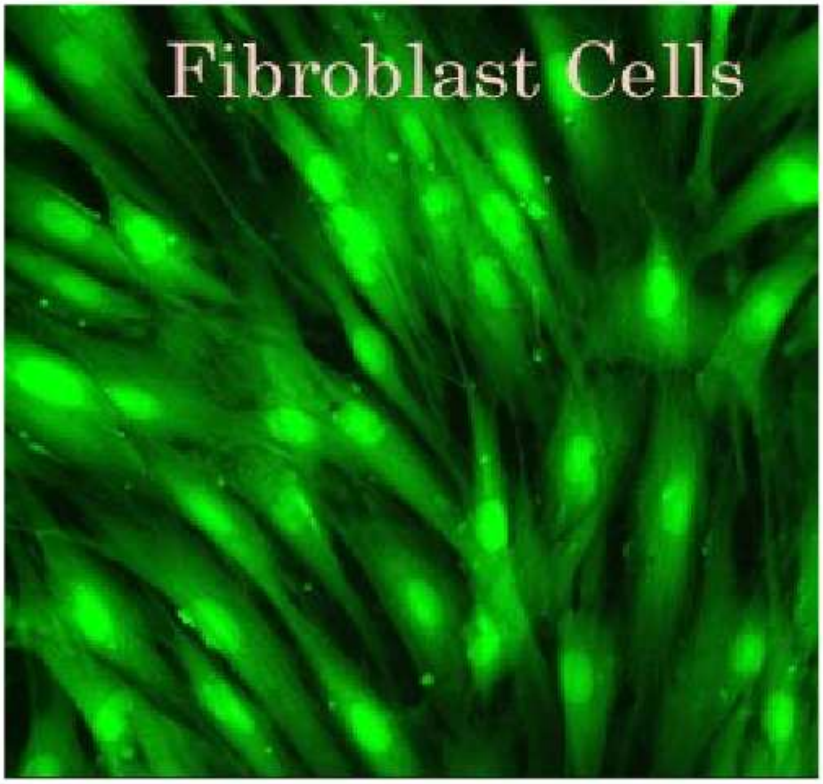

Figure 2.24: Fibroblast cell [33]

2.4.5 Silicon (Si)

Silicon is the second most abundant element in the earth's crust by mass but does not occur as free element. With atomic number of 14 and chemical

symbol as Si, it crystallizes in a diamond cubic crystal structure with lattice spacing of 5.430710 $\mathring{A}$. The outer orbital of silicon has four valence electrons. 1s, 2s, 2p, 3s subshells are completely filled while the 3p shell has two electrons. Silicon finds its major applications in electronic devices and is known to be the one of the best materials to make transistors and computer chips. A number of silicon compounds have important uses. Silicon dioxide (sand) is used in the manufacturing of glass, ceramics, abrasives, food additive, in water filtration systems, as an insulating material, in cosmetics and pharmaceuticals (drugs), in the manufacture of paper, rubber, and insecticides. Another important silicon group is the silicones. The silicones have an amazing range of uses. These include toys, lubricants, weatherproofing materials, adhesives, foaming agents, brake fluids, cosmetics, polishing agents, electrical insulation, materials to reduce vibration, shields for sensitive equipment, surgical implants, and parts for automobile engines.

Silicon exhibits a special kind of face-centered cubic structure known as the diamond lattice [34]. This lattice structure is a combination of two face centered cubic unit cells in which one cell has been displaced along the main diagonal of the cube one-fourth of the distance along the diagonal. Figure. 2.25 shows this structure. There are eight atoms in this structure, four from each cell. Each Si atom is surrounded by four nearest neighbors in a tetrahedral configuration with the original Si atom located at the center of the tetrahedron. Since Si has four valence electrons, it shares these electrons with its four nearest neighbors in covalent bonds. Modeling Si atoms as hard spheres, the Si radius is 1.18$\mathring{A}$ with a lattice constant of 5.43$\mathring{A}$ [35] (figure 2.25).

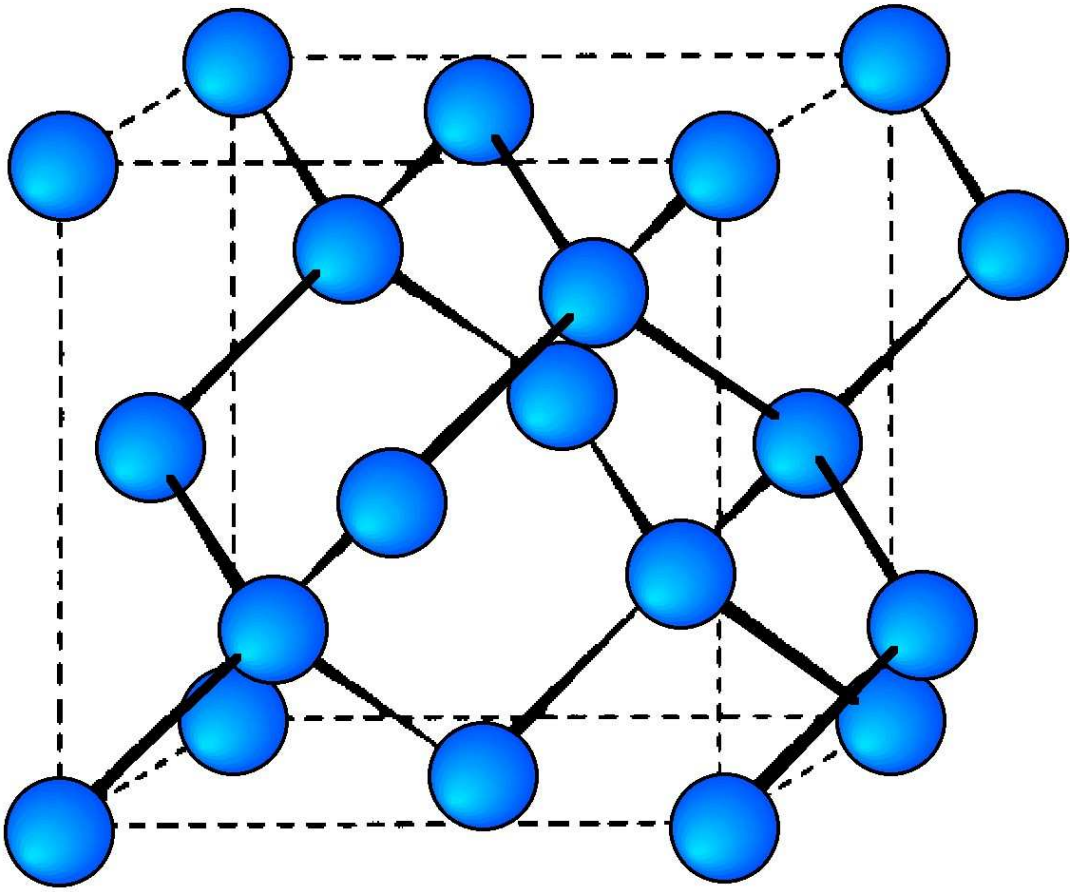

Figure 2.25: Crystal Structure of silicon [36].

2.4.6 Poly dimethyl Siloxane (PDMS)

Polydimethylsiloxane (PDMS) is an polymeric organosilicon compound commonly referred to as silicones. This polymer is mainly used in the silicon -based organic polymer and is known for rheological properties. The polymer is an optically clear, inert, non toxic and non flammable material. It is an elastomeric silicone material that is widely used for rapid prototyping microfluidic systems and cell-chip devices, due to its chemical inertia, thermal stability, permeability to many gases, simple preparation, optical transparency, and low cost [37]. It can be easily integrated with electrodes,

heaters, and sensors, which are fabricated on substrates, to generate multi-functional devices for biomedical applications [38]. Chemical formula of PDMS is $CH_3[Si(CH_3)_2O]_nSi\ (CH_3)_3$, where n is number of monomer (Figure. 2.26) .

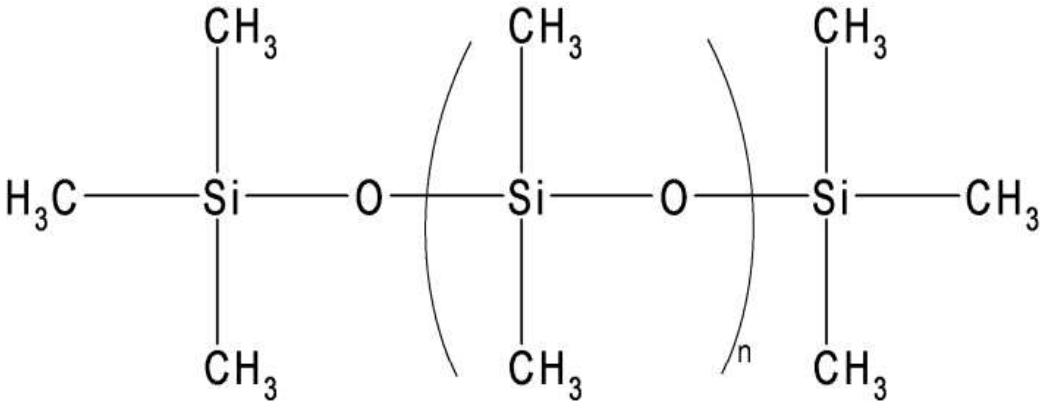

Figure 2.26: Chemical Formula of PDMS

2.4.7 Natively Oxidised Si (Si/SiO_x)

The surface of Si semiconductor wafers is generally covered by a thin oxide layer. The growth of SiO_x films is due to a combination of the natural passivation in air and the effect of several production steps, such as washing, thermal treatments, etc.. The oxide film developed under such conditions, soon ceases to grow because it forms a solid barrier, between the semiconductor surface and the atmospheric oxygen through which ions have difficulty in moving. With increasing industrial importance of silicon in semiconductor devices, studies have been done by means of different surface techniques on the nature of the Si/SiO_x interface [39]. Figure. 2.27 shows the removal

of dangling bonds by oxidation of surface. The Si/SiO_x interface has been the subject of intense study' because of its dominant role in silicon technology. Interaction of Si-based microelectronic and micro-mechanical systems and their external environment are of importance when their surfaces are in contact with an atmospheric or physiological milieu. For example the preparation of silicon-on-insulator devices takes advantage of the strong adhesion between the oxidized and hydrated Si surfaces with the crystalline wafers, while, the implantation of Si-based devices into tissues or into the bloodstream results in immediate protein and cell adsorption onto the material surface. The key to successful device implantation is the ability of the surface to control protein adsorption and, hence, guide cell assembly and promote compatability with the surrounding tissue [40]. In both these applications, the adhesive properties of Si devices are determined by the surface chemistry of the thin, native oxide layer SiO_x that passivates the Si surface under normal conditions [41].

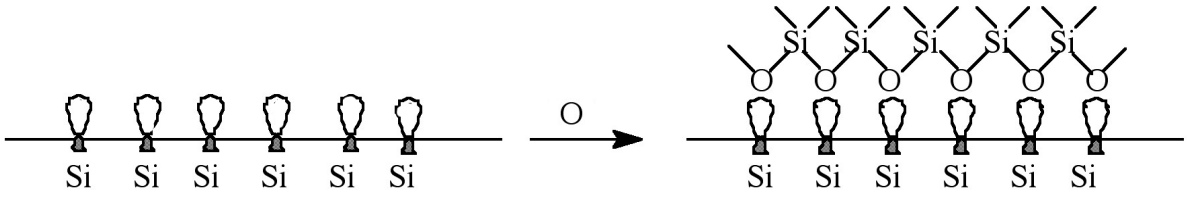

Figure 2.27: Removal of dangling bonds by oxidation of surface [39].

2.4.8 Titania (TiO_2)

Titanium dioxide, commonly referred to as Titania, is a non-toxic, wide band gap semiconductor which has become one of the most-commonly investigated metal oxide systems in surface science [42, 43]. Titanium dioxide is a material that has found applications in variety of areas, including catalysis, photo-catalysis, photovoltaics, energy storage, gas sensors and biocompatible

materials [44–46]. TiO_2 is an intrinsic n-type semiconductor that exists in three naturally occurring crystal phases known as anatase (a = b = 3.782 , c = 9.502), rutile (a = b = 4.584 , c = 2.953) and brookite (a =5.436 , b = 9.166 , c = 5.135). All three phases are composed of Ti^{4+} and six O^{2-} atoms

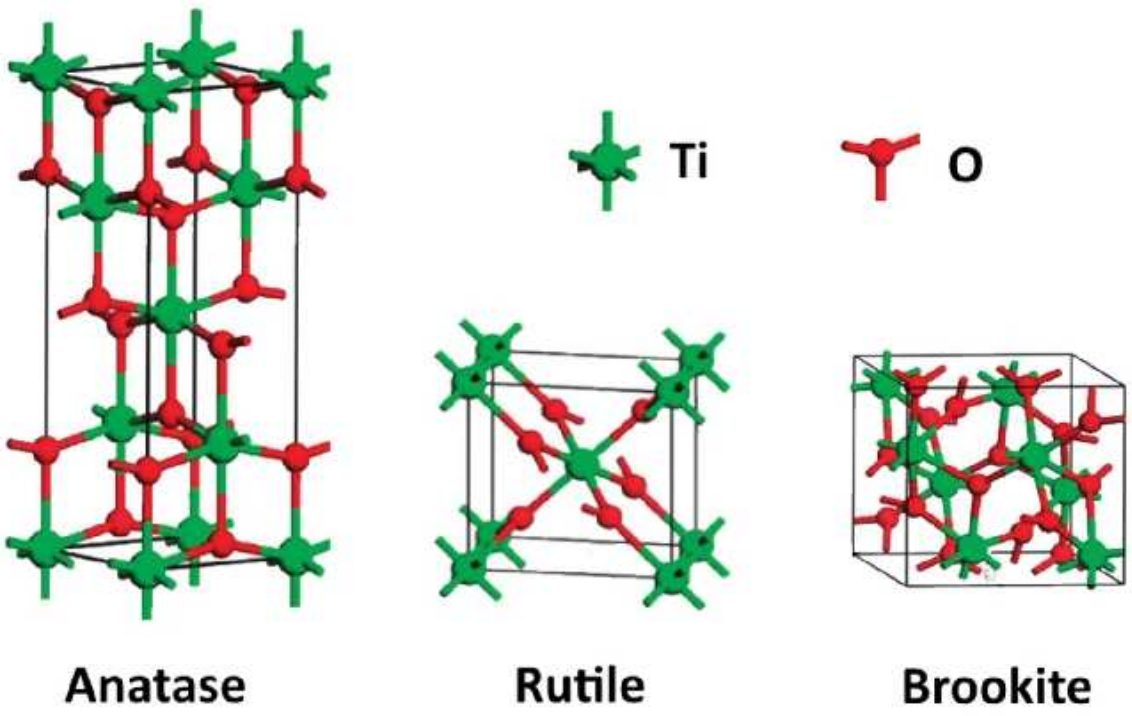

Figure 2.28: The three polymorphs of TiO_2: anatase, rutile and brookite are shown [48]

coordinated together to form a TiO_6 octahedron. Distortions in the octahedra of each phase result in the formation of crystal structures that differ in configuration from others. Both anatase and rutile have a tetragonal crystal structure, while brookite is orthorhombic. Figure 2.28 shows the three naturally occurring phases of TiO_2. The band gap values of anatase, rutile

and brookite are reported to be 3.2 eV, 3.0 eV and 3.3 eV, respectively [47]. Density of states (DOS) considerations and density functional theory (DFT) calculations [48] have shown that anatase has an indirect band gap whereas both rutile and brookite have direct band gap transitions. Due to its availability and stability, the rutile polymorph of TiO_2 has become the benchmark surface for fundamental studies of metal oxide.

Bibliography

[1] J. Xu, X. Deng, J. Zhang, W. Lu, and T. Ma, Thin Solid Films, **390**, 107 (2001).

[2] Thermo Electron Corporation, Application note : AN300262-E.

[3] P. Suominen and F. Wenander, Rev. Sci. Instrum. **79**, 02A305 (2008).

[4] P. Spdtke, Review of Scientific Instruments, **81**, 02B725 (2010).

[5] S. Eliezer and Y. Eliezer, The Fourth State of Matter. IOP, 2001.

[6] H. G. Jain, H. Karacuban, D. Krix, H. W. Becker, H. Nienhaus and V. Buck, Carbon, **49**, 4987 (2011)

[7] K. Siegbahn, "Electron Spectroscopy for Atoms, Molecules and Condensed Matter", Nobel Lecture, December 8, 1981

[8] D. Briggs and M. P. Seah,Practical Surface Analysis- Auger and X-ray Photoelectron Spectroscopy,(Wiley Interscience, 1990).

[9] J. C. Riviere, Practical Surface Analysis: Auger and X-ray Photoelectron Spectroscopy, 2nd edn (New York: Wiley (1990).

[10] J. C. Riviere, S. Myhra, Handbook of Surface and Interface Analysis: Methods for Problem-Solving (New York: Marcel Dekker (1998)).

[11] D. A. Shirley, Phys Rev B **5**, 4709.(1972)

[12] S. Tougaard and P. Sigmund, Physical Review B **25**, 4452 (1982).

[13] K. J. Laidler and J. H. Meiser, Physical Chemistry, 2nd edn (Boston: Houghton Mifflin Company (1995)).

[14] John F. Watts, John Wolstenholme, An introduction to surface analysis by XPS and AES,(Wiley Interscience, (2003)).

[15] "Scanning Probe Microscopy and Spectroscopy: Methods and Applications", R. Wiesendanger (Cambridge University Press, 1998); "Scanning ProbeMicroscopy and Spectroscopy: Theory, Techniques, and Applications", 2nd ed., D. Bonnell, (Ed.), (Wiley-VCH, New York, 2001); "Introduction to Scanning Tunneling Microscopy", C.J. Chen (Oxford University Press, 1993). "Scanning TunnelingMicroscopy", Vol. I, II, and III, H.-J. Guentherodt, R. Wiesendanger (Eds.), (Springer, 1993, 1995, 1996).

[16] G. Binning, H. Rohrer, Helv. Phys. Acta **55**, 726 (1982)

[17] G. Binning, H. Rohrer, Ch. Gerber, and E. Weibel, Phys. Rev. Lett. **50(2)**, 120 (1983).

[18] Y. Zhao, G. C. Wang and T. M. Lu, Characterization of Amorphous and Crystalline Rough Surface: Principles and Applications (Experimental Methods in the Physical Sciences b vol 37)ed R Celotta and T Lucatorto (San Diego,CA: Academic Press)(2001).

[19] V. Constantoudis , G. P. Pastis, L. H. A. Leunissen , E.Gogolides , JVST B, **22**, 4 2004.

[20] S. K. Sinha, E. B. Sirota, and S. Garoff, Phys. Rev. B **38**, 2297 (1988).

[21] Jean Bennett and Lars Mattsson , Introduction to surface roughness and scattering (Optical Society of America , Washington DC, 1999).

[22] T. Young, Philos. Trans. R. Soc. Lond. **95**, 65 (1805)

[23] P. B. Coleman, Practical Sampling Techniques for: Infrared Analysis, CRC Press, (1993).

[24] D. W. Ball, The basics of spectroscopy, SPIE PRESS, (2001).

[25] B. C. Smith, Fundamentals of Fourier Transform infrared spectroscopy, CRS Press, (1996).

[26] J. Goldstein, D. Newbury, P. Echlin, D. C. Joy, A. D. Romig, C. E. Lyman, C. Fiori, and E. Lifshin. Scanning Electron Microscopy and X-Ray Microanalysis, 2nd Ed. Plenum Press, (1992).

[27] B. Alberts, A. Johnson, J. Lewis, et al."The Structure and Function of DNA." Molecular Biology of the Cell. 4th edition. New York: Garland Science; (2002).

[28] J. D. Watson and F. H. C Crick, Nature **171**, 737 (1953).

[29] E. Chargaff, R. Lipshitz, C. Green and M. E. Hodes, Journal of Biological Chemistry, **192**, 223 (1953).

[30] P. Balbs, X. Sobern, E. Merino, M. Zurita, H. Lomeli, F. Valle, N. Flores, Bolivar F.Gene.**50**, 3 (1986).

[31] O. Smithies, Science, **169(3948)**, 882(1970).

[32] Nadrian C. Seeman. Nature, **421**, 427 (2003).

[33] Fibroblast (Encyclopedia Brittanica).

[34] Thomas M. Adams, Richard A. Layton ,"Introductory MEMS: Fabrication and Applications", (Springer Science Business Media, 08-Dec-2009).

[35] O'Mara, C. William, Handbook of Semiconductor Silicon Technology. William Andrew Inc. pp. 349352. ISBN 0-8155-1237-6 (1990).

[36] N. W. Ashcroft, and N. D. Mermin, Solid State Physics, Saunders, (1976).

[37] X. Q. Brown, K. Ookawa and J. Y. Wong, Biomaterials **26**, 3123 (2005).

[38] Yon Jin Chuah, Yi Ting Koh, Kaiyang Lim, Nishanth V. Menon, Yingnan Wu and Yuejun Kang. Scientific Reports, **5**, 18162 (2015).

[39] M. Morita, T. Ohmi, E. Hasegawa, M. Kawakami and M. Ohwada. J. Appl. Phys. **68**, 1272 (1990).

[40] D. Cole, Surface chemistry and adhesive properties of Oxidised Si Surfaces, (Thesis Queens College, University of Cambridge, 2007).

[41] Mizuho Morita1, and Tadahiro Ohmi.Japanese Journal of Applied Physics, **33**, 1B (1994)

[42] U. Diebold. Applied Physics A.,**76(1)**, 681 (2003).

[43] Y. Lai Y, J. Huang, Z. Cui, M. Ge , K. Q. Zhang, Z. Chen, L. Chi, Small, **12(16)**, 2203 (2016).

[44] S. Majumder, I. Mishra, U. Subudhi, Shikha Varma, Appl. Phy. Lett. **103**, 063103 (2013).

[45] S. Majumder, D. Paramanik, V. Solanki, B. P. Bag, Shikha Varma, Appl. Phys. Lett., **98**, 053105 (2011).

[46] V. Solanki, S. Majumder, I. Mishra, P. Dash, C. Singh, D. Kanjilal, S. Varma, J. Appl. Phys. **115**, 124306(2014).

[47] M. Pelaez, N. T. Nolan, S. C. Pillai, M. K. Seery, P. Falaras, A. G. Kontos, P. S. M. Dunlop, J. W. J. Hamilton, J. A. Byrne, K. OShea, M. H. Entezari, D. D. Dionysiou, Appl. Catal. B Environ., **125**, 331 (2012).

[48] J. Zhang, P. Zhou, J. Liu, J. Yu, Phys. Chem. Chem. Phys., **16 (38)**, 20382 (2014).

Chapter 3

Nano-patterning of SiO_x Surfaces with Low Energy Ion Beams, and Their Interaction with DNA

3.1 Introduction

Nano-structures and nano-patterned surfaces can exhibit many fascinating properties not expressed by their bulk counterparts. The novel characteristics are predominantly derived via low dimensional confined sizes, large surface to volume ratio of nano-dimensional structures, changes in electronic structure and associated modifications in variety of other properties. Possibility of tuning these factors has stimulated frontier research in many disciplines. Nanostructured surfaces also present several attractive and selective responses to bio-molecular adhesion [1]. Various techniques have been utilized to control the behavior, properties and functionality of the surfaces by locally altering the surface chemistry. Understanding adsorption of polymers and biopolymers on heterogeneous surfaces is of fundamental importance and is also crucial for many applications in industry and medical fields [2, 3]. Many characteristic properties of the biosensors and microarrays depend upon the

surfaces they are fabricated on [4].

Ion beam irradiation (IBI) is an appealing technique for the fabrication of nanopatterned surfaces without complex lithographic processes. It often promotes the spontaneous pattern formation on the surfaces leading to the creation of self organised corrugations, ripples, array of dots etc. [5, 6]. According to the Bradley Harper (BH) theory, pattern formation through IBI, is controlled by surface instability that develops due to the competition between curvature dependent ion sputtering, which roughens the surface, and various smoothing processes [5–8]. Various parameters like the angle of incidence, flux, fluence, energy of the ion beam, substrate temperature and beam divergence induce variety of patterns on surfaces. The IBI technique provides an efficient method for producing self assembled arrays of nanostructures over a large area in a single technological step.

DNA is one of the nature's stiffest polymer and its rigidity is the combinatorial effect of negative charges on the phosphate back bone, that electrostatically repel each other, as well as its compressive base pair stacking. The structural nature of DNA on any surface is thus extensively guided by the surface- charge distribution. Flexibility and immobilization of DNA are important factors in many biological functions as well as in the development of biosensors and medical research [9]. For cell packaging, high DNA flexibility is an essential criteria [9].

Several top-down techniques like Dip pen nanolithography (DPN), nanoshaving, nanografting, electron beam lithography (EBL), nanocontact printing, etc. have been employed to control the immobilization of DNA on surfaces [10–14]. Many of these techniques crucially depend on the chemical functionalization or prior surface processing. Interacting DNA with silicon oxide based materials display many attractive behaviors [15–19] and SiO_2 nanoparticles functionalized with DNA demonstrate biosensing proper-

ties [15, 16]. Teshome et.al. have investigated the alignment of synthesized DNA on the nano patterned natively oxidised SiO_x surfaces [20]. Studies of DNA adhesion on $TiO_2(110)$ surfaces by Majumder et.al. show that chemical interactions and associated charge transfer play important role in these processes [1].

Present chapter investigates the nano-patterning of natively oxidized Silicon (Si/SiO_x) surfaces via the technique of ion irradiation. The surfaces show the development of nanostructures and ripples upon irradiation. These nanostructures grow in size, and ripples become more distinct with increasing fluence. The pristine and ion irradiated surfaces were also interacted with plasmid DNA. Adsorption of a single monolayer of DNA and formation of a 2-dimensional DNA network, composed of loose DNA circles and their crossovers, is observed on the SiO_x surfaces. The results presented here show that the diameter of loose DNA circles as well as DNA persistence length reduce on the ion irradiated surfaces. This indicates an increased flexibility of the DNA molecule on the nanopatterned surfaces. Surface morphology as well as the chemical interactions of the adsorbed DNA molecule with SiO_x surface may be responsible for these observations. Results show that this adsorption on ion irradiated surfaces leads to rupturing of some DNA bases and formation of Si_3N_4 complexes due to conjugation of DNA bases on SiO_x. Absence of $H_2PO_4^-$ is also noticed at the highest fluence. All these results suggest that chemical interactions occur when DNA molecule adsorbs on the SiO_x surfaces.

3.2 Experiment

Single crystals of commercially obtained Si(100), passivated under normal conditions with thin layers of native oxide SiO_x, were utilized. These Si/SiO_x surfaces were irradiated at two fluences of 6×10^{15} and 1.8×10^{16} ions/cm^2 in

UHV with 3 keV Ar^+ ions (with flux of 1×10^{13} ions/cm^2.sec) at 15° incident angle with respect to surface normal.

Irradiated and unirradiated Si/SiO_x surfaces were interacted with plasmid DNA. The DNA (pBR322, 4361 base pair) was purchased from Fermentas (SD0041) and was stored at -20°C. 10nM of this DNA was prepared in 1x TAEM (40 mM TRIS-HCl, 20 mM acetic acid, 2 mM EDTA and 12.5 mM Mg(Ac)2) buffer (pH 8.3). The solution of plasmid pBR322 was further diluted in the buffer solution to a concentration of 0.1 nM. 10μl of this solution was dropped onto the substrates and incubated for 2 hrs. Post incubation, i.e. after DNA immobilization, the surfaces were thoroughly rinsed with Mili Q water several times to remove any residuals. These substrates were then dried.

The surface morphologies, both prior to and post DNA interaction, have been investigated by Scanning Probe Microscope (AFM mode using Nanoscope V Multimode) from Bruker in tapping mode. Atomic Force microscopy was conducted using tapping mode tips (model RTESP tips) with a radius of curvature R of about 5 nm, force constant κ of about 80 N/m and resonant frequency of 316 KHz under ambient conditions. Nearly 250 AFM images have been utilized in the the analysis here.

X-ray photoelectron spectroscopy (XPS) measurements have been undertaken on a VG system with Mg Kα source, under UHV conditions. XPS spectra were acquired for photoelectron emission angles of 30°, with respect to surface normal, providing information from surface to about 1 nm below. This surface sensitivity is a result of shorter attenuation length of electrons from the sample. A Shirley background has been removed from all the XPS data. The charging in the spectra have been corrected using the C(1s) feature at 284.6 eV. XPS studies on DNA are constrained by several competing factors. Good S/N ratio is very difficult to obtain, since long exposures to

x-ray beam can destroy the DNA molecule. Hence, usually a compromise between these factors is attained. Furthermore, low concentration of DNA, as in the present study, produces low XPS signal. Large DNA concentrations were not used as they will cause aggregation, instead of single monolayer of 2-dimensional DNA network as observed here.

3.3 Results and Discussions

Morphology of the pristine (un-irradiated) and ion irradiated SiO_x surfaces is shown in fig. 3.1. Pristine surface displays a very smooth surface with an rms roughness of 0.072 nm. These surfaces were ion irradiated with 3 keV Ar^+ ions at two fluences of 6×10^{15} and 1.8×10^{16} ions/cm^2. The ion beam irradiated (IBI) surfaces demonstrate the development of nanostructures as well as some ripple patterns. After the fluence of 6×10^{15} ions/cm^2, the surface shows increase in rms roughness to 0.192 nm along with the generation of a weak rippling behavior and formation of small nanostructures (see fig. 3.1 (b)). A high resolution AFM image from this surface is presented in fig. 3.2(a) which shows the presence of nanostructures on ripple like structures (a typical ripple (red line) and nanostructure (blue line) is marked). The nanostructures display a density of 5×10^{11} cm^{-2} and appear slightly elongated, having an average length of about 25 nm (along ripple) and width of about 20 nm. The ion beam direction (shown by arrow) is perpendicular to the ripple orientation, i.e. the wave vector **k** of the ripples is aligned along the direction of incident ion beam (fig. 3.1(b)). The Fast Fourier Transform (FFT) of this surface (in fig. 3.2(c)) also suggests a mildly ordered patterning which is aligned perpendicular to the ion beam.

The SiO_x surfaces were also irradiated with a fluence of 1.8×10^{16} ions/cm^2

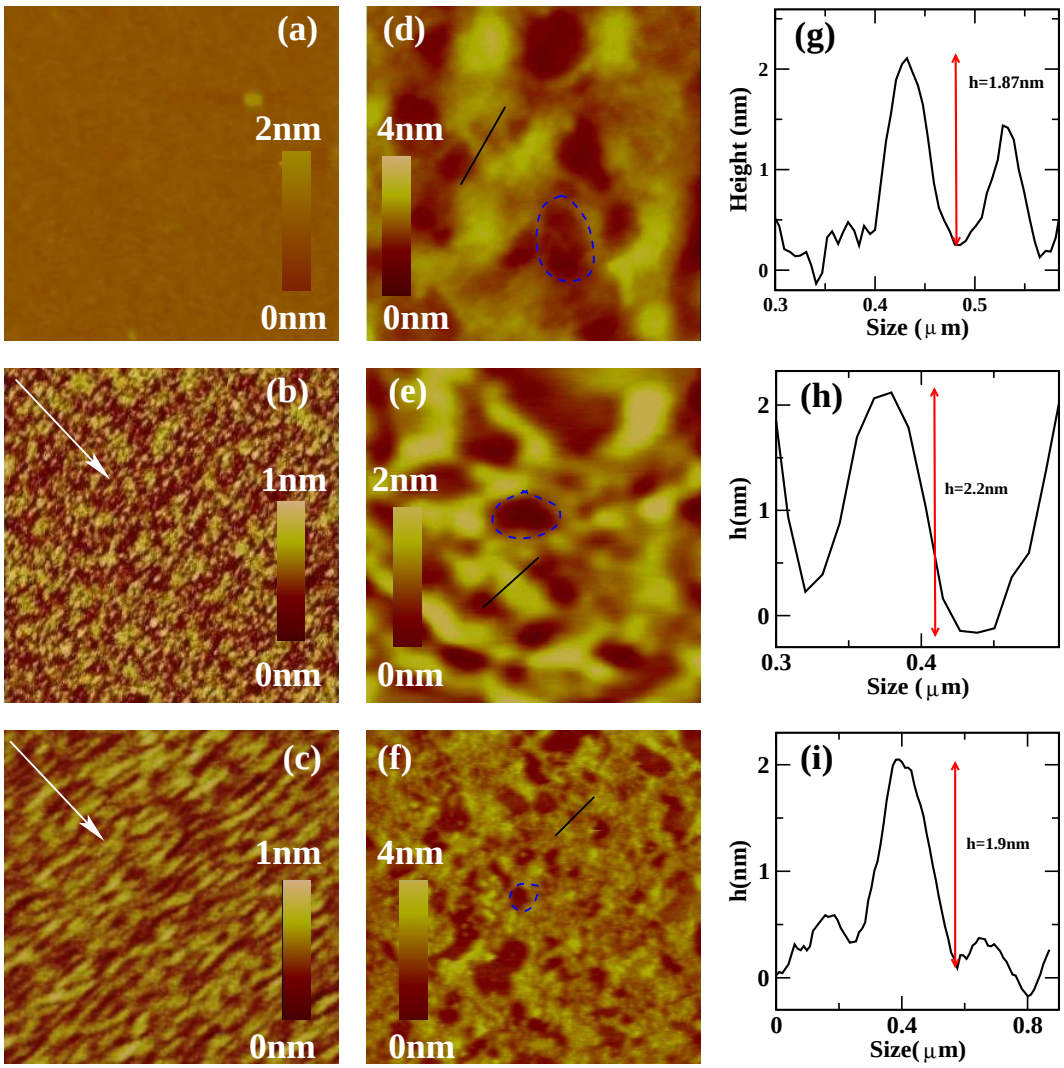

Figure 3.1: 1x1 μm^2 AFM images are shown in the left panel for (a) pristine SiO_x surface as well as for SiO_x surfaces irradiated with fluences of (b) 6×10^{15} ions/cm^2, and (c) 1.8×10^{16} ions/cm^2. The arrows indicates the direction of the ion beam and remains same for all the ion irradiated surfaces. Right panel shows corresponding SiO_x surfaces after they are interacted with plasmid DNA. A typical DNA is marked by dashed line in all the images. The solid line indicates the region of section analysis which is presented in the rightmost panel.

and show an rms roughness of 0.139. The surface morphology now delineates very well ordered ripples (fig. 3.1(c)) with a wavelength of about 150 nm, that

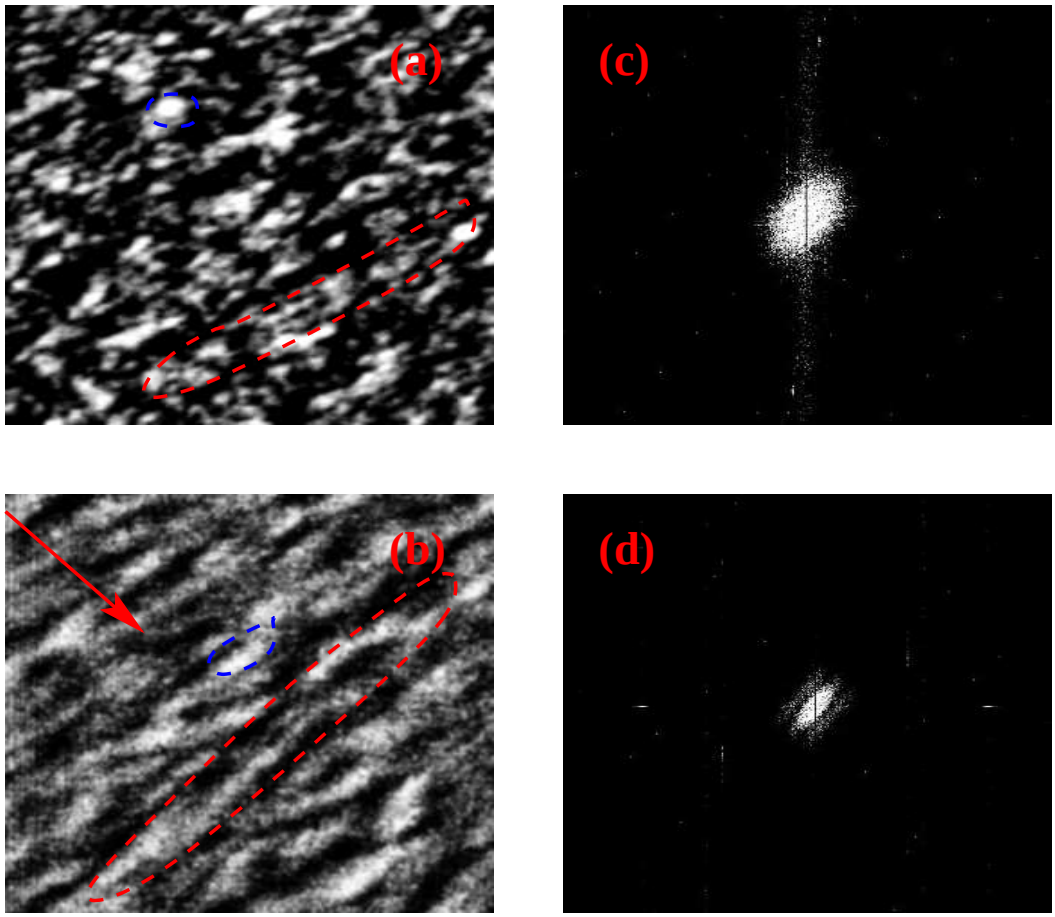

Figure 3.2: 500×500 nm^2 AFM images are shown in the left panel for SiO_x surfaces irradiated with fluences of (a) 6×10^{15} ions/cm^2, and (b) 1.8×10^{16} ions/cm^2. The arrow shows the ion beam direction which is same in all the images. A typical ripple is marked by (red) dashed line and a typical nanostructures is marked by (blue) dashed line. Right panel (c) and (d) show the corresponding FFT images.

are again aligned with **k** parallel to the ion beam direction. In contrast to the lower fluence (6×10^{15} ions/cm^2), now the nanostructures on the ripples appear more elongated with an average length of 46 nm (along the ripple) and width of 25 nm. Their density is about $1{\times}10^{11}$ cm^{-2}. A high resolution image from this surface is presented in fig. 3.2(b). Distinct ripples decorated with nanostructures are observed. The FFT (fig. 3.2(d)) reflects the well

ordered pattering nature as well as the orientation of the ripples.

Ziberi et.al have investigated the ion bombardment of silicon surfaces with low energy ($\leq$5 keV) noble gas ions at room temperature and have observed the formation of ripple patterns at near normal ion incidence angles (5-30°) with **k** oriented parallel to the ion beam direction, as also observed here, and the ripple wave-length increasing with energy [21]. For Kr^+ ions, however, ordering of ripples is independent of ion energy [22]. The surface diffusion coefficient and angular distribution of the ion beam play an important role in the determination of wavelength and amplitudes of the patterns [23].

AFM images presented in fig. 3.1 were utilized to obtain 1d-iso Power Spectral Density (PSD) functions with the range of frequencies ν ($\kappa = 2\pi\nu$) between $1/L$ (L being the image scan size) and the Nyquist frequency $N/2L$ (N being the number of pixels of the image). PSD for pristine and ion irradiated surfaces are shown in fig. 3.3 as a function of spatial wave vector κ. The low frequency plateau reflects the un-correlated white noise spectrum whereas the power law decaying nature at high frequencies indicates the spatial correlations. This latter high frequency behavior can be described by the following equation and provides a crucial exponent γ which is important for understanding and expressing the surface evolution processes [24]:

$$PSD \sim \kappa^{-\gamma} \tag{3.1}$$

For the pristine surface a γ of 3.7$\pm$0.1 is observed whereas the ion irradiated surfaces show γ of 3.3$\pm$0.1 and 3.2$\pm$0.1 at the fluences of 6.0×10^{15} ions/cm^2 and 1.8×10^{16} ions/cm^2, respectively. The exponent γ can reveal the nature of the surface growth processes. At $\gamma = 2$ knock off processes are important for the evolution of the surface, at $\gamma = 3$ bulk diffusion becomes crucial, and at $\gamma = 4$ diffusion dominated surface smoothening processes become signif-

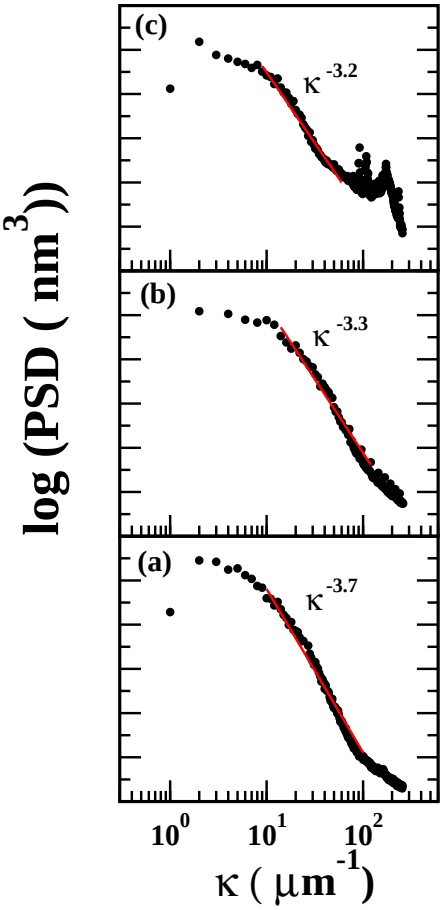

Figure 3.3: PSD for (a) pristine SiO_x surface and for SiO_x surfaces irradiated with fluences of (b) 6×10^{15} ions/cm^2, and (c) 1.8×10^{16} ions/cm^2. κ is spatial wave vector.

icant [24–26]. Thus for ion irradiated SiO_x surfaces with γ of 3.2±0.1 and 3.3±0.1, the evolution of surfaces and their nanopatterning is predominantly controlled through the bulk diffusion processes.

The pristine (un-irradiated) as well as ion beam irradiated Si/SiO_x surfaces were interacted with pBR322 plasmid DNA. Surface morphology of all the surfaces, after DNA interaction, are shown in the right panel of fig. 3.1. pBR322 is a circular DNA and figure 3.1 displays adsorption of DNA on the SiO_x surfaces along with the formation of 2- dimensional DNA networks.

The phosphate backbone of DNA makes it a negatively charged molecule, and at the buffer pH of 8.3 (used in the present study) SiO_x surface also becomes negatively charged [27]. As the DNA and surface both are negatively charged, the interaction between them is of repulsive nature. The adsorption of DNA molecule on the SiO_x surface is then promoted by the Mg^{2+} divalent cations present in the buffer solution. These divalent cations induce a charge inversion on Si/SiO_x and enable the adsorption of DNA onto the surface via weak electrostatic interaction through the formation of an electrical double layer (EDL) [28]. This EDL layer forms a bridge between the surface and the DNA backbone [29], producing a double layer force [28] such that the electrostatic attraction overcomes the thermal repulsion and a stable configuration is formed [28]. Mica surfaces have been investigated earlier with the same Mg cation concentration, as used in the present study, and the debye length for the electrostatic potential between the cations was estimated to be greater than the average separation between the charges [28]. As the charge density of SiO_x surface is less than the mica [30], the charge separation here is smaller than the screening length, creating correlations between the cations. This leads to less staggered geometries for cations on the surface [28] and creates a 2-dimensional DNA -networks on the SiO_x surfaces [31], instead of isolated supercoiled DNA structures. Thus, DNA in the presence of divalent cations can extend into loose circles which can also overlap or cross each other to form a DNA networks. The formation of DNA network depends upon the concentrations of DNA as well as counter-ions (Mg^{2+}) in the solution, and surface properties of the substrate [32]. Studies have shown that a single mono-layer of DNA network is about ~ 2 nm high whereas multiples of this height (i.e. 4 and 6 nm) are seen in the case of two or three mono-layered DNA [33–35]. It is also expected that the aggregation of DNA will lead to much larger height profiles.

Fig. 3.1 (right panel) displays the surface morphology of the pristine and ion irradiated SiO_x surfaces after they were interacted with DNA. No isolated supercoiled DNA structures are noticed, rather 2-dimensional DNA network with loose and crossed DNA circles are observed, as expected under the concentrations of divalent (Mg^{2+}) cations and DNA used here. The profile of DNA circles is fuzzy and not very distinct as has also been observed in many studies on mica earlier [33, 34]. The section analysis further shows that the DNA layer is about 2 nm high on all the surfaces, un-irradiated as well as irradiated, suggesting formation of nearly a single DNA monolayer on SiO_x. The loosened DNA circles show a size (diameter) distribution on the surfaces.

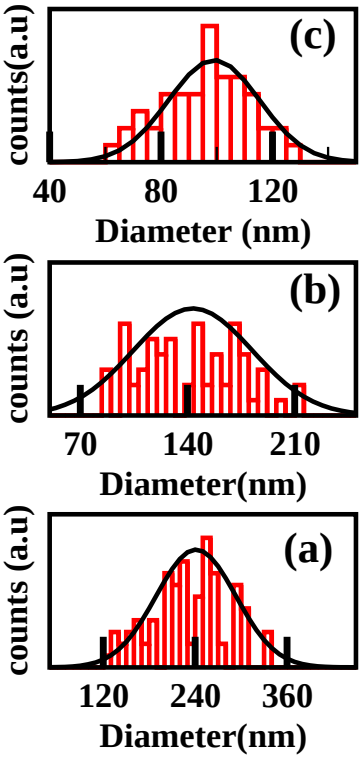

Figure 3.4: DNA size (diameter) distribution on (a) pristine SiO_x surface and on SiO_x surfaces irradiated with fluences of (b) 6×10^{15} ions/cm^2, and (c) 1.8×10^{16} ions/cm^2.

Typical DNA circles are marked in fig. 3.1(d,e,f) and their size distributions are shown in fig. 3.4. Both these figures delineate that DNA circles are largest on the pristine but reduce on the ion irradiated SiO_x surfaces, decreasing in size with fluence.

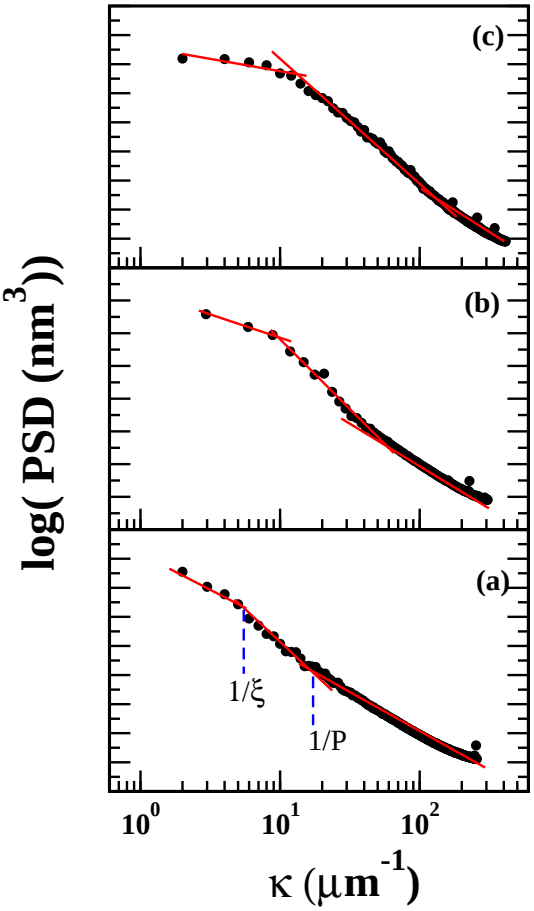

Figure 3.5: PSD after DNA interaction with (a) pristine SiO_x surface and with SiO_x surfaces irradiated with fluences of (b) 6×10^{15} ions/cm^2, and (c) 1.8×10^{16} ions/cm^2. κ is spatial wave vector. Intersection points of changing slopes indicate ξ and P.

PSD function in fourier space, is a unique and efficient formalism for accessing the morphological parameters like the size and persistence length of

DNA [1,36]. Persistence length represents the stiff- straight section of a DNA molecule and is a crucial signature of the DNA and its environment. Quasi periodicity delineated by the distinct frequencies in PSD, where different regions intersect, provide important *correlation lengths* related to the size (ξ) and the persistence length (P) of DNA [1]. PSD spectra, obtained using SPM images (of fig. 3.1) are presented in fig. 3.5 for all DNA interacted SiO_x surfaces.

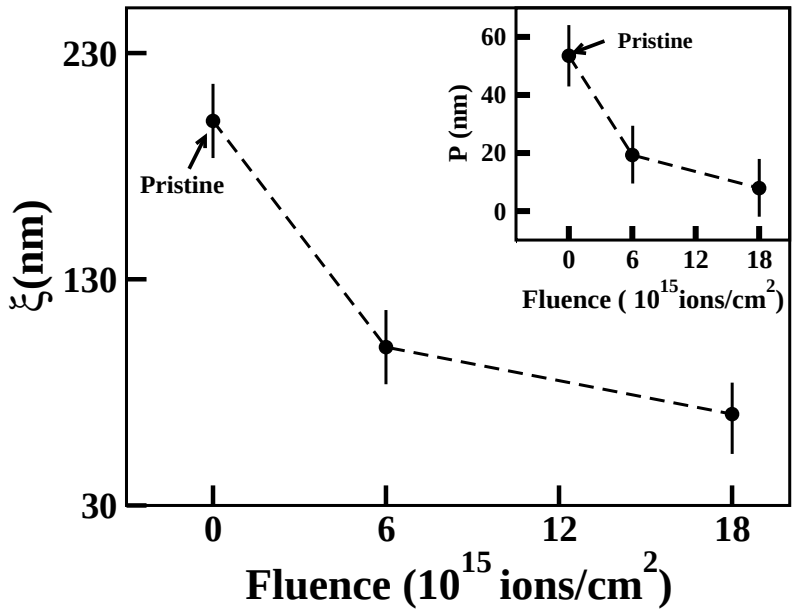

Figure 3.6: Size (ξ) and persistence length (P) of DNA on the pristine SiO_x as well as for ion irradiated SiO_x surfaces. The error bars are shown.

The unique features of these spectra are the low frequency plateau, due to the long ranged correlations, followed by two power law decaying regions in high frequency regime (with slopes intersecting at 1/P and 1/ξ) [1]. The size of DNA (ξ) as well as the persistence length (P) are found to be largest on the un- irradiated surface and are, respectively, 200 and 53.5 nm. These DNA parameters are found to be smaller on ion irradiated surface, being

respectively 100 and 19.3 nm after 6×10^{15} ions/cm^2, but 70.4 and 7.9 nm after 1.8×10^{16} ions/cm^2 (see fig. 3.6). The DNA- size from PSD shows similar trends as obtained in fig. 3.4 from AFM images, where DNA diameter is observed to decrease with ion fluence. Reducing the DNA size and enhancing it flexibility (by reducing P), are very attractive characteristics due to their importance in many areas including DNA packaging [37, 38]. In solutions, DNA exhibit ξ= 425 and P= 15 nm [36] whereas on polyamine coatings P of 11 nm has been observed [37]. In the present study, the SiO_x irradiated at the highest fluence shows the lowest values of DNA size and Persistence length (fig. 3.6) indicating good DNA flexibility on these surfaces. Electrostatic charge transfer from DNA moiety to SiO_x nanostructures during their chemical interactions, as discussed below, can promote the DNA flexibility observed here.

The Si(2p) XPS spectrum from pristine surface (fig. 3.7(a)) displays two features. Peak at 99.6 eV is related to the elemental silicon whereas the feature at 103.9 eV is due to SiO_x [39]. The intensity of SiO_x feature decreases with ion irradiation, as expected (fig. 3.7(b,c)). By utilizing angular dependent XPS results, thickness of SiO_x is estimated to be $\sim$ 20 $\mathring{A}$ on the pristine surface which decreases to 5 and 4 $\mathring{A}$ after ion irradiation of 6×10^{15} and 1.8×10^{16} ions/cm^2, respectively. Presence of a small SiO_x feature, after irradiation, is reflected in fig. 3.7(b,c).

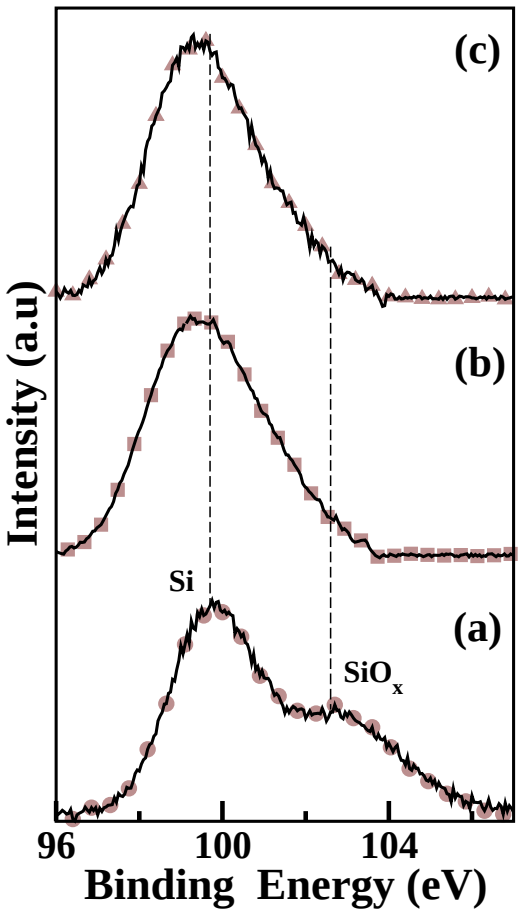

Figure 3.7: Before DNA interaction: XPS spectra of Si(2p) region from (a) pristine SiO_x surface as well as for SiO_x surfaces irradiated with fluences of (b) 6×10^{15} ions/cm^2, and (c)1.8×10^{16} ions/cm^2.

XPS technique has been utilized to understand the nature of chemical states involved in the interaction between DNA and nanopatterned SiO_x surfaces. Fig. 3.8 displays the Si(2p) XPS spectra (in red dashed line) after DNA interaction with SiO_x surfaces. The spectra prior to interaction (from fig. 3.7) are also shown for reference (black solid line). Upon interaction of DNA with pristine SiO_x surface, two features at 98.2 and 101.8 eV can be observed in fig. 3.8(a). The DNA backbone (PO_4^-) possess negative charges, and the feature at 98.2 eV can be related to transfer of these charges from

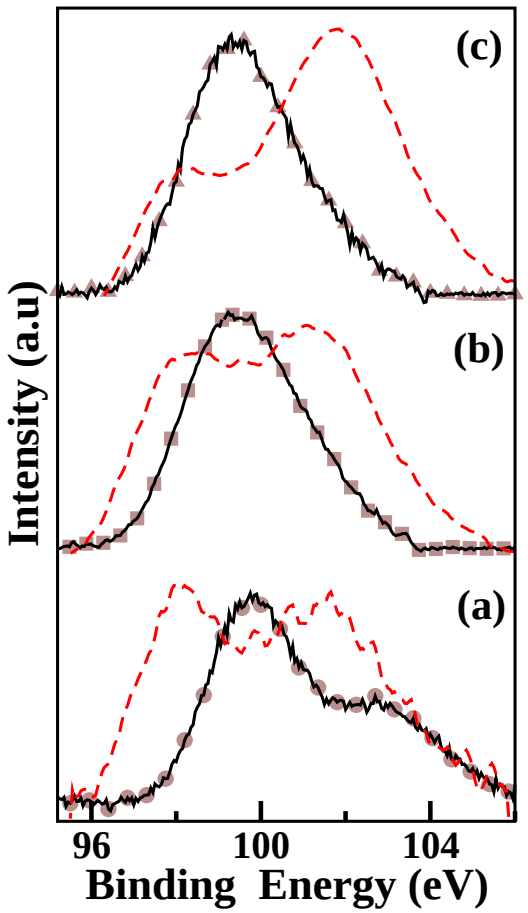

Figure 3.8: After DNA interaction: Dashed (red) line show XPS spectra from DNA interacted surfaces, Si(2p) region from (a) pristine SiO_x surface as well as for SiO_x surfaces irradiated with fluences of (b) 6×10^{15} ions/cm^2, and (c)1.8×10^{16} ions/cm^2. For reference, XPS spectra taken prior to DNA interaction are also included as (black) solid lines.

backbone to the surface during interaction [19]. A decrease in the intensity of this feature is observed for ion irradiated surfaces. This can be due to the presence of nanostructures on these surfaces, which can produce saturation in the charge transfer [1, 19]. Bigger nanostructures (with more surface negative charge) will be able to accept less charge from the DNA backbone. The feature at 101.8 eV may be caused by DNA interaction with Si-oxide component.

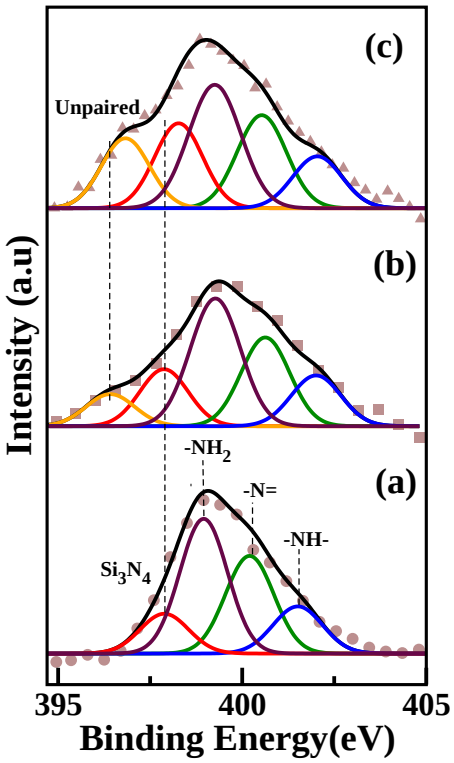

Figure 3.9: After DNA interaction:XPS spectra from N(1s) region from DNA interacted surfaces for (a) pristine SiO_x surface as well as for SiO_x surfaces irradiated with fluences of (b) 6×10^{15} ions/cm^2, and (c)1.8×10^{16} ions/cm^2. The XPS intensity for all these spectra are normalized w.r.t $-NH_2$ state.

The N(1s) XPS spectra after DNA interaction of the SiO_x surfaces are presented in fig. 3.9. On pristine surface three features at 399.0, 400.2 and 401.5 eV, respectively, represent amino(-NH_2), imine (-N=) and amine(-NH-) components from DNA. Similar features have also been observed in earlier studies [40–43]. However surprisingly, a feature related to the formation of Si_3N_4 complex is also observed here at 397.9 eV (fig. 3.9(a)). Development of similar DNA- metal complexes, e.g with Hg ions, have been reported [40] as well as proposed by Quantum Chemical calculations [44]. After interaction of DNA molecule with ion irradiated SiO_x surfaces, the intensity of

Si_3N_4 feature enhances. Moreover, remarkably a new feature (not seen for pristine surface) develops at $\sim$ 396.4 eV in fig. 3.9(b,c). This is caused by the un-pairing or unzipping of DNA bases via denaturing of associated exocyclic groups (e.g. -NH, -NH_2, C=O) [40, 45]. Hence this feature has been labeled as *unpaired* in fig. 3.9. Creation of Si_3N_4 feature on all SiO_x surfaces after DNA interaction, and development of additional *unpaired* feature on ion irradiated surfaces suggest strong chemical interaction between the SiO_x surfaces and the DNA moiety. Presence of nanostructured surfaces as well as charge transfer from DNA may be responsible for these observations on the ion irradiated surfaces.

Fig. 3.10 shows the XPS results from the P(2p) features for DNA interacted SiO_x surfaces. The pristine surface shows the presence of phosphate PO_4^{3-}, from the DNA backbone, as well as HPO_4^{2-} and $H_2PO_4^-$ features due to the phosphate hydration on SiO_x surface [46]. Similar features are also observed for DNA interaction with 6.0×10^{15} ions/cm^2 irradiated SiO_x surfaces. However on 1.8×10^{15}ions/cm^2 irradiated surfaces, the highest binding energy feature related to $H_2PO_4^-$ is not observed, suggesting transfer of electron from Phosphate backbone to the surface. Donation of lone pair of electrons to partially filled Si d-orbitals, on SiO_x surfaces is also shown to take place during water adsorption, and leads to creation of reactive sites on the surface by breaking of Si-O bonds which facilitates further reaction [47]. Absence of high energy feature in fig. 3.10(c) may also be ascribed to increased interaction of DNA with the surface.

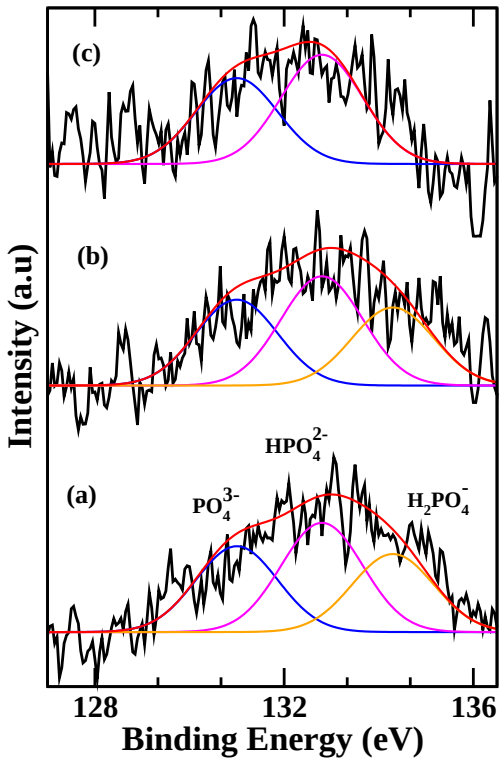

Figure 3.10: After DNA interaction: XPS spectra from P(2p) region from DNA interacted surfaces for (a) pristine SiO_x surface as well as for SiO_x surfaces irradiated with fluences of (b) 6×10^{15} ions/cm^2, and (c)1.8×10^{16} ions/cm^2. Fittings for various states are shown.

3.4 Conclusion

Ion beam irradiation technique has been utilized to fabricate the nanopatterns on SiO_x surfaces. Fabrication of nanostructures as well ripple patterns is observed, on surfaces, as a result of competition between the sputter induced erosion, and smoothening due to bulk diffusion. These nanopatterns evolve with fluence, such that the nanostructures become bigger and ripples get more distinct and well defined. These nanopatterned surfaces were interacted with circular plasmid DNA. The results show that DNA molecules adsorb on the SiO_x surface in a single monolayer, forming a 2-dimensional

network of loose DNA circles and crossovers. The size of these circles (ξ) as well as the persistence length (P) of DNA decrease on the ion irradiated surfaces, indicating that DNA becomes a more flexible molecule on these surfaces. Both ξ and P can be tuned and are found to be smallest on SiO_x surfaces irradiated at the highest fluence. Furthermore, the results also show that the adsorption of DNA is promoted by several chemical interactions. This is reflected by rupturing of DNA bases on ion irradiated surfaces, formation of Si_3N_4 complexes due to the conjugation of DNA bases with SiO_x, as well as absence of $H_2PO_4^-$ at the highest fluence. These results are important as they can be very significant in many biosensing applications and cell packaging.

Thus, this chapter discussed the morphological as well as the chemical compositional changes for the ion irradiated Si/SiO_x surfaces, both before and after their interaction with DNA. The roughening and scaling behavior of these Si/SiO_x surfaces, both prior to and after DNA interaction, are discussed in chapter 4.

Bibliography

[1] Subrata Majumder, I. Mishra, U Subudhi, Shikha Varma, Appl. Phy. Lett. **103**, 063103 (2013).

[2] F. Ricci, N. Zari, F. Caprio, S. Recine, A. Amine, D. Moscone, G. Palleschi, K. W. Plaxco, Bioelectrochemistry. **76**, 208 (2009).

[3] C. Fan, K. W. Plaxco, A. J. Heeger, Proc. Natl. Acad. Sci. U.S.A. **100**, 9134 (2003) .

[4] Santanu Bhattacharya, Subhrangsu S. Manda, Biochimica et Biophysica Acta. **1323**, 29 (1997).

[5] F. Frost, A. Schindler and F. Bigl, Phys. Rev. Lett., **85**, 4116 (2000).

[6] S. Facsko, T. Dekorsy, C. Koerdt, C. Trappe, H. Kurz, A. Vogt, and H. L. Hartnagel, Science, **285**, 1551 (1999).

[7] S. Majumder, D. Paramanik, V. Solanki, B. P. Bag, and Shikha Varma, Appl. Phys. Lett., **98**, 053105 (2011).

[8] Vanaraj Solanki, Subrata Majumder, Indrani Mishra, P. Dash, C. Singh, D. Kanjilal and Shikha Varma, Jour. Appl. Phy., **115**, 124306 (2014).

[9] T. J. Richmond and C. A. Davey, Nature, **423**, 145 (2003).

[10] G. Shekhawat, S. H. Tark, V. P. Dravid, Science, **311**, 1592 (2006).

[11] V. V. Demidov, Expert Rev. Mol. Diagn., **4**, 267 (2004).

[12] B. Gao, K. Sarveswaran, G. H. Bernstein and M. Lieberman, Langmuir, **26**, 12680 (2010).

[13] A. E. Gerdon, S. S. Oh, K. Hsieh, Y. Ke, H. Yan and H. T. Soh, Small, **5**, 1942 (2009).

[14] B. Ding, H. Wu, W. Xu, Z. Zhao, Y. Liu, H. Yu and H. Yan, Nano Lett., **10**, 5065 (2010).

[15] Luca De Stefano, Paolo Arcari, Annalisa Lamberti, Carmen Sanges, Lucia Rotiroti, Ilaria Rea and Ivo Rendina, Sensors, **7**, 214 (2007).

[16] Robert Jenison, Helen La, Ayla Haeberli, Rachel Ostroff, and Barry Polisky, Clinical Chemistry, **47** ,10, 1894 (2001).

[17] Soonshin Kwon, Zack C. Y. Chen, Hyunwoo Noh, Ju Hun Lee, Hang Liu, Jennifer N. Chac and Jie Xiang, Nanoscale, **6**, 7847 (2014).

[18] H. B. Yin, T. Brown, J. S. Wilkinson, R. W. Eason and T. Melvin, Nucleic Acids Research, **32**, 14 (2004).

[19] Kim. S. Midwood, Michael. D. Carolus, Michael. P. Danahy, Jean. E. Schwarzbauer and Jeffrey Schwartz, Langmuir, **20**, 5501 (2004).

[20] Bezuayehu Teshome, Stefan Facsko and Adrian Keller, Nanoscale., **6**, 1790 (2014).

[21] B. Ziberi, F. Frost, T. Hche and B. Rauschenbach, Phys. Rev. B, **72**, 235310 (2005).

[22] B. Ziberi, M. Cornejo, F. Frost and B. Rauschenbach, J. Phys.: Condens. Matter, **21**, 224003 (2009).

[23] B. Ziberi, F. Frost, M. Tartz, H. Neumann, and B. Rauschenbach, Appl. Phys. Lett., **92**, 063102 (2008)

[24] E. A. Eklund, E. J. Snyder, R. S. Williams, Surf. Sci., **285**, 157 (1993).

[25] Tong, M. William. ; Williams. R. Stanley. Annu. Rev. Phys. Chem., **45**, 401 (1994).

[26] D. Paramanik, S. Varma, Nucl. Instru. Meth. B, **244**, 81 (2006).

[27] R. J. Kershner, L. D. Bozano, C. M. Micheel, A. M. Hung,A. R. Fornof, J. N. Cha, C. T. Rettner, M. Bersani,J. Frommer, P. W. K. Rothemund and G. M. Wallraff, Nat.Nanotechnol.,**4**, 557 (2009).

[28] David Pastré, Olivier Piétrement, Stephane Fusil, Fabrice Landousy, Josette Jeusset, Marie-Odile David, Loc Hamon, Eric Le Cam and Alain Zozime, Biophysical Journal, **85**, 2507 (2003).

[29] J. N. Israelachvili, Intermolecular and Surface Forces. (AcademicPress Inc., San Diego, 1992).

[30] Michelle A. Pillers, Rebecca Shute, Adam Farchone, Keenan P. Linder, Rose Doerfler, Corey Gavin, Valerie Goss, Marya Lieberman, Journal of Visualized Experiments **101**, e52972 (2015).

[31] X. Dai, C. Wei, F. F. Su, Z. Y. Li, Z. F.Sun and Y. Zhang, RSC Adv., **3**, 16116 (2013).

[32] F. Nagami, G. Zuccheri, B. Samori, and R. Kuroda, Anal. Biochem. **300**, 170 (2002).

[33] T. Kanno, T.Tanaka, N.Miyoshi, and T. Kawai, Jpn. J. Appl. Phys. **39**, L269 (2009).

[34] Aiguo Wu, Zhuang Li, Hualan Zhou, Jianping Zheng and Erkang Wang, Analyst.**127**, 585 (2002).

[35] Jing Yong Ye, Kazuo Umemura, Mitsuru Ishikawa, and Reiko Kuroda, Analytical Biochemistry. **281**, 21 (2000).

[36] A. Calò, P. Stoliar, E. Bystrenova, F. Valle and F. Biscarini, J. Phys. Chem. B. **113**, 15, 4987 (2009).

[37] A. Podesta, M. Indrieri, D. Brogioli, G. S. Manning, P. Milani, R. Guerra, L. Finzi, and D. Dunlap, Biophys. Jour. **89**, 2558 (2005).

[38] C. G. Baumann, S. B. Smith, V. A. Bloomfield and C. Bustamante. Proc.Natl. Acad. Sci.USA. **94**, 6185 (1997).

[39] S. Bhandaru, E. X. Zhang, D. M. Fleetwood, R. A. Reed, R. A. Weller, R. R. Harl, B. R. Rogers, S. M. Weiss. Surface Science. **635**, 49 (2015).

[40] Subrata Majumder, M. Priyadarshini, U. Subudhi, M. Umananda, G.B.N. Chiny, P.V. Stayam, Shikha Varma, Appl. Phys. Lett. **94**, 073110 (2009).

[41] A. Haug, S. Schweizer, F. Latteyer, M. B. Casu, H. Peisert, C. Ochsenfeld, T. Chass, Chem. Phys. Chem. **9**, 740 (2008).

[42] J. Peeling, F. E. Hruska, and N. S. McIntyre, Can. J. Chem. **56**, 1555 (1978).

[43] Dmitri Y. Petrovykh, Hiromi Kimura Suda, Lloyd J. Whitman, and Michael J. Tarlov, J. Am. Chem. Soc. **125**, 5219 (2003).

[44] J. V. Burda, J. Sponer, J. Leszczynski, and P. Hobza, J. Phys. Chem. B. **101**, 9670 (1997).

[45] J. Duguid, V. A. Bloomfield, J. Benevides, and G. J. Thomas Jr., Biophys. J. **65**, 1916 (1993).

[46] T. Hanwa and M. Ota, Appl. Surf. Sci. **55**, 269 (1992).

[47] D.Cole, Surface chemistry and adhesive properties of oxidised Si Surface, (thesis Queens College, University of Cambridge) (2007).

Chapter 4

Roughening, Wetting and Scaling properties of Self Affine Nanopatterned SiO_x Surfaces and after DNA Interaction

4.1 Introduction

Silicon, and silica, based nanomaterials demonstrate numerous technological benefits with wide range of applications in the fields of energy, environment, biology and biomedicine [1, 2]. Advantages of excellent electronic and mechanical properties added to well developed silicon technology have assisted these nanostructures in becoming excellent candidates for the development of high performance sensors [3, 4]. Nanostructured silicon based sensors are extensively utilized in the detection of biological targets like DNA [5], proteins [6], virus [7] as well as for analyte -receptor binding [8]. Silica nanoparticles, functionalized with oligonucleotides, have been utilized as templates for hybridization and development of DNA biosensors and biochips [9]. In many such applications, the adhesive properties of Si devices are guided and determined by the roughness, surface chemistry and interactions of the thin, native oxide layer that passivates the Si surface under normal conditions [10].

The natively oxidised silicon surfaces (Si/SiO_x) display non-covalent type interactions with molecules and bio-species, and play crucial role in many disciplines of biological cell integration and development of biomimetic materials for tissue engineering etc. [10, 11]. For these applications, however, regulation, monitoring and understanding of many inter-related properties of the surfaces, like roughness characteristics, wetting behavior, chemical nature etc., will be essential. Wetting phenomenon is ubiquitous to nature with widespread technological implications and the importance of Si/SiO_x surfaces stems from their omnipresence in most silicon based wetting explorations.

Real surfaces are always characterized through roughness which depends on the fabrication process and existence of adsorbed species. Many surfaces in nature, e.g. surfaces prepared by ion irradiation, vapor deposition of metal films, fractures (crack propagation), corrosion or wear of surfaces, and many other natural surfaces are described by roughness with self affine fractal properties [12]. A self-affine fractal remains statistically invariant under an anisotropic dilatation. This is in contrast to self-similar fractal which is invariant only under isotropic dilatation.

Scaling studies present an attractive formalism to describe surfaces grown under non-equilibrium conditions, e.g ion beam bombarded, molecular beam epitaxially grown, wave-patterns on sand dunes, growth of bacterial colony etc., under a common framework. Under the *theory of kinetic roughening* a flat surface essentially grows and roughens with time, evolving under varying scenarios [13–15]. The *dynamic scaling hypothesis* by Family-Vicsek shows that rms roughness, σ, of such growing surfaces demonstrate scaling behavior [16, 17] and the exponents describe the evolution process. Understanding surface evolution after ion bombardment is a complicated process due to the involvement of several components like ion beam parameters, surface properties etc. [18–21]. In this respect scaling parameters like roughness expo-

nents or Hurst exponent H, obtained via height-height correlation methods provide essential salient characteristics of the surface evolution, as well an understanding on the fractal nature of the surface [17].

Rough surfaces exhibit fluctuations in height h(ṙ) at position $\dot{r}$, relative to a smooth mean height value, and are characterized by a mean square roughness σ. For an isotropic rough surface, the height-height correlation (HHC) function, G(r), is represented as $G(r) = \langle [h(\dot{r}+r) - h(\dot{r})]^2 \rangle$, where the ensemble average is taken over all pairs of points on the surface, which are separated by an in- plane length r. For a self affine surface this correlation function displays an asymptotic behavior, saturating at $2\sigma^2$, beyond the in-plane correlation length ξ, with HHC displaying scaling relation [17]:

$$G(\mathbf{r}) \sim r^{2H} g(r/\xi). \tag{4.1}$$

with $g(x) \sim$ constant for $x \ll 1$ and $g(x) \sim x^{-2H}$ for $x \gg 1$. Then, $G(\mathbf{r}) \sim r^{2H}$ for $r \ll \xi$ and $G(\mathbf{r}) = 2\sigma^2$ for $r \gg \xi$. H is referred to as the roughness exponent or Hurst parameter ($0 < H < 1$). It describes the scaling and fractal properties of the surface and characterizes the degree of surface irregularity. Small values of H (H$\sim$0) correspond to extremely jagged or irregular surface, whereas large values H$\sim$1 are related to smooth topography. The fractal dimension (D_f) of the surface is further related to the Hurst exponent, $D_f = 3 - H$ [22]. The correlation length ξ represents the separation among the correlated structures on the surface.

Wetting on a smooth flat solid substrate can be expressed by Young's relation [23], $\gamma_{sl} + \gamma_{lv}\, cos\, \theta_0 = \gamma_{sv}$, where the contact angle θ_0 between a surface and a liquid droplet depends on the interfacial free energies of the solid/vapor γ_{sv}, solid/liquid γ_{sl} and liquid/vapor γ_{lv} interfaces. Surfaces are hydrophilic at low values of θ_0, with complete wetting at $\theta_0 = 0°$, and hydrophobic for $\theta_0 > 90°$. With the introduction of roughness on the surface, the above rela-

tion does not remain valid and wetting is usually described approximately by two classical thermodynamic models of Wenzel [24] and Cassie- Baxter [25]. The Wenzel model is based on complete contact at the solid- liquid interface whereas Cassie- Baxter model is applicable for interfaces that are only partially wetted [26]. Some Molecular Dynamics simulations have discussed the influence of correlated roughness on the wetting of self affine ($0.5 < H < 1$) surfaces [27]. With correlations, distant events can affect each other through interactive fluctuations on a rough surface, and may produce disorder in wetting. With this description, wetting on the surface may depend on the morphological parameters of the surface viz. σ, ξ and H (or D_f).

For most surfaces, modification in their roughness also leads to simultaneous changes in the chemical properties [28]. Surface roughening can sometimes expose new lattice planes having different interfacial energies or can modify defects e.g. ionic states or unsaturated dangling bonds on the surface. Such modifications have been investigated in molecular dynamic simulations [27].

The efficiency and rapid growth of DNA-based bio-devices, including DNA micro- and nano arrays and lab-on-chip, demand high concentration of DNA molecules immobilized on easily manufacturable surfaces [29]. The nanotopography of the surface also play role and modulate the DNA conformations. Sadana et.al [30] have attempted to study the use of fractal approach to analyze the influence of degree of heterogeneity of the surface on the binding, dissociation- rate- coefficient and affinities in biosensor applications. Fractal surfaces display scale invariant morphology across various spatial length scales, and exploration of DNA conformations as well as interactions on them can also identify the relevant length scales of interaction.

This chapter discusses the roughening behavior and fractal properties of the SiO_x surfaces irradiated by low energy ion beams. At low ion fluences,

SiO_x surfaces show development of nanostructures and ripples, which grow and evolve at higher fluences. The surface roughness increases after low ion irradiation fluences but then systematically decreases. Height-height correlation technique has been utilized here to obtain the roughness exponent or Hurst exponent (H). These exponents present very crucial scaling parameters providing important insight into the growth processes that occur at any surface, growing under non-equilibrium conditions. Here the obtained H values indicate that the surfaces are of self affine nature, i.e they show self similar properties only under asymmetric expansions. Such surfaces show fractal behavior. An increase in the correlation length on the ion irradiated surfaces indicates the evolution nanostructures. The un-irradiated SiO_x surfaces show hydrophilic nature which reduces on the nanopatterned surfaces. The interaction of ion irradiated SiO_x surfaces, with plasmid DNA, has also been investigated. The Scaling properties show that the surfaces are no more of self - affine nature after DNA adsorption. They have instead developed a more flat 2-dimensional character. The fractal dimension of the DNA also indicates that on ion beam modified surfaces DNA has flatter geometry.

4.2 Experiment

Commercially available epi-polished p-Si(100) single crystals ($1cm \times 1cm \times 0.1cm$) with native surface oxide (SiO_x) have been used here. Off normal ion irradiations (with ions incident at an angle of 15^o from the normal) were performed on the Si/SiO_x substrates at room temperature under UHV conditions using 3keV Ar^+ at the fluences of 6×10^{15}, 1.2×10^{16} and 1.8×10^{16} ions/cm^2.

pBR322 with 4361 base pairs was purchased from Fermentas (SD0041) and was stored at -20^o C. 10 nM of pBR322 was prepared in 1x TAEM (40 mM Tris-HCl, 20 mM acetic acid, 2 mM EDTA and 12.5 mM Magne-

sium Acetate) buffer of pH=8.3. pBR322 was further diluted to 0.1 nM for the adsorption studies. DNA was adsorbed on pristine (un-irradiated) and ion irradiated substrates by dropping a 10 μl of this 0.1 nM pBR322 buffer solution on each of the substrates. After 2 hr, the DNA interacted Si substrates were thoroughly rinsed with MQ water, to remove any residual DNA molecules. Substrates were then dried in air. They were blown with N_2 gas prior to imaging.

Morphology of the surfaces, prior to and after interaction with DNA, have been investigated by Scanning Probe Microscope (Atomic Force Microscope mode using Nanoscope V Multimode) from Bruker. All images reported here have been acquired in tapping mode under ambient conditions using phosphorus doped (n-type) Si tips. The tips have a radius of curvature R of about 5 nm, force constant κ of about 80 N/m and resonant frequency of 316 KHz. The results presented here are based on nearly 300 AFM images of various scan sizes. X-ray Photoelectron spectroscopy (XPS) measurements were performed using a VG instrument with Mg K_α source (1256.6eV), under UHV conditions. A standard shirley type background was removed from all the XPS spectra before analysis and C(1s) feature has been utilized for charge corrections. The contact angle (CA) measurements were performed with water droplets in static mode using a commercial CA goniometer (OCA15EC) from Dataphysics. Contact angles where measured from right and left- side view of the image with an accuracy of ± 0.10. An average of both angles for 8 images are reported here.

4.3 Results and Discussions

Figure 4.1 shows SPM images from pristine (un-irradiated) Si/SiO_x surface as well as after ion irradiation at various fluences. The morphological properties of these ion irradiated surfaces have been discussed in detail in chapter 3.

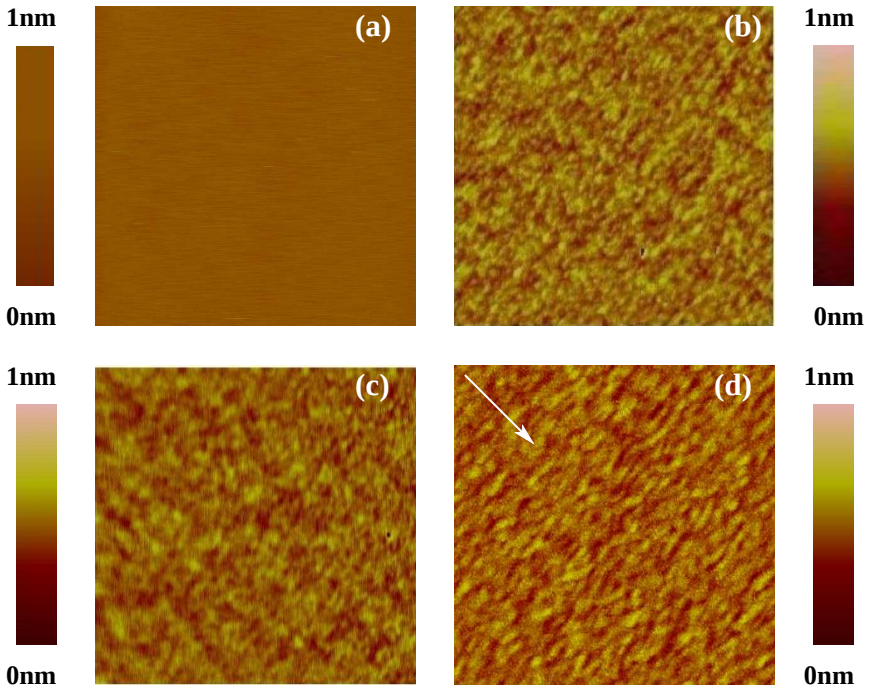

Figure 4.1: 700×700 nm^2 AFM images for (a) unirradiated surface as well as after irradiation with fluences of (b) 6×10^{15}, (c) 1.2×10^{16} and (d)1.8×10^{16} ions/cm^2. Ion beam direction is shown by arrow.

The pristine surface is smooth with an rms roughness of 0.072 nm. After irradiation at low fluences of 6×10^{15} and 1.2×10^{16}ions/cm^2, development of weak ripple patterns and nanostructures is observed with overall surface rms roughness of 0.192 and 0.187 nm, respectively. A well defined ripple pattern is observed after the fluence of 1.8×10^{16}ions/cm^2. The rms roughness at this stage is 0.139 nm. As discussed in chapter 3, these ripples are decorated with nanostructures which evolve and grow with fluence. The ripple patterns become more distinct at the highest fluence with their wave vector **k** oriented parallel to the ion beam direction. Spontaneous formation of self organized nanoscale patterns on surfaces, during ion irradiation, is controlled by the competition between the erosion on the surface and smoothening by diffusion processes [31].

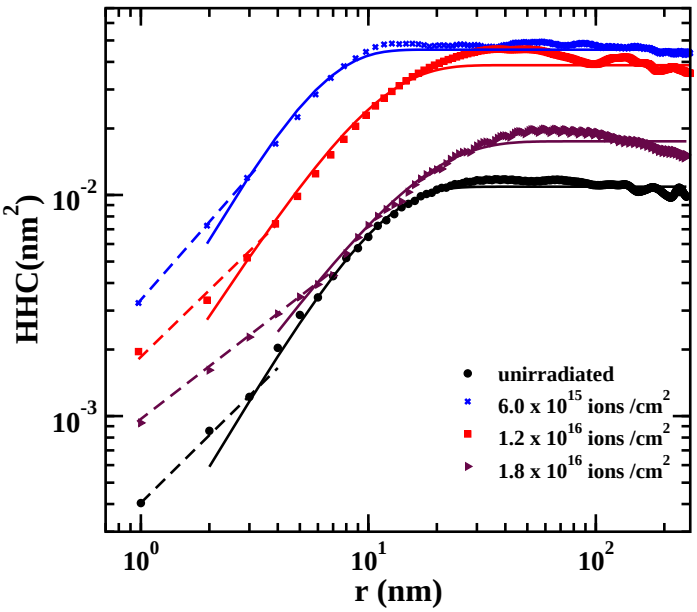

Figure 4.2: HHC function for unirradiated as well as after irradiation with fluence of 6×10^{15} ions/cm^2, 1.2×10^{16} ions/cm^2 and 1.8×10^{16} ions/cm^2. Fittings are shown with solid lines. Dashed lines indicate second exponent H below the cross over point.

Figure 4.2 presents HHC results for pristine as well as ion irradiated surfaces. With $HHC \propto r^{2H}$ when $r \ll \xi$ and $HHC \sim 2\sigma^2$ when $r \gg \xi$, a phenomenological scaling function of form $HHC \sim \frac{\sigma^2}{2}\left(1 - \exp(-(r/\xi)^{2H}\right)$ has been utilized [32] to obtain values of σ, ξ and H (table 4.1) from the fit.

The roughness σ, is 0.10 nm for the un-irradiated surface but increases to 0.21 nm after irradiation of $6{\times}10^{15}$ $ions/cm^2$. For higher fluences this rms roughness decreases. However, the decrease is small. σ obtained by HHC studies here are similar to the rms roughness values obtained by AFM images (fig. 4.1), as discussed earlier. The height fluctuations or the patterning on a surface are a combination of several factors like sputter induced surface

Table 4.1: HHC fitting parameters(σ, ξ, H, D_f), and Contact Angle (CA) of surfaces

sample	$\sigma(nm)$ (± 0.01)	ξ(nm) (± 0.9)	H (± 0.01)	D_f (± 0.01)	CA (± 0.1)
un-irradiated	0.10	10.4	0.87	2.13	53.5
6.0×10^{15} ions/cm^2	0.21	5.6	0.97	2.03	59.7
1.2×10^{16} ions/cm^2	0.19	10.0	0.80	2.20	64.1
1.8×10^{16} ions/cm^2	0.13	15.3	0.70	2.30	69.6

erosion, bulk and surface diffusion during irradiation. The decrease in rms roughness can be due to the enhanced role of diffusion processes as well as nano patterning of the surfaces. For the un-irradiated surface a high ξ is observed, which decreases on the surface irradiated at $6{\times}10^{15}$ $ions/cm^2$. With further irradiation a systematic increase in ξ indicates enlarging nanostructures and evolution of ripples (fig. 4.1d). This also suggests an increased long-ranged roughness. Hurst parameter H, on the other hand is related to the short wavelength roughness [22]. With $0.5 < H < 1$, all these surfaces are characterized as self affine fractals [17]. Self affine surfaces have property that under suitable scale transformations, the statistical properties of the surfaces remain invariant [17]. Highest H is observed here for the surfaces irradiated with $6{\times}10^{15}$ $ions/cm^2$ and decreases systematically for higher fluences. Qualitatively, decrease in H (or increase in fractal dimension D_f) suggests increase in the short- ranged roughness [22]. Moreover, with $\sigma/\xi \ll 1$ and $H \geq 0.5$, these surfaces have weak roughness which can cause liquid drop to wet the crevices on the surface upon contact [33, 34]. Interestingly, for all the surfaces, a crossover in the roughness exponent H (shown by dashed lines in fig. 4.2) at small r is also observed. For the un-irradiated surface e.g. the crossover point in roughness exponent is observed at $r = 2.9$ nm, while for the irradiated surfaces this cross over occurs at 3.9, 4.9 and 5.9 nm for fluences of $6{\times}10^{15}$, $1.2{\times}10^{16}$ and $1.8{\times}10^{16}$ $ions/cm^2$,

respectively, indicating that in the region below crossover point the surface is becoming more jagged or spiky [33], due to reduced H, compared to at larger r. Thus, all these surfaces exhibit some hierarchical structures with multi-scale roughness. Theoretical results show that this type of hierarchical morphologies will exhibit dewetting properties in general [35]. Here SiO_x surfaces exhibit hydrophilic behavior. This wetting nature, however, degrades with ion irradiation, as discussed below.

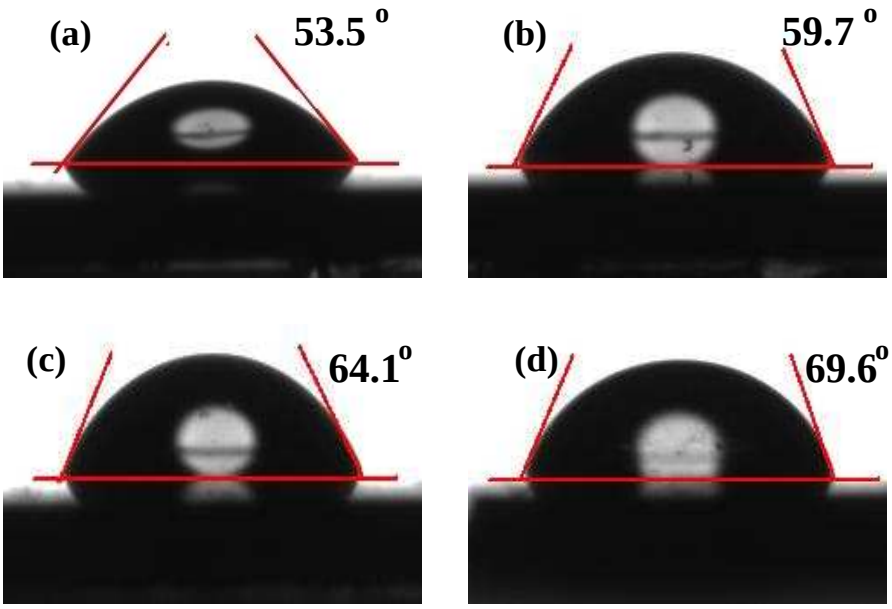

Figure 4.3: Contact angle measurements for (a) unirradiated surface as well as after irradiation with fluences of (b) 6×10^{15}, (c) 1.2×10^{16} and (d) 1.8×10^{16} ions/cm^2.

The contact angle measurements for all the Si/SiO_x surfaces are presented in fig. 4.3. For the un-irradiated surface a contact angle of 53.5^0 is obtained. Although silicon is hydrophobic, SiO_x has hydrophilic nature [36]. After irradiation, contact angle systematically increases (table 4.1). The ion sputtered surfaces, thus, tend to wet less than the pristine (un-irradiated) surface. With

the fractal dimension of the surface, D_f, also reasonably increasing with fluence (table 4.1), contact angle and wetting behavior demonstrate dependence on the fractal properties of the surface. Reduced D_f at $6{\times}10^{15}$ $ions/cm^2$, compared to un-irradiated surface, can be related to the diminishing thickness of the oxidised layer at the surface, with irradiation, as discussed below. For the irradiated surfaces, D_f systematically increases with fluence, while wetting correspondingly decreases. Increasing fractal dimension increases the short wavelength roughness, indicating that surface jaggedness is playing a crucial role along with other morphological parameters, σ and ξ [34]. With H measuring the degree of sharp local surface irregularity, σ/ξ^H determines the slope of short wavelength undulations on a surface [34] whereas σ/ξ measures the slope of long wavelengths. A close correspondence of decreasing H (or increasing D_f) with reduced wetting, as observed here with increasing fluence, suggests a significant role of fractal dimension of surface as well as short wavelength undulations (i.e. σ/ξ^H) on the wetting behavior.

Ion irradiation of the surfaces can also simultaneously produce changes in their chemical properties. Figure 4.4 displays Si(2p) XPS spectra from Si/SiO_x surfaces both prior to as well as after ion irradiation. These spectra have been collected at an emission angle ($\theta = 0^o$) along the analyzer axis. On the other hand, results presented in chapter 3 were along $\theta = 30^o$ making them surface sensitive, from nearly top 1 nm of the surface layers. Here, the spectrum from pristine surface (Fig. 4.4(a)) displays two peaks. Peak at 99.6 eV is related to the elemental silicon whereas the feature at 103.9 eV is due to SiO_x [37]. Angular dependent XPS results have been utilized to estimate the thickness of the native oxide SiO_x and is found to be 20 $\mathring{A}$ for pristine surface. This thickness decreases after irradiation, as expected (Fig. 4.4(b,c)) and is observed to be $5\mathring{A}$ for the fluence of $6{\times}10^{15}$ and $4\mathring{A}$ after

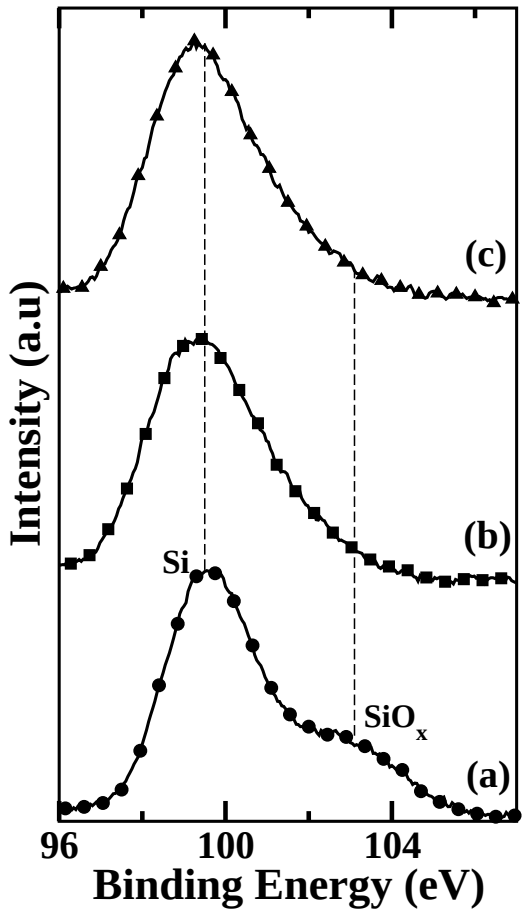

Figure 4.4: XPS spectra of Si(2p) region from (a) unirradiated surface as well as surfaces irradiated with fluences of (b) 6×10^{15}, and (c) 1.8×10^{16} ions/cm^2.

1.8×10^{16} ions/cm^2 .

Scaling and fractal properties of the pristine (unirradiated) and ion irradiated Si/SiO$_x$ surfaces have also been investigated after their interaction with DNA. The SiO$_x$ surfaces are negatively charged under the present buffer conditions (pH = 8.3) [38, 39]. The divalent Mg cations in the buffer solution produce the charge- inversion on the surface so that the negatively charged DNA can be adsorbed on it. The adsorption of the DNA on the SiO$_x$ surfaces is produced by a weak electrostatic interaction by the formation of an electrical double layer (EDL) [40]. On the SiO$_x$ surface, negative- charges are located

on the oxygen sites. When DNA in buffer solution (containing divalent Mg^{2+} ions) is interacted with the surface, an EDL forms with divalent ions forming a bridge-like layer between the surface and the negative- backbone of the DNA. This EDL layer also produces a double- layer force [41]. A stable configuration is produced when the electrostatic attraction overcomes the thermal repulsion [40]. At the Mg^{2+} concentration of the present study, the Debye length or the screening length for the electrostatic potential between cations has been shown to be greater than the average separation between the charges on mica surface [40]. However, with SiO_x having less charge density on the surface than mica [42] the screening length will be greater than the charge separation leading to correlations between the divalent-ions. This produces less staggered geometries for cations on the surface [40, 43] and creates 2-dimensional DNA -network on SiO_x surfaces.

HHC of all the surfaces, after DNA immobilization, were investigated and are shown in fig. 4.5. Interestingly only one H, and no crossover point is observed. Moreover $H \sim 1$, and $D_f \sim 2$, is observed (table 4.2) for all the surfaces. Consequently all the surfaces have become nearly flat- smooth 2 dimensional type after DNA immobilization, and are no more of self affine fractal type. Thus, DNA with its nano sizes is able to probe the small length scales of the surfaces e.g. the jagged and spiky regions of the order of few nanometers. The roughness σ of all the surfaces is observed to increase after DNA immobilization. This is due to the formation of 2-dimensional DNA network on SiO_x surfaces, as discussed below.

The super-coiled circular plasmid DNA (pBR322) can be unfolded into rings and circles. These extended DNA- circles can cross or overlap each other

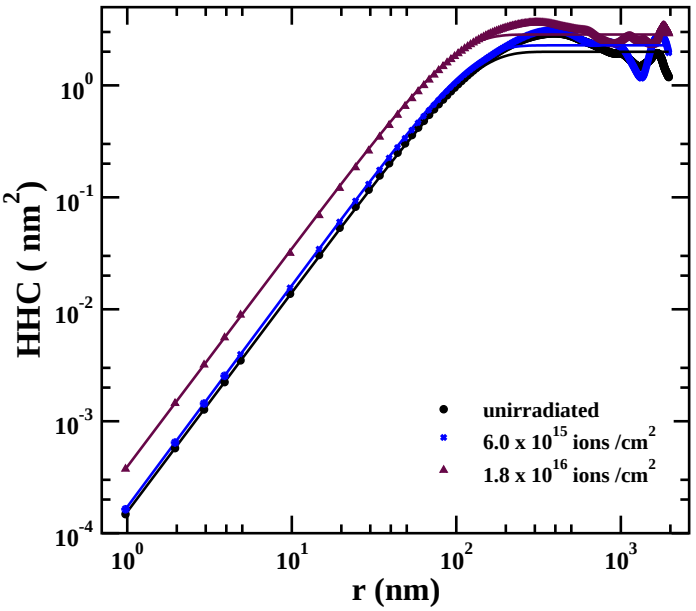

Figure 4.5: HHC function after DNA is immobilized on unirradiated surface and on surfaces irradiated with fluence of 6×10^{15} ions/cm^2, and 1.8×10^{16} ions/cm^2. Fittings are shown with solid lines.

Table 4.2: HHC fitting parameters(σ, ξ, H, D_f,) of surfaces and D_{dna} after DNA immobilization

sample	σ(nm)	ξ(nm)	H	D_f	D_{dna}
pristine	1.41	121.5	0.98	2.02	1.53
6.0×10^{15} ions/cm^2	1.51	118.0	0.99	2.01	1.65
1.8×10^{16} ions/cm^2	1.68	94.8	0.99	2.01	1.72

and can form DNA-networks owing to the divalent cation which act as bridges [44]. In other words, the divalent cations can open the plasmid DNA (pBR322) super-coils into loosened circles. Cations further assist these DNA circles in crossing and overlapping each other to form DNA network. Though at low cation concentrations, super-coiled plasmid DNA cannot be unfolded into loose circles and 2-dimensional networks do not form, this can take place at higher divalent cation concentration [44]. For the concentrations of the plasmid DNA and divalent Mg^{2+} cations used in the present study,

2-dimensional DNA networks are expected [44]. Though a single mono-layer of DNA network will be about 2 nm in height, larger heights (4 or 6nm respectively) will form for two or three mono-layers [45–47]. Aggregation of DNA also leads to higher profiles. AFM images from the DNA immobilized SiO_x surfaces are shown in fig. 4.6. A 2-dimensional network of DNA is observed on all the surfaces. The section analysis is also presented which shows a height for DNA network to be about 1.8 - 2.2 nm on all the surfaces. Thus on all the surfaces, pristine as well as ion irradiated, the DNA network is nearly a monolayer high with no aggregation [45–47]. However, the diameter of DNA (outline of one shown) reduces on the ion sputtered surfaces, decreasing with fluence. This reduction in DNA size, with fluence, has been discussed in detail in chapter 3. Surface morphology as well as the charge transfer from DNA to the SiO_x surface is responsible for this reduction.

The outline of a DNA (as shown by dashed line in Fig. 4.6c) is like a "shoreline of a lake" and can exhibit fractal dimensions [17]. This fractal dimension of DNA, D_{dna}, has been measured here using AFM images by utilizing the box counting algorithm [17] where the number of boxes N(L) containing a part of the molecule are evaluated as a function of the box size L. The curves for N(L) present the scaling regime, $N(L) = L^{-D_{dna}}$, as shown in fig. 4.6. On pristine surface D_{dna} is 1.53, but increases to 1.65 and 1.72 on surfaces irradiated with fluences of 6.0×10^{15} and 1.8×10^{16} ions/cm^2, respectively. Although a fractal dimension of 1 will indicate a linear- loop like DNA structure on the surface, fractal dimension of 2 will be for a flatter configurations [17]. Hence D_{dna} values obtained here indicate that DNA, on ion irradiated SiO_x surfaces, have more flatter geometry. This is also caused by the reduction in DNA- size (fig. 4.6) which make them compacter on ion irradiated surfaces. Thus, ion irradiated SiO_x surfaces exhibit development of more 2-dimensional DNA network with DNA fractal dimension varying

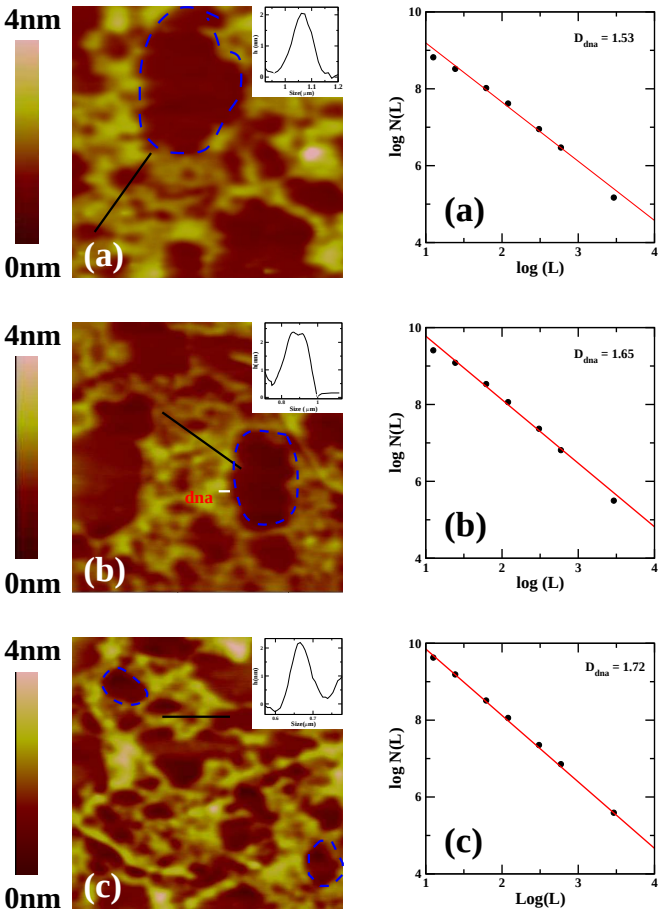

Figure 4.6: 500×500 nm^2 AFM images after DNA is immobilized on (a) unirradiated surface and on surfaces irradiated with fluences of (b) 6×10^{15}, and (c) 1.8×10^{16} ions/cm^2. Typical examples of DNA are shown by dashed lines. The section analysis of the black line is shown in the inset. Fractal dimension of DNA, calculated by Box counting method, on these surfaces, is also shown.

from 1.65 to 1.72. Such 2-dim DNA network on the mica surfaces exhibit DNA fractal dimensions between 1.3 and 1.7 [48]. Immobilization of DNA on polymer surfaces also produces two dimensional DNA network with fractal dimensions of nearly 2.5 [49].

4.4 Conclusion

Present chapter discusses the roughening and scaling properties of SiO_x surfaces that have been modified via low energy ion beams. The surfaces display development of nanostructures and ripple patterns upon irradiation, and their growth and evolution when the fluence is increased. All these nanopatterned surfaces indicate a decrease in roughness as well as reduction in their hydrophilic property upon increasing the fluence. Height-height correlation technique has been applied here to understand the scaling behavior and to obtain the roughness parameter Hurst (H) exponent. These studies indicate that the SiO_x surfaces have fractal properties and are self-affine in nature. The ion irradiated SiO_x surfaces have also been interacted with plasmid DNA. Interestingly, the scaling results show that that the surfaces are no more of self-affine nature. The DNA rather make a 2-dimensional adhesive layer on the nano patterned surfaces. The fractal dimension of DNA (D_{dna}) has also been measured here. This also suggests that DNA is transforming into flatter and compact units on the ion irradiated surfaces. Miniaturization is a major criteria for a biosensor. Smaller DNA sizes and flatter 2-dimensional DNA flims have increased areal density, less sample consumption and reduced sample diffusion. These can enhance the sensing properties and reduce the recording of error signals.

Thus, chapters 3 and 4 discussed the chemical composition, scaling properties, roughening nature as well as the fractal properties of the self assembled nanostructures created on the ion irradiated Si/SiO_x surfaces, both prior to and after interaction with DNA. TiO_2 is an attractive biomaterial and is extensively utilized for bio-implants. Biocompatible properties make it suitable for applications in binding with proteins and DNA. Chapter 5 discusses the chemical composition, scaling properties and roughening behavior of self assembled nanostructures created on ion irradiated TiO_2 surfaces. The in-

teraction of DNA with ion beam irradiated and UV beam modified TiO_2 surfaces is presented in chapter 6.

Bibliography

[1] Hak Soo Choi, Wenhao Liu, Preeti Misra, Eiichi Tanaka, John P Zimmer, Binl Itty Ipe, Moungi G Bawendi, John V Frangioni, Nature Biotechnology. **25**, 1165 (2007).

[2] Norah O Farrell, Andrew Houlton, and Benjamin R Horrocks, Int. J. Nanomedicine. **4**, 451 (2006).

[3] T. Tanaka, L. S. Mangala, P. E. Vivas-Mejia, R. Nieves-Alicea R, A. P. Mann , E. Mora , H. D. Han, M. M. Shahzad, X. Liu, R. Bhavane, J. Gu, J. R. Fakhoury, C. Chiappini, C. Lu, K. Matsuo, B. Godin, R. L. Stone, A. M. Nick, G. Lopez-Berestein, A. K. Sood, M. Ferrari, Cancer Res. **70**, 3687 (2010).

[4] Rong Xu, Yi Huang, Junhua Mai, Guodong Zhang, Xiaojing Guo, Xiaojun Xia, Eugene J. Koa, Guoting Qin, Donald R. Erm, Qingpo Li, Xuewu Liu, Mauro Ferrari1, and Haifa Shen, Small. **9**, 1799 (2013).

[5] Y. F. Zhang, Y. H. Tang, N. Wang, D. P. Yu, C. S. Lee, I. Bello, S. T. Lee, Applied Physics Letters. **72**, 1835 (1998).

[6] Yanli Wang, Tianyu Wang, Peimei Da, Ming Xu, Hao Wu, Gengfeng Zheng, Advance Materials. **25**, 5177 (2013).

[7] Zhuang Liu, Xiaoming Sun, Nozomi Nakayama-Ratchford and Hongjie Dai, ACS Nano. **1**, 50 (2007).

[8] Gu Luo, Laura E. Ruff, Zhengtao Qin, Maripat P. Corr, Stephen M. Hedrick, and Michael J. Sailor, Adv Mater. **24**, 3981 (2012).

[9] L. R. Hilliard, X. Zhao, W. Tan, Anal Chim Acta. **470**, 51 (2002) .

[10] D. Cole, Surface chemistry and adhesive properties of Oxidised Si Surfaces, (Thesis Queens College, University of Cambridge, 2007).

[11] B. A. Weisenberg and D. L. Mooradian, J. Biomed. Mater. Res. **60**, 283 (2002) .

[12] B. B. Mandelbrodt, The Fractal Geometry of Nature, (Freeman New York 1982).

[13] J. J. Ramasco, J. M. Lopez and M. A. Rodriguez, Phys. Rev. Lett. **84**, 2199 (2000).

[14] J. Krim and G.Palasantzas, Int. J. Mod. Phys. B **9**, 599 (1995).

[15] G. Palasantzas and J. Krim, Phys. Rev. B. **48**, 2873 (1993).

[16] F. Family, T. Vicsek, *Dynamics of fractal Surface*, World Scientific, Singapore, **1991**.

[17] A. L. Barabasi, H. E. Stanley, Fractal Concepts in Surface Growth,(Cambridge University press 1995).

[18] V. Solanki, S. Majumder, I. Mishra, P. Dash, C. Singh, D. Kanjilal, and S. Varma, J. Appl. Phys. **115**, 124306 (2014).

[19] S. Majumder, D. Paramanik, V. Solanki, B. P. Bag, and S. Varma, Appl. Phys. Lett. **98**, 053105 (2011).

[20] G. Carter and V. Vishnyakov, Phys. Rev. B **54** 17647 (1996).

[21] S. Rusponi, G. Costantini, C. Boragno, and U. Valbusa, Phys.Rev. Lett. **81** 2735 (1998).

[22] C. Yang, U. Tartaglino and B. N. J. Persson, Phys. Rev. Lett. **97**, 116103 (2006).

[23] T. Young, Philos. Trans. R. Soc. London. **95**, 65 (1805).

[24] N. Wenzel, Ind. Eng. Chem. **38**, 988 (1936).

[25] B. D. Cassie and S. Baxter, Trans. Faraday Soc. **40**, 546 (1944).

[26] X. B. Zhou and J. Th. M. De. Hosson, J. Materials Res. **10**, 1984 (1995).

[27] T. S. Chow, J. Phys. Condens. Matter. **10**, L445 (1998).

[28] D. J. Durian, C. Franck, Phys. Rev. Lett. **59**, 555 (1987).

[29] U. Muller and D. V. Nicolau, Microarray Technology and Applications, (Springer, Heidelberg, 2004).

[30] A. Sadana, Biosensors Bioelectronics. **13**, 1127 (1998).

[31] A. Keller and S. Facsko, Materials. **3**, 4811 (2010).

[32] K. Vanormelingen, B. Degroote, and A. Vantomme, J. Vac. Sci. Tech. B. **24**, 725 (2006).

[33] S. Sarkar, S. Patra, N. Gayathri, S. Banerjee, Appl. Phys. Lett. **96**, 063112 (2010).

[34] G. Palasantzas and J. Th. M. De. Hosson, Acta. Mater. **49**, 3533 (2001).

[35] S. Herminghaus, Europhys. Lett. **52**, 165 (2000).

[36] R. Williams and A. M. Goodman, Appl. Phys. Lett. **25**, 531 (1974).

[37] S. Bhandaru, E. X. Zhang, D. M. Fleetwood, R. A. Reed, R. A. Weller, R. R. Harl, B. R. Rogers, S. M. Weiss. Surface Science. **635**, 49 (2015).

[38] R. J. Kershner, L. D. Bozano, C. M. Micheel, A. M. Hung, A. R. Fornof, J. N. Cha, C. T. Rettner, M. Bersani, J. Frommer, P. W. K. Rothemund and G. M. Wallraff, Nat.Nanotechnol, **4**, 557 (2009).

[39] Bezuayehu Teshome, Stefan Facsko and Adrian Keller, Nanoscale, **6**, 1790 (2014).

[40] David Pastré, Olivier Piétrement, Stephane Fusil, Fabrice Landousy, Josette Jeusset, Marie-Odile David, Loc Hamon, Eric Le Cam and Alain Zozime, Biophysical Journal, **85**, 2507 (2003).

[41] J. N. Israelachvili, Intermolecular and Surface Forces. (Academic Press Inc., San Diego, 1992).

[42] Michelle A. Pillers, Rebecca Shute, Adam Farchone, Keenan P. Linder, Rose Doerfler, Corey Gavin, Valerie Goss, Marya Lieberman, Journal of Visualized Experiments **101**, e52972 (2015).

[43] X. Dai, C. Wei, F. F. Su, Z. Y. Li, Z. F.Sun and Y. Zhang, RSC Adv., **3**, 16116 (2013).

[44] F. Nagami, G. Zuccheri, B. Samori, and R. Kuroda, Anal. Biochem. **300**, 170 (2002).

[45] T. Kanno, T.Tanaka, N.Miyoshi, and T. Kawai, Jpn. J. Appl. Phys. **39**, L269 (2009).

[46] J. Y. Ye, K. Umemura, M. Ishikawa, and R. Kuroda, Anal. Biochem., **281**, 21 (2000).

[47] Aiguo Wu, Zhuang Li, Hualan Zhou, Jianping Zheng and Erkang Wang, Analyst, **127**, 585 (2002).

[48] S. Kawano, Jap. Soc. of Mech. Engr. **48**, 191 (2005).

[49] P. D. Sawant, D. V. Nicolau, Appl. Phys. Lett **87**, 223117 (2005).

Chapter 5

Evolution of Surface Morphology and Scaling Studies of Nanopatterned $TiO_2(110)$ Surfaces created by Low Energy Ion Irradiation

5.1 Introduction

The nanostructure formation on rutile TiO_2 surfaces has been demonstrated to be significant for many advanced properties like enhanced photo- absorbance, photo-catalysis as well as for bio- molecular conjugation [1, 2]. These behaviors however, crucially depend on many surface properties related to morphology, electronic structure as well as presence of defect states [1, 2]. Though numerous methods have been utilized for the formation of nanostructures on TiO_2 [3, 4], fabrication via ion beam irradiation is an attractive technique since it demands simple methodology usually requiring only single step processing [5]. With immense potential in technology, this route for nanostructure fabrication has become an active area of research. Tuned with

controlled ion parameters, many surfaces demonstrate spontaneous development of a rich variety of nanoscale patterns by this method [2, 5].

The pattern formation on a bi-atomic metal oxide surface, through ion irradiation, is more complex than usual semiconductor or metallic surface [6]. This is caused by the preferential sputtering of oxygen atoms from the surface. As a result, the surface develops some metal-rich centers. These sites are crucial as they become the centers for the nucleation of nanostructures. On a crystalline rutile TiO_2 (110) surface, understanding of pattern formation is even more complicated due to the presence of anisotropic diffusion of atoms on the surface. Non-symmetric diffusion leads to the development of elongated nanostructures and ripple patterns on the surface [7]. *First Principal studies* and *Partial density of state* (PDOS) calculations have shown even modification of electronic structure due to irradiation [8]. TiO_2 nanostructures patterned via ion irradiation show many advanced functional properties [6]. Their understanding is significant for designing structures with desired properties. Scaling properties in this respect can play a vital role in developing any pattern-formation theory as they reflect many crucial features of patterns, periodicities, and correlation on the surface not provided by simple morphology studies [9].

The major effect of ion irradiation is the direct transfer of energy and momentum to the surface, via ion- atom collisions. In the process many erosive and diffusive processes take place on the surface. Competition between such processes becomes the dominant factor that control the surface morphology. This sometimes results in the formation of the self assembled nanostructures or nano-patterns on surfaces [10]. On multi-component surfaces, like metal oxides, ion beams can in addition also produce preferential sputtering of low mass ions leading to the generation of variety of defect states. The generation of surface morphology and nano-patterning by ion

irradiation is thus complex and for their systematic understanding scaling techniques can play an important role. Scaling theories can also reveal the underlying physical processes controlling the morphology [11, 12]. Theoretical understanding, through scaling studies, can also be useful in designing desired surfaces [11, 12].

Recent studies have shown that the scaling theories developed for non-equilibrium film growth may also be applicable to ion bombarded surfaces [9, 11, 12]. Growing interfaces and surfaces often show self affine properties [11, 12]. According to the definition, a self affine function f(x) of a single variable x satisfy the relation [11, 12]:

$$f(x) \sim \lambda^{-H} f(\lambda x) \tag{5.1}$$

where λ is a parameter and H is the roughness or Hurst exponent. Further, for self affine surfaces, Family and Vicsek [12] have analyzed the growth behavior and show that their rms roughness or the interface width $w(L, t)$ behaves like :

$$w(L, t) \sim L^{H} s(t/L^{z}) \tag{5.2}$$

where L is the length scale over which the roughness is measured and t is the time during growth. The scaling function $s(u)$ behaves as $s(u) \sim u^{\beta}$ for $u \ll 1$ and $s(u) \sim constant$ for $u \gg 1$. The parameter β is the growth exponent and $z = H/\beta$ is the dynamic exponent. Exponents are very useful as they reflect the growth conditions but do not depend on the microscopic details of the system.

The self affine surfaces are usually investigated by the scaling properties of the surface fluctuations [11, 12]. Rough surfaces can be described by a height profile $h(r)$ at position r w.r.t. smooth mean height, mean square roughness σ, lateral correlation length ξ, and roughness exponent H. For an

isotropic rough surface, the height-height correlation function (HHCF) G(r) is given by [11, 12]:

$$G(r) = \langle [h(\acute{r} + r) - h(\acute{r})]^2 \rangle, \tag{5.3}$$

where the ensemble average is taken over all pairs of points. This correlation function asymptotically saturates at a value related to the rms surface roughness and displays the scaling relation of the type [11] :

$$G(r) \sim r^{2H} g(r/\xi). \tag{5.4}$$

with $g(x) \sim$ constant for $x \ll 1$ and $g(x) \sim x^{-2H}$ for $x \gg 1$. These conditions lead to $G(r) \sim r^{2H}$ for $r \ll \xi$ and $G(r) = 2\sigma^2$ for $r \gg \xi$. The roughness exponent H $(0 < H < 1)$ characterizes the degree of irregularity of the surface as well as its scaling and fractal properties. Small H values correspond to extremely jagged or irregular surface whereas large values refer to smoother topographies [13].

HHCF presents the topographical properties of a surface in real space. Power Spectral Density(PSD), on the other hand, exploits Fourier space or reciprocal space representation via spatial frequency (κ) mapping of topography and can provide valuable information even for surfaces with complex morphologies. Containing full information on the contribution of each spatial frequency to the topography, PSD can provide spatial distributions and periodic characteristics of the surface across multiple length scales [14, 15]. PSD function is the square of Fourier transformation of a surface profile $h(r)$ and is defined as:

$$PSD(\kappa) = \frac{1}{L} \left| \int_{-L/2}^{L/2} h(r) \exp^{-i\kappa r} \, dr \right|^2. \tag{5.5}$$

Correlation length $(=1/\kappa_0)$ of any surface denotes the lateral extent of fluctuations or corrugations on it. The surface can be considered to be flat for

lengths larger than correlation length i.e. PSD function becomes independent of κ in the region $\kappa < \kappa_0$. On the other hand, corrugations are significant for lengths smaller than correlation length (i.e. when $\kappa > \kappa_0$), and a κ dependent PSD is obtained [16]. Surface scaling analysis via power spectral density (PSD) evaluation can be utilized to determine the processes dominating the surface evolution [17].

The present chapter investigates the scaling studies of the ion irradiated TiO_2 surfaces. Low energy ions have been utilized for ion irradiation. The surfaces demonstrate the formation of self-assembled nanostructures. These nanostructures (NS) are Ti-rich and their nucleation gets initiated by the presence of Ti^{3+} vacancy states on the surface. At low fluences these NS are of elliptical shape but transform to less elliptical form at higher fluences. Scaling studies of ion beam modified surfaces have been performed using height-height scaling function (HHCF) as well as Power spectral density function. Both these studies have been utilized for investigating the roughness exponents which show that, the surfaces are self affine in nature and with fluence, their roughness in short length scales decreases. This can be caused via increase in surface diffusion as shown by scaling studies. Studies also reveal that upon increasing fluence the regions of correlated fluctuations increase. These results can be attributed to increase in the nanostructure dimensions.

5.2 Experiment

Single crystals ($5mm \times 5mm \times 1mm$) of $TiO_2(110)$ were irradiated with 3 keV Ar^+ ions at an incidence angle of 15^o, from surface normal, at room temperature in a chamber with a base vacuum of 10^{-8} Torr. Ion beam spot was sub-millimeter in size which was de-focused to a 2mm x 2mm area. Fluences of 6.0×10^{15} and 1.8×10^{16} (flux = 1x10^{13} ions/cm^{2}sec) were used. Higher

fluence of 1.5×10^{19} ions/cm^2 (flux = 3x10^{16} ions/ cm^{2}sec) was also used. Surface morphology has been investigated with Atomic Force Microscopy (AFM) using Scanning Probe Microscope (Nanoscope V from Bruker) in tapping mode with 256×256 data points. For Power Spectral Density(PSD) and Height -Height Correlation function(HHCF) analysis, nearly 200 AFM images were analyzed and statistically averaged results are presented here. X-Ray Photoelectron Spectroscopy (XPS) studies were performed using a VG scientific instrument with MgKα (1256.6 eV) source under a vacuum of 8.0×10^{-11} $Torr$. The spectra were acquired at an angle of 30^0, with respect to surface normal, and were charge corrected using C1s level at 284.6 eV after removing Shirley-type background.

5.3 Results and Discussions

Evolution of the surface morphology of rutile TiO_2 (110) surfaces, both prior to and after ion irradiation, is displayed in fig. 5.1. The pristine (un-irradiated) surface displays steps, as expected for such surfaces [18], and a very small rms roughness of 0.096 nm. Irradiation with Ar ions with fluences of 6.0×10^{15} and 1.8×10^{16} ions/cm^2 leads to the nano-patterning of the TiO_2 surfaces (fig. 5.1(b,c)). Such spontaneous formation of self organized nanoscale patterns is controlled by the competition of erosive and smoothening processes that undergo on the surface upon irradiation [11]. Preferential sputtering of oxygen atoms from TiO_2 surfaces, as discussed below, also plays a crucial role in the formation of these nano-patterns. After an irradiation with 6.0×10^{15} ions/cm^2, elliptical shaped nanostructures (NS) are noticed on the surface. These can be distinctly observed in the high resolution 3-dimensional image (fig. 5.1(b)).

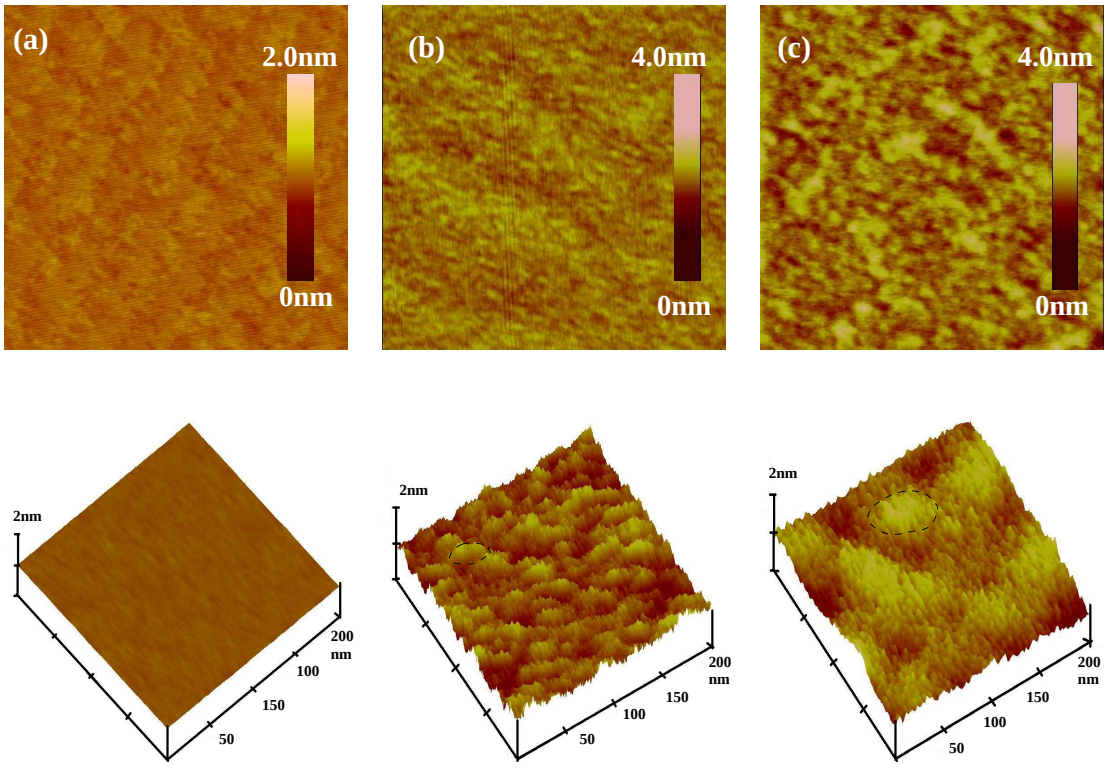

Figure 5.1: Top: 2-dimensional AFM images (a) ($1.5\mu m \times 1.5\mu m$) of Pristine rutile TiO_2(110) and after ion irradiation with fluences of (b)(500 nm × 500 nm) 6×10^{15} and (c) (500 $nm \times 500$ nm) 1.8×10^{16} $ions/cm^2$. Bottom: 3-dimensional high resolution AFM images from 200 $nm \times 200$ nm regions from samples same as above. A representative nanostructure is marked by (----) ellipse at both irradiation fluences.

Figure 5.2(a) displays distributions of the major (L1) and minor (L2) axes for these nanostructures with average values of $\langle L1\rangle =$ 29 nm and $\langle L2\rangle =$ 13 nm. These nanostructures thus have a high eccentricity of 0.89. Furthermore, the height (h) distribution of NS in fig. 5.2 displays an average $\langle h\rangle$ of only 0.19 nm indicating that these NS are essentially 2-dimensional in nature. After irradiation with the fluence of 1.8×10^{16} ions/cm^2 also, the nanostructures appear 2-dimensional oblong- shaped with $\langle L1\rangle$ and $\langle L2\rangle$ of 57 and 26 nm, respectively(fig. 5.2(b), table 5.1). Though nanostructures have enlarged along

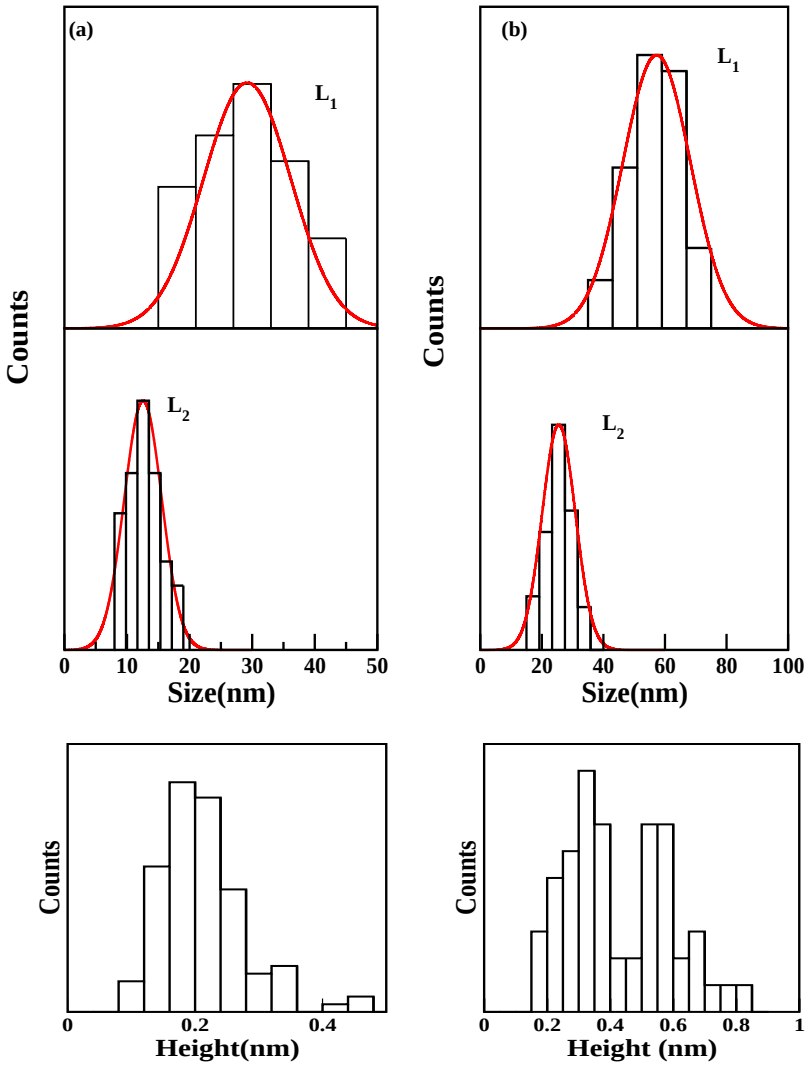

Figure 5.2: The major axis (L1), minor axis (L2) and height (h) distributions of nanostructures on $TiO_2(110)$ surfaces created after irradiation with fluences of (a) 6×10^{15} and (b) 1.8×10^{16} $ions/cm^2$.

both the axes at this stage, surprisingly, their eccentricity remains same as 0.89. The rms roughness of the surfaces (w) is observed to increase with irradiation (table 5.1). The height distribution of NS indicates a bimodal behavior, with large number NS of $\langle h \rangle$ at 0.33 nm. The distribution also displays a tailing behaviour with the highest NS of about 0.8 nm.

Table 5.1: Results from AFM analysis

sample	w(nm)	$\langle h \rangle$(nm)	$\langle L1 \rangle$(nm)	$\langle L2 \rangle$(nm)	eccentricity
pristine	0.096	–	–	–	–
6.0×10^{15} ions/cm^2	0.128	0.19	29	13	0.89
1.8×10^{16} ions/cm^2	0.206	0.33	57	26	0.89
1.5×10^{19} ions/cm^2	2.520	2.45	55	38	0.72

Height-height correlation functions (HHCF) have been evaluated using Eq. (5.3) for all possible pair of points in the AFM images. HHCF for the pristine and ion irradiated TiO_2 surfaces are presented in fig. 5.3 and show, consistent with the behavior predicted by Eq. (5.4), a power law behavior at small r

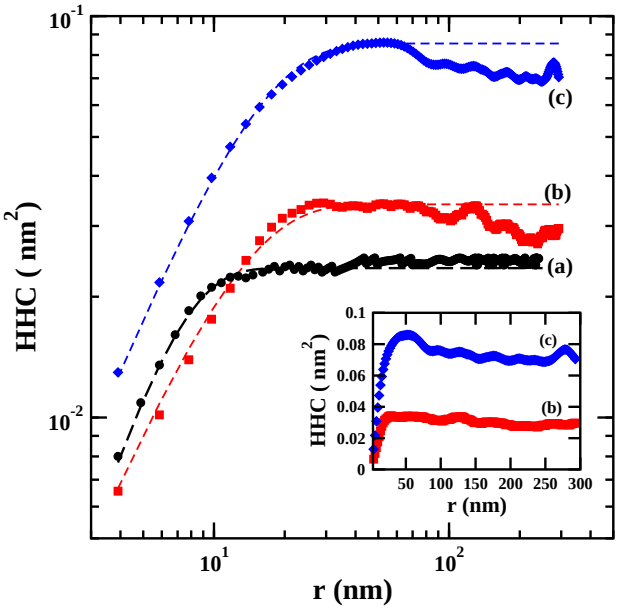

Figure 5.3: Height Height correlation function (HHCF) for (a) Pristine rutile TiO_2 and after ion irradiation with fluences of (b) $6{\times}10^{15}$ and (c) $1.8{\times}10^{16}$ $ions/cm^2$. Inset shows oscillations in linear scale.

A generic function of the form $\frac{\sigma^2}{2}\left(1\text{-}\exp(-(r/\xi)^{2H}\right)$ has been proposed to describe HHCF [19]. It has been utilized here to evaluate the modifications

in rms roughness σ, correlation length ξ and roughness exponent H upon ion irradiation. The surface rms roughness (σ) values obtained here (in table 5.2) reflect similar trends to roughness (w) from the AFM images (table 5.1).

Table 5.2: HHCF results

sample	σ(nm) ($\pm$0.003)	ξ(nm) ($\pm$0.05)	H ($\pm$0.01)
pristine	0.108	6.41	0.93
6.0×10^{15} ions/cm^2	0.130	11.63	0.69
1.8×10^{16} ions/cm^2	0.206	13.84	0.72
1.5×10^{19} ions/cm^2	2.420	22.68	0.90

Surface roughness is small for the pristine but increases upon irradiation. The correlation length, ξ, represents the distance within which the surface fluctuations are correlated but beyond which they are un-correlated. Pristine surface being flat has small ξ, increase in ξ after irradiation from 11.63 nm (at 6.0×10^{15} ions/cm^2) to 13.84 nm (at 1.8×10^{16} ions/cm^2) is related to the presence of nanostructures, created after irradiation, which become bigger with fluence (fig. 5.1,5.2). Though ξ reflects the long ranged correlations, roughness exponent H is related to the short wavelength roughness [13]. Surfaces with $0.5 < H < 1$ are defined as self affine and exhibit many unique properties considered fundamental for understanding the evolving surfaces [11, 12]. Pristine surfaces show a high H = 0.93 which decreases to 0.69 after irradiation with 6.0×10^{15} ions/cm^2. A larger value of H indicates a smoother surface in short range, while a smaller value corresponds to a more jagged local surface morphology [11, 12]. Thus, though the pristine surface is very smooth (H being very close to 1) at short lengths as expected, after irradiation the surface becomes more spiky or jagged at small scales. This is also reflected by the 3-dimensional AFM image (fig. 5.1(b)). With further irradiation of 1.8×10^{16} ions/cm^2, H increases to 0.72. Higher H and higher ξ at 1.8×10^{16} ions/cm^2 compared to the lower fluence of

6.0×10^{15} ions/cm^2, reveal that though the surface becomes smoother at small length scales (higher H), the region of correlations or fluctuations also becomes wider (higher ξ). For $r \geq \xi$, periodic modulations are also observed in HHCF (inset fig. 5.3). Presence of nanostructures on the surface produce these oscillating features [20]. The wavelength of the oscillating function reflects average separation between nanostructures i.e. the long range quasi-periodic nature [21] of the surface. The average wavelengths is nearly 70 and 100 nm for fluences of 6.0×10^{15} and 1.8×10^{16} ions/cm^2, respectively.

AFM images were also utilized to obtain 1d-iso PSD plots using Eq. (5.5). The range of frequencies ν ($\kappa = 2\pi\nu$) investigated by this method fall between $1/L$ (L being the image scan size) and the Nyquist frequency $N/2L$ (N being the number of pixels of the image). Fig. 5.4 displays the PSD for pristine and ion irradiated surfaces as a function of spatial wave vector κ. The low frequency plateau is related to the un-correlated white noise spectrum and is followed by a power law decaying behavior at high frequencies which reflect the spatial correlations in the system. Specific frequencies where different regions intersect or high intensity features appear correspond to quasi periodicity in the system given by corresponding correlation lengths. The power law behavior at high frequencies is important in describing the surface evolution process through the exponent γ with the relation of form [22]:

$$PSD \sim \kappa^{-\gamma} \tag{5.6}$$

Ion irradiated surfaces display γ of 2.3 and 2.5 at the fluences of 6.0×10^{15} ions/cm^2 and 1.8×10^{16} ions/cm^2, respectively. γ provides a signature of the evolutionary process on the surface. Knock off phenomenon is predominantly expected to control the surface-evolution at $\gamma = 2$ and bulk diffusion is most significant at $\gamma = 3$ [23]. Thus the γ values obtained here (between 2 and 3) suggest that for the evolution of ion irradiated TiO_2 sur-

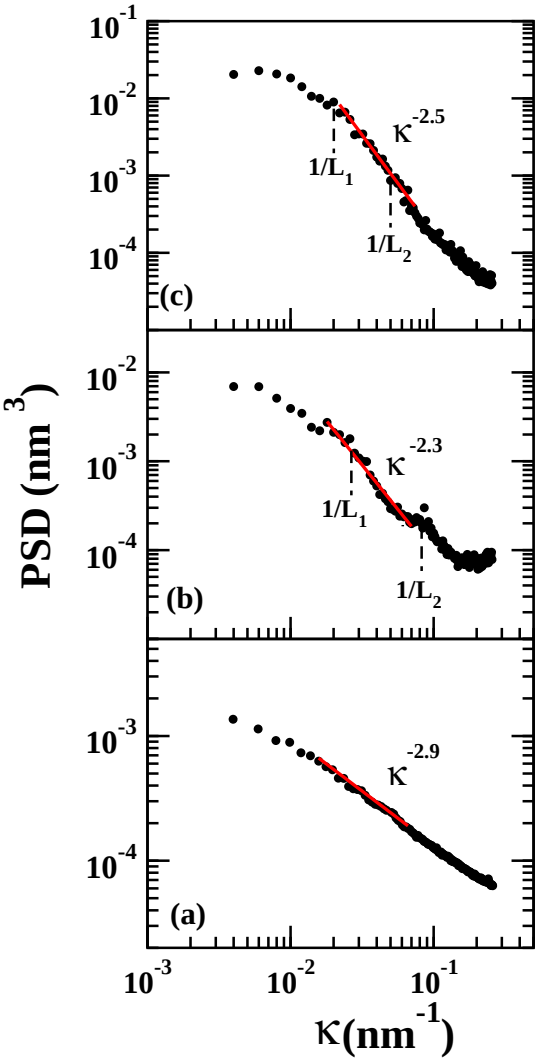

Figure 5.4: PSD for (a) Pristine rutile TiO_2 and after ion irradiation with fluences of (b) 6×10^{15} and (c) 1.8×10^{16} $ions/cm^2$.

faces both sputtering caused by erosion as well as diffusive processes are important, latter becoming more important at higher fluence. Roughness exponent H can also be evaluated using exponent γ ($H = \frac{\gamma-d}{2}$, with d being 1 for one-dimensional PSD function) [14], and is found (table 5.3) to be very similar to that obtained by HHCF analysis (table 5.2) confirming the results.

After irradiation of 6.0×10^{15} ions/cm^2, PSD in fig. 5.4(b) displays two

Table 5.3: PSD results

sample	γ ($\pm$0.1)	H ($\pm$0.01)	L1=$\frac{1}{\kappa_1}$(nm)	L2=$\frac{1}{\kappa_2}$(nm)
pristine	2.9	0.93	–	–
6.0×10^{15} ions/cm^2	2.3	0.65	33.3	12.5
1.8×10^{16} ions/cm^2	2.5	0.79	52.6	23.2
1.5×10^{19} ions/cm^2	2.8	0.90	55.5	34.4

kinks indicating two correlation lengths of 33.3 nm (at κ_1= 0.030 nm^{-1}) and 12.5 nm (at κ_2= .080 nm^{-1}). These interestingly correspond to the major (L1) and minor (L2) axes, respectively (labeled $\kappa_1 = 1/L1$ and $\kappa_2 = 1/L2$ in fig. 5.4(b)), of the elliptical nanostructures as seen in AFM images (fig 5.1, 5.2). After the fluence of 1.8×10^{16} ions/cm^2 also two kink sites reflecting the correlations lengths, L1 and L2, of nanostructure are observed (table 5.3) and are similar to those calculated from AFM images (table 5.1).

The results from the TiO_2 sample irradiated at the highest fluence of 1.5×10^{19} ions/cm^2 are presented in figure 5.5. The nanostructures produced here are much bigger and significantly (30 - 60 times) higher than observed at lower fluences indicating that these NS are no more 2-dimensional type. This is reflected by much higher data-scale associated with 2-dimensional and high resolution 3-dimensional AFM images (fig. 5.5(a,b)). The rms roughness is also much higher (table 5.1) than at lower fluences. With $\langle L1 \rangle$, and $\langle L2 \rangle$ of 55 and 38 nm, respectively, NS are still oblong-shaped but their eccentricity has become much smaller (0.72) indicating that NS are of less elliptical nature (table 5.1 and fig. 5.5(c)).

For the fluence 6×10^{15} $ions/cm^2$ (with L1 =29 nm and L2 = 13 nm) L1/L2 = 2.23, for $1.8 \times 10^{16} ions/cm^2$ (with L1 =57 nm and L2 = 26 nm) L1/L2 =2.19 and for $1.5 \times 10^{19} ions/cm^2$ (with L1 =55 nm and L2 =38 nm) L1/L2 = 1.4 (see table 5.1 and figs. 5.2, 5.5). So for lower fluences (6×10^{15} and 1.8×10^{16} $ions/cm^2$) L1/L2 is nearly 2.2 whereas for the highest flu-

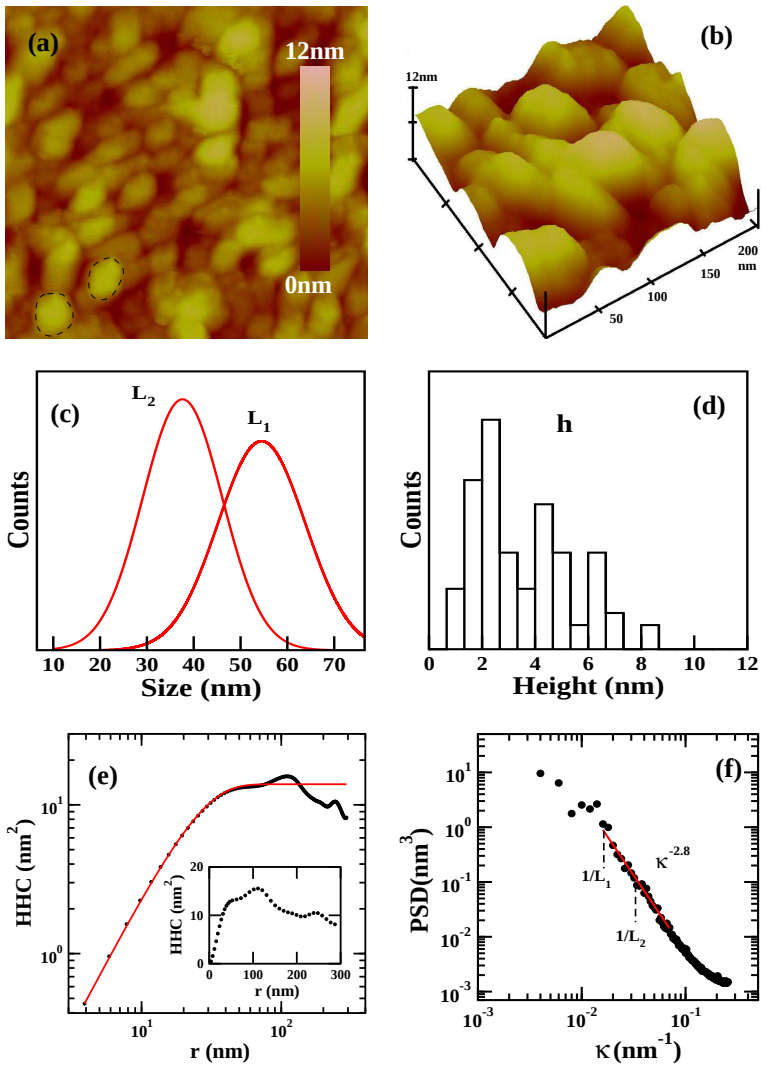

Figure 5.5: Results after irradiation of rutile $TiO_2(110)$ with $1{\times}10^{19}$ $ions/cm^2$: (a) 2-dimensional AFM image from 500 $nm \times 500$ nm region, two representative nanostructures are marked by (----) ellipses (b) high resolution 3-dimensional AFM image from 200 $nm \times 200$ nm region (c) major axis (L1) and minor axis (L2) distributions for nanostructures (d) height, h, distribution of nanostructures (e) height-height correlation function (HHCF), inset shows oscillations in linear scale, and (f) power spectral density (PSD) from the surface.

ence it decreases to 1.4. This suggests that L1 and L2 have become more similar at the highest fluence. Eccentricity (e) defined as $\sqrt{1-(L2/L1)^2}$,

with L1 being the length of major axis and L2 being the length of minor axis, gives a more rigorous definition. For a circle e=0 (L1=L2) whereas for an ellipse $0 < e < 1$ ($L2 < L1$). We have calculated eccentricity and at low fluences (6×10^{15} and 1.8×10^{16} $ions/cm^2$) eccentricity is found to be 0.89, suggesting nanostructures to be of elliptical nature (table 5.1). At the highest fluence (1.5×10^{19} $ions/cm^2$) however eccentricity reduces to 0.72 indicating nanostructures to be becoming less elliptical (table 5.1). However, they are not completely circle (as for complete circle e=0). Similar shape transformation of nanostructures, from being more elliptical to less elliptical, have been observed earlier also [24] by ion irradiation of silicon surface. The height distribution, however, still displays a tailing nature with a large number of NS at $\langle h \rangle$ of 2.45 nm and highest NS of nearly 9 nm (table 5.1 and fig. 5.5(d)). Analysis via HHCF indicates a very high surface roughness (table 5.2), similar to that by AFM results (table 5.1). A high H=0.9 and highest ξ are also observed at this fluence (table 5.2, fig. 5.5e). The former indicates a smoother, or less jagged, surface at the small length scales due to the presence of large nanostructures. Large ξ is due to correlations extending in bigger regions, again due to these bigger NS. Moreover, oscillations are also observed in HHCF for $r \geq \xi$ (similar to fig. 5.3). The wavelength of modulations ($\sim$ 115 nm) provides an approximate separation between the nanostructures. γ of 2.8 (fig. 5.5(f)) indicates the diffusion is possibly becoming more significant at this stage than at lower fluences. This can also contribute to the increase in correlation length ξ and smoothening at lower length scales. PSD, again displays two kink sites (marked as $\frac{1}{L1}$ and $\frac{1}{L2}$) and reflect the inverse of the major and minor axes of nanostructures (table 5.3, fig. 5.5(f)).

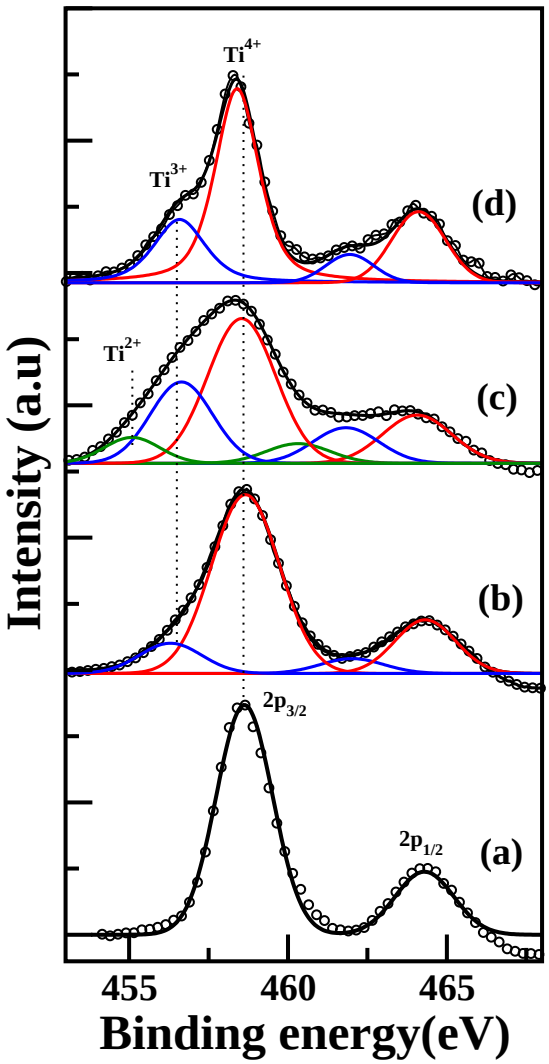

Figure 5.6: Ti(2p) XPS core level spectra for (a) Pristine TiO_2 and after ion irradiation with fluences of (b) 6×10^{15}, (c) 1.8×10^{16} and (d) 1×10^{19} ions/cm^2. Features related to Ti^{4+}, Ti^{3+} and Ti^{2+} are marked.

Ti(2p) core level XPS spectra from pristine and ion irradiated TiO_2 are presented in fig. 5.6. The spectrum from the pristine can be resolved into $2p_{3/2}$ and $2p_{1/2}$ spin orbit components, respectively, at the binding energies of 458.6 and 464.3 eV due to the Ti^{4+} states [25]. After ion irradiation at the fluence of 6×10^{15} ions/cm^2, both these features display another feature

at the lower BE side (fig. 5.6(b)) reflecting the formation of Ti^{3+} oxygen vacancy states [26]. This occurs due to the preferential sputtering of low mass oxygen atoms from the TiO_2 surface upon ion irradiation. During this process, 2p-electrons from oxygen get transferred to the empty 3d orbitals of the neighboring Ti atoms on the surface and lead to the formation of two Ti^{3+} oxygen vacancy sites. These oxygen vacancy sites reveal metal rich, Ti states, which become the nucleation sites during creation of nanostructures [2] observed in fig. 5.1. XPS technique is very surface sensitive and the photo-electron intensity is primarily from top 1 nm of TiO_2 surface [6]. Under this scenario, with $\langle h \rangle$ of NS being only 0.19 nm at this stage, XPS is predominantly reflecting the results from NS and top surface. Similar situation is observed after the fluence of 1.8×10^{16} ions/cm^2. However, another lower BE feature related to Ti^{2+} oxygen vacancy state [6] is also observed (fig. 5.6(c)). At the highest fluence of 1.5×10^{19} ions/cm^2, NS are much higher in size ($\langle h \rangle = 2.45$ nm) and XPS results show presence of Ti^{3+} oxygen vacancy states from nanostructures, indicating them to be Ti rich.

5.4 Conclusion

In conclusion, the present chapter investigates the shape transformation of nanostructures and scaling studies of low energy ion irradiated TiO_2 surfaces. The ion irradiation leads to the preferential sputtering of oxygen ions and consequently creates Ti^{3+} vacancy sites on the surface. With this process, Ti-rich zones develop on the surface promoting the formation of nanostructures. These nanostructures demonstrate a shape transition from being more elliptical at low fluence to becoming less elliptical at higher fluences. The scaling properties of these surfaces have been investigated by Height -height correlation functions (HHCF) as well as power spectral density (PSD) function and they together reveal, via roughness exponent (H) and γ investigations, that

with increasing fluence the surfaces are becoming less jagged at small length scales due to the increased diffusion. Furthermore, regions with correlated fluctuations are widening as demonstrated by increase in ξ . Both these observations can be attributed to the enlarging nanostructures.

This chapter discussed the chemical composition, scaling properties and roughening behavior of the self assembled nanostructures created on ion irradiated TiO_2 surfaces. The interactions of DNA with ion irradiated and UV beam modified TiO_2 surfaces are presented in chapter 6.

Bibliography

[1] S. Majumder, I. Mishra, U. Subudhi, , Shikha Varma, Appl. Phy. Lett. **103**, 063103 (2013).

[2] S. Majumder, D. Paramanik, V. Solanki, B. P. Bag, Shikha Varma, Appl. Phys. Lett. **98**, 053105 (2011).

[3] Jina Choi, H. Park, M. R. Hoffmann,. J. Phys. Chem. C. **114**, 783 (2010).

[4] F. Dong, W. Zhao, Zu. Wu, Nanotechnology. **19**, 365607 (2008).

[5] S. Facsko, T. Dekorsy, C. Koerdt, C. Trappe, H. Kurz, A. Vogt, H. L. Hartnagel, Science. **285**, 1551 (1999).

[6] V. Solanki, S. Majumder, I. Mishra, P. Dash, C. Singh, D. Kanjilal, S. Varma, J. Appl. Phys. **115**, 124306 (2014).

[7] M. Kolmer, A. A. Zebari, M. Goryl, F. Buatier de Mongeot, F. Zasada, W. Piskorz, P. Pietrzyk, Z. Sojka, F. Kork and M. Szymonski, Phys. Rev. B **88**, 195427 (2013).

[8] E. Cho, S. Han, H. S. Ahn, K. R. Lee, S. K. Kim, and C. S. Hwang, Phys. Rev. B, **73**, 193202 (2006).

[9] Shalik. R. Joshi, Trilochan Bagarti, Shikha Varma, Surf. Sci. **641**, 170 (2013).

[10] R. M. Bradley, J. M. E Harper, J. Vac. Sci. Technol. A. **6**, 2390 (1988).

[11] A .L. Barabsi, H. E. Stanley, *Fractal Concepts in Surface Growth*, Cambridge University Press, (1995).

[12] F. Family, T. Vicsek , *Dynamics of fractal Surface*, World Scientific, Singapore, (1991).

[13] C. Yang, U. Tartaglino,B. N. J. Persson, Phys. Rev. Lett. **97**, 116103 (2006).

[14] F. Biscarini, P. Samori, O. Greco, Zamboni, R. Phys. Rev. Lett. **78**, 2389(1997).

[15] Jean Bennett, Lars Mattsson, *Introduction to surface roughness and scattering*, Optical Society of America , Washington DC, (1999).

[16] R. Petri, P. Brault, O. Vatel, D. Henry, E. Andre, P. Dumas, F. Salvan, J. Appl. Phys. **75**, 7498 (1994).

[17] J. P. Singh, R. Singh, N. C. Mishra, D. Kanjilal, V. Ganeshan, J. Appl .Phys. **90**, 5968 (2001).

[18] Stefan Fischer, W. Andreas. Munz, Klaus Dieter Schierbaum, Wolfgang Gopel, J. Vac. Sci. Tech. B. **14** , 961 (1996).

[19] K. Vanormelingen, B. Degroote, A. J. Vantomme, Vac. Sci. Tech. B. **24**, 725 (2006).

[20] E. Gogolides, C. Boukouras, G. Kokkoris, O.Brani, A. Tserepi, and V.Constantoudis, Micro. Eng. **73**, 312 (2004).

[21] Evolution of Thin Film Morphology-Modelling and Simulation, by M. Pelliccione and T. Lu, *Springer Series in Materials Science*, Eds. R. Hull, R. M. Osgood, Jr. J. Parisi, H.Warlimont (2008).

[22] E. A. Eklund, E. J. Snyder, R. S. Williams, Surf. Sci. **285**, 157 (1993).

[23] Tong, M. William, Williams. R. Stanley. Annu. Rev. Phys. Chem. **1994**, 45, 401-438.

[24] Soma Dey, Dipak Paramanik, V. Ganesan, S. Varma, Appl. Surf. sci., **253**, 1116, (2006).

[25] C. D. Wanger, W. M. Riggs, L. E. Davis, J. F. Moulders, G. E. Mullenberg, *Handbook of X-ray Photoelectron Spectroscopy*, Perkin Elmer Corporation, Eden, Prairie , MN, 1979.

[26] M. A. Khan, A. Kotani, J. C. Parlebas, J. Phys. Condens. Matter. **3**, 1763 (1991).

Chapter 6

Interaction of Branched DNA with UV irradiated and Ion beam patterned $TiO_2(110)$ surfaces

6.1 Introduction

The Deoxyribonucleic acid popularly known as "DNA" is the stiffest polymer [1], and interestingly it is one of the longest biological molecule in nature. This makes the DNA a flexible chain at large distance, but very stiff at short scale [2]. In the living organisms the space available for the DNA in vivo is much smaller in comparison to the space it would occupy in the case of free diffusion. Thus to cope up with such high volume constraints, the DNA has a characteristic property to pack itself in a very tiny volume through manipulating the steric environment using the ions. DNA condensation is a process of compacting DNA molecules in vitro or in vivo. Condensation of DNA is one of the most lively areas of research, as it represents a process by which genetic material is packed and protected. The process presents intriguing problems of phase transition, liquid crystal behavior and polyelectrolytes. Condensed DNA structure have potential application in medicine

and biotechnology for gene therapy and engineering of biosensors. DNA condensation and decondensation are involved in gene expression, chromosomal changes during cell cycle and it also provides a promising means whereby DNA containing genes of therapeutic interest can be prepared for transfer from solution to target cells for gene therapy applications. As the DNA is a highly charged polyelectrolyte, packing the DNA into small volumes requires overcoming of enormous columbic barrier. The energetic barriers to such tight packaging, the loss of configurational entropy of the long DNA molecule, the tight bending of the stiff double helix, the electrostatic repulsion of the negatively charged DNA phosphates requires organisms to spend considerable metabolic energy. This energy is required to accomplish task like collapse or condensation of DNA in the test tube [3], or on surface [4] upon addition of a low concentration of multivalent cation to low ionic strength aqueous buffer.

DNA molecules condense in many different forms. Some of the commonly observed forms are toroids [5], rods [6], flower like structure [4] and globular structure [7]. The dimensions and morphology of condensed DNA particles depend greatly on the size of the DNA and its steric conditions. Widom and Baldwin [8] have discovered that DNA fragments that are shorter than about 400 base pairs will not condense into orderly, discrete globule or higher order structures as the attractive interaction per base pair is very small. Hence hundreds of base pairs must interact simultaneously for condensation.

DNA condensation is an example of a polymer's coil to globule transition. The general features of the coil-globule transition like topology of the condensed DNA states are mostly determined by the polymer and solution properties, such as DNA length, concentration, solution temperature and

pH, etc., and not by the DNA sequence. DNA sequence determines the local interaction and recognition between the double helices in the condensed DNA. Due to the stiffness of DNA polymer, the coil-globule transition is very abrupt in nature. The high stiffness of the DNA double helix is due to sugar-phosphate backbone with stacked base pairs and charged phosphates which repel each other and resist DNA bending. The morphology of the condensed DNA molecules is most commonly that of a compact, orderly toroid which is strongly reminiscent structure of intraphage DNA lysed from virus capsid. Grosberg and Zhestkov [9] explained the reason for DNA condensed forms to be mostly of torioidal nature. The total free energy of DNA is the sum of compressive (because of external osmotic pressure or poor solvent quality), repulsive (due to the excluded volume of the DNA, and high asymmetry) and elastic contributions (from bending and other conformational entropy terms free energy). Importance of these free energy terms also depend on polymer chain length. Phase diagram shows that short DNA molecules will form toroids, while very long molecules will form spherical globules. Bigger compressive forces prefer spherical globules without an inner hole, while greater stiffness and excluded volume will favor toroids. Rodlike particles are sometimes also seen, but rarely in high proportion unless the solvent or the condensing agent is nonpolar, as the nonpolar environment lowers the free energy of exposed heterocyclic bases, favoring sharp local kinking.

DNA condensation formation has been shown to be a nucleation growth phenomenon [3, 10].

1. The first step in toroid formation is the spontaneous formation of a nucleation loop.

2. This loop acts as the nucleation site for condensation on which the remainder of the DNA polymer condenses to form a proto-toroid.

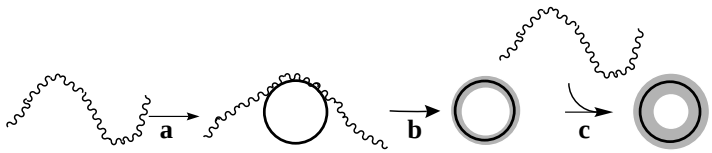

Figure 6.1: Toroid nucleation and growth with equal outward and inward growth from the nucleation loop. The black circle on the proto-toroid (second from right) and the fully grown toroid (right) illustrates the size of the nucleation loop.

3. The proto-toroid grows equally inward and outward by the addition of free DNA polymers from the solution. The black circle on the proto-toroid (structure second from right) and the fully grown toroid (rightmost structure) illustrate the size of the nucleation loop

Condensation of DNA on various surfaces such as hydrophobic, hydrophilic, moderately hydrophilic, in the presence of monovalent, divalent and trivalent cations have been studied for long [11–14]. Substrate surface energy mediated DNA/DNA interaction leads to the formation of a variety of structures. It is observed that DNA could condense on hydrophobic surface, even in the absence of multivalent cations. DNA forms larger condensates when condensation occurs on the sample surface than when condensation occurs in solution. For example, DNA on mica condenses into distinct toroids when protamine is added [15]. When DNA and protamine are preincubated in a test tube and deposited onto mica, a network of DNA, with a few thin toroids in it, occurs. Similarly, mobile cationic silanes on a silicon surface condensate DNA into distinct toroids whose size depends on the length of the DNA [16]. Interestingly when silanes in solution and DNA are preincubated in a test tube, looped structures that include flower and sausage shapes form. As noted by various studies, nanoparticle structures are formed with DNA, depending on whether the condensation process is performed in solution or on a solid surface [15,16]. Metal oxides have been used for a range of biological

applications, such as for the detection of DNA [17]. Among the metal oxides, TiO_2 has been of great interest because it exhibits high stability over a wide range of pH values and has good optical [18] and electrical properties, making it of interest for applications in sensing and renewable energy. TiO_2 is also of importance as a naturally forming surface coating on Ti and Ti alloys that are widely used as implantable prosthetic devices [19]. Bonding of short biomolecules to the (oxidized) Ti surfaces can also be used to control how cells such as osteoblasts interact with the surface. The biocompatible nature of TiO_2 makes it one of the most suitable materials for application of binding of proteins, nucleic acids, antibodies and cell [20–24]. Studies describing the direct adsorption of DNA on rutile TiO_2 has been reported which highlights the relevance of surface chemical properties for adsorption [25]. Controllable changes in the surface properties such as topography, morphology and surface chemistry of TiO_2 play very important role in the interaction with bio molecules, which could have application in enhancement of bio-sensing and 3D cellular scaffolding.

Out of the other procedures for modifications of oxide surfaces and cleaning, UV light exposure is used for sterilization of surfaces which could be employed satisfactorily for photo-immobilization [26]. Irradiation of TiO_2 surfaces with UV light promote certain chemical changes, which are important for selective binding of molecules to the surface [27].

UV illumination of TiO_2

The underlying mechanism of surface modification by UV illumination of TiO_2 is the generation of e- h+ pairs. When irradiated with light, of energy ($h\nu$) equal or greater than band gap energy of TiO_2, electrons in the valence band can be excited to the conduction band and leave a positively charged electron vacancy (hole) in the valence band. As a result, free e_{CB} (elec-

trons) and positively charged holes h_{VB}, with strong reducing and oxidizing potentials, are generated. The process can be summarized below:

$$TiO_2 + h\nu \longrightarrow e_{CB} + h_{VB} \tag{6.1}$$

These electron and hole generated through UV irradiation will then recombine through releasing energy as heat. However if electrons and or holes migrate to the surface of the crystal, they participate in various oxidation or reduction reactions with molecules adsorbed to the surface, such as oxygen, water organic species etc.. When interacting with water molecule, the hydroxyl ions are formed or hydroxide ions are trapped in the holes.

$$H_2O + h^+_{VB} \longrightarrow \cdot OH + H^+ \tag{6.2}$$

$$OH + h_{VB} \longrightarrow \cdot OH \tag{6.3}$$

Ti^{4+} sites on the surface of TiO_2 crystal trap the conduction band electrons, which leads to the formation of reduced states of Ti^{3+}. The oxygen molecules adsorbed on the surface react with these Ti^{3+} sites and generate superoxide radicals O_2^-.

$$Ti^{4+} + e_{CB} \longrightarrow Ti^{3+} \tag{6.4}$$

$$Ti^{3+} + O_2 \longrightarrow Ti^{4+} + O_2^- \tag{6.5}$$

$$2O_2^- + 2H^+ \longrightarrow H_2O_2 + O_2 \tag{6.6}$$

$$\cdot OH + \cdot OH \longrightarrow H_2O_2 \tag{6.7}$$

$$O_2^- + H_2O_2 \longrightarrow \cdot OH + OH^- + O_2 \tag{6.8}$$

$$O_2^- + H^+ \longrightarrow \cdot OOH \tag{6.9}$$

$\cdot$OH , O_2^- and H_2O_2 are the key reactive oxygen species. It is known that the atomic co-ordinations at the TiO_2 surface differ from those in the bulk since

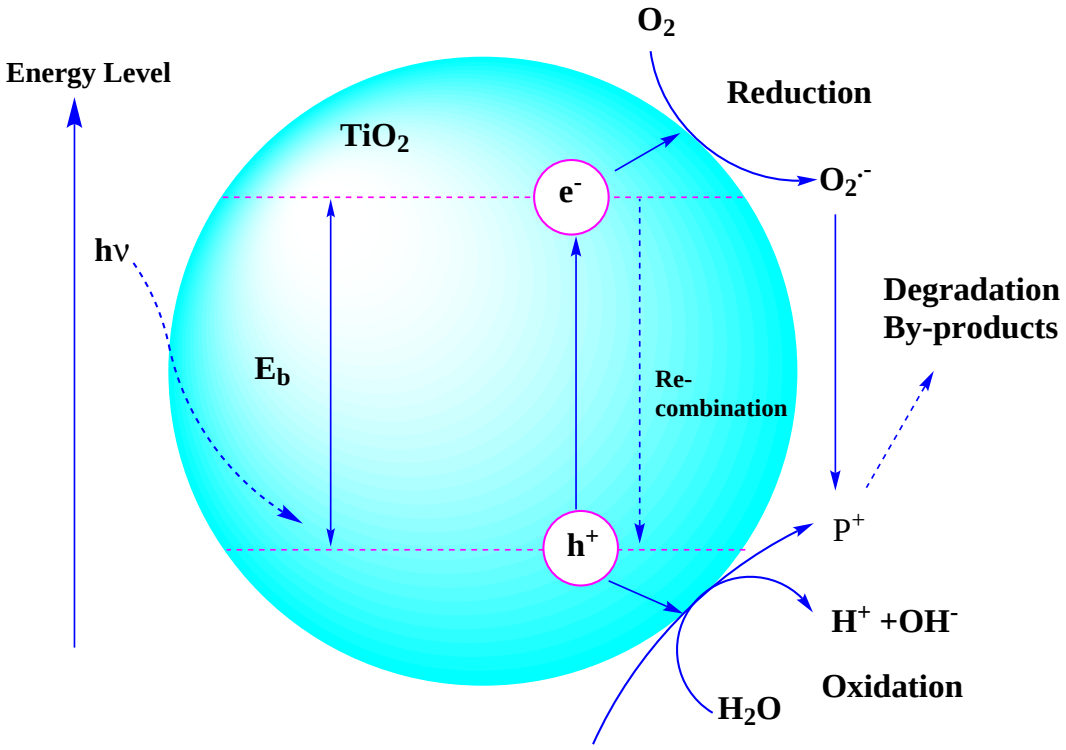

Figure 6.2: Schematic diagram of UV irradiated TiO_2 semiconductor.

the atom arrangements are truncated on the surface. The nanostructured TiO_2 generates five-coordinated Ti atoms and two-coordinated O atoms, which are more energetically reactive than the six-coordinated Ti and three-coordinated O atoms in the bulk. By UV illumination, oxygen vacancies are most likely created at the two-coordinated bridging sites, resulting in the conversion of the corresponding Ti^{4+}sites to Ti^{3+} sites [28], which are favorable for dissociative water molecules adsorption [29] on the surface. These defects influence the affinity to chemisorbed water of their surrounding to the five-coordinated Ti sites and thus result in the formation of the hydrophilic domains. Hydrophilicity originates from the polar surface chemical functionalities i.e. Ti-OH, or because of under coordinated metal ions Ti^{3+}at the surface. The presence of such sites determines the bio-molecular adsorption.

It is known that the binding of organic molecules to mineral surfaces occurs via minimization of hydrophobic effects and optimization of covalent, ionic, hydrogen bonding and van der Waals interactions. Zhu [30] reported that DNA with P=O and C-O-P groups could be adsorbed onto the surface of TiO_2 by chemical adsorption. Oxygen based free radical such as superoxides anion i.e. $\cdot O_2^-$ and hydroxyl ions i.e. OH·, are the reactive oxygen species. Modification of DNA via OH· includes single strand DNA break, base modification and conformal changes. Nitrogenous bases preferentially react with OH· ions in comparison to the sugar moiety by 4-6 fold. The hydroxyl radical reacts with the DNA backbone, when initiated by hydrogen abstraction from deoxyribose carbon, this leads to the eventual denaturing or breakage and base release. OH· radical reacts with the various hydrogen atom or deoxyribose base in the following order $\grave{5}H > \grave{4}H > \grave{3}H \sim \grave{2}H \sim \grave{1}H$.

The hydroxyl radicals react with DNA bases by adding to the electron-rich, π bonds. These π bonds in the bases are located between C5-C6 of pyrimidines and N7-C8 in purines [31]. Upon addition of the hydroxyl radical, many stable products can be formed. Bases with exocyclic amino groups i.e. adenine and cytosine, have several potential binding modes to maximize surface interaction. These potential points of protonation, including ring nitrogen atoms and functional groups, can develop charges depending on the solution. These compounds have inner- or outer-sphere interactions with surface functional groups, $\equiv TiOH_2^+$,$\equiv TiO^-$, TiOH, or surface-adsorbed water.

The interactions of Cytosine (C), Adenine (A) with the surface of TiO_2 have contributions from electrostatic, van der Waals and hydrogen bonding [32]. It is also known that the bases coordinate with metal ions through various combinations of the ring nitrogen atoms and the exocyclic groups [33].

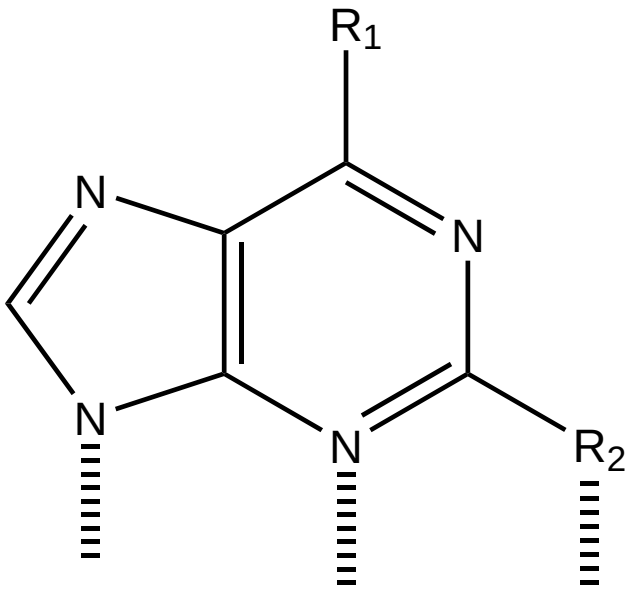

Figure 6.3: Potential binding reaction of Adenine (A) with mineral surface, where R1 is NH_2 and R2 is H.

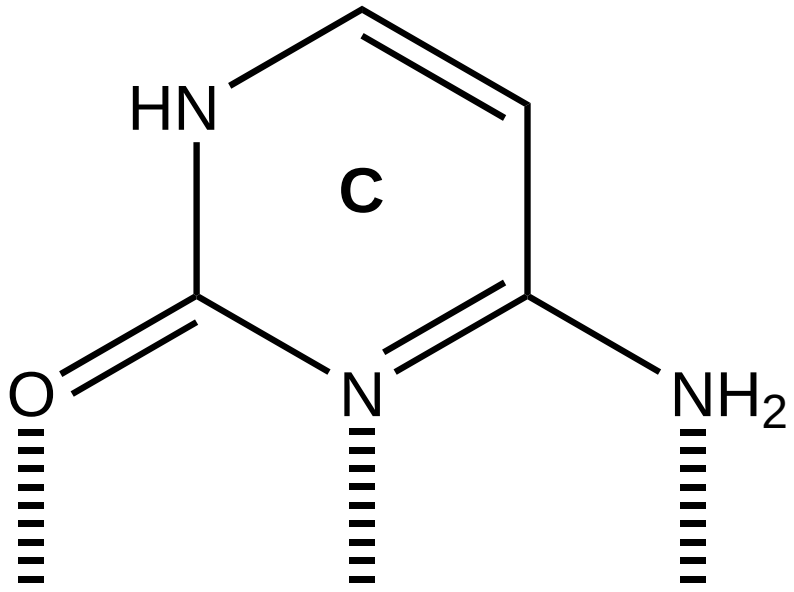

Figure 6.4: Potential binding reaction of Cytosine (C) with mineral surface.

The present chapter reports chemical as well as topographical changes on surface of rutile TiO_2 after UV illumination. Creation of reactive oxygen species which leads to formation of surface hydroxyl state i.e. Ti-OH and physically adsorbed water molecules are observed by AFM and XPS techniques. The irradiation modified as well as pristine surfaces are interacted with branched DNA, a DNA constructed in lab with the utilization of four oligonucleotide. Condensed structures of this DNA are seen on the pristine and irradiation modified surfaces. The interaction of surface states of $\equiv TiOH_2^+$, $\equiv TiO^-$, TiOH, or surface-adsorbed water with the nitrogens bases of DNA resulting in base type stacking reaction, and also interaction of phosphate backbone with the surface charges could be a possible mechanism for condensation of the DNA. The interaction of the branched DNA with Ar ion irradiated surfaces of TiO_2 is also reported in the present chapter. However instead of toriod condensed structures as observed on the UV irradiated surfaces, long elongated structures of DNA are observed on ion sputtered TiO_2.

6.2 Experiment

Single crystals of rutile TiO_2 (110) (commercially bought from macteck) were used as received, for all studies. A UV lamp (EiKO F15T8/BLB 18 inch, 15 watt tube, with a T-8 bulb and wavelength of 365 nm) was used for irradiation of the TiO_2 surfaces for 2, 5 and 10 minutes.

To study the effect of ion irradiation, the single crystal of TiO_2 were also irradiated with 3 keV Ar^+ at an incident angle of 15^o, from surface normal, at room temperature in a chamber with a base vacuum of 10^{-8} Torr at a fluence of 6.0×10^{15}ions/cm^2. The pristine as well as irradiated surfaces were interacted with the branched DNA. This branched DNA was synthesized by self assembly method utilizing four oligonucleotide derived from the genomic

sequences of Rattus Norvegicus. The sequence of each oligo used are as follows:-

1. Oligo 1 -5′-AGG ACG ATT TTC AGC ACG CGT TCC TCC AGC TTT TTG GAG TAA AGC T-3′, Molecular Weight (MW)-14,131.2, Transition temperature (T_m)-69C.

2. Oligo 2 -5′-CGA TGA ACT TTA GCT GGA GGA ACG CGT GCT GTT TGT AGA AGG CAA G-3′ MW-14,334.3, T_m-68.2C.

3. Oligo 3 -5′-CCT TCT ACT TTA CCA CGA GGG CCT GGC CAA GTT TGT TCA TCG CTT G-3′ MW-14,034.1, T_m-69.2C.

4. Oligo 4 -5′-GCT ACT GTT TTC TTG GCC AGG CCC TCG TGG TTT TCA TCT TCC GAT C-3′ MW-14,007.1, T_m-69.1C.

The self assembled fabrication of branched DNA has been discussed elsewhere [34]. In short, hybridizing portion of each oligo was derived from primers of different genes. Two sets of four oligos with 3′ or 5′ sticky ends in the loop were designed to self assemble for rigid or flexible monomeric structure. These consecutive oligos have nearly 50% complementary, hence self assembly between two oligos either forms internal bubble or external single stranded overhangs. 10 μg DNA were dissolved in 20μl stock buffer composed of 40 mM Tris, 20mM acetic acid, 2 mM EDTA, and 12.5 mM magnesium acetate at pH of 8, was diluted with ultra pure water to make the final concentration of 1 ng/μl. Typically, 10 μl of this solution was dropped on pristine as well as irradiation modified surfaces of TiO_2 and was incubated overnight. Post incubation and after DNA immobilization, the surfaces were washed off with Milli-Q water for 20 secs and the process were repeated few times to remove any residuals on the surface completely. The surface morphology prior and post immobilization of DNA on irradiated surfaces has been investigated using Scanning Probe Microscope (Bruker, Nanoscope V

Multimode), in tapping mode under ambient conditions. The vertical resolution of the scanner used is 0.01 nm. X-ray Photoelectron spectroscopy (XPS) measurements were performed using a VG microtek instrument with Mg K_α radiation (1256.6eV) source. A standard shirley type background was removed from all XPS spectra before analysis and C(1s) position (284.6 eV) has been utilized for charge correction.

6.3 Results and Discussions

Fig. 6.5(a) shows SPM image from pristine TiO_2 surface. It shows several steps, as expected [35], and has a rms roughness of 0.096 nm. Fig. 6.5(b,c,d) display the modifications of TiO_2 surfaces after their UV irradiation at 2, 5 and 10 min, respectively. Their rms roughness is shown in fig. 6.6. On the UV irradiated surfaces, a few (white) domains are observed. These reflect the adsorption of some water droplets on the surface. At the highest exposure time (fig. 6.5(d)) a hazy morphology further suggests formation of a weak water droplet layer.

Fig. 6.6 shows that UV illumination changes the rms roughness of the TiO_2 surfaces. The roughness increases upto the UV exposure of 5 min, but decreases for 10 min. The decrease may be related to the formation of the mild water layer at this stage. It has been shown earlier that once the water coverage becomes larger then 0.5, surface roughness gradually decreases [36].

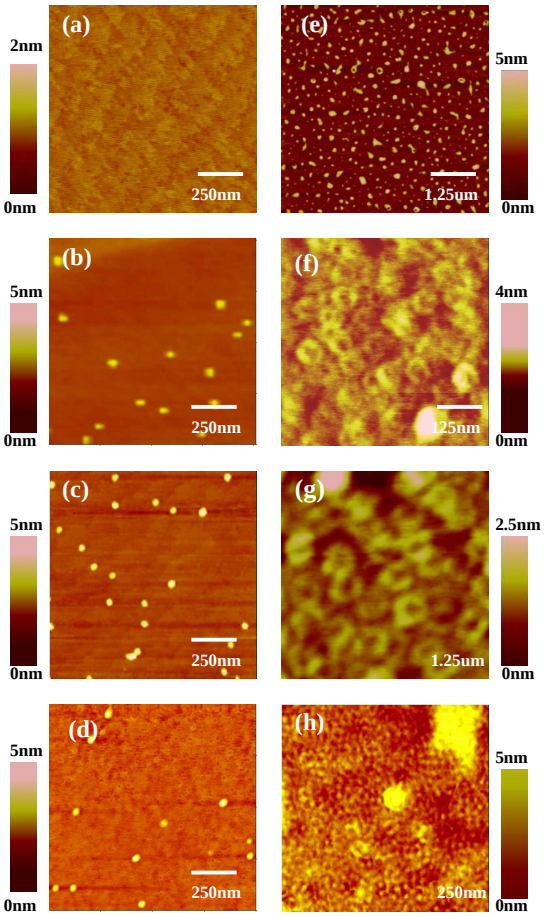

Figure 6.5: AFM images are shown in left panel for (a) unirradiated surface as well as after UV irradiation for (b) 2 mins (c) 5 mins (d) 10 mins. Right panel shows AFM images of corresponding surfaces after they are interacted with Branched DNA.

Creation of electron-hole pairs is a result of UV illumination of TiO_2. The process of photo-excitation competes with the process of recombination between excited electron- hole pair. When an electron is photo-excited from valence band to the conduction band it can diffuse to the surface leading to charge transfer to an adsorbed species or get trapped within the electron trap in the band gap [37]. If none of the processes occur within the excited electron's lifespan, deactivation of electron hole pair will occur with the release

of either heat or photons. A variety of defects can be created by thermal annealing at high temperature through electron bombardment. Oxygen vacancies are the primary defects states for the surface adsorption/desorption reactions. These oxygen vacancies can be created at either the bridging oxygen sites or at the planar oxygen sites. Bridging oxygen defects are created more easily because of lower atomic coordination. An enhanced surface reactivity is observed as a consequence of the oxygen vacancy defect formation.

The right panel of fig. 6.5 shows the corresponding surfaces after DNA interaction. Toroids as well as rods structures of DNA are observed when interacted with the pristine TiO_2 surface as seen in fig. 6.5(e). However only condensed toroidal structures of DNA are observed on the UV illuminated surfaces (fig. 6.5(f,g,h)). The size of these toroids appear to decrease for 2 mins UV irradiated surface in comparison to the pristine surface. For 5 mins illuminated surface the size of these toroids increases, however for the 10 mins illuminated surface a further decrease in the size of the toroidal condensed structure is observed. The size of toroidal structures increases on surfaces irradiated upto 5 min, where surface roughness is highest, but decreases on 10 min irradiated surfaces. These results suggest that size of toroids may be controlled by the surface roughness. The surface states on TiO_2 created due to UV irradiation induce globule like conformal transitions of DNA.

Fig. 6.6 shows the roughness plot of the pristine as well as UV irradiation modified surfaces. For UV illuminated surfaces the roughness of the surface initially increase for 2 and 5 mins of irradiation, however a decrease in roughness is observed after UV illumination of 10 mins. The roughness trend of these samples, post interaction, with branched DNA is also shown.

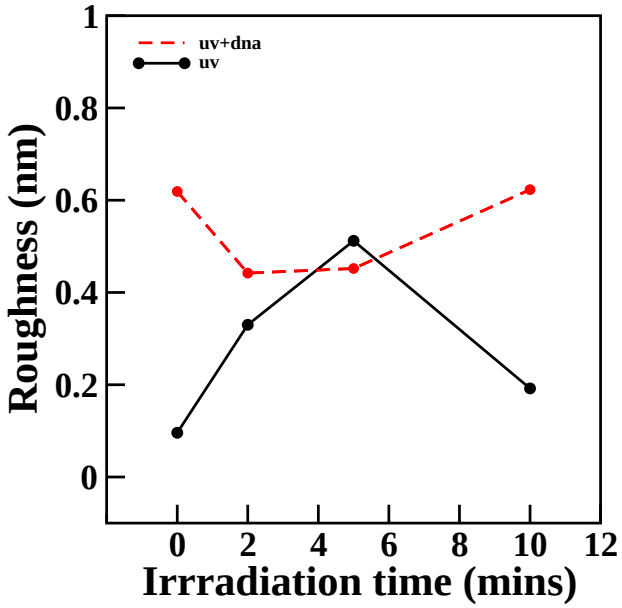

Figure 6.6: Roughness of TiO_2 surfaces for (a) unirradiated surface as well as after UV irradiation for (b) 2 mins (c) 5 mins (d) 10 mins is shown with a solid line, also the roughness of corresponding surfaces post interaction with branched DNA is shown as dashed line.

The roughness of the pristine surface after interaction with DNA increases to 0.619 nm. On interaction of DNA with UV illuminated surfaces the rms roughness changes and is observed to be 0.442, 0.452, and 0.632 nm for the 2, 5, 10 mins UV illumination, respectively.

The left panel of fig. 6.7 shows the zoomed AFM images of the toroidal condensed nanostructures of DNA on pristine as well as UV irradiated surfaces. The section analysis of the corresponding condensed structure is reported in the right panel. The section analysis show two peaks for each structure indicating that these structures are toroidal in nature. The peak to peak measurements of the DNA toroidal structures show that the size of these toroids is about 86 nm for the pristine surface. However the size of these toroids is about 43, 525, 55 nm on 2, 5, 10 mins UV illuminated surfaces

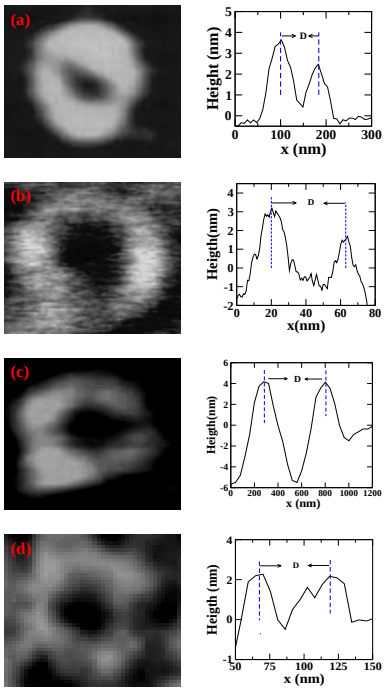

Figure 6.7: Zoomed AFM images of toroid DNA structures are shown in the left panel for DNA interacted with (a) unirradiated surface as well as with surfaces UV irradiated for (b) 2 mins (c) 5 mins (d) 10 mins. Right panel shows the section analysis for corresponding toroids.

respectively.

Fig. 6.8 shows the high resolution O(1s) spectra for the pristine as well as UV illuminated surfaces. Fitting for various states are also shown. The Gaussian fitting of the pristine spectrum shows that the O1s peak is composed of three subpeaks originating from lattice oxygen(O-Ti-O-) at 529.8 eV, Hydroxyl group (-Ti-OH) at 531.3 eV and adsorbed Oxygen (-Ti-O-C) at 532.8 eV [38]. The spectra from UV illuminated surfaces also show same subpeaks. However a shift towards lower binding energy is observed for O-Ti-O feature. O-Ti-O peak for 5 mins and 10 mins UV illuminated surfaces are

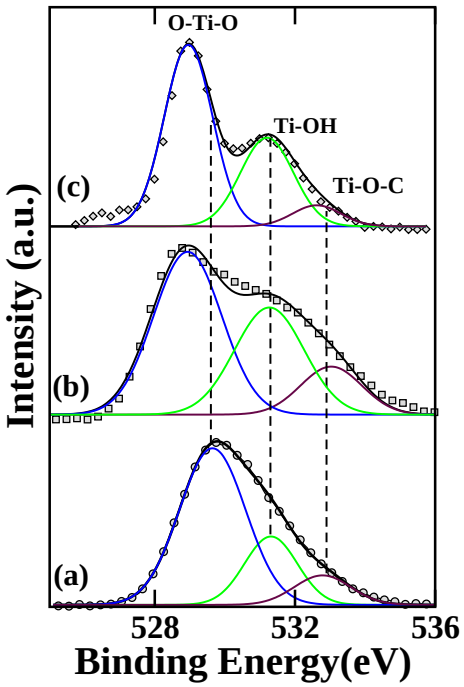

Figure 6.8: Before DNA interaction: XPS spectra of O (1s) region from (a) unirradiated surface as well as after UV irradiation for (b) 5 mins (c) 10 mins. Fittings for various states are shown.

positioned at 529.1 and 528.9 eV, respectively. A decrease in binding energy could be attributed to the creation of vacancy states due to UV illumination of the surface. Also an enhancement in the Ti-OH peak is observed after irradiation. UV illumination of TiO_2 crystal generates surface defects, which are accompanied by electronic charge transfer from oxygen to titanium. It creates holes and electrons at definite sites on the crystal surface. The photo generated holes produced in the bulk of the crystal, diffuse to the surface and are trapped at the lattice oxygen sites. The hole created due to UV illumination react with the adsorbed organics or water molecule to produce OH radicals. These holes also react with TiO_2 crystal, which leads to breaking of bond between titanium and oxygen by coordination of water molecules at the titanium sites. The coordinated water molecules release a photon for

charge compensation and then a new OH group forms, leading to increase in the OH group at the surface.

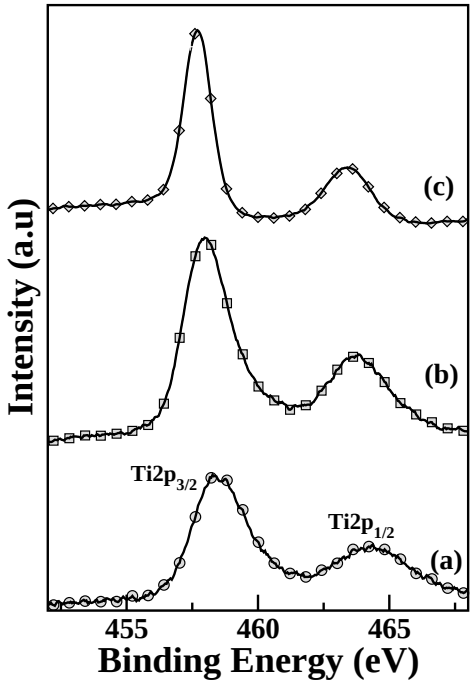

Figure 6.9: Before DNA interaction: XPS spectra of Ti (2p) region from (a) unirradiated surface as well as after UV irradiation of (b) 5 mins (c) 10 mins.

The high resolution Ti 2p spectra show two peaks due to spin-orbital coupling effect. Ti $2p_{3/2}$ at 458.8 eV and Ti $2p_{1/2}$ at 464.2 eV have been fitted by one Gaussian peak each (fig. 6.9(a)). However a shift towards lower binding energy in the spectra is observed for the 5 and 10 mins UV illuminated surfaces (fig. 6.9(b,c)), indicating creation of surface defects, which is accompanied by the electronic charge transfer from oxygen to titanium.

Fig. 6.10 shows the XPS spectra of O(1s) region from pristine as well as UV irradiated surfaces after interaction with the DNA. XPS spectra of uninteracted surfaces are shown for reference. A shift towards higher binding energy

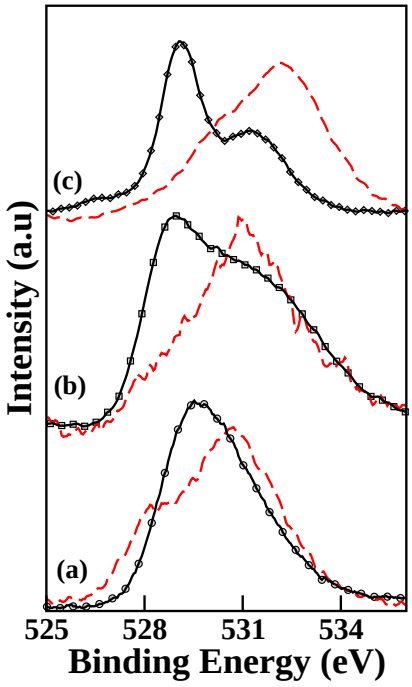

Figure 6.10: After DNA interaction: XPS spectra of O(1s) region for DNA interacted (red dashed lines) surfaces of (a) pristine and UV irradiated surface for (b) 5 mins (c) 10 mins. For reference, XPS spectra from un-reacted surfaces (black line) are also included.

in the spectra after interaction with DNA is observed for all the surfaces. This indicates a strong interaction of the DNA with the Ti-OH and Ti-O-C groups present on the surface of the TiO_2 crystal. It has been observed in earlier studies that the bases with exocyclic amino group i.e. A and C showed greater binding affinity, because of several potential binding modes for surface interaction. These compounds generally form the inner or outer sphere interaction with surface functional groups such as $TiOH_2^+$, TiO, TiOH or surface adsorbed water. Such kind of surface binding could lead to stacking -type interactions [39]. The phosphate at the DNA backbone is adsorbed on hydrated TiO_2 surfaces through a condensation process that forms Ti-O-PO_3H_2 groups. $H_2PO_4^-$, $H_2PO_4^{2-}$ can be adsorbed through an exchange reaction with

the basic hydroxyl groups given as: $TiOH + H_2PO_4^- = TiH_2PO^+ + OH^-$. Therefore, the bonding in these groups is of a transitional type between ionic and covalent [40].

XPS spectra of Ti (2p) region from the pristine and UV illuminated surfaces after interaction with DNA (red dashed lines) is presented in fig. 6.11. For reference the spectra of uninteracted surfaces from fig. 6.9 are also shown. The interaction of DNA with pristine TiO_2 surface causes a slight shift of Ti^{4+} feature towards lower binding energy, compared to the uninteracted surface (black line) as seen in fig. 6.11(a). A possible reason for such shift could be transfer of electrons from negatively charged phosphate backbone of the DNA to the surface. After interaction of DNA with 5 mins UV illuminated surface (fig. 6.11(b)), further shift towards lower binding energy in the Ti^{4+} component is observed, suggesting more transfer of electrons from DNA backbone to the surface. For UV illumination of 10 mins, after interaction of DNA a shift towards higher binding energy for the Ti^{4+} feature is seen (fig. 6.11(c)). A gain in electron by the surface from the DNA backbone can make the surface more Ti^{4+} in nature thus saturating the effect of the defect states created during UV irradiation. This could be a possible reason for the Ti feature to shift towards higher binding energy after interaction with the DNA.

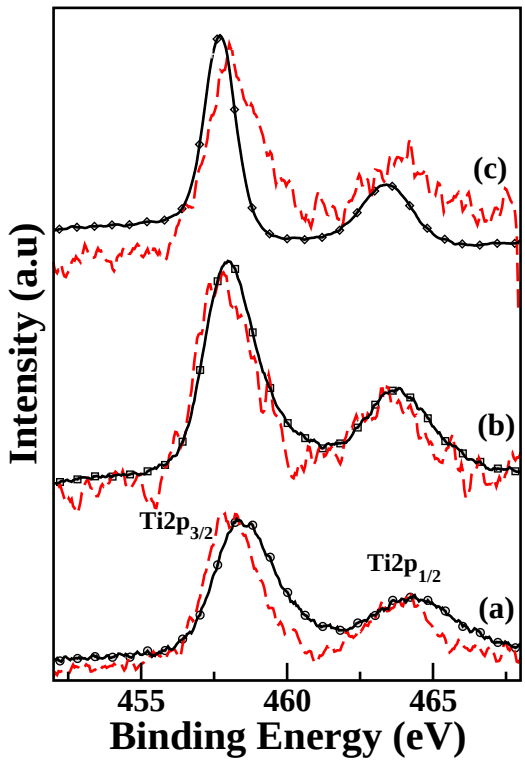

Figure 6.11: After DNA interaction: XPS spectra of Ti(2p) region for DNA interacted (red dashed lines) surfaces of (a) pristine and UV irradiated surface for (b) 5 mins (c) 10 mins. For reference, XPS spectra from un-reacted surfaces (black line) are also included.

The N(1s) XPS spectra for post-DNA interacted TiO_2 surfaces are presented in fig. 6.12. On pristine surface three features, representing amino ($-NH_2$), imine (-N=) and amine (-NH-) components, from DNA are noticed. Similar features have also observed in earlier studies [41]. After interaction of DNA with the UV irradiated surfaces no extra feature is observed. However, a shift towards higher binding energy for all the features of nitrogen is seen, supporting a strong interaction of the nitrogen bases of DNA with the surface states i.e.$TiOH_2^+$, TiO, TiOH. An enhancement in the peak intensity of amino and amine group is seen after the DNA is interacted with the UV illuminated surfaces. This suggests that the amino and amine groups of the

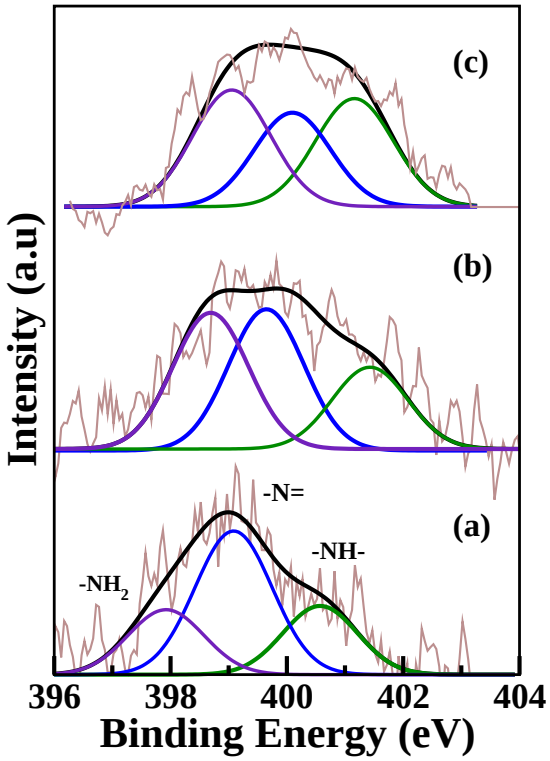

Figure 6.12: After DNA interaction: XPS spectra of N(1s) region for DNA interacted surfaces of (a) pristine and TiO_2 surfaces UV irradiated for (b) 5 mins (c) 10 mins. Fittings for various states are shown.

DNA have higher affinity to interact with the surface states created after UV irradiation.

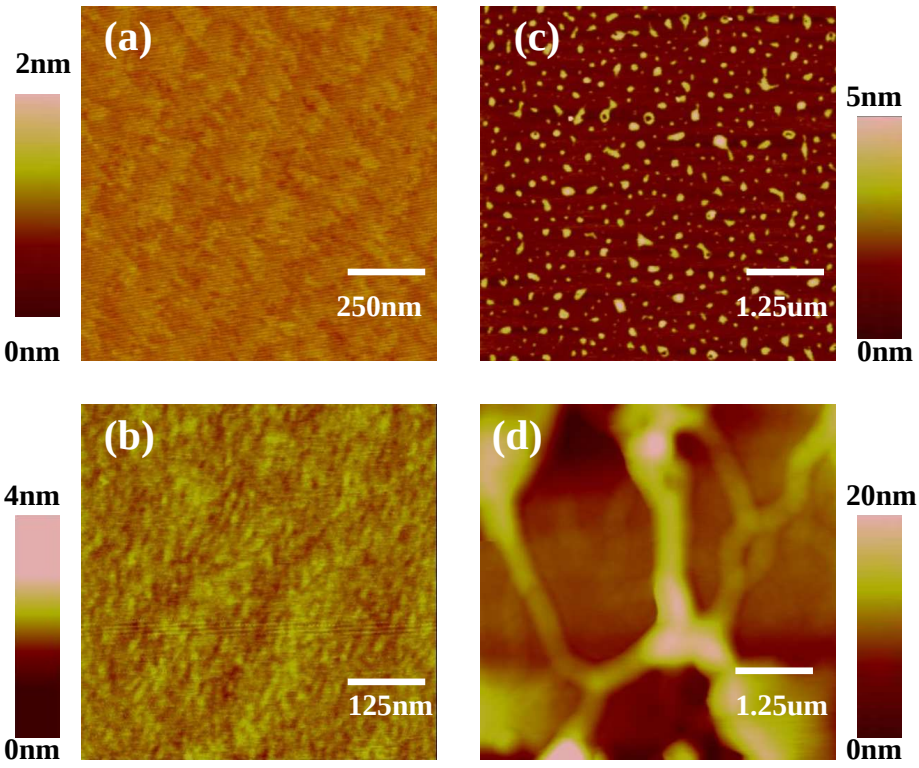

Figure 6.13: AFM images are shown in left panel for (a) pristine surface as well (b) surface sputtered at fluence of 6×10^{15} ions/cm^2 Right panel shows AFM images of corresponding surfaces after they are interacted with Branched DNA.

Branched DNA have also been interacted with Ar^+ irradiated TiO_2 surfaces. The irradiation was carried out at a fluence of 6×10^{15} ions/cm^2 by 3keV Ar^+, under same conditions as discussed in chapter 3, 4 and 5 for nanopatterning of SiO_x and TiO_2 surfaces. AFM images of the pristine and Ar^+ irradiated TiO_2 surfaces are shown in fig. 6.13. Ion irradiation of TiO_2 surfaces produces nanopatterns (fig. 6.13(b)). The morphology and roughening behavior of these nanostructures have been discussed in details in chapter 5. Spontaneous formation of self organized nanoscale patterns by ion irradiation, on any surface is controlled by the competition between the erosion of the surface and its smoothening by diffusion processes. Pref-

erential sputtering of oxygen atoms due to its low mass also play a role in the pattern formation. The pristine as well as ion irradiated surfaces were interacted with branched DNA. The pristine surfaces exhibit formation of rods and toroidal DNA structures as shown in fig. 6.13(c). These have been also discussed earlier in fig. 6.5(e). Fig. 6.13(d) shows ion irradiated TiO_2 surfaces after their interaction with branched DNA. Instead of toroidal condensed DNA structures as observed on the UV irradiated surfaces (fig. 6.5), now elongated DNA structures are observed. Although the ion irradaited surfaces (fig. 6.13(b)) has low rms roughness (0.130 nm), after DNA interaction it becomes 0.921 nm (fig. 6.13(d)).

Fig 6.14 shows the O(1s) XPS spectra for the pristine as well as ion irradiated surfaces. For the pristine surface, three features related to O-Ti-O, Ti-OH and Ti-O-C are observed (fig. 6.14(a)). After ion irradiation, the feature related to Ti-O-C is absent. The Ti-OH feature reduces in intensity, as expected, whereas O-Ti-O feature shifts towards lower binding energy. This shift is related to the formation of oxygen vacancies on the surface.

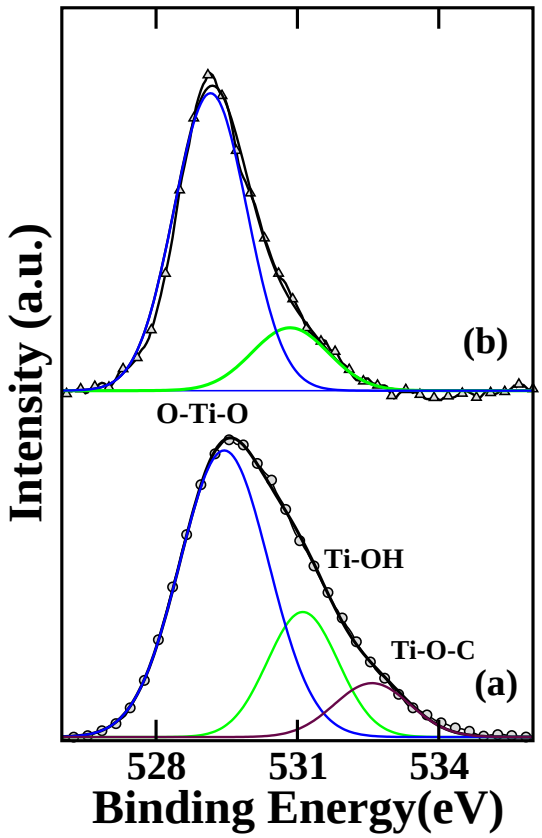

Figure 6.14: Before DNA interaction: XPS spectra of O (1s) region from (a)pristine TiO_2 and TiO_2 surface ion irradiated at fluence of (b) 6×10^{15} ions/cm^2. Fittings for various states are shown.

Fig 6.15 presents the Ti 2p XPS spectra for the pristine as well as ion irradiated surfaces. The pristine surface shows the Ti^{4+} feature from TiO_2. On the ion irradiated surfaces a broadening of Ti^{4+} feature and a shoulder related to Ti^{3+} (456.6 eV) is observed. The formation of Ti^{3+} defects after sputtering are related to the formation of oxygen vacancies on the TiO_2 surfaces and have been discussed in details in chapter 5.

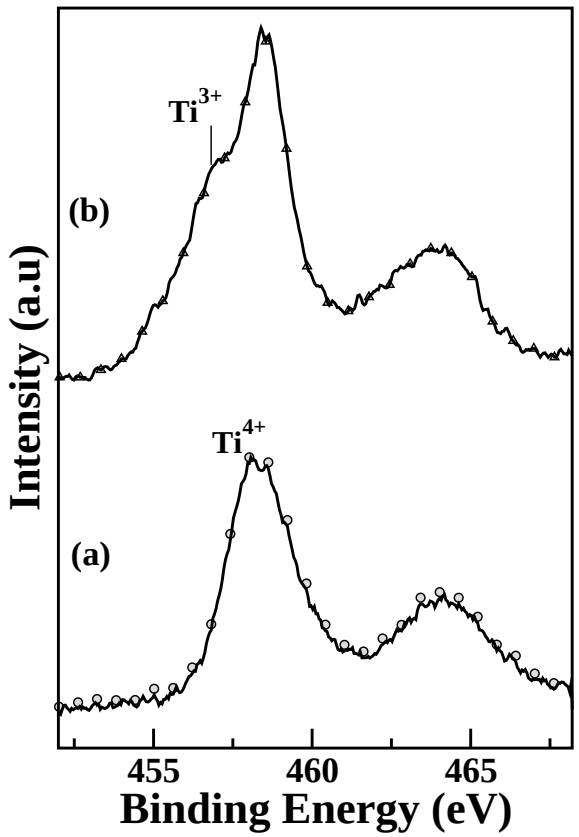

Figure 6.15: Before DNA interaction: XPS spectra of Ti (2p) region from (a) pristine TiO_2 and TiO_2 surface ion irradiated at fluence of (b) 6×10^{15} ions/cm^2

Fig. 6.16 shows the XPS spectra for O(1s) from pristine and ion irradiated TiO_2 surfaces after their interaction with branched DNA (red dashed line). For reference, the XPS spectra of uninteracted surfaces (from fig. 6.14) are also shown (black line). For the irradiated surfaces, a large shift of XPS spectra towards higher binding energy is observed (fig. 6.16). Presence of oxygen vacancy state, on ion irradiated TiO_2 surfaces (as seen in fig 6.15) may be responsible for this.

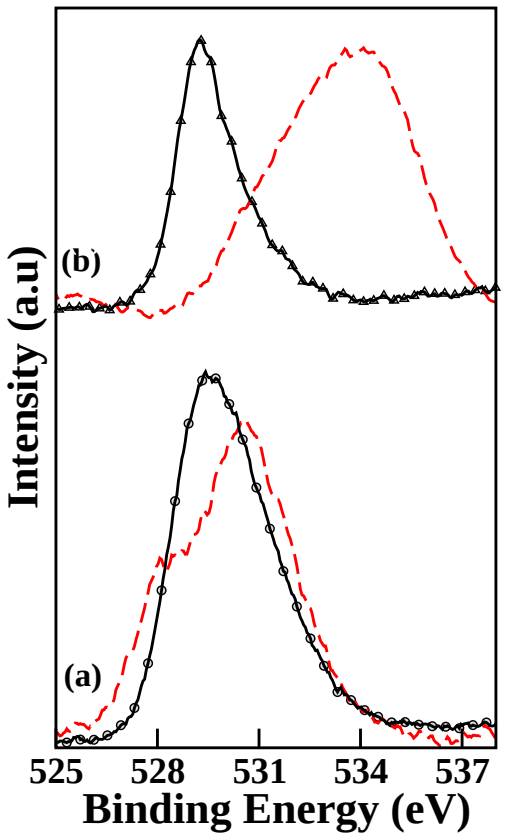

Figure 6.16: After DNA interaction: XPS spectra of O(1s) region for DNA interacted (red dashed lines) surfaces of (a) pristine TiO_2 and TiO_2 surface ion irradiated at fluence of (b) 6×10^{15} ions/cm^2. For reference, XPS spectra from un-reacted surfaces (black line) are also included.

Fig 6.17 shows the XPS spectra for Ti (2p) feature for the pristine as well as ion irradiated TiO_2 surfaces after their interaction with the branched DNA. A slight shift towards lower binding energy is observed, after DNA interaction, for both the pristine as well as ion irradiated surfaces. This may be related to the charge transfer from DNA backbone to the Ti^{4+} states of the surface.

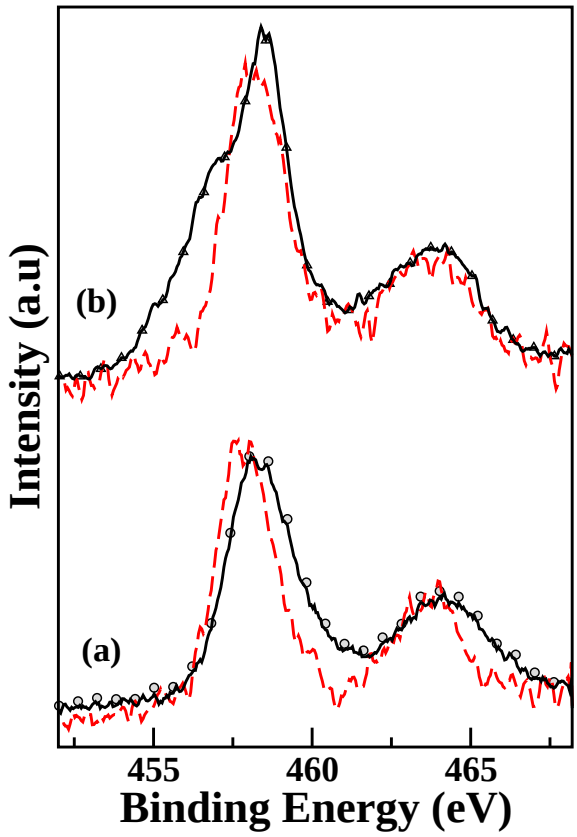

Figure 6.17: After DNA interaction: XPS spectra of Ti(2p) region for DNA interacted (red dashed lines) surfaces of (a) pristine TiO_2 and TiO_2 surface ion irradiated at fluence of (b) 6×10^{15} ions/cm^2. For reference, XPS spectra from un-reacted surfaces (black line) are also included.

N(1s) XPS region from the pristine and ion irradiated surfaces after their interaction with branched DNA are presented in fig. 6.18. The pristine surface indicates presence of amino(-NH_2), imine (-N=) and amine (-NH-) groups of DNA bases. These features have also been observed earlier [41]. All these features show a systematic shift towards higher binding energies for the ion irradiated surfaces due to the presence of oxygen vacancies. The amine feature indicates a slightly higher intensity on the ion irradiated surfaces suggesting the interaction with DNA to be promoted through this group. A new feature related to O-Ti-N state [42] at 402.20 eV is surprisingly observed

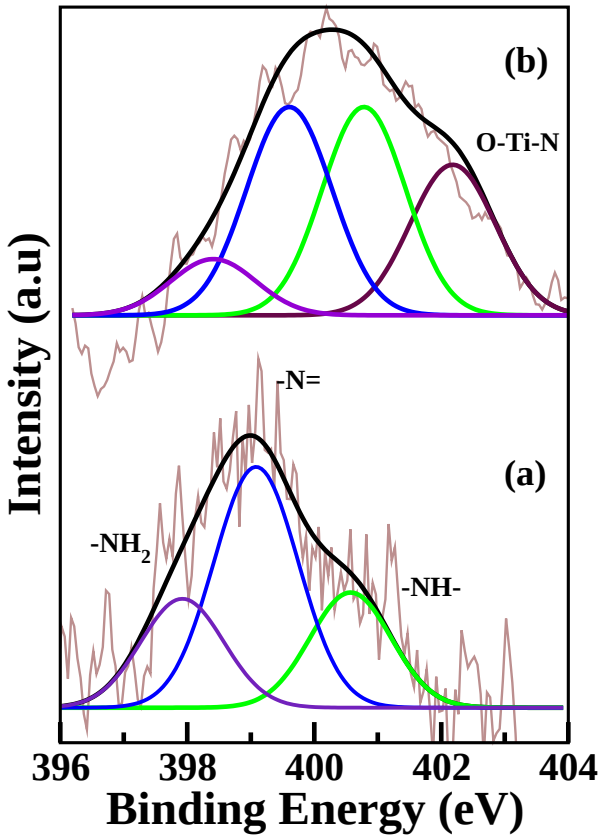

Figure 6.18: After DNA interaction: XPS spectra of N(1s) region for DNA interacted surfaces of (a) pristine TiO_2 and TiO_2 surfaces ion irradiated at fluence of (b) 6×10^{15} ions/cm^2

here. This may be due to the formation of some DNA - metal complex. Such complexes have been observed earlier [43]. Development of this new feature indicates strong interaction of DNA with ion irradiated TiO_2 surfaces.

6.4 Conclusion

This chapter discusses the interaction of branched DNA with UV irradiated and ion irradiated TiO_2 surfaces. The UV irradiated surfaces indicate the development of oxygen vacancy and surface defect states. In addition, reactive oxygen species are also created on the surface which promote the develop-

ment of surface hydroxyl states like Ti-OH as well as physically adsorbed water molecules. Upon interaction with the pristine surface, branched DNA forms rod and toroid like structures. However on UV irradiated surfaces only toroidal structures are observed. The sizes of these toroidal structures depend on the surface roughness of the UV-irradiated surfaces, increasing up to the exposure of 5min but decreasing for higher exposures. The results indicate a chemical interaction between the DNA moiety and the UV irradiated surfaces through the oxygen vacancies and other defect states present on the surface. The branched DNA has also been interacted with ion irradiated TiO_2 surfaces. Elongated DNA structures and network are observed on the ion irradiated surfaces, rather than the toroidal structures. Strong chemical interaction, as observed via the formation of O-Ti-N complex, may be responsible for this. The development of the complex appears to be related to the conjugation of DNA bases with the defect sites on the irradiated TiO_2 surfaces.

This chapter discussed the interactions of DNA with ion irradiated and UV beam modified TiO_2 surfaces. The polymeric materials have immense applications in biomedical devices. Chapter 7 discusses the modifications of PDMS polymer through plasma treatment as well as its interaction with cells. Cell viability and biocompatibility of PDMS has also been discussed.

Bibliography

[1] Justin P. Peters, Shweta P. Yelgaonkar, Seergazhi G. Srivatsan, Yitzhak Tor, and L. James Maher, Nucleic Acids Res., **41(22)**, 1059 (2013).

[2] C. Yuan, H. Chen, X. W. Lou, L. A. Archer, Phys Rev Lett., **100(1)**, 018102 (2008).

[3] V. A. Bloomfield, Biopolymers, **31**, 1471 (1991).

[4] Y. Fang and J. H. Hoh, Nucleic Acids Res.**26(2)**, 588 (1998).

[5] P. G. Arscott, A. Z. Li, V. A. Bloomfield, Biopolymers, **30**, 619 (1990).

[6] R. Golan, L. I. Pietrasanta, W. Hsieh, H. G. Hansma, Biochemistry, **38(42)**, 14069 (1999).

[7] T. Blessing, J. S. Remy, J. P. Behr, Proc Natl Acad Sci U S A., **95(4)**, 1427 (1998).

[8] J. Widom and R. L. Baldwin, J. Mol. Biol.,**144**, 431 (1980)

[9] A. Grosberg, A. V. Zhestkov, J. Biomol.Struct. Dyn., **3**, 859 (1986).

[10] C. C. Conwell, I. D. Vilfan, N. V. Hud, Proc. Natl. Acad. Sci. USA, **100**, 9296 (2003).

[11] J. C. Sitko, E. M. Mateescu, H. G. Hansma, Biophys. J. **84**, 419 (2003).

[12] S. Han, R. I. Mahato, S. W. Kim, Chem. **12**, 337 (2001).

[13] Y. B. Lim, S. O. Han, H. U. Kong, Y. Lee, J. S. Park, B. K. Jeong, W. Sung, Pharm. Res.,**17**, 811 (2000).

[14] H. Isobe, S. Sugiyama, K. Fukui, Y. Iwasawa, E. Nakamura, Angew. Chem. (Int. Ed.) **40**, 3364 (2001).

[15] M. J. Allen, E. M. Bradbury, R. Balhorn, Nucleic Acids Res., **25**, 2221 (1997).

[16] Y. Fang, J. H. Hoh, FEBS Lett. **459** ,173 (1999).

[17] J. W. Hao, L. Z. Wu, J. F. J. Zhi, Mater. Chem., **18**, 2459 (2008).

[18] R. Doong, H. Shih, Biosens. Bioelectron, **22**, 185 (2006).

[19] H. Chliephake, D. J. Scharnweber, Mater. Chem. **18**, 2404 (2008).

[20] R. Carbone, M. De Marni, A. Zanardi, S. Vinati, E. Barborini, L. Fornasari, P. Milani. Anal. Biochem., **394**, 7 (2009).

[21] R. Carbone, L. Giorgetti, A. Zanardi, I. Marangi, E. Chierici, G. Bongiorno, F. Fiorentini, M. Faretta, P. Piseri, P. G. Pelicci, P. Milani. Biomaterials , **28**, 2244 (2007).

[22] R. Carbone, I. Marangi, A. Zanardi, L. Giorgetti, E. Chierici, G. Berlanda, A. Podest, F. Fiorentini, G. Bongiorno, P. Piseri, P. G. Pelicci, P. Milani . Biomaterials, **27**, 3221 (2006).

[23] M. L. De Marni, A. Monegal, S. Venturini, S. Vinati, R. Carbone, A. de Marco. Methods., **56**, 317 (2012).

[24] Y.-Y. Song, F. Schmidt-Stein, S. Berger, S. and P. Schmuki., Small, **6**, 1180 (2010).

[25] D. P. Song, M. J. Chen, Y. C. Liang, Q. S. Bai, J.X. Chen, X. F. Zheng. Acta Biomater.,**6**, 684 (2010).

[26] R. Wang, K. Hashimoto, A. Fujishima, M. Chikuni, E. Kojima, A. Kitamura, M. Shimohigoshi, T. Watanabe. Nature, **388**, 431 (1997).

[27] J. Singh, J. E. Whitten. Langmuir, **26**, 17795 (2010).

[28] M. A. Henderson,Langmuir, **12**, 5093 (1996).

[29] J. G. Highfield, M. Grtzel,J. Phys. Chem, **92**, 464 (1988).

[30] R. R. Zhu, S. L. Wang, X. Y. Sun, R. Zhang, S. D. Yao, Sci China Ser B-Chem,**50(2)**, 272 (2007).

[31] S. Steenken, Chem. Rev., **89**,503 (1989).

[32] N. Kochetkov and E .I. Budovskii, Organic Chemistry of Nucleic Acids,Plenum Press, New York (1972)..

[33] L. G. Marzilli, L.G. Metal-ion interactions with nucleic acids and nucleic acid derivatives. In Progress in Inorganic Chemistry, Vol. 23, edited by S.J. Lippard, John Wiley, New York, (1977).

[34] Ashok K. Nayaka and Umakanta Subudh, RSC Adv.,**4**, 54506 (2014).

[35] Stefan Fischer, W. Andreas. Munz, Klaus Dieter Schierbaum, Wolfgang Gopel, J. Vac. Sci. Tech. B. **14** , 961 (1996).

[36] N. Yoshida, S. Suzuki, J. Song, M. Sakai, Y. Kameshima, A. Nakajima. Proceedings of the Annual Meeting of the Ceramic Society of Japan, Okayama (2005).

[37] Paulina Grskaa, Adriana Zaleskaa, Ewa Kowalskaa, Tomasz Klimczukb, Janusz W. Sobczakc, Ewa Skwarekd, Wadysaw Januszd, Jan Hupkaa, Applied Catalysis B: Environmental, **84**, 440 (2008).

[38] B. S. Liu, X. J. Zhao, L. P. Wen .Surf. Coat. Technol.,**201**, 3606 (2006).

[39] James Cleaves II, Caroline M. Jonsson, Christopher L. Jonsson,Dimitri A. Sverjensky,and Robert M. Hazen, Astrobiology **10**, 3 (2010).

[40] Q. Yang, Analytica Chimica Acta **597(1)**, 58 (2007).

[41] A. Haug, S. Schweizer, F. Latteyer,M. B. Casu, H. Peisert, C. Ochsenfeld, T. Chass, *Chem. Phys. Chem.*, **9**, 740 (2008).

[42] B. Viswanathan and K. R. Krishanmurthy, International Journal of Photoenergy **2012**, 269654 (2012).

[43] Subrata Majumder, M. Priyadarshini, U. Subudhi, M. Umananda, G. B. N. Chainy, P. V. Satyam, and Shikha Varma, Appl. Phys. Lett., **94** ,073110 (2009).

Chapter 7

Surface Modification of poly(dimethylsiloxane) through Oxygen and Nitrogen Plasma Treatment to Improve its Characteristics towards Biomedical Applications

7.1 Introduction

During the past few decades, polymeric materials, due to the wide range of physical properties and ease of processing to manufacture biomedical devices, have been successfully applied in biomedical applications such as various implants, biosensor and tissue engineering in the place of metals and ceramics. Nevertheless, an essential issue, the poor surface properties of the materials which may restrict their applications as biomaterials, should be addressed before they are implanted in the body. There have been several studies focusing on how surface properties of biomaterials influence the cellular adhesion and motility [1–6]. PDMS is widely used in microfluidic devices and biochip technology due to their desirable properties of optical transparency,

chemical inertness, permeability to gases. However, the hydrophobic nature of PDMS necessitates the tailoring of the surface properties to make the surface suitable for biomedical application. There has been a great deal of interest in designing PDMS with hydrophilic surface suitable for biomedical applications. The surface properties of the biomaterials may be improved by surface treatment to make it hydrophilic. There have been various researchers focusing their attention on influence of surface properties on biocompatibility of the material [7–10]. The most important parameters influencing the performance of a material in biomedical applications are surface energy, presence of functional groups, and surface roughness [11–15]. Among the various surface modification techniques, plasma surface modification has many advantages such as modification to a limited depth of 50 $\mathring{A}$ to 10 μm without affecting their bulk properties, eco-friendly, low temperature, dry and rapid process. Oxygen and nitrogen plasma treatment of PDMS removes methyl groups and replaces with polar groups and thus increases the hydrophilicity. Formation of micro and nano scale wavy structures on PDMS surface by means of appropriate plasma process conditions was reported [16, 17]. Despite the importance of surface properties in determining biocompatibility very few researchers addressed surface energy, surface chemistry and surface morphology of PDMS in the context of biomedical applications [18–21]. Consequently a detailed investigation on the effect of plasma treatment of PDMS on its biocompatibility is required. Therefore in the present chapter, the effects of oxygen and nitrogen plasma treatment of PDMS on its surface morphology and chemistry and enhancement of biocompatibility were studied. Plasma treated PDMS surfaces were characterized using contact angle measurement, Fourier transform infrared spectroscopy (FTIR), X-ray photoelectron spectroscopy (XPS), atomic force microscopy (AFM) for its hydrophilicity, surface chemistry and morphology respectively. The influ-

ence of plasma surface modification of PDMS on its biocompatibility was analysed by cell adhesion and cell viability tests. An attempt was made to quantify the cell adhesion area in untreated and oxygen and nitrogen plasma treated PDMS using ImageJ analysis.

7.2 Experiment

7.2.1 Materials

PDMS with a specific gravity of 0.9 g/cm^3 was supplied by GE silicones, India. Oxygen and nitrogen gases used for plasma generation with 99.99% purity were purchased from Tapaswi enterprise, Kharagpur, India. Deionized water, formamide (99% purity, procured from M/s. Merck Specialities Pvt. Ltd., Mumbai, India) and diiodomethane (98% purity, procured from M/s. Spectrochem Pvt. Ltd., Mumbai, India) were used for the measurement of contact angle.

7.3 Methods

7.3.1 Plasma treatment

The plasma treatment of PDMS was carried out in a plasma reactor (M-PECVD-1A [S]) procured from M/s, Milman Thin Film Systems, Pune, India. The samples were placed on the substrate holder inside the reactor chamber. The reactor was evacuated to 0.1 Pa during the roughing stage and the desired process pressure was obtained through closed loop pressure control during which the pressure was maintained by butterfly valve. Capacitively coupled RF discharge at the frequency of 13.56 MHz was created by supplying 50 W power between the powered electrode and grounded electrode by ionizing the process gas that was supplied to the reactor at the flow rate of 10 sccm. The polymer samples were exposed to the plasma for the

desired time (1 min/5 min) at the desired pressure of 20 Pa. After the treatment, the reactor chamber was brought to the atmospheric condition. The experiments were conducted using two different process gases namely oxygen and nitrogen. The treated samples were characterized through various surface characterization techniques.

7.3.2 Wettability studies

Static contact angle measurements were done on polymer surfaces before and after plasma treatment to determine the changes in the surface wettability by the sessile drop method using Rame-Hart 500-F1 advanced goniometer (Rame-Hart Instrument Co., Netcong, NJ, USA) at ambient humidity and temperature. Each contact angle reported in this work is the average of the values obtained from at least five different positions of the polymer sample surface. The contact angle measurements of post treated samples were carried out at an interval of 30 min till it reaches a plateau.

7.3.3 Estimation of surface energy

Contact angle measurements for surface energy estimation were performed at 72 h post-treatment to take into account the effect of any molecular reorientation. In order to determine the surface energy of the polymer, static contact angles of three liquids namely, deionized water, formamide and diiodomethane, with different surface free energies covering a wide range of polar and dispersion components were measured on the material surface. The surface free energies of the probe liquids with their polar and dispersion components have been presented elsewhere [22]. The method by Owens and Wendt was adopted here to calculate the surface energy of a solid (γ_s), using their polar (γ_s^p) and dispersion components (γ_s^d), contact angle (θ), surface free energy of probe liquid (γ_l) and its polar (γ_l^p) and dispersion (γ_l^d) com-

ponents (equation 7.1). The surface polarity (P) was estimated as the ratio of polar component to the total surface energy [23].

$$[(1 + cos(\theta)/2][\gamma_l/(\gamma_l^d)^{1/2}] = (\gamma_s^p)^{1/2}(\gamma_l^p/\gamma_l^d)^{1/2} + (\gamma_s^d)^{1/2} \qquad (7.1)$$

Polar and dispersion components of PDMS surface were obtained from the slope and intercept of the plot of the equation (7.1) respectively.

7.3.4 Surface chemistry

The effect of various plasma treatments on the surface chemistry of PDMS was investigated from Fourier transform infrared (FTIR) spectra of untreated and modified polymers obtained in attenuated total reflectance (ATR) mode using a Thermo Nicolet Nexus 870 FTIR (Thermo Nicolet Corporation, North America, Madison, WI) equipped with ZnSe crystal. They were recorded for the range of 4000-600 cm^{-1} with a resolution of 4 cm^{-1}. Surface chemistry changes caused by the plasma treatment were also analyzed by XPS measurements using an ESCA-2000 Multilab apparatus (VG Microtek) equipped with Mg-Al anode. The analysis was performed using Mg-K_α (1253.6eV) excitation source at take off angle of 30^o.

7.3.5 Surface morphology

The surface morphology of untreated and plasma treated polymers were examined with Jeol JSM-5800 scanning electron microscope (SEM) (JEOL, Tokyo, Japan). SEM examination of polymers was conducted to provide a qualitative assessment of surface roughness. Samples were coated with a thin conductive layer of gold in vacuum conditions prior to analysis. The surface topography of oxygen and nitrogen plasma treated PDMS at different treatment time were also studied using atomic force microscopy (AFM). The AFM analyses were performed in tapping mode with Veeco-CP2, (model:

RTESPA-CP) using phosphorous doped Si tip. The images were taken for an area of 10 μm x 10μm at the scan rate of 1 Hz. Root mean squared roughness (R_{rms}) of the untreated and plasma treated polymers that quantifies the effect of plasma etching were evaluated using the software WSxM 4.0.

7.4 Bio-Studies

7.4.1 Cell culture

The 3T3 fibroblasts cells preserved by freezing were thawed to room temperature to prepare the fibroblast suspension. They were diluted with an appropriate amount of Dulbeccos Modified Eagle Medium (DMEM) supplemented with 10% fetal bovine serum. The fibroblast suspension was centrifuged to remove the supernatant at 300G for 10 min. After washing with DMEM, the cells were seeded in the T-25 tissue culture flask and incubated in humidified atmosphere of 5% CO_2 in air at 37 ^oC. Confluent cells were trypsinized and approximately 2.5 x 10^4 cells were seeded to each polymer sample. They were inoculated for 4 h, 24 h for cell adhesion tests and 24 h for MTT test.

7.4.2 Cell morphology

Both untreated and plasma treated polymer samples seeded with 3T3 fibroblasts cells were examined through SEM to observe the morphology of the cells. The adhered cells were washed with phosphate buffered saline (PBS) and fixed with 2.5% glutaraldehyde. Series of graded alcohols were used to dehydrate the cells and dried to critical point. Gold coated samples were examined for their morphology using secondary electrons in JEOL JSM-5800 microscope.

7.4.3 MTT Assay

To determine the cell viability, colorimetric MTT assay (3-(4,5-dimethylthiazol-2-yl)-2,5-diphenyltetrazolium bromide) was used. In this method, mitochondria of the living cells reduce the tetrazolium bromide salts to formazan. Since the functional mitochondria becomes inactive within few minutes after cell death, reduction of tetrazolium bromide to formazan is used as a measure of viable cells. Formation of the coloured formazan product during incubation was analysed spectrophotometrically at 595 nm using ELISA plate reader.

7.5 Results and Discussion

7.5.1 Surface energy

The contribution of the various components of surface energy to the total surface free energy were determined through the contact angle measurements using three liquids namely deionized water, formamide, and diiodomethane on the untreated and plasma treated surfaces. The total surface energy, including dispersion and polar components, along with the polarity for the untreated and plasma surface modified PDMS are presented in table 7.1.

Table 7.1: Surface energy of untreated and plasma treated PDMS

sample	Contact Angle (degree)			Surface Energy (N/mm^2)			Polarity
	DI	FA	DIM	γ_p	γ_d	γ	
Untreated	106	87	81	0.92	15.81	16.7	0.05
O_2 -1 min	89	60	76	6.58	15.47	22.1	0.30
O_2- 5 min	88	48	79	8.71	14.44	23.4	0.38
N_2- 1 min	82	34	57	6.62	26.06	32.7	0.20
N_2- 5 min	72	28	63	13.4	19.87	33.3	0.40

Untreated surfaces exhibited a hydrophobic nature that is characterized by relatively lower surface energy. Plasma surface modification of PDMS

using oxygen and nitrogen caused significant enhancement on its wettability. The total surface energy, including dispersion (γ_d) and polar (γ_p) components, along with the polarity for the untreated and plasma surface modified PDMS are presented in table 7.1. Both oxygen and nitrogen plasma treatment led to increased hydrophilicity through increased polarity varying from 0.2-0.4 whereas untreated samples were found to be strongly hydrophobic with low surface energy and a low polarity of 0.05. Wettability was particularly increased in the case of nitrogen plasma treatment for 5 min with a surface energy of 33.3 N/mm^2 (0.40 polarity). Surface energy is affected by both chemical composition and microstructural topography. However polar component is reported to be the most determinant of cellular adhesion strength [24].

7.5.2 Ageing effect

PDMS wettability introduced by plasma treatment decreased as a function of time. It was reported that ageing occurs mainly due to either of the two principal mechanisms namely post-treatment chemical reactions or surface relaxation [25]. It is known that hydrophobic recovery of PDMS surface is mainly due to reorientation of surface molecule and migration of low molecular weight species from the bulk. However the physical surface recovery of silicone rubber due to its elastic nature also causes hydrophobic recovery [26]. In order to examine the effect of aging on wettability, the water contact angle of plasma treated surface exposed to air was measured as a function of time. Figure 7.1 illustrates the aging effect of different plasma treated PDMS surfaces in terms of their wettability measured through water contact angle. Significant hydrophobic recovery was observed in the first 30 min which is indicated by the increased contact angle. After 90 min of ageing, stability was reached for all the plasma treated conditions. Highest hydrophobic

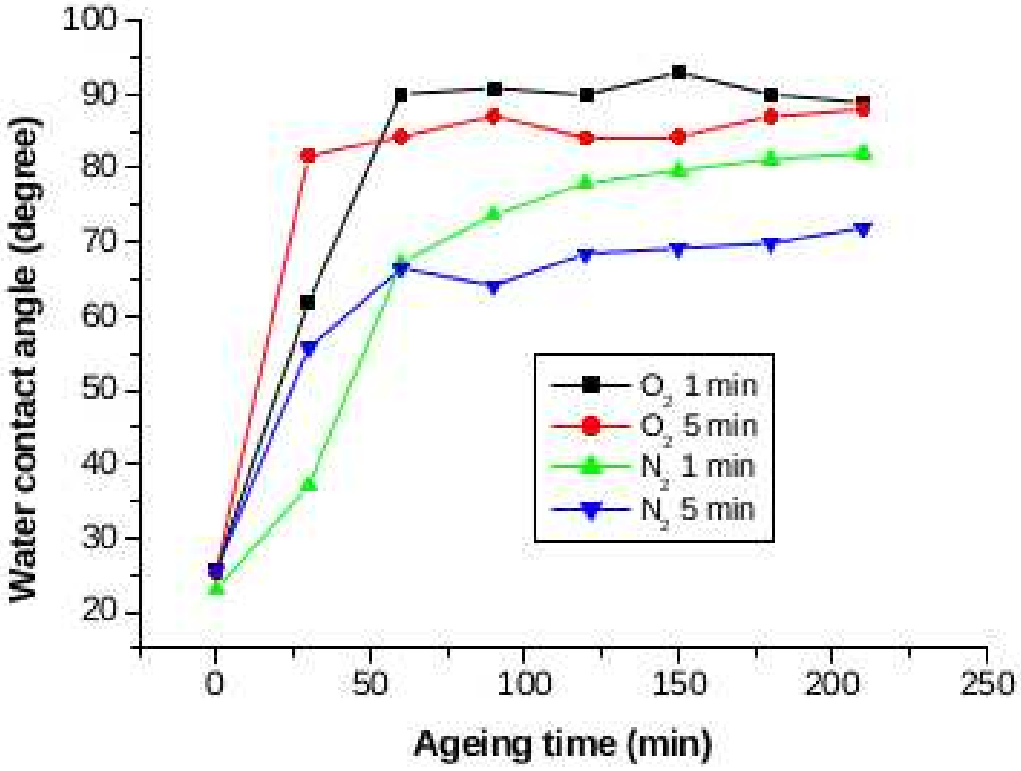

Figure 7.1: Ageing analysis of plasma treated PDMS

recovery was observed in the case of oxygen plasma treatment for 1 min whereas the lowest recovery was in the case of nitrogen plasma treatment for 5 min. Hydrophobic recovery in nitrogen plasma treated PDMS was inferior for oxygen plasma treated PDMS for both 1 min and 5 min treatment time. Hydrophobic recovery is slightly delayed in case of shorter plasma treatment time in both oxygen and nitrogen plasma treatment. It is reported that oxygen plasma treatment causes the formation of a layer of silica like structure with free siloxanes. Removal of silica like groups causes reduction in wettability [25].

7.5.3 Surface Chemistry

The changes in the elemental composition of untreated and plasma treated PDMS were assessed by XPS. The presence of methyl groups on the surface is the reason for the hydrophobicity of PDMS. Since the chain exposes maximum number of methyl groups to outside they shield the main chain. Bond dissociation energy of Si-O bond (809 kJ/mol) is higher than that of Si-C bond (451 kJ/mol). For this reason Si-O bonds are difficult to be broken compared to Si-C bonds. The changing elemental composition of PDMS as a result of plasma treatment due to the interaction of the active species is shown in table 7.2. As can be seen from table 7.2 carbon content is decreasing after oxygen plasma treatment with increase in oxygen content. Increase

Table 7.2: Atomic composition of untreated and plasma treated PDMS by XPS analysis

Sample	Carbon%	Oxygen%	Silicon%	O/C	O/Si
Untreated	51.3	11.8	36.7	0.23	0.32
$O_2$1-min	44.8	14.9	41.8	0.33	0.36
O_2-5 min	43.2	17.1	39.5	0.40	0.43
N_2 1-min	65	15.1	19.6	0.23	0.78
N_2 5-min	55	18	26	0.33	0.69

in the ratio of O/C indicates that oxygen containing groups are attached to PDMS as a result of oxygen plasma treatment. Increased treatment time results in higher O/C ratio. Atomic composition of silicon is found to be higher than the theoretical value which decreases significantly with nitrogen plasma treatment but is not affected significantly during oxygen plasma treatment. Decrease in silicon content is more pronounced compared to that of carbon in the case of nitrogen plasma treatment. The XPS spectra of C1s for PDMS samples are presented in figure 7.2 and are charge corrected considering 284.4 eV as the reference peak corresponding to $SiCH_x$ [27]. For the untreated PDMS, the peaks are observed at 286.1, 284.4, 282.1 and 280.3 eV

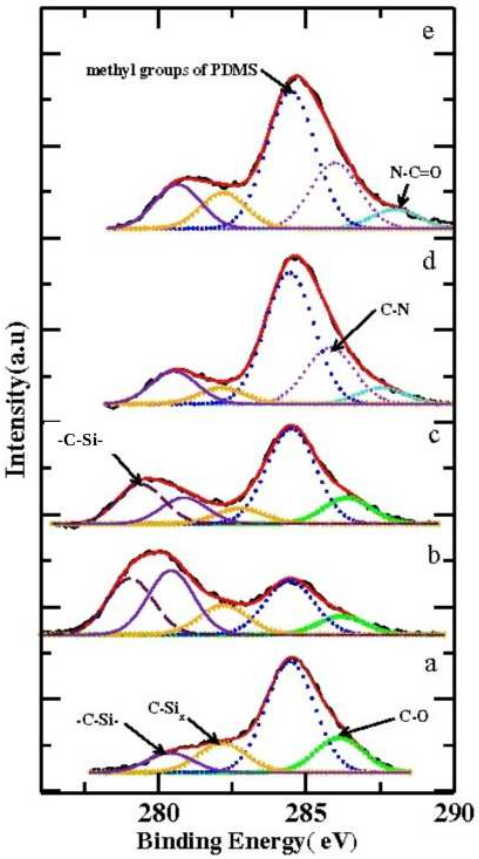

Figure 7.2: C1s peak of (a) untreated PDMS and oxygen plasma treated PDMS for (b) 1 min, (c) 5 min and nitrogen plasma treated PDMS for (d) 1 min and (e) 5 min.

which are associated with C-O, -SiCH$_x$, C-Si$_x$ and C-Si bonds respectively. The relative composition ratio of different C1s based on the peak areas is presented in table 7.3.

Additional peaks are observed at 279.0 and 279.3 eV in the case of 1 min and 5 min treatment with oxygen plasma treatment which are respectively attributed to the -C-Si bonds. In the case of nitrogen plasma treatment of PDMS, two new peaks are observed at 285.9, 288 eV after treatment for 1 min. These features correspond to C-N and N-C=O, respectively and confirm

Table 7.3: Binding Energy in eV (%concentration) of C1s core level component

Sample	-C-Si-	-C-Si-	C-Si$_x$	methyl groups on the PDMS chain	C-N	C-O	N-C=O
Untreated		280.3(10)	282.1(16)	284.4(59)		286.1(18)	
$O_2$1-min	279.0(25)	280.4(28)	282.2(14)	284.4 (25)		286.2(8)	
O_2-5 min	279.3(19)	280.8(12)	282.7(8)	284.4(48)		286.3(13)	
N_2 1-min		280.5(12)	282.2(6)	284.4(53)	285.9)23)		288.0(6)
N_2 5-min		280.6(14)	282.2(12)	284.4(46)	285.8(22)		287.5(6)

the incorporation of nitrogen containing groups in PDMS. The same peaks were also observed in XPS of nitrogen plasma treated PDMS for 5 min. They were centered at 285.8 and 287.5 eV. It can be noticed that plasma treatment decreases the carbon content in the form of C-Si$_x$, hydrocarbon and for carbon that is singly bonded to oxygen (C-O). The XPS spectra of O1s and the relative composition of different O1s peak based on peak areas are presented in figure 7.3 and table 7.4 respectively.

Table 7.4: Binding Energy in eV (%concentration) of O1s core level component

Sample			Surface Oxygen	OH	O-Si	CONH	C-O	O-NO_2
Untreated			528.3(8)	530.3(13)	531.9(65)		533.8(14)	
$O_2$1-min	524.1(8)	526.1(22)	528.4(16)		531.8(25)		533.2(19)	
O_2-5 min	523.7(9)	526.1(16)	528.3(11)		531.8(44)		533.7(26)	
N_2 1-min			528.1(4)		531.9(56)	532.9(29)		534.4(11)
N_2 5-min			528.1(7)		532.1(37)	533.4(42)		534.7(15)

The peak observed at 531.9 eV corresponds to oxygen singly bonded to Si which is a characteristic of Si-O in PDMS. Peak corresponding to C-O was observed at 533.8 eV. After oxygen plasma treatment of PDMS for 1 min a surface oxygen features observed at 524.1 and 526.1 eV. For 5 min oxygen plasma treatment also the same peaks were observed at 523.7 and 526.1 eV. The OH peak at 530.3 eV present in the untreated PDMS was not detected after the plasma treatment. Nitrogen plasma treatment resulted in

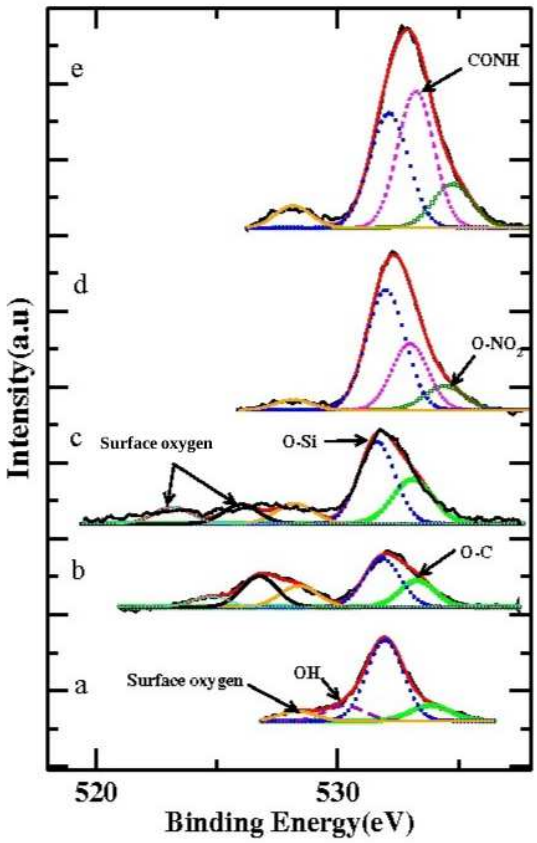

Figure 7.3: O1s peak of (a) untreated PDMS and oxygen plasma treated PDMS for (b) 1 min, (c) 5 min and nitrogen plasma treated PDMS for (d) 1 min and (e) 5 min.

incorporation of CONH group which is evident from the new peaks observed at 532.9 eV after 1 min of nitrogen plasma treatment time. This peak was observed at 533.2 eV for the 5 min nitrogen plasma treated samples. C-O peak present in the untreated as well as oxygen plasma treated samples is not observed in the nitrogen plasma treated PDMS. A peak at 534.4 (for 1 min) and 534.7 eV (for 5 min) corresponding to O-NO_2 was detected for nitrogen plasma treated samples.

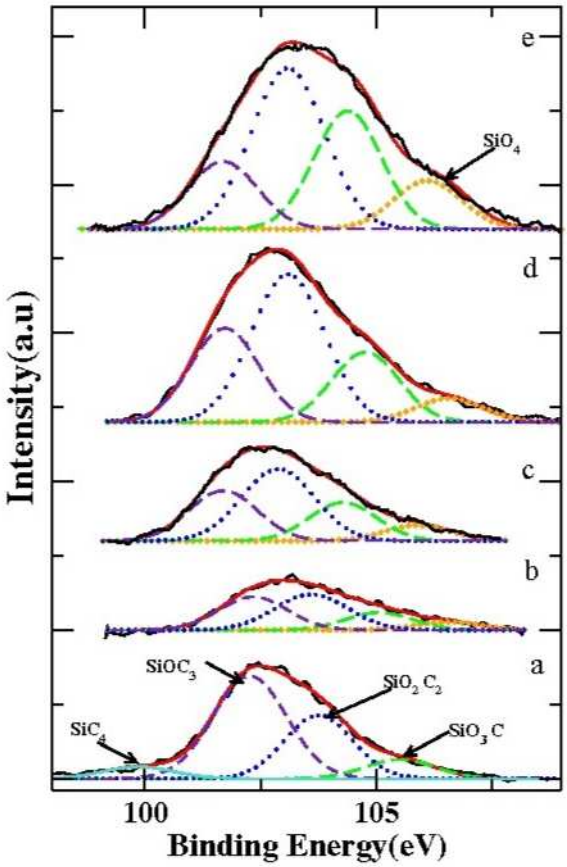

Figure 7.4: Si2p peak of (a) untreated PDMS, oxygen plasma treated PDMS for (b) 1 min, (c) 5 min and nitrogen plasma treated PDMS for (d) 1 min and (e) 5 min.

Table 7.5: Binding Energy in eV (%concentration) of Si 2p core level component

Sample	SiC_4	$SiOC_3$	SiO_2C_2	SiO_3C	SiO_4
Untreated	99.6(6)	102.0(54)	103.5(31)	105.3(9)	
$O_2$1-min		102.1(34)	103.4(40)	104.8(18)	106.3(18)
O_2-5 min		101.6(28)	102.8(43)	103.9(21)	105.9(8)
N_2 1-min		101.4(27)	102.8(46)	104.5(26)	106.4(7)
N_2 5-min		101.6(17)	103.0(42)	104.5(29)	106.3(12)

The detailed spectra of Si 2p for untreated and plasma treated PDMS presented in figure 7.4 and table 7.5 exhibit the changes in the peaks and formation of new peaks. Data evidenced the disappearance of SiC_4 peak and formation of SiO_4 after oxygen and nitrogen plasma treatment.

The FTIR studies of untreated and plasma treated PDMS, presented in

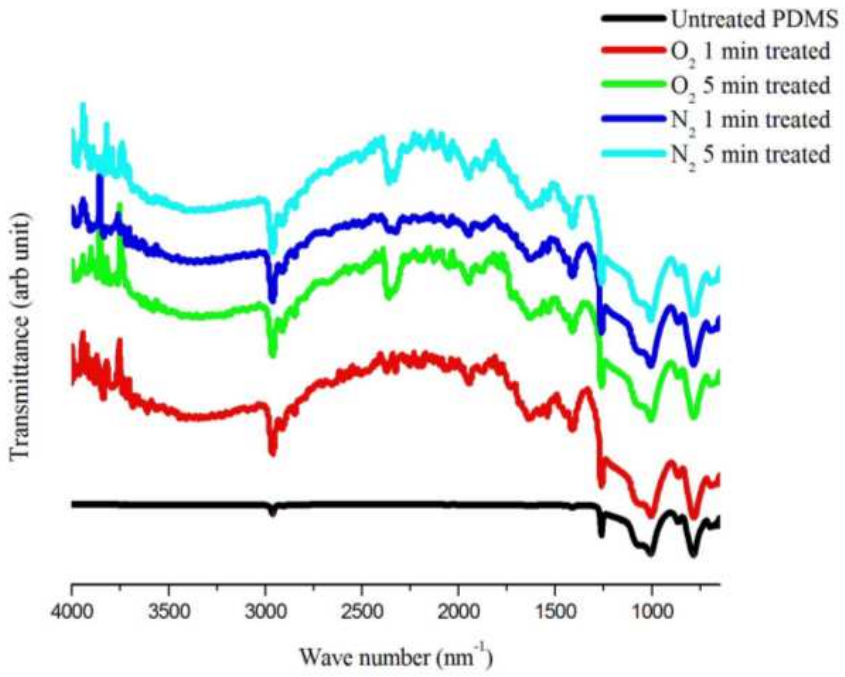

Figure 7.5: FTIR spectra of untreated and treated PDMS

figure 7.5 and table 7.6, also explain the surface chemistry changes that have occurred as a result of plasma treatment. Addition of polar groups in O_2 plasma treated PDMS were evidenced from the new peaks observed at 1630 or 1628 cm^{-1} corresponding to C=O stretch and corresponding to OH stretch at 3340 or 3330 cm^{-1} after 1 min and 5 min treatment with oxygen plasma respectively. The characteristic amide peak of N_2 plasma treated PDMS at 1542 cm^{-1} was observed. The peaks corresponding to NH

Table 7.6: FTIR peaks of untreated and plasma treated PDMS

Untreated	O_2 1 min	O_2 5 min	N_2-1min	N_2 -5min	Peak Assignment
787	787	787	787	787	Si-$(CH_3)_2$
864	864	864	864	864	Si-C
1008	1008	1008	1008	1004	Si-O-Si asymmetric deform
1259	1259	1259	1259	1259	CH_3 symmetric deform
	1413	1413	1412	1412	CH_3 asymmetric deform
			1542	1542	Characteristic strong adsorption peak for amide
	1630	1628	1641	1631	CH_2
				2850	C=O stretch
	2907				CH_2 symmetric stretching vibration of CH_2-NH_2
			2916	2918	CH_3asymmetric
2963	2963	2963	2963	2962	CH_3 symmetric
				3306	OH/NH stretch
	3340	3330	3335		OH/NH stretch

stretching and C=O stretching were observed at 3355 or 3306 and 1641 or 1631 cm^{-1} with the treatment times of 1 min and 5 min respectively. In the case of nitrogen plasma treatment for 5 min, a new peak was observed at 2850 cm^{-1} corresponding to CH_2 symmetric stretching vibration of -CH_2NH_2.

7.5.4 Surface Morphology

Untreated PDMS exhibits a relatively smooth surface with few micro pores on the surface as shown in figure 7.6(a). Both oxygen and nitrogen plasma treated PDMS are found to be rough and porous as shown in figure 7.6 (b-e). Oxygen plasma treated PDMS resulted in relatively increased surface roughness compared to nitrogen plasma treated PDMS. Increased exposure to oxygen plasma increases the pore size as shown in figure 7.6(b-c). Formation of nanosized periodic structure through controlled plasma process parameters like electrode temperature and exposure dose was reported [17]. Formation of bumped structure was observed with nitrogen plasma as shown in figure. 7.6(e). The representative AFM images of untreated and plasma

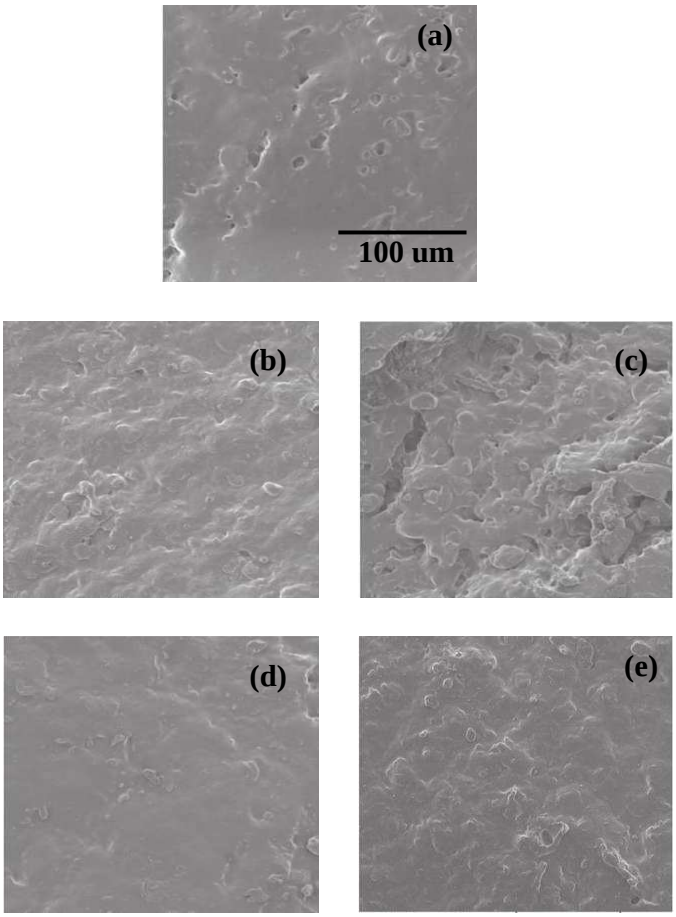

Figure 7.6: SEM images of (a) untreated PDMS, oxygen plasma treated PDMS for (b) 1 min (c) 5 min, nitrogen plasma treated for (d) 1 min (e) 5 min.

treated PDMS surfaces are depicted in figure 7.7.

As shown in figure 7.7(a-e), untreated PDMS exhibits a surface with few micropits with the roughness of 78.8 nm. The right panel shows the partial density function of height distributions on the surface and provides root mean square roughness (R_{RMS}), average roughness (R_a), average height (h_a) and surface skewness. The presence of micropits on its surface is indicated by the negative value of the surface skewness which is a measure of the average of the first derivative of the surface. The negative value of the surface

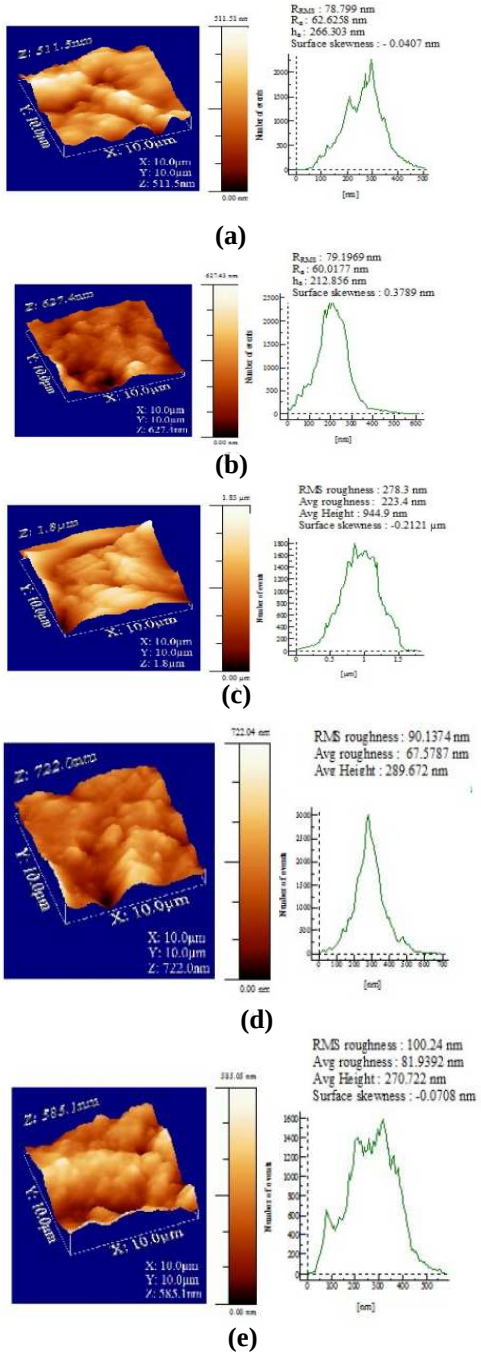

Figure 7.7: 10x10 μm^2 AFM images of (a) untreated, oxygen plasma treated for (b) 1 min, (c) 5 min, nitrogen plasma treated for (d) 1 min and (e) 5 min.

skewness indicates the presence of valley structure. No significant change in the surface roughness of PDMS was observed in the case of oxygen plasma treated PDMS with treatment time of 1 min (roughness = 79.2 nm). Instead of the valley structure the surface contains peaks and asperities as shown in figure 7.7(b). However the prolonged exposure of PDMS surface to oxygen plasma resulted in the formation of valley structure with increased micropit size as shown in figure 7.7(c) which is evidenced from the negative value of the surface skewness. This leads to increased surface roughness. Nitrogen plasma treatment of PDMS for 1 min results in increased roughness due to the etching effect of the active species in the plasma. Roughness further increases when it was treated for 5 min. Increased roughness factor in the case of nitrogen plasma treatment is mainly due to the peaks and asperities as clearly seen from figure 7.7(d-e). Similar kinds of morphologies are also observed in SEM.

7.5.5 Cell adhesion

Representative images of 3T3 fibroblast cells showing the quality of the cells adhered to the surface are presented in Figure. 7.8(a-e) for 4 h and Figure. 7.8(f-j) for 24 h incubation. Compared to the cells on untreated PDMS surface, cell elongation is observed in all the cases of cells attached to plasma treated PDMS surface. Plasma etched surface provide the local density variation of cell adhesion substratum topography. The surface topography was composed of micro-pits as a result of simultaneous etching effect of plasma treatment apart from polarization. These micropits act as dynamic focal adhesion sites where the cells are getting attached to. Cells are observed to be more rounded on untreated surface even after 24 h of incubation. Elongated and increased number of cells on the plasma treated surface indicate improved cell adherence on the surface. Polarized morphology, with a distinct

asymmetry indicating the front and rear ends clearly, is observed with the cells attached to the plasma treated polymer surface. The adhered cells are also well spread and protruded along the edges of the cell membrane. Formation of filopodia (microspike or slender cell projection) was observed in the case of oxygen plasma treated PDMS while the SEM analysis revealed that in addition to the filopodia, cells also formed flattened lamellipodia (projection on the leading edge of the cell) in the case of nitrogen plasma treated PDMS as shown in figure 7.8(g-j). The presence of nitrogen containing groups in nitrogen plasma treated PDMS may help in cell polarization. Amide groups incorporated onto PDMS surface may cause cross linking of actin filaments which may lead to the formation of lamellipodia.

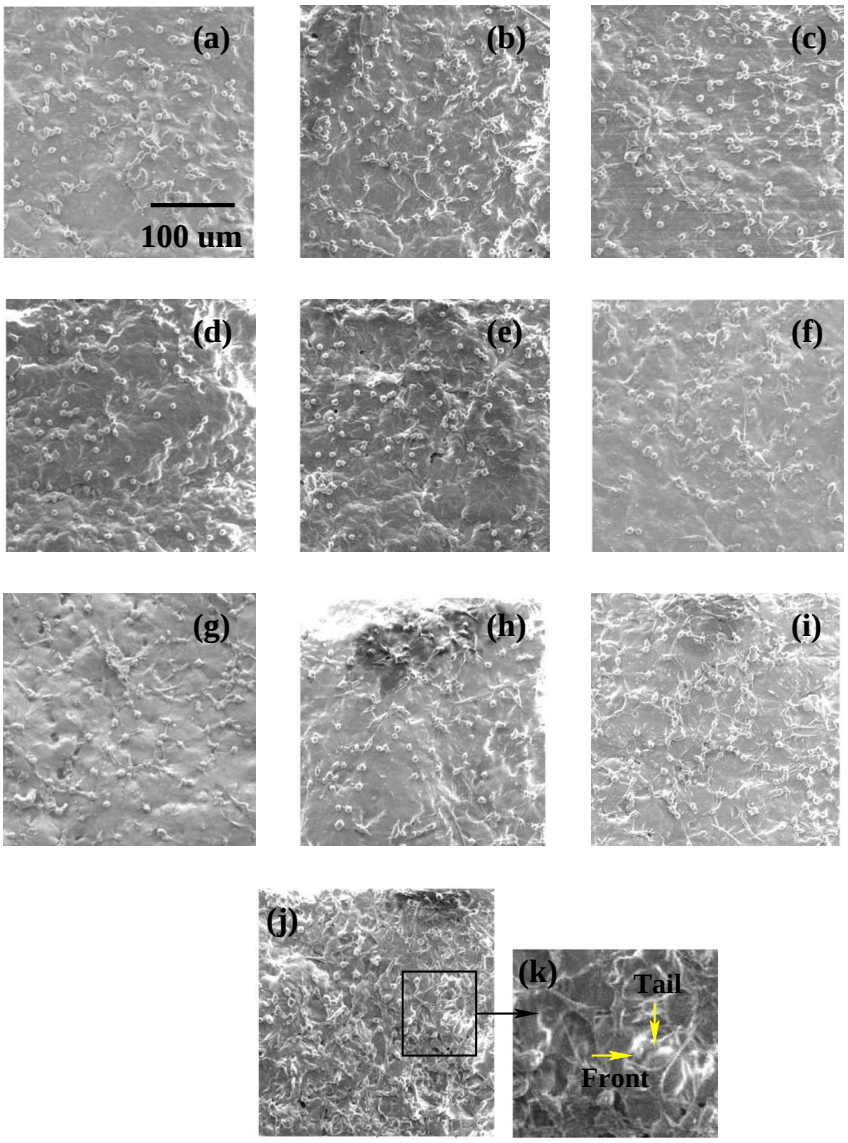

Figure 7.8: Cell adhesion after 4 h and 24 h respectively on (a), (f) untreated PDMS, (b), (g) oxygen plasma treated PDMS for 1 min, (c), (h) oxygen plasma treated PDMS for 5 min, (d), (i) nitrogen plasma treated PDMS for 1 min, (e), (j) nitrogen plasma treated PDMS for 5 min (k) magnified image showing front and tail end morphology of 3T3 fibroblast cell.

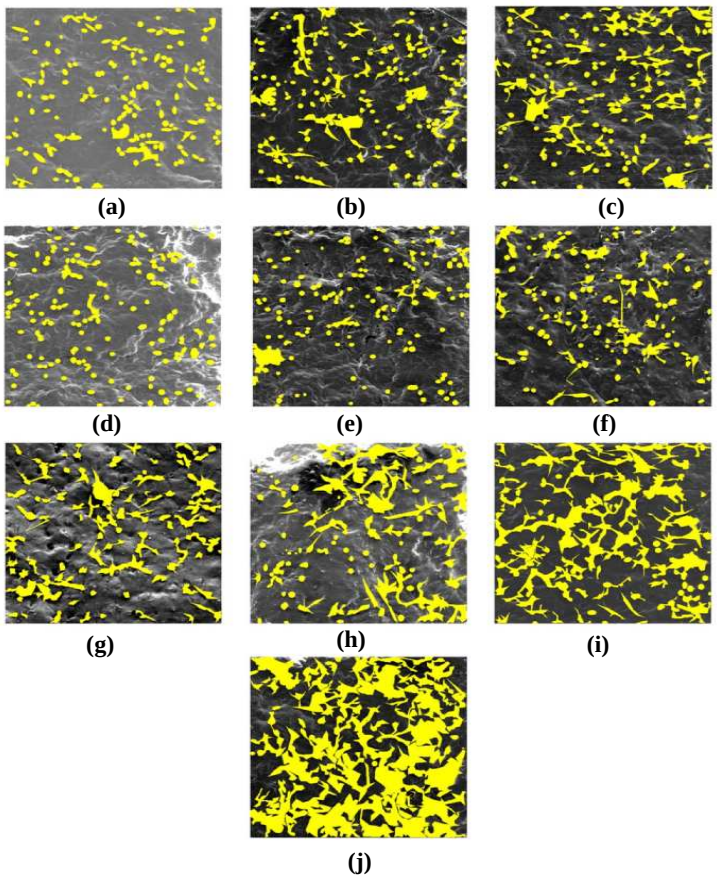

Figure 7.9: Image analysis of 3T3 mouse fibroblast cell adhesion after 4 h and 24 h respectively on (a), (f) untreated PDMS, (b), (g) oxygen plasma treated PDMS for 1 min, (c), (h) oxygen plasma treated PDMS for 5 min, (d), (i) nitrogen plasma treated PDMS for 1 min, (e), (j) nitrogen plasma treated PDMS for 5 min.

The SEM images of cells adhered onto the surfaces were analysed by imageJ software and are depicted in figure 7.9(a-e) for 4 hour incubation and figure 7.9(f-j) for 24 hour incubation. Area covered by cells was quantified using the image analysis. When the cells were seeded on PDMS surface treated with oxygen plasma no significant difference in cell spreading with incubation period was observed as compared to that of nitrogen plasma treated PDMS. In the case of 5 min treatment with nitrogen plasma the area covered by the

cells shows the highest value as depicted in table 7.7. figure 7.10 shows that the plasma treatment resulted in increased cell viability. Among the different plasma treatment conditions, N_2 plasma treatment for 5 min exhibited the better biocompatibility in terms of cell viability as indicated by its higher optical density (OD) value as a result of plasma treatment.

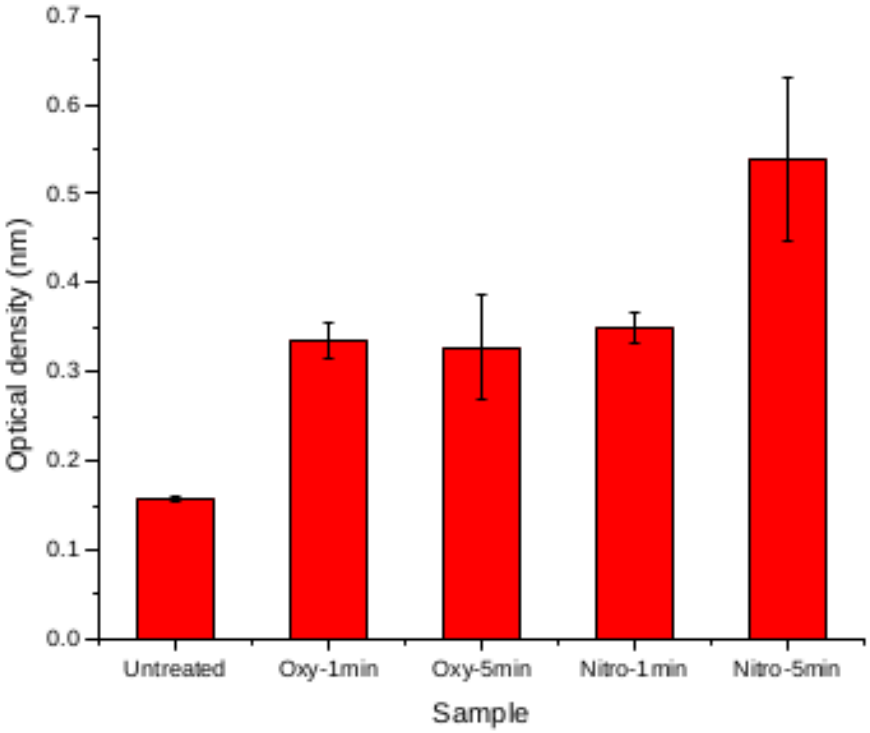

Figure 7.10: Cell viability after 24 h for untreated and plasma treated PDMS.

Table 7.7: Area covered by cell on untreated and plasma treated PDMS surface

Sample	Cell area after 4h incubation	Cell area after 24h incubation
Untreated	3.046	3.08
$O_2$1-min	3.878	4.544
O_2-5 min	4.615	5.594
N_2 1-min	7.25	8.174
N_2 5-min	2.545	13.028

7.6 Conclusion

Plasma surface modification of PDMS using oxygen and nitrogen gases were performed for the treatment time of 1 min and 5 min. Polarity ranging between 0.2-0.4 for plasma treated PDMS was observed, which was increased from 0.05 corresponding to untreated PDMS. Increase in surface energy ranging between 22.1-33.3 N/mm^2 was observed in oxygen and nitrogen plasma treated PDMS. Nitrogen plasma treated PDMS for 5 min was exhibiting highest polarity (0.4) and surface energy (33.3 N/mm^2) due to the incorporation of oxygen and nitrogen containing groups compared to the untreated and other plasma treated PDMS. Increased hydrophilicity and surface roughness was found to increase the biocompatibility. This is evident from the SEM analysis of cells adhered onto PDMS surfaces. Despite the fact that both surface roughness and polar groups help in enhancing biocompatibility, moderate roughness only was observed to favor cell adhesion. Analysis of SEM images using imageJ quantified the cells adhered onto the surface which clearly evidenced that nitrogen plasma treatment for 5 min resulted in the highest cell adhesion and spreading. Cell viability test also evidenced more enhanced biocompatibility in the case of N_2 plasma treatment for 5 min among the different treatment conditions.

Bibliography

[1] H. Mirzadeh, M. Dadsetan, Radiat Phys Chem. **67**, 381 (2003).

[2] P. Favia, R. d'Agostino, Surf Coat Tech.**98**, 1102 (1998).

[3] A. Parker, P. Reynolds, A. Lewis, L. Kirkwood, L. G. Hughes, Colloids Surf. B. **46**, 204 (2005).

[4] Z. Ma, Z. Mao, C. Gao, Colloids Surf. B. **60**, 137 (2007).

[5] X. Yang, K. Zhao, G. Q. Chen, Biomaterials **23**, 1391 (2002).

[6] D. T. Lin, T. H. Young, Y. Fang, Biomaterials, **22**, 1521 (2001).

[7] X. Li, S. Luan, S. Yuan, L. Song, J. Zhao, J. Ma, H. Shi, H. Yang, J. Jin, J. Yin, Colloids Surf. B. **112**, 146 (2013).

[8] M .Nitschke, S. Ricciardi, S. Gramm, S. Zschoche, M. Herklotz, P. Rivolo, C. Werner, Colloids Surf. B. **90**, 41 (2012).

[9] V. Gubala, N. C. H. Le, R. P. Gandhiraman, C. Coyle, S. Daniels, D. E. Williams, Colloids Surf. B. **81**, 544 (2010).

[10] P. M. Lpez-Prez, R. M. P. da Silva, R. A. Sousa, I. Pashkuleva, R. L. Reis, Acta Biomaterialia **6**, 3704 (2010).

[11] L. D. Bartolo, S. Morelli, A. Bader, E. Drioli, Biomaterials **23**, 2485 (2002).

[12] B. D. Boyan, T. W. Hummert, D. D. Dean, Z. Schwartz, Biomaterials **17**, 137 (1996).

[13] Y. Ikada, M. Suzuki, M. Taniguchi, H. Iwata, W. Taki, H. Miyake, Y. Yonekawa, H. Handa, Radiat Phys Chem. **18**, 1207 (1981).

[14] M. S. Kim, G. Khang, H. B. Lee, Progress Polym. Sci. **33** 138 (2008).

[15] J. C. Lin, S. L. Cooper, Biomaterials **16** 1017 (1995).

[16] N. Bowden, W. T. S Huck, K. E. Paul, G. M. Whitesides, Appl. Phys. Lett. **75**, 2557 (1999).

[17] A. Tserepi, E. Gogolides, K. Tsougeni, V. Constantoudis, E. Valamontes, J. Appl. Phys. **98**, 113502 (2005).

[18] S. Pinto, P. Alves, C. M. Matos, A. C. Santos,L. R. Rodrigues, J. A. Teixeira, M. H. Gil, Colloids Surf. B. **81**, 20(2010).

[19] D. Fuard, T. Tzvetkova-Chevolleau, S. Decossas, P. Tracqui, P. Schiavone, Microelectron Eng. **85**, 1289 (2008).

[20] V. Sharma, M. Dhayal, S. M. Govind Shivaprasad, S. C. Jain, Vacuum **81**, 1094(2007).

[21] M. T. Khorasani, H. Mirzadeh, P. G. Sammes, Radiat Phys Chem. **55** 685 (1999).

[22] N. Gomathi, S. Neogi, Appl. Surf. Sci. **255**, 7590 (2009).

[23] D. K. Owens, R. C. Wendt, J. Appl. Polym. Sci. **13**, 1741 (1969).

[24] N. J. Hallab, K .J. Bundy, K. O. Connor, R. L. Moses, J. J. Jacobs, Tissue Eng. **7**, 55 (2001) .

[25] R. L. Williams, D. J. Wilson, N. P. Rhodes, Biomaterials **25**, 4659(2004).

[26] D. Bodas, C. K. Malek, Sensor Actuat. B. **123**, 368 (2007).

[27] J. Bacharouche, P. Kunemann, P. Fioux, M. F. Vallat, J. Laleve, J. Hemmerlb, V. Roucoules, Appl.Surf. Sci. **270**, 64 (2013).

Chapter 8

Summary

Present thesis discusses the modification of SiO_x, TiO_2 and PDMS surfaces through various techniques. Surfaces were ion beam irradiated (IBI) to create self assembled nanostructures. The patterning of surfaces by IBI method is a result of competition between surface erosion and diffusion mechanisms. PDMS being a chemically inert and hydrophobic polymer, was oxygen and nitrogen plasma etched to make it bio-compatible for cell adhesion. Single crystals of TiO_2 were UV illuminated, leading to chemical modification of the surface, thus creating functional groups for site specific attachment of molecules to these surfaces. The modified surfaces were interacted with DNA and cell. The salient points of the studies presented in this thesis are given here.

Chapter-1 presents basic concepts, theoretical description of nanostructure formation and nano-patterning of surfaces along with their importance in current research. Effects of UV illumination and Plasma etching on surfaces are also discussed. The chapter also reports the interaction mechanism of DNA with surfaces. Surfaces have been modified through several methods like ion irradiation, UV illumination and plasma etching. The synthesis methods, characterization techniques utilized in the studies reported in this

thesis, and the properties of materials are discussed in **chapter-2**.

In **Chapter-3** low energy ion irradiation with 3 keV Ar^+ ions at two fluences, 6×10^{15} and 1.8×10^{16} ions/cm^2, has been utilized to create nanopatterns on the SiO_x surfaces. These surfaces display formation of nanostructures as well as ripple patterns. These morphologies have been induced via competitive phenomenon of erosion and diffusion processes that take place on the surface during ion irradiation. The nanostructures grow in size and the ripple patterns become more distinct with fluence. The ripples show alignment behavior, with their wave vector **k** oriented along the ion beam direction. The results presented here show that the evolution of these SiO_x surfaces as well as their patterning, during irradiation, is primarily controlled by bulk diffusion processes. These surfaces were also interacted with circular plasmid DNA. With both DNA backbone and SiO_x being negatively charged, divalent (Mg^{2+}) cations play an important role, by making bridging layers, to induce DNA adsorption on the surface. Formation of nearly a single DNA monolayer, constituting of many loose DNA circles and their crossovers, is observed on the pristine (un-irradiated) surfaces. On the ion irradiated surfaces also, adsorption of a single DNA monolayer is observed. The diameter of the loose DNA circles in the network, however, appears to decrease with fluence. The Persistence length of the DNA, that defines its stiffness, is also observed to reduce on ion irradiated surfaces. Decrease in the size (ξ) and Persistence length (P) of DNA on the nanopatterned SiO_x is an important result indicating increased DNA flexibility which has enormous significance in cell packaging and medicine. Surface morphology as well as interactions with the surface, may be contributing to this flexibility. DNA adsorption on SiO_x surfaces indicates several types of chemical interactions as well as charge transfer. In addition to amino (-NH_2), imine (-N=) and amine(-NH-)

components from DNA bases, formation of Si_3N_4 confirms chemical interaction of DNA with SiO_x surfaces. Furthermore on ion irradiated surfaces, unzipping or unpairing of DNA bases, and absence of $H_2PO_4^-$ at the highest fluence, is also noticed. These results suggest severe modifications in the DNA moiety upon adsorption. These results can be important in biosensor related applications.

Chapter-4 investigates the roughening, wetting and scaling properties of the nanopatterned SiO_x surfaces. The nanopatterns were created using the low energy ion irradiation technique and have been discussed in detail in chapter 3. The nano patterns show formation of nanostructures and ripples which evolve with fluence. The pristine SiO_x surface has low rms roughness which initially increases after low irradiation fluence, but then shows a systematic decrease at higher fluences. Scaling studies demonstrate an attractive framework for understanding the evolution of non-equilibrium growing surfaces. Characteristic scaling parameter, roughness exponent or Hurst exponent (H) has been derived here by utilizing the height-height correlation function technique. The results show that these ion irradiated SiO_x surfaces are self-affine in nature i.e. they show self similar behavior upon asymmetric dilatation only. This self affine attribute reflects the fractal character of the SiO_x surfaces. The correlation lengths (ξ) increase on ion irradiated surfaces indicating the presence of long ranged correlations, due to enlarging nanostructures. These nano-patterned SiO_x surfaces show hydrophilic behavior. This however degrades with increasing fluence. The scaling properties of SiO_x surfaces have also been investigated after the adsorption of Plasmid DNA. Formation of 2-dimensional DNA network is observed on all the surfaces as discussed in chapter 3. Here, the height-height correlations results show that, after DNA adsorption, surfaces do not exhibit self affine

or fractal character anymore rather they now have 2- dimensional flat morphology. The surface roughness with $\sigma \leq 2$ further suggests that DNA form a single monolayer of adhesive layer on SiO_x. The fractal dimension of DNA (D_{dna}) has also been measured here using box-counting method. This fractal dimension is smallest on the pristine surface but increases on ion irradiated surfaces, indicating compactification of DNA towards a smaller- flatter unit on the nano-patterned surfaces.

The scaling properties of $TiO_2(110)$ surfaces, after irradiation with 3 keV Ar ions, have been discussed in **Chapter-5**. Ion irradiation leads to the spontaneous formation of self-assembled Ti-rich nanostructures (NS) as well as Ti^{3+} vacancy states. The NS thus formed are elliptical in shape and exhibit a shape transformation to less elliptical nature at high fluences. Scaling studies also reflect this transition. Scaling studies further reveal that the surfaces are self-affine in nature and with increasing fluence the regions of correlated structures, or fluctuations, spread and become bigger. This is connected to the formation of bigger NS, causing long-ranged correlations on the surface. On the other hand, at short length scales, the surfaces become less jagged as reflected by the roughness exponent of irradiated surface.

Chapter 6 presents the modifications of the TiO_2 surfaces upon UV irradiation as well as their interaction with the branched DNA. The UV irradiated TiO_2 surfaces show modifications in surface morphology, with their roughness increasing initially but then decreasing at the highest exposure. UV irradiation produces reactive oxygen species on the surface which contribute to the formation of surface hydroxyl states like Ti-OH as well as physically adsorbed water molecules. These UV modified surfaces have been interacted with branched DNA, which can be synthesized by self-assembly

techniques. The pristine (un-irradiated) TiO_2 displays formation of rod and toroid like structure of DNA on the surface. On the UV irradiated surfaces, however, only toroid like structures are observed. The sizes of toroids are initially observed to increase for surfaces irradiated up to 5min, however it decreases for higher exposure. This is related to the modifications of the surface roughness, which also initially increases but decreases at higher exposure. Role of interaction of DNA with the oxygen vacancies and surface states, created on the TiO_2 surface during UV irradiation, is also important. Interaction of branched DNA with ion irradiated TiO_2 surfaces has also been investigated here. After ion irradiation nano-patterns are created on the TiO_2 surfaces. These surfaces now, however, show very different morphology for DNA. Elongated networks of DNA rather than toroid structures are observed. Interaction of DNA with the oxygen vacancy as well as defect states present on the ion irradiated TiO_2 is again observed. Interestingly, a new state due to the formation of O-Ti-N complex is noticed. This suggests strong interaction of nitrogen bases with surface states on ion irradiated TiO_2.

Aim of **Chapter-7** is to study the effect of oxygen and nitrogen plasma treatment on physico-chemical properties of poly(dimethylsiloxane) (PDMS) and enhancement in its bio compatibility. It reports changes in the wettability after plasma treatments and the effects of ageing on wettability by contact angle measurement. Ageing studies presented in this chapter show that the contact angle becomes stable after two hours. The effect of plasma treatment on biocompatibility has been investigated through cell adhesion and MTT using 3T3 fibroblast cells. The analysis of morphology of cells on treated and untreated sample obtained through SEM with the utilization of ImageJ software show, substantial enhancement in bio-compatibility for nitrogen plasma treated surfaces. Nitrogen plasma treated PDMS for 5 min

presents highest cell area from cell adhesion test and highest cell viability observed from MTT test. This may be probably due to its highest polarity (0.4) and surface energy (33.3 Nmm^2) with a moderate surface roughness (R_{rms} 100.24 nm) among the other treated and untreated samples.

In conclusion, this thesis discusses the modifications of SiO_x, TiO_2 and PDMS surfaces as well as their interactions with DNA and the cell. Silicon is a widely used substrate for the immobilization of DNA. It provides an opportunity for integrating DNA with microelectronic technologies based on semiconductor industry. A natively oxidized silicon surface exhibits non-covalent type interactions with biological molecules. This promotes widespread development of such surfaces for biomimetic materials useful in tissue engineering and biological cell integration. In the present thesis, natively oxidized silicon SiO_x surfaces have been modified using ion beam irradiation technique. Ion irradiation leads to morphological as well as chemical compositional changes on the surface. Ion irradiation is a single step, cost effective technique which leads to the formation of self-assembled nanostructures on the surface, thus avoiding the utilization of expensive lithographic techniques for site specific immobilization of DNA. Ion beam irradiated SiO_x surfaces here display formation of ripple structures. Furthermore, these surfaces exhibit self-affine and fractal nature. These SiO_x nanostructured surfaces have been interacted with circular plasmid DNA and a 2-Dimensional DNA network is observed. The strong interaction of DNA with SiO_x surfaces is reflected by the unzipping of DNA bases as well as by the formation of Si_3N_4 complexes. TiO_2 is an immensely important materials for biomedical and dental implants because of its comparatively high corrosion resistance, good biocompatibility, light weight and high mechanical strength. In the present thesis TiO_2 surfaces have been modified through ion beam irradiation as well as by UV irradiation. Photo-

irradiation of TiO_2 surfaces with UV radiation promotes chemical changes of the surface, which are important for site specific binding of molecules. Controlled modifications in the chemistry as well as topography of surfaces play an important role in interaction with biomolecules. These can have potential applications in the enhancement of biosensing as well as 3D cellular scaffolding. The ion and UV irradiated TiO_2 surfaces have been interacted with branched DNA. Branched DNA structures play an important role in many applications in nanotechnology as they have been used for tailoring many impressive 3-dimensional objects, periodic array and nano-mechanical devices. In the present thesis, higher order condensed DNA structures, like toroids and rods have been observed on the UV beam modified surfaces whereas elongated network of DNA are observed on the ion irradiated surfaces. Formation of a new feature related to O-Ti-N further indicates strong interaction of nitrogenous DNA bases with ion irradiated TiO_2 surfaces. PDMS is a low cost polymer material exhibiting many exciting properties like gas permeability, optical transparency, low auto fluorescence and easy moldability. It has achieved immense attention as a substrate in mechno-biological as well as microfluidic applications. In the present thesis, PDMS surfaces have been modified by plasma etching technique using nitrogen and oxygen plasma. The energetic photons, electrons and ions present in the plasma break the polymer surface resulting in many surface modifications. The wetting behavior as well as the effect of aging on the wettability of PDMS surfaces have been investigated here. Furthermore, biocompatibility tests on these surfaces have been performed using cell adhesion and MTT for the fibroblast cells. Since the fibroblast cells are immortalized cells which can grow indefinitely in a culture, they present a cost effective route for monitoring the toxicity in compounds and drugs. Results presented here show that the PDMS surfaces irradiated by 5 mins of nitrogen plasma exhibit highest biocompatibility.

The results presented in this thesis on the controlled surface modifications of SiO_x, TiO_2 and PDMS surfaces, and their interaction with DNA and cell, can be important in bio -devices, bio-sensors, surgical implants and microarray related applications.